BULGARIAN CHEMICAL COMMUNICATIONS

2025 Volume 57 / Number 3

Papers presented at the 11th International Conference on New Trends in Chemistry, April 25-27, 2025, Bologna, Italy

Journal of the Chemical Institutes
of the Bulgarian Academy of Sciences
and of the Union of Chemists in Bulgaria

Bulgarian Chemical Communications, Volume 57, Issue 3 (pp. 139-143) 2025 DOI: 10.34049/bcc.57.3 BE-YG

Theoretical examination of paroxetine HCl, the active ingredient of the drug marketed as Paxil, used in antidepressant treatment, using the DFT method

B. Eren[1*], Y. Yalcin Gurkan[2]

[1] *Tekirdag Namik Kemal University, Tekirdag, Turkey*
[2] *Tekirdag Namik Kemal University, Department of Chemistry, Tekirdag, Turkey*

Received May 7, 2025; Accepted: August 15, 2025

Paroxetine HCl (PA) is a non-steroidal anti-inflammatory drug active ingredient, marketed as Paxil, a selective serotonin reuptake inhibitor antidepressant. In this study, PA was theoretically examined according to this pharmaceutical effect, that is, treatment group and site of action. Selected molecule is used for therapeutic purposes, but their fate in nature is not taken seriously when it is eliminated from the body or become waste when it is not used. The aim of this study is to theoretically explain the traces of both the molecule and its hydroxylated fractions in nature, which are included in the natural cycle via wastewater as a result of the unused Paroxetine HCl molecule being thrown into the garbage and therefore into nature.

In order to theoretically determine the degradation mechanism of the selected molecule, geometric optimizations were performed on the DFT/B3LYP/6-31G(d) basic DFT set. Mulliken charges of electronegative atoms in the molecule, arrangement of atoms, double and single bonds, calculated energy values, bond lengths and bond angles between atoms were effective in selecting all the parts that would determine the degradation mechanism. As a result of examining the reactions of molecules with the OH radical in air or water, the degradation paths they would follow in nature were determined.

Keywords: Paroxetine HCl, Paxil, DFT, antidepressant, OH radical, drug

INTRODUCTION

In this study, Paroxetine HCl (PA), one of the five molecules investigated in the scientific research project titled "Investigation of Theoretical Degradation Mechanisms of Selected Pharmaceutical Product Active Ingredients", is examined.

PA is a non-steroidal antidepressant drug active ingredient, marketed as Paxil, a selective serotonin reuptake inhibitor antidepressant. It is used to treat major depression, obsessive compulsive disorder, panic disorder, social anxiety disorder, post-traumatic stress disorder, generalized anxiety disorder, and night sweats associated with menopause. Treatment is stopped by gradually reducing the dose over several weeks to months. It has been observed to cause an increase in suicidal thoughts in depressed children and adolescents. It also has temporary side effects such as nausea, diarrhea, constipation, dry mouth, drowsiness, insomnia, headache, blurred vision, irritability, dizziness, tremors, and sexual dysfunction [1-6]. PA, which is an odorless off-white powder with a molecular formula of $C_{19}H_{20}FNO_3$ and a molecular weight of 329.4 g/mol, has a melting point of 120-138 °C, a melting point of solid PA of 147-150 °C, a boiling point of 451.7 °C, and water solubility of 1.131 mg/L at 25 °C [7].

In this study, PA was theoretically examined according to its pharmaceutical effect, that is, treatment group and site of action. Selected molecule is used for therapeutic purposes, but its fate in nature is not taken seriously when it is eliminated from the body or becomes waste when it is not used. The aim of this study is to theoretically elucidate the fate of both the main molecule and its hydroxylated fragments in nature as they enter the natural cycle by mixing with wastewater.

PA is a biomolecule with hydroxylation ability, in other words, it can interact with OH radicals. Radical attack on an aromatic ring can result in the formation of a new fragment that can be much more harmful than the starting molecule. Therefore, it is very important to know the degradation mechanism of the molecule [8]. Organic compounds undergo photolysis by reacting with the OH radical, and this reaction is the main cause of decomposition reactions in the atmosphere. In reactions between hydroxyl radicals and organic molecules, the OH

* To whom all correspondence should be sent:
E-mail: *beren@nku.edu.tr*

radical acts as an electrophile and the O radical acts as a nucleophile. Therefore, the OH radical easily binds to unsaturated bonds, while the O radical cannot interact with them. In addition, in the presence of an aliphatic side chain attached to an aromatic molecule, the OH radical prefers to bind to the aromatic ring [8-15].

This study examines the possibility of obtaining more hazardous substances through hydroxylation of the PA molecule, whether it is released into the atmosphere in the gas phase or into the water cycle *via* wastewater. As we mentioned in the article of the first researched molecule of our project, what is ignored or not given much importance when pharmaceutical products are launched on the market is the question of what would happen if the product used for treatment mixes with nature [16].

MATERIALS

Theoretically, geometric optimizations were performed in the DFT/B3LYP/6-31G(d) basis set of Quantum Mechanical Density Functional Theory, one of the electronic structure methods, to determine the degradation pathways of PA. Geometric optimizations for all parts were performed using Gauss View 5.0.8 molecular representation program. In this study, CPCM in the COSMO (conductor-like screening solvation model) solvent model in the Gaussian 09 package program was used to explain the solvent effect of H_2O on the reaction energy between PA and OH radical [17].

RESULTS AND DISCUSSION

When theoretical chemists look at a molecule they are studying, they think about where it will start to break apart. To avoid any doubt, they start by breaking off the atoms at the ends of the molecule one by one and examine the consequences of each separation. In order to make a decision, firstly the geometric optimization of the molecule under study, that is, its three-dimensional appearance, then the bond lengths and bond angles between atoms, the Mulliken charges of electronegative atoms and most importantly the energy values of each fragment are examined [16, 18, 19].

Although it is predicted that the longest bond and the widest bond angle between atoms in any molecule will break first, the decision is made by examining the multivalent charges of electronegative atoms and the energy values of each fragment. It should be kept in mind that double-bonded or closed-ring structures are more stable than others and that if fragmentation occurs, the breakage from these stable structures will be at the last stage, in other words, the single bonds at the end of the molecule will tend to separate from the molecule more easily [16, 18, 19].

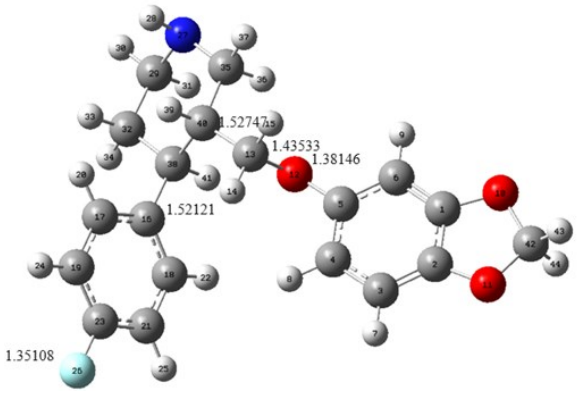

PA(a)

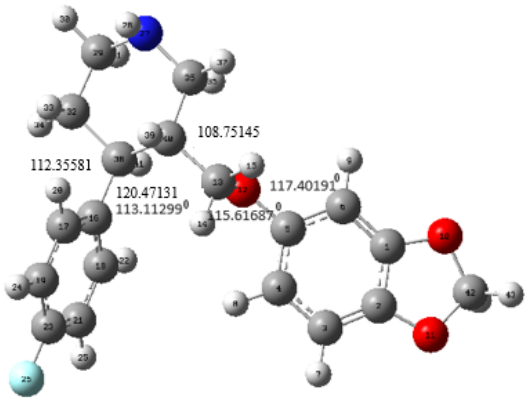

PA(b)

Figure1. The bond lengths between atoms in the PA molecule are shown in PA(a) and the bond angles in PA(b) (C atom is represented in grey, O atom in red, N atom in dark blue, F atom in blue and H atom in white).

According to PA (a) in Figure 1, it is predicted that the bond breaking will be first around the bond length of $C_{13}C_{40}$ and $C_{16}C_{38}$, respectively; and when we look at PA (b) in Figure 1, it is predicted that the bond breaking will be first around the bond angle of $C_{38}C_{16}C_{18}$.

According to the Mulliken charges of the PA molecule presented in Table 1, the electronegative atoms are O_{12}, O_{11}, O_{10}, F_{26}, N_{27}, respectively. Since O_{11}, O_{10} and N_{27} are in a closed ring, the first degradation is not expected to occur here. We can say that O_{12} is the most electronegative atom and one of the degradation paths starts with breaking away from here. Although F_{26} is the 4th electronegative atom, it is located at the end of the molecule. In molecules, the terminal parts are the first parts to be separated in the fragmentation path, unless there are any special conditions (closed ring, double bonded atom, etc.).

The energy values of the possible reaction paths for the studied molecule PA and all its fragments

were calculated both in the gas phase and in the water phase. Every fragment that may be formed because of the interaction of the PA with the OH radical was included in the study. As clearly seen in Table 2: PA1, PA3 and PA2 fragments are the most stable fragments and, respectively, have the lowest energy.

Table 1. Bond lengths and bond angles between atoms in the PA molecule and Mulliken atom charges of the PA molecule

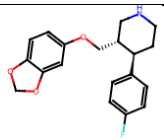

Bond lengths	(A^0)	Bond angles	(^{0})	Mulliken atom charges	
C_5O_{12}	1.38146	$C_5O_{12}C_{13}$	115.61687	C_3	-0.044557
$C_{13}O_{12}$	1.43533	$O_{12}C_{13}C_{40}$	108.75145	C_4	-0.049626
$C_{13}C_{40}$	1.52747	$C_{32}C_{38}C_{16}$	112.35581	C_6	-0.084981
$C_{16}C_{38}$	1.52121	$C_{38}C_{16}C_{18}$	120.47131	O_{10}	-0.532583
$C_{23}F_{26}$	1.35108	$C_{40}C_{38}C_{16}$	113.11299	O_{11}	-0.533305
				O_{12}	-0.551004
				C_{17}	-0.055576
				C_{18}	-0.051571
				C_{19}	-0.052870
				C_{21}	-0.052294
				F_{26}	-0.299715
				N_{27}	-0.241867
				C_{32}	-0.007642
				C_{38}	-0.027975
				C_{40}	-0.007487

Table 2. ΔE (energy), ΔH (enthalpy) and ΔG (Gibbs free energy) values of PA molecule and its fragments in gas and water phases

(Au)	PA	PA1	PA2	PA3
ΔE	-1115.901943	-1016.661385	-696.425937	-785.699939
ΔH	-1115.900999	-1016.660441	-696.424993	-785.698994
ΔG	-1115.974133	-1016.732302	-696.480191	-785.757346
		-1016.671934	-696.435342	-785.708994
Water phase		-1016.670990	-696.434398	-785.708050
		-1016.742818	-696.489460	-785.766289
	PA4	PA41	PA42	PA5
	-621.228352	-521.987682	-581.943520	-535.139137
Gas phase	-621.227408	-521.986738	-581.942575	-535.138193
	-621.279685	-522.036912	-581.992043	-535.182765
	-621.234407	-521.993481	-581.949644	-535.145383
Water phase	-621.233463	-521.992537	-581.948699	-535.144439
	-621.285699	-522.042637	-581.998093	-535.189027
	PA6	PA7		
	-495.863539	-420.655009		
Gas phase	-495.862594	-420.654065		
	-495.902120	-420.690901		
	-495.871824	-420.659593		
Water phase	-495.870880	-420.658649		
	-495.910451	-420.695505		

The C_{23}-F_{26}, C_{16}-C_{38} and O_{12}-C_5 bonds in Figure 1 were broken, resulting in the formation of PA1, PA3 and PA2 fragments. As we clearly observe in Table 2, these three fragments have the lowest energy values, meaning that they participate in the fragmentation process voluntarily (no external energy is required). According to the broken C_{23}-F_{26}, C_{16}-C_{38} and O_{12}-C_5 bonds in Figure 1, PA1, PA3 and

PA2 are formed, respectively, as shown in the degradation mechanism in Figure 2. The bond length of C_{16}-C_{38} has already been stated in Table 1 as the second-longest bond length, 1.52121 Å. Although C_{23}-F_{26} has the shortest bond length with a value of 1.35108, it is ready to break at the very end of the molecule. Since the lowest Mulliken charge in Table 1 is -0.551004 (O_{12}), this is reason enough to pay attention to the arrangement of this electronegative atom and its surrounding atoms. For each atom in the PA molecule, the Mulliken charges in Table 1, stable double bonds, weak single bonds at the end of the molecule, the calculated energies given in Table 2, the bond angles and lengths between the atoms shown in Figure 1 and Table 1 were considered as a whole. All these data helped us to determine the parts in the degradation mechanism. PA1, PA2 and PA3 parts were determined, and it was also clarified which of the three branches the degradation would start from. After this, the degradation up to the stable rings or carbon dioxide and water molecules that will be formed with their degradation can be written with similar thinking. In this study, the sample degradation prediction is shown in Figure 2.

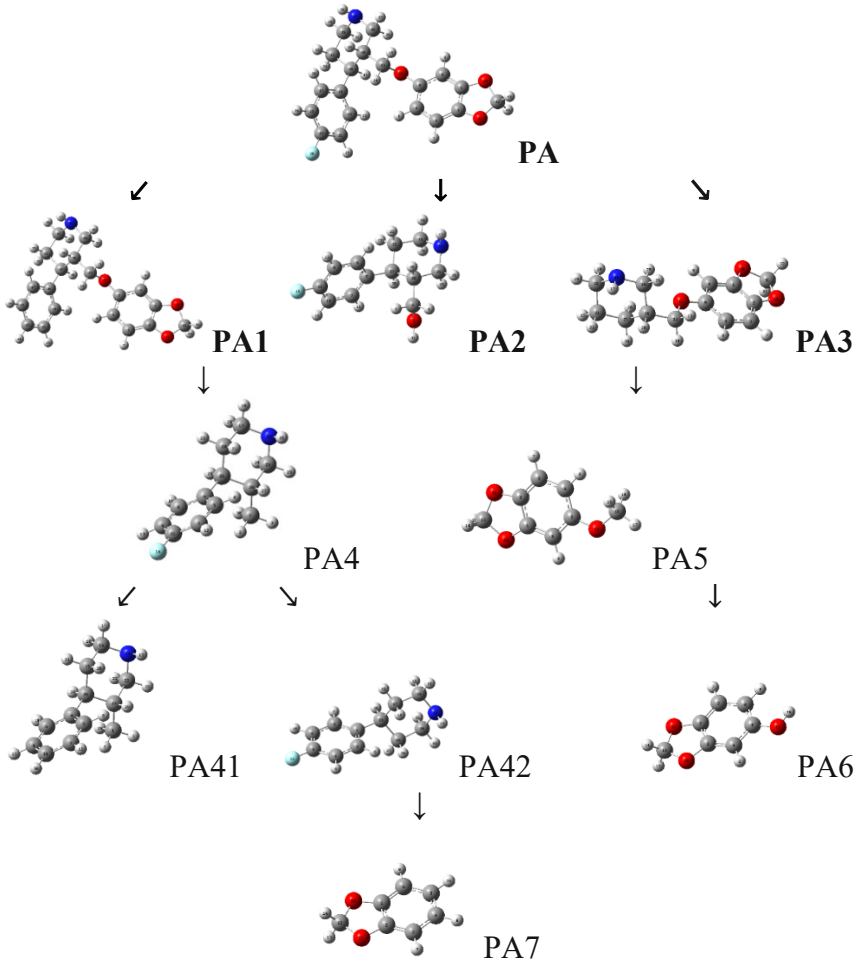

Fig. 2. Pathway of PA molecule (degradation mechanism) (C atom is represented in grey, O atom in red, N atom in dark blue, F atom in blue and H atom in white)

CONCLUSION

The fate of pharmaceutical products, commonly known as drugs, in nature has not yet been investigated when they are used and excreted from the body or when they become waste without being used. PA is one of the molecules selected for our completed project from three different groups, which are effective as anti-inflammatory, antidepressant and calcium channel blocker, according to their pharmaceutical effects (in other words, treatment groups) and effect regions. The degradation mechanism for Apranax (AP), marketed as Naproxen or Naproxen sodium (NS), which has analgesic and anti-inflammatory effects, has been determined and published [16]. The degradation mechanism of Paroxetine HCl (commercial name Paxil), an antidepressant, is shown in Figure 2.

The main purpose of this study is to explain theoretically what will happen to the PA molecule and its hydroxylation products during degradation in nature. The OH radical is a selective organic molecule scavenger. As a result of the reaction of the

PA molecule with hydroxyl radicals in air or water, the mechanism was written starting from the low energy parts. In our study, the path followed by the investigated active pharmaceutical ingredient in nature, water or atmosphere was theoretically examined without using any chemical substance. If desired, when the necessary samples are taken from wastewater and analysed with HPLC, they can be compared with the fragments determined in our fragmentation reactions. Our previous experimental study on the removal of carbamate and organophosphate pesticides from nature using advanced oxidation techniques will also guide researchers who want to use UV in this regard [19].

Acknowledgement: *The current study was supported by Tekirdag Namik Kemal University Scientific Research Project Coordination Centre, (Project No: NKUBAP.00.GA.23.506).*

REFERENCES

1. P. L. Hensley*, Journal of Affective Disorders*, **92**, 117 (2006).
2. A. Venkatachalam, V. S. Chatterjee, *Analytica Chimica Acta*, **598**, 312 (2007).
3. V. Stearns, C. L. Loprinzi, *The Journal of Supportive Oncology*, **1**, 11 (2003).
4. A. Bakker 1, A. J. van Balkom, R. van Dyck, *Int. Clin. Psychopharmacol.*, **15**, 25 (2000).
5. R. Ommaty, Vademecum: medical drug reference book, Tribune publishing ltd company. Istanbul, 2008.
6. https://www.drugbank.ca/drugs/DB00788
7. M. J. O'Neil, The Merck Index- An Encyclopedia of Chemicals, Drugs, and Biologicals. Cambridge, UK, 2013.
8. B. Eren, Y. Yalcin Gurkan, *J. Serb. Chem. Soc*., **82**, 277 (2017).
9. M. Anbar, P. Neta, *Int. J. Appl. Radiat. Isot*., **18**, 493 (1967).
10. S. M. Aschmann, E. C. Tuazon, R. Atkinson, *J. Phys. Chem.,* A, **109**, 11828 (2005).
11. S. M. Aschmann, R. Atkinson, *J. Phys. Chem.,* A, **110**, 13029 (2006).
12. S. M. Aschmann, E. C. Tuazon, W. D. Long, R. Atkinson, *J. Phys. Chem*., A, **114**, 3523 (2010).
13. R. Atkinson, S. M. Aschmann, M. A. Goodman, A. M. Winer, *Int. J. Chem. Kinet*., **20**, 273 (1998).
14. R. Atkinson, J. Arey, *Chem. Rev.,* **103**, 4605 (2003).
15. B. Halliwell, M. Grootveld, J. M. C. Gutteridge, *Methods Biochem. Anal.,* **33**, 59 (1998).
16. B. Eren, Y. Yalcin Gurkan*, Bulgarian Chemical Communications*, **56**, 3 (2024).
17. Gaussian 09, Revision B.04, Gaussian, Inc., Pittsburgh, PA, 2009.
18. B. Eren, Y. Yalcin Gurkan, Innovative Research in Engineering, Duvar Publishing, İzmir, Turkey, 2023, 4, p. 49.
19. B. Eren, Y. Yalcin Gurkan, *International Journal of Advanced Natural Sciences and Engineering Researches,* **7**, 7 (2023).

Bulgarian Chemical Communications, Volume 57, Issue 3 (pp. 144-147) 2025 *DOI: 10.34049/bcc.57.3.BC-IK*

Effect of heavy metals in metal plating plant waste sludge on tea plant primary development

B. Didem Çorbacıoğlu*, İ. Küçük

Yildiz Technical University, Department of Chemical Engineering, Istanbul, Türkiye

Accepted: August 17, 2025

Heavy metals, some of the elements that damage nature, are known to have macroscopical, microscopical, and physiological effects on plants' vegetative organs. All living creatures that continue to live active lives in nature are impacted by this unfavorable circumstance, including the generative and vegetative organs of plants. Without understanding the consequences, people have been using heavy metals for ages in a variety of applications, including jewelry, weaponry, water pipes, etc. Coal that contained heavy metals started to be burned as a result of industrialization, and because our world is exposed to more and more industrial areas and traffic every day, the amount of heavy metal pollution combined with many other pollutants has increased to extremely high levels.

In addition to building up in living things, these compounds can persist in ecosystems for extended periods of time at hazardous amounts and move up the food chain. It is widely accepted that humans are the primary source of heavy metals' expansion and ecological harm when taking into account their dispersion in nature. Heavy metal concentrations are high in the environment due to ongoing pollution and usage-related factors. This concentration has a detrimental effect on natural plants and produces highly hazardous compounds for human health. This study used data from the greenhouse study on the tea plant to evaluate the sludge released for waste disposal in the metal coating facility in fertilizer production. Significant statistical results were obtained in terms of agricultural chemistry, and the topic of evaluation within the framework of the circular economy was discussed.

Keywords: tea plant, heavy metal, toxic effect, boron fertilizer, compound fertilizer

INTRODUCTION

People have always been fascinated by the natural world and the things that happen there. The development of organs like roots, stalks, and leaves by seeds that sprout in specific soil circumstances was one of the major topics that early humans were interested in because plant life has always been essential to human survival as a source of food, raw materials, and energy. Through their roots, plants may readily absorb the materials they require to grow and finish their physiological phases from the earth. In the same form as they are present in plants, these chemicals can also be found in soil. Many people think that these compounds that are present in plants are imported [1]. In plant nutrition, each nutritional component plays a distinct purpose and needs to be delivered to the plant in a balanced way. As they absorb nutrients, plants—which are extremely important to agriculture—face a variety of external factors. These adverse impacts are a major factor in reducing the plant's vitality. "Plant nutrient elements" are the components that plants require in order to survive. When plant tissues are analyzed, practically every element present in nature can be detected. Despite the fact that plants are selective in their nutrient ion intake, some heavy metals that can passively enter the plant body are absorbed by the plants and added to the food chain as the percentage of nutrients in a usable form in the growing environment rises. They may therefore be harmful to plants, as well as to people and animals that consume plants because plants absorb elements from their surroundings, whether or not they are essential to them, even in trace amounts. Nonetheless, all plants require 16 of these elements—C, H, 0, N, P, K, S, Ca, Mg, Fe, Zn, Mn, Cu, B, CI, and Mo—as vital nutrients. The remaining six elements—Co, AI, Na, Si, Ni, and V—are helpful but only deemed essential for specific plants or processes [2]. The number of heavy metals and several other contaminants in the environment is increased by both fast industrialization and exposure to growing traffic density. Numerous negative effects result from this circumstance, including the loss of products in plants that are unable to move [3]. Environmental pollution is seen as one of the most significant issues brought about in nature by urbanization and industrialization [4]. Fungicides and wood preservatives that contain metals have been said to damage soil and plants.

* To whom all correspondence should be sent:
E-mail: *bcorbaci@yildiz.edu.tr*

These products are commonly employed by mining, metal and chemical companies, and gases and dusts are released by major industrial complexes [5]. For plants that grow in this kind of soil, heavy metal pollution in particular presents a serious risk. In order to boost production, extensive research is being conducted on soils containing this kind of heavy metal pollution using various reclamation techniques [6].

The productivity of soil and plants is negatively impacted by the amount of different gases and particles in the atmosphere, air pollution, and waste from manufacturing chimneys. All living creatures are now at risk from air and heavy metal pollution, which began as a result of industrial development and has been becoming worse since the second part of the 20th century. Since plants are the main producers in ecosystems, they are far more at risk. Numerous studies have found that these metals have a major impact on plants' vegetative organs. However, according to Kapitonova (2002), metal contamination impacts both the generative and vegetative organs [7].

"A metal with a relatively high density and which is toxic or poisonous even at low concentrations" is the definition of a heavy metal, which is typically encountered when environmental issues arise. In actuality, metals with a density greater than 5 g/cm^3 in terms of physical characteristics are classified as heavy metals. This category comprises over 60 metals, such as lead, cadmium, chromium, iron, cobalt, copper, nickel, mercury, and zinc. Because of their nature, these elements are typically found on Earth in stable compounds like carbonates, silicates, and sulfates, or bonded in silicates [8]. High amounts of some heavy metals can harm humans, animals that eat plants, and plants themselves. If soil contains 10–100 mg/kg of chromium, nickel, and lead, and less than 1 mg/kg of cadmium, these elements are regarded as typical. As environmental contaminants, cadmium and lead pose major health risks to both humans and animals. While nickel may be carcinogenic to the same group of organisms, chromium is an important microelement that is harmful to mammals and other animals at high doses. Nonetheless, it is now acknowledged that nickel is a necessary nutrient for higher plants. When extractable heavy metal concentrations in soils exceed 1 mg/kg for Cd, 10 mg/kg for cobalt, 0.1 mg/kg for copper, 10 mg/kg for selenium, 0.5-1 mg/kg for vanadium, and 100 mg/kg for nickel, toxic effects may ensue [9]. Cd, Pb, and Hg are said to be the most hazardous heavy metals [10]. Some metals are actual components of global ecosystems, and they are found in nature. Life depends on metals like zinc and copper. The system of enzymes that controls plant metabolism depends on zinc. Nevertheless, it is unknown if other metals, such lead and mercury, have any practical biological purpose [11]. Except for mercury and lead, which are toxic and unnecessary elements, copper and zinc are micronutrients required for the majority of enzyme activities and are part of molecules that play a crucial role in photosynthetic electron transport, even though they are toxic at high concentrations [12].

EXPERIMENTAL

ICP-OES ion chromatography analysis

In the study, HORIBA France SAS brand Ultima Expert LT Model ICP OES device was used for heavy metal content analysis of damaged tea leaves in the greenhouse. The 25.5.10 fertilizer used during the study was produced under laboratory conditions and the relevant composition was prepared by using the chemical compounds shown in Table 1.

Table 1. 25.5.10 compound fertilizer chemical composition

Chemical composition	Chemical formula	CAS number	Amount (%)
Diammonium phosphate	$(NH_4)_2HPO_4$	7783-28-0	9,3
Urea	CH_4N_2O	57-13-6	49,4
Potassium chloride	KCl	7447-40-7	15,2
Volcanic ash-perlite	SiO_2	93763-70-3	24,5
Wet mud/ dry mud/ dry phosphate/ wet phosphate/ dry carbonate/ wet carbonate	-/-/PO_4/CO_3	-	1

During the preparation of 25.5.10 fertilizer, the contribution of “wet mud/ dry mud/ dry phosphate/ wet phosphate/ dry carbonate/ wet carbonate” was 1%.

RESULTS AND DISCUSSION:

For the 25.5.10 compound fertilizer, which is the most produced and has the highest sales potential fertilizer for the tea plant as a waste material in the electrolytic metal coating industry, 6 different chemical compositions were studied depending on the trace element content of the raw material source. The toxic effect of the 25.5.10 fertilizer of these 6 different chemical compositions on the tea plant, especially on the leaves, during its development is shown in Figures 1-6. In this respect, the toxic effect of the waste material number 1 in Figure 1 during the

development of the plant is seen as a brown-yellow color effect.

The aluminum and boron contents, in the concentrations specified in Table 1, were obtained by adding 1% to the 25.5.10 fertilizer of wet sludge, as shown in Figure 1. As can be seen in Figure 1, in a greenhouse application for 1 month, at 35 °C and 65% humidity, the metal concentration was as follows: brown and yellow spots formed from the outside to the inside of the leaf.

Figure 1. Effect of 25.5.10 fertilizer with wet sludge additive on tea leaves

Figure 2. Effect of dry sludge added 25.5.10 fertilizer on tea leaves

Figure 3. Effect of wet carbonate added 25.5.10 fertilizer on tea leaves

On the other hand, when waste number 2, expressed as dry sludge, was added to 25.5.10 fertilizer at 1%, a result like in Figure 2 was obtained. As seen in Figure 2, brown and yellow areas are more than 25.5.10 fertilizer with wet sludge content. The reason for this is that in the ICP OES analysis, especially Al and B content is higher than wet sludge content.

However, the heavy metal analysis of wet carbonate sludge released as a result of the phosphatization process as a metal industry waste is shown in Table 2. Based on this, in the greenhouse study conducted, as a result of the addition of a maximum of 5 g of 25.5.20 fertilizer per pot, brown and yellow color decreases were observed in tea leaves from the outside to the inside under the same greenhouse conditions (35 °C, 65% humidity) (Figure 3).

Unlike the wet carbonate-containing waste, dry carbonate contains approximately 20% moisture, however, a dramatic decrease in heavy metal concentrations is observed from the ICP-OES analysis results in Table 1. Based on this, in the results of the greenhouse study conducted, in the same amount of 25.5.10 fertilizer, a decrease in the rate of brown and yellow spots is observed compared to the images in Figures 1, 2 and 3, as seen in Figure 4.

Figure 4. Effect of dry carbonate added 25.5.10 fertilizer on tea leaves

Figure 5. Effect of 25.5.10 fertilizer with wet phosphate additive on tea leaves

Figure 6. Effect of dry phosphate added 25.5.10 fertilizer on tea leaves

Another material used in the fertilizer industry as metal industry waste is phosphate. Carbonate is evaluated in terms of moisture content according to the process in which it is produced and is called dry phosphate and wet phosphate. As can be seen from the ICP-OES results in Table 2, metal contents are close to each other, and as a result of the greenhouse study, the healthiest leaves were seen in the greenhouse study of 25.5.10 fertilizer to which this waste material was added in order to preserve its natural color (Figures 5, 6).

The effect of only 25.5.10 fertilizer on the development of tea plants in the greenhouse without the addition of the metal industrial waste, which is the subject of the study here, is shown in Figure 7. As shown in Figure 7, since 25.5.10 fertilizer does not contain any heavy metal content, it can be stated that there is no toxic effect, because no brown or yellow spots are observed on the tea leaves.

Figure 7. Effect of 25.5.10 fertilizer without any waste material additive on tea leaves

Table 2. Heavy metal ICP-OES content analysis of 6 different compositions added to 25.5.10 fertilizer as metal industry waste

		Al	B	Co	Cr	Cu	Fe	Mn	Ni	Pb	Zn	Ca	K	Mg	P	S	K_2O	P_2O_5	SO_3
Sample	No	ppm	ppm	ppm	ppm	ppm	ppm	ppm	ppm	ppm	ppm	ppm	ppm	ppm	ppm	ppm	ppm	ppm	ppm
Wet mud	1	186596	207	477	6845.5	861.37	142364	15004	21772	230	218020	12.56	4.38	0.95	27.14	0.57	5.28	62.25	1.43
Dry mud	2	777334	1140	2166	33124	4545.6	438036	60365	91839	989.4	348800	58.85	24.85	4.28	118.45	2.84	29.94	271.68	7.1
Dry phosphate	6	2697.6	35	2.73	2983.4	217.92	584053	92377	81131	1292	318462	4.91	21.45	0.09	152.72	0.21	25.84	350.27	0.52
Wet phosphate	5	899.19	13.3	34.7	1055.9	71.11	368403	38226	29272	463.9	197378	1.63	7.14	0.03	65.54	0.09	8.61	150.33	0.21
Dry carbonate	4	120.56	104	2.73	5.14	26.21	364.93	6.4	941.66	2.49	11255	0.03	2.1	0	-0.07	17.5	2.53	-0.16	43.75
Wet carbonate	3	98.19	133	3.5	5.63	13.55	194.26	6.43	909.35	-0.52	10539	0.07	1.53	0.03	-0.15	23.22	1.84	-0.35	58.04

Heavy metals endanger the development of plants and animals, and also pose a hazard to human health in particular. Our environment is heavily polluted with heavy metals from industrial wastes that are growing daily as a result of growing industrialization and the acceleration of motor vehicle production. Agricultural areas also bear a portion of this pollution. European nations, which are especially concerned about the environment, have passed strict environmental laws and regulations and protected their soil and water resources, which are the most prized assets in agriculture. From an industrial standpoint, it is very pleasant that lead-containing gasoline production has ceased in recent years; yet, this is not thought to be adequate to reduce industrial waste. Enacting strict laws and regulations as soon as possible is crucial to protecting our water and soil resources from the dangers posed by heavy metal pollution.

The most harmful effects of heavy metals in soil include their ability to penetrate plant structures, their ability to mix with groundwater when they become mobile (as free ions), their ability to damage microorganisms, their ability to enter the food chain and indirectly harm other living things, their ability to cause plasma hardening in cells, swelling and shrinkage, protein precipitation, and a decrease in respiratory intensity and, consequently, oxygen consumption. The concentration of heavy metals, their form of presence (metal, ion, organic compound, etc.) species, duration of action, location, etc., all affect how poisonous they are. Agronomic practices like pH adjustments, organic matter and fertilizer management, proper plant selection, physical stabilization, strong acid washing, liming, phosphorus fertilizer application, washing with heavy metal chelators, and phytoremediation techniques can all help reduce the amount of heavy metals in soil.

As can be seen from the current results of this study, when the chemical compositions prepared in the form of wet sludge, dry sludge, wet phosphate,dry phosphate, wet carbonate and dry carbonate of the metal plating industry were compared with the 25.5.10 fertilizer which does not contain any of these additives, the toxic effect of this waste material was revealed by brown and yellow spots on the development of the tea plant which was the subject of the greenhouse study, as can be seen from the analysis results.

REFERENCES

1. D. S. Newsome, *Catal. Rev.–Sci. Eng*., **21**, 275 (1980).
2. H. A. Hassoon, *Iraqi J. Agric. Sci.,* **49**, 5 (2018).
3. M. Imtiaz, M.S. Rizwan, M. A. Mushtaq, M. Ashraf, S.M. Shahzad, B. Yousaf, S. Tu, *J. Environ. Manag.*, **183**, 521(2016).
4. M. Farooq, A. Wahid, N. S. M. A. Kobayashi, D. B. S. M. A. Fujita, & S.M. Basra, Plant drought stress: effects, mechanisms and management. In Sustainable agriculture, Dordrecht, Springer Netherlands, **1**, 153 (2009)
5. Y. Hu, X. Liu, J. Bai, K. Shih, E.Y. Zeng, & H. Cheng, *Environ. Sci. Pollut. Res. Int.,* **20**, 6150 (2013)
6. V. Chopra, A. Sharma, in: Evaluation of Environmental Contaminants and Natural Products: A Human Health Perspective , **1**, 23, Bentham Science Publishers, 2019.
7. M.A. Ashraf, I. Hussain, R. Rasheed, M. Iqbal, M. Riaz, & M.S. Arif,. *J. Environ. Manag.*, **198**, 132 (2017).
8. O.A. Kapitonova, *Russ. J. Ecol.*, **33**, 59(2002).
9. C. Thomazo, D.L. Pinti, V. Busigny, M. Ader, K. Hashizume, P. Philippot, *Comptes Rendus Palevol.,* **8**, 665 (2009).
10. K.W. Fried, K.K. Rozman, K.H. Summer, S. Halbach, H. Kappus, H. Greim, T. Zilker, Toxicology and risk assessment: A comprehensive introduction, Chichester, UK, John Wiley & Sons Ltd, **1**, 2008, p. 513.
11. Z. Rahman, V.P. Singh, *Environ. Monit. Assess*, **191**, 1 (2019).
12. M. Balali-Mood, K. Naseri, Z. Tahergorabi, M.R. Khazdair, M. Sadeghi,. *Front. Pharmacol.*, **12**, 643972 (2021).
13. D.K. Tripathi, S. Singh, S. Mishra, D.K. Chauhan, N.K. Dubey, *Acta Physiol. Plant*, **37**, 1 (2015).

Bulgarian Chemical Communications, Volume 57, Issue 3 (pp. 148-153) 2025 DOI: 10.34049/bcc.57.3.DU-GC

Obtaining valuable components from various citrus product wastes by different extraction methods

D. Uygunöz, G. Çifçi, Ö. Ozan Demirci, E. Möröydor Derun*

Department of Chemical Engineering, Yildiz Technical University, 34210, Istanbul, Türkiye,

Accepted: August 17, 2025

This study aimed to obtain valuable components from various citrus product wastes using conventional and ultrasonic-assisted extractions. Wastes obtained from orange, mandarin, and lemon fruits, the three most commonly grown citrus fruits in Türkiye and around the world, were used as raw material sources [1]. Green extraction techniques stand out with features such as higher efficiency, shorter time requirement, and lower cost when compared to traditional extraction techniques [2]. By comparing extraction techniques, multifaceted comparisons were made between the citrus types used as raw materials and the properties of the valuable components to be obtained. The valuable components targeted to be extracted from citrus fruits were determined as pectin and hesperidin, considering their industrial usage areas [3]. Citrus fruit wastes were dried, and the moisture content of each citrus species was determined, then the citrus species were extracted by using conventional and ultrasonic-assisted extraction methods. Extracts were characterized by using Fourier transform infrared spectrometry (FTIR), ultraviolet-visible spectrometry (UV-VIS) and liquid chromatography-mass spectrometry (LC-MS) analyses. According to UV-Vis analysis, the band covering the range of 240–280 nm (max absorbance around 255–265 nm) was attributed to the A–C benzoyl system, confirming the flavonoid structure. All extracts showed similar peaks in FTIR analysis [4]. Hesperidin content of the optimized mandarin extract determined by LC-MS analysis was 430.2 $mg.L^{-1}$. It is envisaged that the extracted valuable components will be used in various industrial areas. In the future, it is aimed to add the bioactive component data obtained as extracts to the literature.

Keywords: Citrus waste; extraction; bioactive component; quantitative analysis

INTRODUCTION

Citrus fruits, known as the *Rutaceae* family, are a fruit family with an annual production exceeding 130 million tons as of 2015. Citrus fruits are crucial for Turkish agriculture, particularly in the Mediterranean region. Around 2168,000 tons of citrus fruits are produced annually, with oranges, tangerines, and lemons being the main varieties. Around 20% of the citrus plants are used for industrial purposes, generating significant waste. The most cultivated citrus species are orange, tangerine, lime, lemon, grapefruit, citrus and bergamot [5].

The peel parts of citrus products, which are produced because of their consumption and use in industrial processes and are called waste, have a high content of valuable components. The by-products can be utilized for livestock feed, biofuel production, and for the extraction of pectin, phenolic compounds, and essential oils. With the extraction applied on citrus waste, it is aimed to prevent the loss of high amounts of valuable components. Examples of components found in citrus fruits include ascorbic acid compounds, carotenoids, essential oils, antioxidants, sugars, flavonoids, dietary fibers, polyphenols, and minor elements. Waste and by-products obtained from citrus fruits contain significant amounts of valuable compounds and offer various opportunities in technological and health-promoting areas. Citrus by-products contain several biologically active compounds (BACs), including polyphenols, carotenoids, and essential oils. Among these, polyphenols and carotenoids are known for numerous health benefits, mostly due to their antioxidant properties. These utilizations of citrus wastes not only help reduce waste but also create value-added products, contributing to the sustainability and economic viability of the citrus processing industry [6, 7]. The economic loss and environmental damage factors that will occur because of the disposal of raw materials that are not subject to extraction, have been reduced.

Citrus waste has become quite useful in various industries, especially in medicine, cosmetics, and food, due to the abundant supply of valuable components [8]. Pectin and hesperidin are important components found in citrus fruits**.** Pectin is widely used as a gelling agent, emulsifier, stabilizer, thickener and heavy metal adsorbent in food, medicine, cosmetics and other industries. Hesperidin is a flavanone glycoside found abundantly in citrus fruits. It has antioxidant activity and plays an important role in the pharmaceutical

* To whom all correspondence should be sent: moroydor@yildiz.edu.tr

industry, which is one of the factors of significance in obtaining these bioactive components [9, 10].

In a study conducted by Du *et al*. (2024), it is aimed to provide a non-thermal approach to obtain pectin from citrus plants with high-intensity pulsed electric field (HIPEF) which features remarkable efficiency and low energy usage. The process analysis performed with ion chromatography, high-performance liquid chromatography, Fourier-transform infrared spectroscopy, proton nuclear magnetic resonance spectroscopy, and rheology. Comparisons were made on two processes for producing pectins; a high-intensity pulsed electric field (HIPEF) pretreatment of citrus peel powder followed by a milder acidic extraction (pH 2, heating at 70 °C for 1 h; pectin termed HIPEF-CP), and a conventional direct hot-acid extraction (pH 2, heating at 90 °C for 2 h; pectin termed CP). The HPIEF with assisted acidic extraction was compared with the acidic extraction method. As a result, it is stated that the amount of antioxidant, emulsifying and emulsion-stabilizing abilities of HIPEF-CP are better than those of CP [11]. In another study by Panwar *et al.* (2023), it is aimed to extract pectin from the peels derived from *citrus limetta* by adopting a process known as ultrasonic-aided extraction (UAE). The utilization of the design of Box-Behnken improved the process, resulting in a maximum pectin yield of 28.82%. The UAEP exhibited superior antioxidant activity and demonstrated comparable water/oil retention capabilities and emulsifying qualities when compared to commercially available pectin. Under ideal conditions, the Box-Behnken design yielded a maximum extraction of 28.73 ± 0.12%. The pectin that was obtained had a high degree of esterification, and it exhibited superior antioxidant and thermal characteristics compared to commercially available pectin. The morphological analysis identified variations on the surface, which enhanced the extraction process [12]. Zhang *et al.,* (2023) conducted a study to examine the characteristics of *citrus maxima* (also known as pomelo fruit) flowers (FCM) and explore potential applications for FCM due to its high concentration of valuable elements such as phenolic compounds, flavonoids, naringin, and hesperidin. The study focused on investigating the qualities of FCM tea by utilizing ultrasonic-assisted extraction and hot water to extract bioactive components. In addition, ethanol extraction was performed to assess the fat-soluble and volatile compounds. The determination process is held by GC-MS technique. In addition, especially for valuable compounds of hesperidin and naringin, solutions are prepared using methanol as a solvent. The results prove that there are 88 compounds obtained in FCM. It is stated that by the help of ultrasonic-aided extraction technique, *citrus maxima* by-products are significant sources for obtaining beneficial elements due to plants' rich components [13].

In this study, it is aimed to compare the extraction processes of different citrus species (orange, mandarin, lemon) waste grown in the Mediterranean region with ultrasound-assisted extraction and traditional extraction methods and to obtain pectin and hesperidin components considering their usage areas in the chemical industry. Within the scope of the study, wastes of orange, mandarin and lemon fruits were extracted by ultrasound-assisted extraction, sequential extraction and conventional extraction methods. The chemical properties of the bioactive components in the extracts were characterized by Fourier transform infrared spectrometry (FTIR) and ultraviolet-visible spectrometry (UV-VIS) analyses.

EXPERIMENTAL

Materials

The raw materials used in the study, citrus fruits (lemon, mandarin, orange), were supplied from the Mediterranean region of Türkiye. Acetone, citric acid and ethanol were used as solvents in the experimental study. Acetone was supplied as 99.5% extra pure acetone from Tekkim Company (product number TK.010050.02501). Citric acid and ethanol were both supplied from Merck Company as citric acid monohydrate (CAS Number: 5949-29-1) and ethanol (CAS Number: 64-17-5). Magnetic stirrer (Wisestir) was used for mixing and shaking processes and an oven (Ecocell 111, Germany) was used for drying processes. Weighing processes were carried out with an analytical balance (Weightlab Instruments). Ultrasonic-assisted extraction was carried out with ultrasonic bath (Isolab, Germany).

Pretreatment and humidity analysis of citrus waste

The peels of orange, mandarin and lemon fruits, supplied from the Mediterranean region, were separated, washed with tap water, then with distilled water. Peels were cut to 1×1 cm size and dried at 60°C, 24 h. After the drying process, peels were weighed, then grinded and sieved to a particle size of 180 μm. Sieved samples were weighed and the amount of moisture in the peels for the dry weights of citrus fruits were calculated using equation (1). Then, the samples were kept in a desiccator for later use.

$$Humidity\ ratio = \frac{Wet\ Weight - Dry\ Weight}{Wet\ Weight} \times 100 \quad (1)$$

Extraction of citrus waste

The conventional extraction process was carried out with the ratios of citrus peel to solvent as 0.05 g/mL, 0.1 g/mL, 2 g/mL and 0.4 g/mL for each species. The determined ratios of citrus peel and acetone:water solution were mixed in a magnetic stirrer at 40 °C for 30 min. The extracts obtained after the mixing process were filtered using filter paper. The filtered extracts were stored at +4 °C to analyze the bioactive components [14].

The ultrasound-assisted extraction process was carried out using an ultrasonic water bath operating at 60 kHz frequency and 40 °C temperature. 50 vol% acetone-water solution was used as the solvent. For sample preparation, proportions of 0.05 g, 0.1 g, 0.25 g and 0.5 g of ground citrus peel samples per 10 mL of solvent were combined in glass vials. Then, the samples were left in the ultrasonic water bath for 30 min [14]. The extracts were filtered and then stored at 4°C for the analysis of bioactive components.

For the sequential extraction process that is studied and reported previously by Zhou *et al*., (2022), 5% citric acid-water solution was used as the solvent. The samples to be used in this process were combined at a 1:15 (g/mL) sample-solvent ratio. Then, the prepared samples were mixed in a magnetic stirrer at 90°C for 100 min. The liquid (filtrate) and solid (extract) phases of the extracts obtained from the mixing process were filtered. The separated liquid phase (filtrate) was centrifuged at 4000 rpm for 4 min. The supernatant was mixed with an equal volume of 99.5% ethanol and left to coagulate for 2 h. Then, the supernatant-ethanol mixtures were centrifuged at 4000 rpm for 4 min. The produced pectin samples were rinsed three times with 99.5% ethanol to form wet pectin. The remaining solid component (extract) was combined with 3% (aq.) NaOH solution at a ratio of 1:8 (g/mL) and subjected to extraction at 60°C for 90 min. After this process, the mixture was brought to ambient temperature and vacuum filtered. The pH of the filtrate was adjusted to 4.0 using 50% HCl solution and allowed to settle for 2 h. Hesperidin was isolated by centrifugation at 4000 rpm for 4 min followed by three consecutive water washings. Wet hesperidin was obtained at the end of this procedure. As a final step, wet hesperidin and pectin were dried until constant weight. Pectin and hesperidin yields were determined using equations (2) and (3), respectively.

$$PEV(\%) = \frac{P}{m} \times 100 \quad (2)$$

$$HEV(\%) = \frac{H}{m} \times 100 \quad (3)$$

where PEV and HEV are the pectin and hesperidin yield, respectively, P is the weight of dried pectin in g, H is the weight of dried hesperidin in g, and m is the amount of dried citrus powder [15].

Characterization

For the analysis of valuable bioactive components, UV-Vis spectrophotometry, FTIR spectroscopy and LC-MS analyses were used.

The phenolic compound content of the extracted samples after the conventional and ultrasonic-assisted extraction processes was qualitatively analyzed by UV-Vis spectrophotometry. This was performed as a first step before further analysis to see if phenolic compounds were extracted from the samples. Samples containing 0.05 g/mL of grinded citrus peel sample-solvent from all 3 species were used for the extract analysis obtained by the conventional method, while samples containing 0.5 g/mL of grinded citrus peel sample-solvent from all 3 species were used for the extract analysis obtained by the ultrasonic-assisted extraction method. 0.1 mL of extracts were mixed with the extraction solvent to make a 5 mL solution. The absorbance of this solution was measured in the wavelength range of 190-1100 nm [16].

FTIR analysis was performed to analyze the functional structures of bioactive components (hesperidin and pectin) found in citrus extracts. The analysis was carried out in the wavelength range of 4000–450 cm^{-1} with ATR technique [17].

LC-MS was used to determine the hesperidin content in the liquid extract. The mandarin extract obtained by ultrasound-assisted extraction was analyzed using an Agilent 6530 LC MS-QTOF system. A standard hesperidin sample was employed, and single mass spectrometry operating in negative mode was used to achieve the quantitative determination.

RESULTS AND DISCUSSION

Humidity ratio results

Humidity ratios of grinded citrus samples were calculated based on equation (1) and are given in Table 1. Humidity ratios of each citrus species were similar and around 74-75%. Mandarin has the highest humidity ratio of 75.5% which may due to its thin peel structure that retains more moisture.

Table 1. Humidity calculations of grinded citrus samples

Sample	Wet weight (g)	Dry weight (g)	Humidity ratio (%)
Lemon	97.4470	25.3360	74.00
Mandarin	114.7380	30.1140	75.50
Orange	266.0710	69.4380	74.00

Humidity ratio results of the produced pectin samples from each citrus species after sequential extraction are presented in Table 2. Humidity ratios of pectin from orange (65.29%) and from mandarin (62.17%) were much higher than that of lemon (26.80%). This difference may be caused by the difference between the chemical compositions of citrus species and peel structures that effect the pectin content.

Table 2. Humidity ratios of pectin samples according to citrus fruits

Sample	Wet weight (g)	Dry weight (g)	Humidity ratio (%)
Lemon	0.7515	0.5517	26.80
Mandarin	3.0500	1.1539	62.17
Orange	5.4422	1.8885	65.29

Humidity ratio results of produced hesperidin samples from each citrus species after sequential extraction are presented in Table 3. Hesperidin products revealed similar humidity ratio varying between 93-98%.

Table 3. Humidity ratios of hesperidin samples according to citrus fruits

Sample	Wet weight (g)	Dry weight (g)	Humidity ratio (%)
Lemon	1.7305	0.0660	96.19
Mandarin	0.8579	0.0600	93.01
Orange	1.1582	0.0250	97.84

Pectin and hesperidin yields of products obtained from sequential extraction are presented in Table 4. Lemon yielded the highest hesperidin as 3.30% while mandarin yielded the highest pectin as 94.625%. Panwar *et al.* (2023) reported a yield of pectin 28.82% using UAE from *citrus limetta* peels [12]. Gu *et al.* (2016) reported a yield of 0.48 ± 0.02 mg/g hesperidin using ionic liquid vacuum microwave-assisted method from *Sorbus tianschanica* leaves [18]. Karbuz &Tugrul (2021) found pectin yield for lemon between 5.97-10.11% and for mandarin between 5.72-11.29% which were obtained *via* ultrasonic-assisted extraction [19].

Table 4. Yields for pectin and hesperidin according to citrus fruits

Sample	Pectin yield (%)	Hesperidin yield (%)
Lemon	27.585	3.30
Orange	57.695	1.25
Mandarin	94.625	3.00

UV-Vis spectrophotometric results

Wavelength/absorbance graphs were plotted as a result of UV/Vis spectrophotometric analyses of citrus extracts obtained from conventional and ultrasonic-assisted extraction processes. UV/Vis graphs of extracted samples of orange (C-O), mandarin (C-M) and lemon (C-L) from conventional extraction are presented in Figure 1. UV/Vis graphs of extracted samples of orange (US-O), mandarin (US-M) and lemon (US-L) from ultrasonic-assisted extraction are presented in Figure 2.

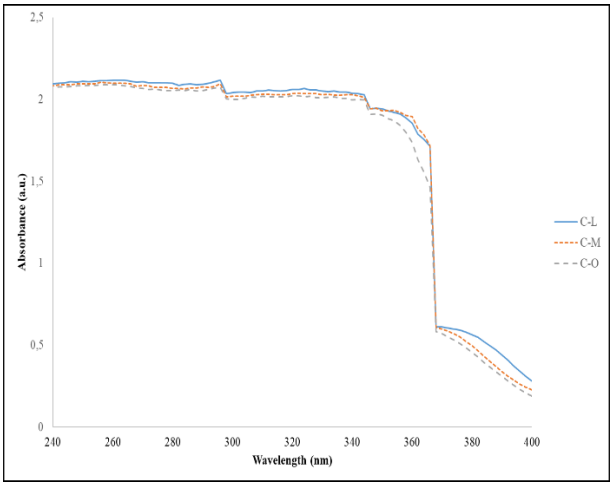

Figure 1. UV-Vis analysis of extracted samples from conventional extraction; C-L for lemon, C-M for mandarin, C-O for orange extract.

As a result of the UV-Vis analyses, the peak wavelength range giving the highest absorbance for all 3 citrus types in extracts obtained by conventional extraction method was observed as 280-290 nm. This range was determined as 290-300 nm wavelength for ultrasonic assisted extraction. Band, covering the range of 240–280 nm (max absorbance around 255–265 nm) attributed to the A–C benzoyl system confirming the flavonoid structure [4].

There is a direct proportion between this absorbance amount and the molecular bonds that the components have. In other words, as the weak bonds between molecules get stronger, the absorbance amount increases.

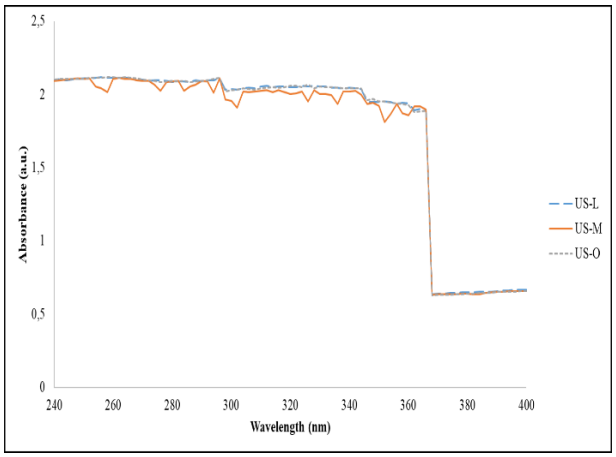

Figure 2. UV-Vis analysis of extracted samples from ultrasonic-assisted extraction; US-L for lemon, US-M for mandarin, US-O for orange extract

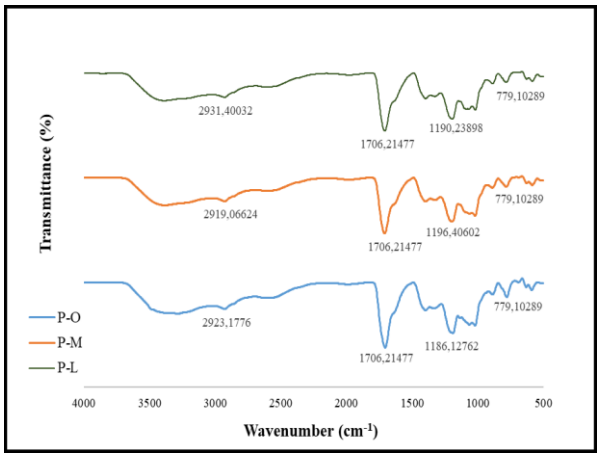

Figure 3. FTIR analysis of pectin samples obtained by sequential extraction; P-O for orange, P-M for mandarin, P-L for lemon peel extracted samples.

FTIR analysis results

FTIR spectra of pectin obtained from the sequential extraction of orange (P-O), mandarin (P-M) and lemon (P-L) was indicated in Figure 3. The wavelength with the lowest transmittance for all three citrus species was determined to be approximately 1706.215 cm^{-1}. In this analysis, it is observed that the transmittance decreases as the substance concentration increases. From this relationship, the existence of an inverse proportion between the substance concentration and transmittance was determined. It can be observed that the spectroscopic profiles of the pectin compound are parallel despite being obtained from different citrus species. Absorption in the 800–1200 cm^{-1} wave range is specified as the fingerprint zone for carbohydrates [19]. The lowest transmittance value determined falls in the FTIR spectrum peak of carbonyl C=O stretch. The bands at 2923.1776 cm^{-1} -2931.40032 cm^{-1} can be determined as alkane C–H stretching vibration. The bands at 1186.12762- 1196.40602 cm^{-1} are attributed to aromatic C=C stretch [20]. The band at 1706.21477 cm^{-1} can determine the bioactive component as pectin due to its stretching vibrations of the carbonyl group (υC=O) which is directly related to its gelling mechanism [21-23].

LC-MS analysis results

The chromatogram of the lowest concentration of hesperidin 0.035 ppm is given in Figure 4. It was concluded that the mandarin extract was rich in hesperidin components observed at an m/z = 609 which is in agreement with the literature [24]. The hesperidin was found as 430.2 mg/L in mandarin extract (Table 1).

Table 1. Determination of hesperidin in mandarin extract

Extract	Extraction method	Hesperidin amount ($mg.L^{-1}$)
Mandarin	Ultrasound-assisted extraction	430.2 ± 3.27*

* n = 3, mean ± SD.

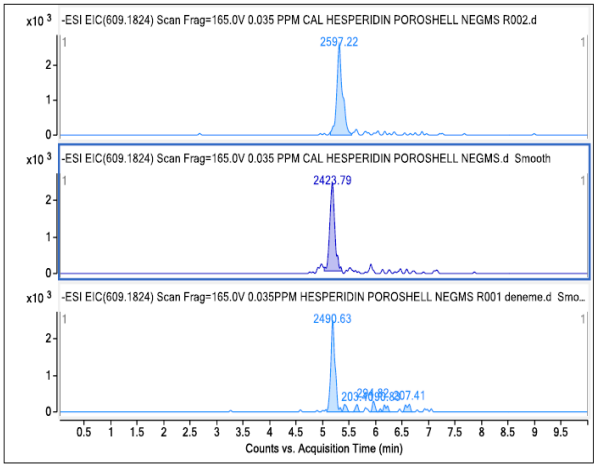

Figure 4. LC-MS spectra of hesperidin observed in the mandarin extract.

Hesperidin, which is known to exhibit strong antioxidant, anti-inflammatory and neuroprotective qualifications, has been reported in the literature to be generally found in citrus fruits [24].

CONCLUSION

In the present study, lemon, mandarin and orange waste peels supplied from the Mediterranean region of Türkiye were evaluated in terms of valuable compound composition. To create a new approach to reduce waste, provide environmental sustainability and prove the importance of environmental waste recycling,

lemon, orange and mandarin wastes were subjected to extraction processes. The pectin and hesperidin contents of these wastes were successfully evaluated using ultrasonic-assisted extraction, conventional extraction and sequential extraction. It was proven that citrus wastes obtained from the Mediterranean region can be used to obtain hesperidin and pectin. In addition, the advantages of different extraction methods were demonstrated. The UV-Vis spectrophotometry and FTIR analyses were successfully applied and the chemical structures of the extracted citrus compounds were characterized. The efficiency of the three extraction methods in obtaining hesperidin and pectin was compared. In addition, the study revealed the level of efficiency of environmentally friendly extraction techniques using the example of the ultrasonic-assisted extraction method. The conditions, efficiency and environmental effects of the whole process were observed. Phenolic compounds in citrus extracts may have potential uses in many areas such as health, food, cosmetics and agriculture, if further analyses are completed.

Acknowledgement: *The work was financially supported by Yildiz Technical University Scientific Research Project Coordination Fund (Project number: fhd-2024-6329).*

Author contributions: *Deniz Uygunoz: Investigation, Methodology, Writing – original draft. Gamzenur Cifci: Investigation, Methodology, Writing – original draft. Ozgur Ozan Demirci: Investigation, Methodology, Writing – original draft. Emek Moroydor Derun: Methodology, Writing - Review & Editing, Supervision, Project administration.*

Declaration of competing interests: *there are no known competing financial interests or personal relationships that could have affected the work reported in this paper.*

Ethical approval: *not needed;*

Informed consent: *not applicable.*

REFERENCES

1. B. Ozkan, H. Akcaoz, F. Karadeniz, *Energy Convers. Manag*., **45**, 1821 (2004).
2. P. Putnik, D. B. Kovaćević, A. R. Jambrak, F. J. Barba, G. Cravotto, A. Binello, J. M. Lorenzo, A. Shpigelman, *Molecules*, **22**, 680 (2017).
3. Z. Maqbool, W. Khalid, H. T. Atiq, H. Koraqi, Z. Javaid, S. K. Alhag, A. Al-Farga, *Molecules*, **28**, 1636 (2023).
4. W. J. Chien, D. S. Saputri, H. Y. Lin, *Curr. Res. Food Sci.,* **5**, 278 (2022).
5. M. Anticona, J. Blesa, A. Frigola, J. M. Esteve, *Foods*, **9**, 811 (2020).
6. P. Putnik, D. B. Kovaćević, A. R. Jambrak, F. J. Barba, G. Cravotto, A. Binello, J. M. Lorenzo, A. Shpigelman, *Molecules*, **22**, 680 (2017).
7. Y. Chen, T. J. Barzee, R. Zhang, Z. Pan, Citrus, Elsevier eBooks, 2019, p. 217.
8. Z. Maqbool, W. Khalid, H. T. Atiq, H. Koraqi, Z. Javaid, S. K. Alhag, A. Al-Farga, *Molecules*, **28**, 1636 (2023).
9. F. Wang, C. Du, J. Chen, L. Shi, H. Li, *Polymers*, **13**, 2847 (2021).
10. P. Alam, A. Alam, M. K. Anwer, S. I. Alqasoumi, Asian Pac. *J. Trop. Biomed*., 4, 262 (2014).
11. Y. Du, S. Zhang, G. I. Waterhouse, T. Zhou, F. Xu, R. Wang, D. Sun-Waterhouse, P. Wu, *Food Hydrocoll*., 146**,** 109291 (2024).
12. D. Panwar, P. S. Panesar, H. K. Chopra, *Food Biosci*., **51**, 102231 (2023).
13. X. Zhang, X. Zhuang, T. Xiong, S. Huang, X. Qian, T. Guo, M. Chen, W. Xie, Y. Huang, *Ultrason. Sonochem*., **100**, 106632 (2023).
14. J. Londoño-Londoño, V. R. de Lima, O. Lara, A. Gil, T. B. C. Pasa, G. J. Arango, J. R. R. Pineda, *Food Chem*., **119**, 81 (2010).
15. P. Zhou, M. Zheng, X. Li, J. Zhou, Y. Shang, Z. Li, L. Qu, *Ind. Crops Prod*., **182**, 114849 (2022).
16. W. J. Chien, D. S. Saputri, H. Y. Lin, *Curr. Res. Food Sci*., **5**, 278 (2022).
17. M. M. Hossain, R. Ara, F. Yasmin, M. Suchi, W. Zzaman, *Meas.: Food*, 100135 (2024).
18. H. Gu, F. Chen, Q. Zhang, J. Zang, *J. Chromatogr.* B, **1014**, 45 (2016).
19. P. Karbuz, N. Tugrul, *J. Food Sci. Technol*., **58**, 641 (2021).
20. S. H. Ali, G. M. Sulaiman, M. M. F. Al-Halbosiy, M. S. Jabir, A. H. Hameed, *Artif. Cells Nanomed. Biotechnol*., **47**, 378 (2019).
21. P. Coimbra, P. Ferreira, H. De Sousa, P. Batista, M. Rodrigues, I. Correia, M. Gil, *Int. J. Biol. Macromol.,* **48**, 1 (2010).
22. R. Ciriminna, A. Fidalgo, R. Delisi, A. Tamburino, D. Carnaroglio, G. Cravotto, L. M. Ilharco, M. Pagliaro, *ACS Omega*, **2**, 11 (2017).
23. C. Lara-Espinoza, E. Carvajal-Millán, R. Balandrán-Quintana, et al., *Molecules*, **23**, 942, (2018)
24. G.D. Sorita, C. Rodríguez-García, M. M. Strieder, et al., *Food Chemistry*, **486**, 144628 (2025).
25.

Bulgarian Chemical Communications, Volume 57, Issue 3 (pp. 154-159) 2025 DOI: 10.34049/bcc.57.3.CK-IK-ID

Effect of different drying techniques on the drying characteristics of celery

C. Kurt, I. Küçük*, I. Doymaz

Yildiz Technical University, Chemical Engineering Department, Davutpasa Campus, Esenler, Istanbul 34220, Türkiye

Accepted: August 17, 2025

Present study investigates the impact of various drying methods on the drying characteristics of celeriac, focusing on parameters like drying rate, moisture loss, and time efficiency. Understanding these kinetic aspects is essential for optimizing drying processes and improving the quality of the final product.

Two drying techniques were applied to reduce moisture content of celery. 55, 65, and 75 ˚C in a cabinet dryer, and at 62, 74, 88 and 104 W power levels in an infrared dryer were chosen as drying conditions. To understand pretreatment effect 1% citric acid solution was used. The variation in moisture content during the drying of celery samples was analyzed using eight different mathematical models. Model efficiency was assessed utilizing statistical indicators such as the coefficient of determination (R^2), root mean square error (RMSE), and chi-square (χ^2) analysis. Among the models considered, the Midilli & Küçük model yielded the closest correlation with the experimental data, indicating its superior ability to characterize the drying behavior of the samples. The estimated effective moisture diffusivity (D_{eff}) for celery dried in a cabinet dryer varied between 1.701×10^{-10} and 3.317×10^{-10} m²/s for untreated (control) samples, whereas those pretreated with citric acid solution exhibited D_{eff} values ranging from 1.753×10^{-10} to 3.797×10^{-10} m²/s.

The corresponding activation energy values were calculated as 31.66 kJ/mol for the control group and 32.70 kJ/mol for the pretreated samples. In the case of infrared drying, the effective moisture diffusivity of celery samples varied between 2.746×10^{-10} and 4.987×10^{-10} m²/s for the control group. The activation energy required for moisture diffusion under infrared drying conditions was calculated as 2.99 kW/kg. In addition, color parameters were evaluated to assess the impact of drying methods on visual quality. Instrumental color measurements based on the CIELAB color space (L*, a*, b*) revealed noticeable changes depending on the drying technique and pretreatment.

Keywords: Celeriac, drying techniques, drying kinetics, mathematical modeling

INTRODUCTION

Celery (*Apium graveolens* L.), high in moisture content (approximately 88%), is a root vegetable with high nutritional value and functional properties. Celery, with its rich content, can positively affect health in many ways by preventing inflammation, regulating blood pressure, supporting digestion, etc. However, its high water activity significantly limits its shelf life, necessitating the use of preservation techniques such as drying [1, 2].

Drying serves as a traditional technique that reduces moisture content in agricultural goods, helping to prevent deterioration and support long-term storage. It significantly reduces the moisture content of food materials, thereby inhibiting microbial growth, enzymatic activity, and other deteriorative reactions [3-5]. Moreover, the reduction in weight and volume resulting from water removal leads to decreased transportation and storage costs. The high water content and water activity inherent in many fresh agricultural products accelerate spoilage processes; therefore, drying serves as an essential technique to enhance product stability, ensure microbiological safety, and maintain quality during storage and distribution.

Drying techniques have significant effects on the drying process, energy consumption and final product quality of food products. Depending on the applied method, parameters such as drying speed, moisture diffusion, color change, nutrient loss and structural integrity may vary. Therefore, the selection of the appropriate drying technique is critical to maximize process efficiency and energy savings while maintaining the desired quality characteristics of the product [6-8].

The present study investigates the impact of various drying methods on the drying characteristics of celeriac, focusing on parameters like drying rate, moisture loss, and time efficiency and color change. Understanding these kinetic aspects is essential for optimizing drying processes and improving the quality of the final product.

* To whom all correspondence should be sent:
E-mail: *kucuk@yildiz.edu.tr*

EXPERIMENTAL

Materials and methods

High-quality fresh celery was sourced from a local vendor in Istanbul, Türkiye. The stalks were thoroughly cleaned and then diced into uniform cubes with an average thickness of approximately 6 ± 0.5 mm. The initial moisture content was measured as 9.43 kg of water per kg of dry matter (d.b.). The prepared samples were categorized into two distinct groups: one batch underwent pretreatment with a 1% (w/v) citric acid (CA) solution, while the second group remained untreated and served as the control. Drying of both sample groups was performed using two different methods: a convective cabinet dryer (APV&PASILAC Limited of Carlisle, UK) and an infrared (IR) dryer (Snijders Tilburg, Holland). In the cabinet drying process, samples were dried at constant temperatures of 55, 65, and 75 °C, whereas in the IR drying process, infrared power levels of 62, 74, 88, and 104 W were applied. During the drying process, the mass of the celery samples was recorded at 15-min intervals. Drying was terminated when the moisture content of the samples reached 0.10 ± 0.02 kg water/kg dry matter (d.b.).

Mathematical modeling and data analysis

To characterize the drying behavior, eight different semi-theoretical models were selected (Table 1). The mathematical expressions utilized for modeling and analyzing the drying data are listed in Table 2. In these models, MR refers to the moisture ratio, M indicates the moisture content (kg water/kg dry matter), W represents the total weight of the sample (kg), and Wd denotes the dry matter weight (kg). The variable t stands for drying duration in min. M_t and M_e correspond to the moisture content at time t and the equilibrium moisture content, respectively, both expressed in kg water/kg dry matter. Since M_e is relatively insignificant compared to the initial (M_0) and time-dependent (M_t) moisture contents, it is commonly omitted, simplifying the moisture ratio (MR) to the ratio M_t/M_0 [9].

Table 1. Mathematical models for kinetic investigation

Model name	Model	Ref.
Wang & Singh	$MR = 1 + at + bt^2$	[7]
Lewis	$MR = \exp(-kt)$	[10]
Henderson & Pabis	$MR = a \exp(-kt)$	[11]
Logarithmic	$MR = a \exp(-kt) + c$	[12]
Page	$MR = a \exp(-kt^n)$	[13]
Midilli & Kucuk	$MR = a \exp(-kt^n) + bt$	[14]
Vega-Lemus	$MR = (a + bt)^2$	[15]
Vega-Galvez	$MR = \exp(n + kt)$	[15]

Statistica 8.0.550 (StatSoft Inc., USA) software package was used to evaluate experimental data. To estimate model parameters a non-linear regression procedure based on the Levenberg-Marquardt algorithm was used. The adequacy of the experimental data fitting to various models was assessed using statistical parameters including the coefficient of determination (R^2), reduced chi-square (χ^2), and root mean square error (RMSE). In this context, MRexp,i and MRpre,i represent the experimental and model-predicted dimensionless moisture ratios, respectively; N denotes the number of observations, and z is the number of model parameters. A good agreement between the model and experimental data is indicated by a higher R^2 value along with lower χ^2 and RMSE values [16]. The effective moisture diffusivity of dried celery can be estimated by applying Fick's second law of diffusion.

The relationship between effective moisture diffusivity and temperature is typically characterized using the Arrhenius-type equation, where D_0 represents the pre-exponential factor (m^2/s), E_a is the activation energy (kJ/mol), R is the universal gas constant [kJ/(mol·K)], and T denotes temperature (°C). However, in the context of this study, temperature was not directly measurable under infrared drying conditions. Therefore, a modified version of the Arrhenius equation was employed to estimate activation energy, expressing the dependence of effective diffusivity on the ratio of infrared power input (p, W) to sample mass (m, kg) [7].

Table 2. Equations for data analysis

$M = \frac{W - W_d}{W_d}$	$R^2 = 1 - \frac{\sum_{i=1}^{N}(MR_{pre,i} - MR_{exp,i})^2}{\sum_{i=1}^{N}(\overline{MR}_{pre} - MR_{exp,i})^2}$
$MR = \frac{M_t - M_e}{M_0 - M_e}$	
$MR = \frac{8}{\pi^2} \exp(-\frac{\pi^2 D_{eff} t}{4 L^2})$	$\chi^2 = \frac{\sum_{i=1}^{N}(MR_{exp,i} - MR_{pre,i})^2}{N - z}$
$ln(MR) = ln(\frac{8}{\pi^2}) - (\frac{\pi^2 D_{eff}}{4 L^2})t$	$RMSE = \left[\frac{1}{N}\sum_{i=1}^{N}(MR_{pre,i} - MR_{exp,i})^2\right]^{1/2}$
$\frac{\partial M}{\partial t} = D_{eff}\nabla^2 M$	$D_{eff} = D_0 \exp\left(-\frac{E_a}{R(T + 273.15)}\right)$
$K = (\frac{\pi^2 D_{eff}}{4 L^2})$	$D_{eff} = D_0 \exp\left(-\frac{E_a m}{p}\right)$

Color analysis

Color evaluation was conducted using a colorimeter (Konica Minolta CR-400, Japan). The analysis was based on the CIE (Commission Internationale de l'Éclairage) color space system, which defines color in three components: lightness (L*), ranging from 0 (pure black) to 100 (pure white); a* value, representing the red-green

spectrum (from −60 for green to +60 for red); and b* value, indicating the blue-yellow scale (from −60 for blue to +60 for yellow). For each sample, measurements were recorded at three different surface locations, and the procedure was repeated six times to ensure accuracy and reproducibility of the average values.

DISCUSSION

Analysis of drying curves

Figure 1 illustrates the influence of air temperature and IR power on the moisture content and drying time of celery samples. The figure depicts moisture content variations as a function of drying time at temperatures of 55, 65, and 75°C, combined with IR power levels of 62, 74, 88, and 104 W. It is evident that moisture content consistently decreases throughout the drying process. Pretreatment was found to have no significant effect on drying time, as samples subjected to pretreatment exhibited drying durations comparable to the control group. Specifically, the drying times required to reduce the moisture content of pretreated samples were 210, 195, and 135 min, respectively, while the corresponding drying times for the control samples were 210, 195, and 150 min at the same temperatures.

The moisture content of the samples showed a clear decreasing trend over time, with a more rapid decline observed under higher infrared power levels. This can be attributed to the increased thermal input, which raised the sample temperature and accelerated moisture migration. Accordingly, the drying time required to reach the final moisture content decreased with increasing infrared power, with values ranging from 165 to 90 min depending on the applied power levels (62 to 104 W). As expected, higher infrared intensities resulted in greater heat absorption, leading to elevated product temperatures, enhanced mass transfer driving forces, and, consequently, faster drying rates and shorter drying times [7-10]. As highlighted in Fig. 1, the drying process typically followed two distinct phases: an initial warming-up stage under non-isothermal conditions, characterized by a rapid temperature increase, followed by a falling-rate period. This latter phase is associated with increasing internal resistance to both heat and mass transfer as the moisture content diminishes. These findings are consistent with established drying behavior of biological materials, where rapid initial moisture loss—mainly due to surface evaporation—is followed by slower diffusion-limited transport. Similar observations have been reported in prior studies on drying various agricultural products [11-14].

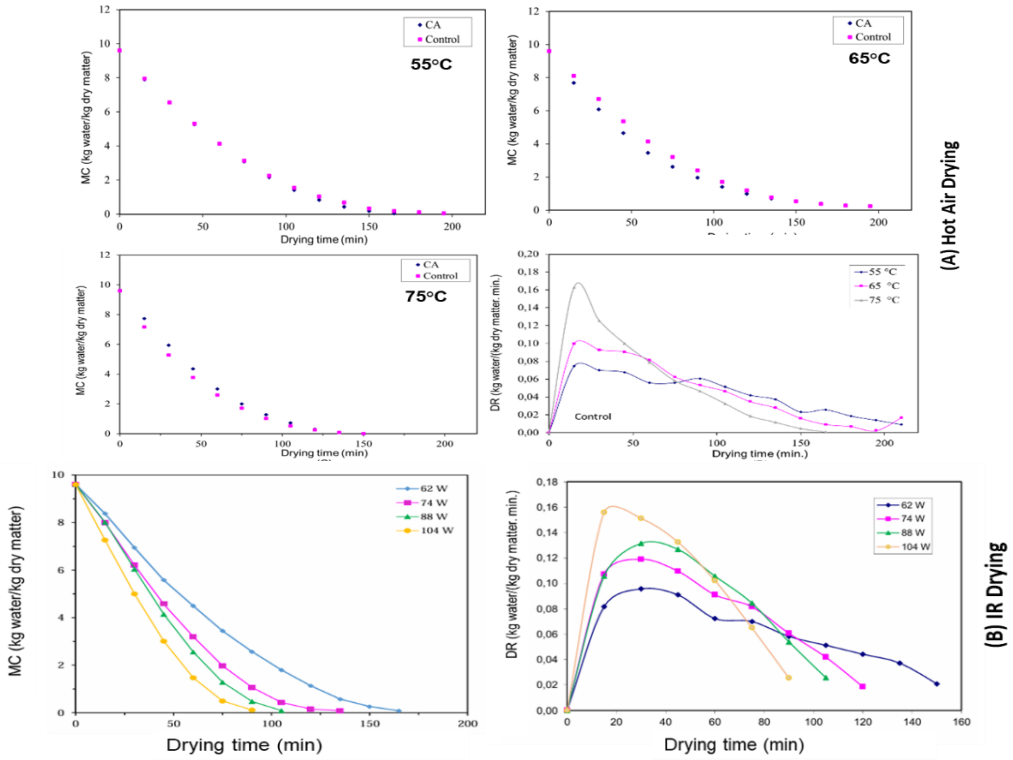

Figure 1. (A) Pretreatment effect on the moisture contents, and drying rate *versus* drying time for control sample, (B) Drying curves and drying rates of celery at different infrared powers

Evaluation of models

Model selection was primarily guided by achieving the highest R^2 along with the lowest χ^2 and RMSE values. As shown in Table 3, at 55 °C, the Wang & Singh model exhibited the strongest agreement with the observed data, reflected by an R^2 of 0.9993, a χ^2 of 0.000074, and an RMSE of 0.028052. However, for higher temperatures (65 °C and 75 °C), the Midilli & Küçük model outperformed the others, attaining R^2 values in the range of 0.9995–0.9998, χ^2 values between 0.000055 and 0.000024, and RMSE values from 0.019765 to 0.010345. Across varying infrared power levels, the Midilli & Küçük model consistently emerged as the most accurate, with R^2 values spanning from 0.9990 to 0.9996, χ^2 ranging from 0.000062 to 0.000194, and RMSE values lying between 0.016719 and 0.028563.

Effective moisture diffusivity and activation energy

The effective moisture diffusivity (D_{eff}) values for celery slices during drying at air temperatures between 55°C and 75°C ranged from 1.701×10^{-10} to 3.317×10^{-10} m²/s for pretreated samples and from 1.753×10^{-10} to 3.797×10^{-10} m²/s for control samples. An increasing trend in D_{eff} values was observed with rising air temperature, with the highest diffusivity recorded at 75°C and the lowest at 55°C. These results fall within the commonly reported range of 10^{-12} to 10^{-8} m²/s for drying of food materials, and show good agreement with previously published values for celery slices [15]. Similarly, the effective moisture diffusivity values for samples subjected to IR drying were determined at power levels of 62, 74, 88, and 104 W. The D_{eff} values ranged from 2.746×10^{-10} to 4.987×10^{-10} m²/s, indicating a positive correlation between IR power and moisture diffusivity. Comparing the two drying methods, it is evident that both higher air temperatures and increased IR power levels enhance moisture diffusivity in celery slices (Figure 2). However, IR drying at higher power levels yields somewhat greater D_{eff} values compared to hot air drying at equivalent temperatures, suggesting that IR drying may accelerate moisture transport more effectively during drying. The activation energy values were found to be 32.70 kJ/mol and 31.66 kJ/mol for pretreated and control samples during hot air drying, respectively, and 2.99 kW/kg for control samples during IR drying. The E_a values lie within the general range of 12.7–110 kJ/mol for food materials [16, 17].

Color evaluation

Color analysis of celery samples dried using two different drying techniques revealed that the L* parameter decreased with increasing drying temperature and IR power, indicating a darkening of the color. Specifically, L* values ranged from 70.75 to 65.05 in the cabinet dryer and from 64.72 to 53.16 in the IR dryer. The a* parameter increased with rising drying temperature (from −0.80 to 1.71) and IR power level (from 0.73 to 5.52), reflecting an increase in redness. Furthermore, pretreated samples exhibited color parameters closer to those of fresh samples compared to control samples across all temperature levels.

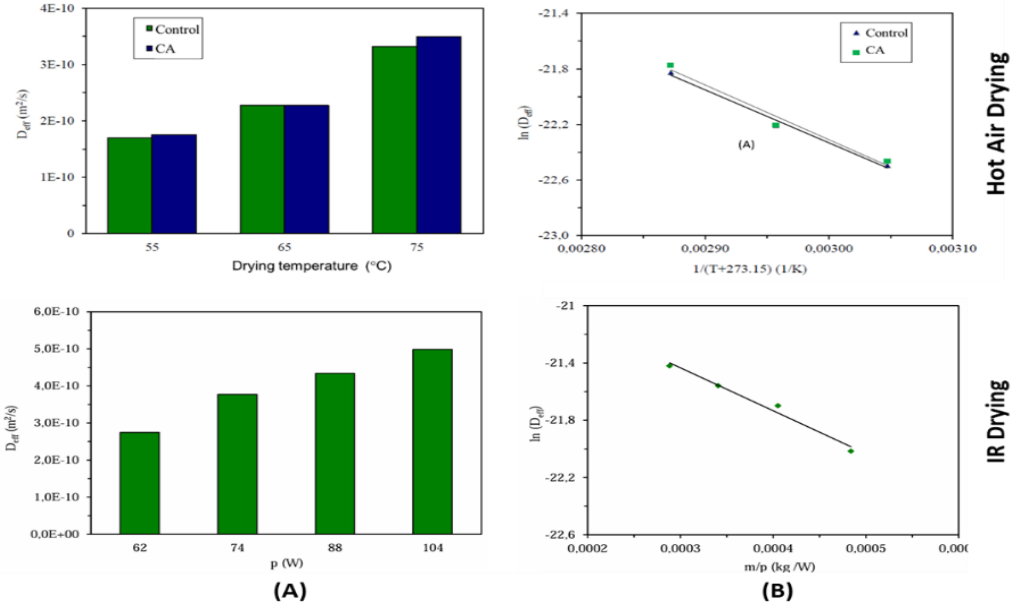

Figure 2. (A) Effective moisture diffusivity as affected by air temperature and IR power. (B) Arrhenius relationship between diffusivity and inverse absolute temperature (1/T) with m/p.

Table 3. Statistical parameters of models for different temperatures and infrared powers

MODELS			Lewis	Henderson & Pabis	Log.	Page	Midilli & Kucuk	Wang & Singh	Vega-Lemus	Vega-Galvez
Hot air	55 °C	R^2	0.9804	0.9855	0.9964	0.9984	0.9992	0.9993	0.9980	0.9855
		χ^2	0.002003	0.001578	0.000412	0.000165	0.000097	0.000074	0.000208	0.001578
		RMSE	0.167481	0.144327	0.069052	0.041601	0.029875	0.028052	0.047162	0.144328
	65 °C	R^2	0.9851	0.9888	0.9961	0.9993	0.9995	0.9981	0.9976	0.9888
		χ^2	0.001576	0.001272	0.000475	0.000070	0.000055	0.000215	0.000272	0.001272
		RMSE	0.132185	0.117040	0.065431	0.022864	0.019765	0.041112	0.050831	0.117040
	75 °C	R^2	0.9800	0.9838	0.9978	0.9986	0.9998	0.9996	0.9992	0.9838
		χ^2	0.002366	0.002159	0.000335	0.000181	0.000024	0.000051	0.000100	0.002159
		RMSE	0.126918	0.121613	0.043699	0.030588	0.010345	0.017603	0.024710	0.121613
IR	62 W	R^2	0.9671	0.9744	0.9977	0.9965	0.9996	0.9991	0.9993	0.9744
		χ^2	0.003810	0.003256	0.000313	0.000437	0.000062	0.000114	0.000088	0.003256
		RMSE	0.177461	0.162827	0.045495	0.058555	0.018325	0.023372	0.022232	0.162827
	74 W	R^2	0.9641	0.9708	0.9937	0.9975	0.9990	0.9975	0.9983	0.9708
		χ^2	0.004599	0.004205	0.001023	0.000352	0.000182	0.000358	0.000239	0.004205
		RMSE	0.181086	0.173649	0.074210	0.046037	0.028563	0.042915	0.038208	0.173648
	88 W	R^2	0.9500	0.9587	0.9936	0.9977	0.9996	0.9946	0.9943	0.9587
		χ^2	0.006866	0.006614	0.001216	0.000354	0.000080	0.000862	0.000914	0.006614
		RMSE	0.188368	0.185113	0.070901	0.037812	0.016719	0.058113	0.066087	0.185113
	104 W	R^2	0.9665	0.9707	0.9958	0.9973	0.9993	0.9982	0.9983	0.9707
		χ^2	0.004685	0.004915	0.000868	0.000444	0.000194	0.000299	0.000281	0.031880
		RMSE	0.143835	0.147733	0.056186	0.038988	0.023007	0.033338	0.004915	0.147729

Figure 3. Visual appearance and color parameter changes of celery dried by two different drying techniques

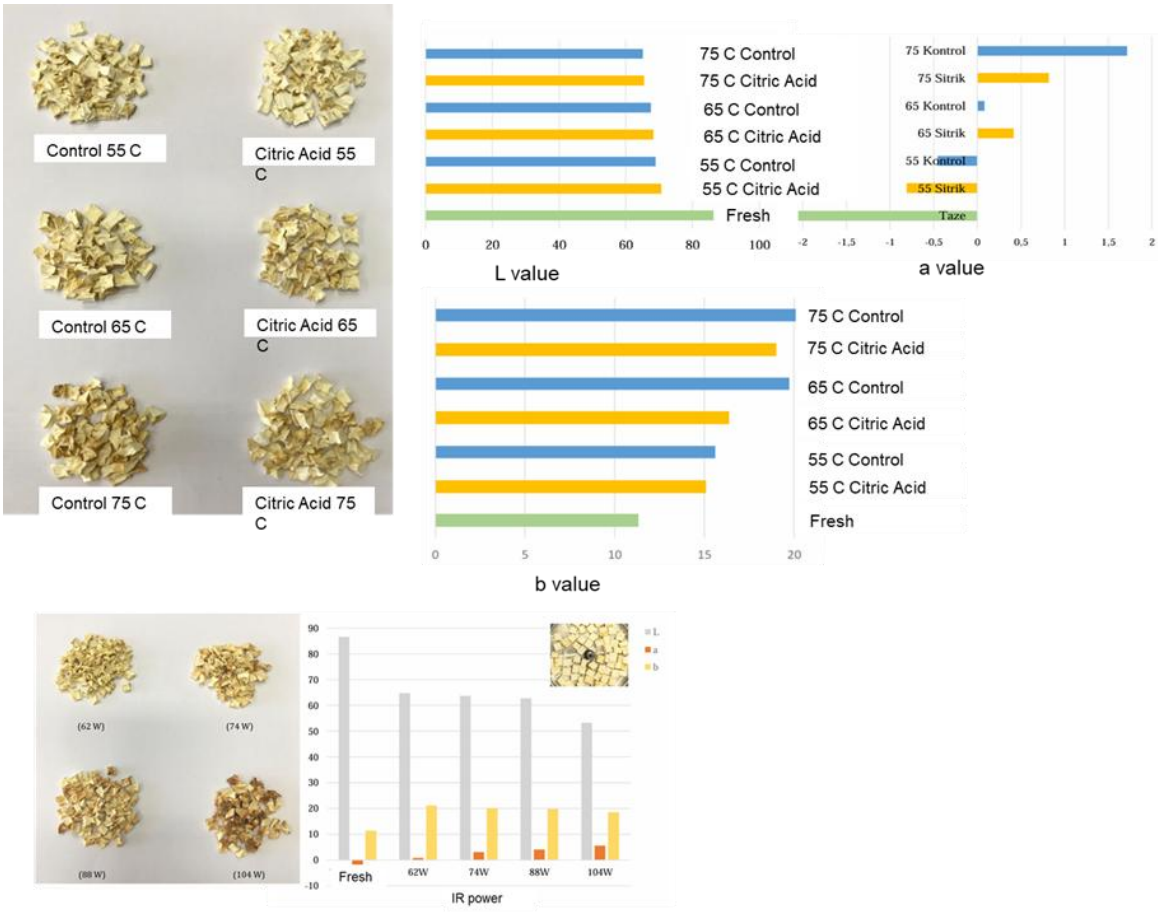

CONCLUSION

Celery, a nutrient-rich vegetable, was dried using hot air cabinet drying and IR drying techniques, and the drying behavior was examined. In hot air drying, increasing the temperature led to faster drying rates and shorter drying times for both pretreated and control samples. It was observed that the citric acid solution, applied as a pretreatment, did not have a significant effect on the total drying time and drying speeds for all temperature values. Diffusion coefficients and activation energies were slightly

higher in pretreated samples compared to controls. For IR drying, raising the drying power similarly increased drying speed and reduced drying time, with diffusion coefficients higher than those in hot air drying and significantly lower activation energy. These findings suggest that IR drying is more effective and energy-efficient for celery than hot air drying.

REFERENCES

1. S. Simamora, M.H. Medan, N. Fithri, *Journal of Health,* **8**, 67 (2021**)**. DOI:https://doi.org/10.30590/joh.v8n2.p67-74.2021
2. C. Xu, D. Liu, C. Guo, Y. Wu, *International Journal of Refrigeration*, **113**, 249 (2020).
3. X. Jin, T. Oliviero, R.G.M. van der Sman, R. Verkerk, M. Dekker, A.J.B. van Boxtel, *LWT – Food Science and Technology*, **59**, 189 (2014).
4. I. Doymaz, I. Kucuk, *Bulgarian Chemical Communications*, **90**, 201 (2017).
5. R. P. Kingsly, R.K. Goyal,M.R. Manikantan. S.M. Ilyas,. *International Journal of Food Science and Technology*, **42**, 65 (2007).
6. G N. An, W. Sun, B.Li, Y. Wang, N. Shang, W. Lv, D. Li, L.Wang, *Food Chemistry*, **373**, Part B, 131412 (2020),
7. L.Z. Deng, X.H. Yang, A.S. Mujumdar, J.H. Zhao, D. Wang, Q. Zhang, J. Wang, Z.J. Gao, H.W. Xiao, *Drying Technology,* **36**, 893 (2018**)**.
8. Q. Yang, X. Yi, H. Xiao, X. Wang, L. Liu, Z. Tang, C. Hu, X. Li, . *Foods*, **13**(9),1295 (2024).
9. O. Ismail, A. Kanturk Figen, S. Piskin, *Heat and Mass Transfer*, **53**, 1277 (2017).
10. A. El-Beltagy, G.R. Gamea, A.H.A. Essa, *Journal of Food Engineering,* , **78**, 456 (2007).
11. Z. Erbay, F. Icier, *Journal of Food Process Engineering*, **33**, 287 (2010).
12. T.J. Afolabi, T.Y. Tunde-Akintunde, J.A Adeyanju, *Journal of Food Science and Technology*, **52**, 2731 (2015).
13. K.O. Falade, O.S. Ogunwolu, *Journal of Food Processing and Preservation*, **38**, 373 (2014).
14. A. Midilli, H. Kucuk, *Energy Conversion and*
15. A. Vega-Galvez, K.D. Scala, K. Rodrguez, R. Lemus-Mondaca, M. Miranda, J. Lopez, M. Perez-Won, *Food Chemistry*, **117**, 647 (2009).
16. V.C. Marianni, C.A. Perussello, A. Cancelier, T.J. Lopes, A. Silva*, Journal of Food Process Engineering*, **37**, 619 (2015).
17. O. T. A. Alshamhazi, I. Küçük, I. Doymaz*, Bulg. Chem. Commun.,* **56** (3), 228 (2024).

Bulgarian Chemical Communications, Volume 57, Issue 3 (pp. 160-165) 2025 DOI: 10.34049/bcc.57.3.SO-AA-PT

Investigating the properties of recycled and virgin poly (ethylene terephthalate) textured yarns: Effect of different blending ratios

S. Özbakış[1,2], A. Aydın[1], P. Terzioğlu[2]*

[1]*Polyteks Textile Industry Research and Education Co., Bursa, Türkiye*
[2]*Bursa Technical University, Faculty of Engineering and Natural Sciences, Department of Polymer Materials Engineering, Bursa, Türkiye*

Accepted: August 17, 2025

Nowadays, there is a growing interest in the use of recycled polyester in the textile industry, driven largely by the sustainability goals of the European Green Deal. These environmental objectives have encouraged both researchers and manufacturers to develop more eco-friendly alternatives to traditional textile production. Recycling polyester from post-consumer and post-industrial waste offers significant environmental benefits, such as reducing landfill accumulation and lowering carbon emissions. However, challenges still remain, including ensuring the quality of recycled material and its compatibility with existing manufacturing processes. This study focuses on investigating the blending of recycled and virgin poly (ethylene terephthalate) (PET) to produce textured yarns suitable for textile applications. Understanding how blending ratios influence yarn performance is crucial for promoting the use of recycled materials in mainstream textile production. In this research, different blend ratios of recycled to virgin PET—100:0, 0:100, 25:75, 50:50, and 75:25 (% w/w)—were used to produce yarns. The resulting yarns were tested for their mechanical, thermal, and color properties. The results showed that the blending ratio significantly effects the thermal and mechanical properties of the yarns, such as tensile strength and elasticity. However, the dyeability and color characteristics were not significantly impacted by the presence of recycled content. These findings suggest that incorporating recycled PET into yarn production can be achieved without compromising visual or dyeing quality, making it a promising approach for sustainable textile manufacturing.

Keywords: recycled polyester, recycling, sustainable textiles, textile waste, thermal properties, blending ratio

INTRODUCTION

Nowadays, plastics are a complementary part of modern life that has a wide range of applications including packaging, construction, agriculture, and households [1]. They have some specific advantages including low production costs, low density, corrosion resistance, potential in molding in different shapes and sizes [1-5]. Global plastic production has a 3–4% annual growth which raised from 322 Mt in 2015 to 367 Mt in 2020 [6, 7]. Additionally, it is estimated that the plastic production will be tripled in the next 30 years [8, 9]. However, the rapid growth of the plastic production leads to resource depletion and ecological destruction problems because most of the plastics are generally discarded in landfills or incinerated [10, 11]. Therefore, there is an urgent necessity to recycle and reclaim the plastics [12, 13].

Polyethylene terephthalate (PET) is one of the most widely used plastic especially in textile fibers and food packaging (film, bottles, etc.) applications. From the view of sustainable and zero waste society, PET is considered as an alternative feedstock not a waste (Fig. 1). Accordingly, PET is the most widely recycled and reused non-renewable plastic globally [14, 15]. Including the reduction of the energy and related carbon footprint of textile industry which is known as one of the world's biggest polluters [17]. Recently, the raise in both the number of studies on rPET fibers and the quality of the rPET fiber-based textile products also supports the significance of recycling applications and the evaluation of rPET fibers in the textile sector [19].

In this study, yarns were obtained by texturing different ratios (100:0, 0:100, 25:75, 50:50, 75:25) (% w/w) of rPET and virgin PET partially oriented yarns. The properties of the final samples were investigated by using color, mechanical, thermal and structural tests.

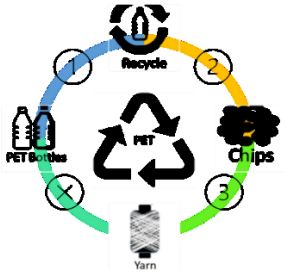

Fig. 1. The cycle of used plastic bottles to become rPET yarn

* To whom all correspondence should be sent:
E-mail: pinar.terzioglu@btu.edu.tr

EXPERIMENTAL

Material

Semi-matte polyester and semi-processed semi-finished polyester chips obtained from INDORAMA Ventures PCL (Thailand) company were used as raw materials. The viscosity of the chips (internal viscosity, IV) is 0.650 dL/g, and the amount of chips per gram is 35 chips/g.

Production of virgin and recycled polyester partially oriented yarn

4 bobbins of partially oriented yarn (POY) and 4 bobbins of rPET POY yarns with the same dtex/filament count feature were produced by melt spinning method using semi-matte polyester and semi- matte rPET chips. Since POY yarns were semi-finished, they are texturized to give the fiber a natural appearance. The operating conditions of the friction texturing machine, used to produce texturized semi-matte POY yarns with different mixing ratios, are shown in Table 1. By texturing POY yarns, 78/72 normal (friction) textured yarns were obtained. Then, POY and rPET POY yarns were 4 times each, rPET POY:virgin polyester POY, in the ratios of 25:75, 50:50, 75:25 % w/w, 4 times rPET POY and 4 times virgin POY, and denier of each is bound to be 300 denier. As a result, 5 pieces of 1 kg 334/288 (dtex/filament number) bobbins were obtained. The yarn samples were named as P1, P2, P3, P4, P5 for 100:0, 0:100, 25:75, 50:50, 5:25 % w/w rPET:PET , respectively (Table 1).

Table 1. Sample codes of yarn samples

Sample code	Blending ratio (rPET: PET)
P1	100:0
P2	0:100
P3	25:75
P4	50:50
P5	5:25

78/72 (dtex/filament count) virgin and recycled semi-matte POY were obtained by melt fiber extraction method using semi-matte polyester and semi-matte rPET chips of filament yarns. The process was carried out at the production unit of Polyteks Textile Industry Research and Education Co. The production speed of rPET semi-dull POY filament yarn is 3000 m/min and the production speed of polyester semi-dull POY filament yarn is 2900 m/min. In the production phase of POY yarns, when the yarn comes out of the nozzle, it comes to the guides and a lubrication process takes place, then it comes to 2 godets and goes around the godets in turn. However, since there is no heating in godets in POY yarn production, the drafting process cannot be fully realized and there is no winding process. The yarn passing through the godets comes first to the centering part and then to the winder, the winder and the last godet are running at the same speed. As a result of these processes, the bobbin winding processes are completed. The obtained values are recorded and the POY yarns are processed into the final product by Polyteks Textile Industry Research and Education Co. The yarns were subjected to texturing process and 334/288 texturized yarns were obtained in the company's own friction texturing machine. The results of texturing tests of 78/72 filament yarns are shown in Table 2. The semi-finished POY yarns and the texturized yarns are shown in Figure 2.

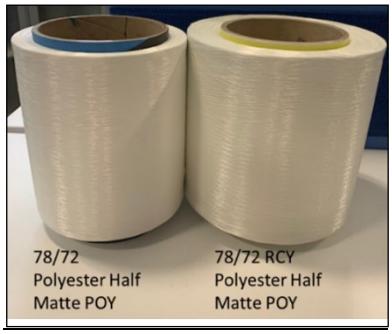

Figure 2. The image of POY yarns

Table 2. Operating conditions of the friction texturing machine

Working conditions of friction texturing machine (AS9-A).	Values
Length (W2) (m/min)	650
Pull (W2/W1)	1.60
Bottom feed (W3)	-3.7
Winding (W4)	-3.2
Winding angle (W5)	32
Disk speed/Yarn speed (W6)	1.80
11 Temperature (°C)	180°C
12 Temperature (°C)	-
Take-up program	55
Oil revolution (rpm)	1.1
Disc combination	1-6-1
Aggregate type	6 mm polyurethane (S-Z-S)
Pressure (bar)	0.3
Type of jet	H.Slide (P203)
Jet zone	Oven
Wx	-2

Bobbin dyeing process

The produced 334/288 (dtex/filament number) textured yarns were sent to Sintas company within the body of Taşdelen Group. Two processes were applied in Sintas company. First, by using a transfer machine, (200 m) 100 g were taken from each of the 5 bobbins, and were turned into a single bobbin (1000 g). The second process is the dyeing process, applied to the resulting bobbin. Bobbin dyeing process was performed in a bobbin dyeing machine from 50°C to 90°C at a speed of 3°C/min, 90°C to 100°C at a speed of 1°C/min, 110°C to 120°C at a speed of 1°C/min, 120°C to 130°C at a speed of 5°C/min and waited for 45 min at the last temperature of 130°C. B.TFBL (1.0 g) was used as a dyestuff. Afterwards, a washing process was started and the dyed bobbin was washed for 20 min at 80°C with the appropriate chemical in a single bath. The last step, the rinsing process, took 20 min at 50°C and the process was completed. The dyed bobbin was divided into 5 equal bobbins by the transfer machine in the twisting unit a speed of 500 m/min and 200 g of yarn was wound on each bobbin at Polyteks company. These coils were correctly numbered according to the order in which they were assembled. Each of the numbered dyed coils was released into the air until they weighed 180 g. Each of the coils given to the air was tested for strength in the STATIMAT brand test device at the laboratory, and then 2 color charts were knitted from each of the coils. Spectrophotometric measurements of the knitted color charts were performed with the X-rite spectrophotometer at the laboratory unit of Polyteks company.

Characterization

- *Characterization of filament yarns.* According to the TS 244 ISO 2060 standard, the weight (yarn number) of the determined length of the yarn was calculated. The tension of 100 m of yarn, which is passed through tension and yarn adjustment guides and tied to the spinning wheel, was determined as 0.051 g/dtex. This process was repeated 5 times for each of the 5 yarn samples. Yarn strength tests were carried out in the STATIMAT brand test device according to the DIN EN ISO 2062 standard. In this device the distance between the clamps is 500 mm, the test speed is 400 mm/min and the pre-tension value is 0.051 g/tex [20, 21]. The results were expressed as mean and coefficient of variation (Table 3).

Table 3. Results of texturing tests of 78/72 filament yarns

Texturation position number	Dtex	Elongation at break (%)	Tenacity (cN/dtex)	Oil
1:3	358.8	21.3±4.4	3.7	1.6
2:2	354.4	23.2±7.7	3.7	1.9
3:1	358.0	21.5±9.4	3.6	1.8

According to the bonding ratios of the POY yarns, they were first sent to the laboratory, their dtex values were measured, then weighed on a precision scale, then oil measurements were made in the Oxford device, and then yarn strength tests were carried out in the STATIMAT brand test device. Afterwards, the bobbins were sent to SİNTAŞ company and were made into a single bobbin (1000 g) in a certain order in the transfer machine (200 m from each bobbin) and then bobbin dyeing was performed. The dyed bobbin was received and separated into 5 different bobbins in order by the transfer machine in the twisting unit of Polyteks.

Yarn strength tests were applied to the 5 bobbins obtained at the laboratory unit with STATIMAT brand test device. Then, the color charts were knitted from each coil and the color charts were measured in CIELAB color space in the X-rite spectrophotometer device. The process steps are described in detail below: In addition, yarn evenness was investigated using an Uster Tester (Uster Technologies, Switzerland) according to the ASTM D1425/1425M.

Characterization of textured yarns

- *Differential scanning calorimetry (DSC).* Thermal analyses of the yarns were carried out in the HITACHI 7020 DSC device according to the ISO 11357-7 standard. Analysis parameters were studied between 30-300°C with 10°C/min temperature increase. The weights of the samples varied between 6-10 mg [22].
- *Characterization of dyed filament yarns.* According to the TS 244 ISO 2060 standard, the weight (yarn number) of the determined length of the dyed yarn was calculated. The tension of 100 m of yarn, which is passed through tension and yarn adjustment guides and tied to the spinning wheel, was determined as 0.051 g/dtex. This process was repeated 3 times for each of the 5 yarn samples. Yarn strength tests were carried out in the STATIMAT brand test device according to the DIN EN ISO 2062 standard. In this device the distance between the clamps is 500 mm, the test speed is 400 mm/min and the pre-tension value is 0.051 g/tex.

Measurements were made on the color charts in CIELAB color space with the X-rite spectrophotometer device at the laboratory unit of

Polyteks. The CIELAB color system is developed from the XYZ color system. This method is used to calculate the color difference between a specified standard color and a sample color. L*: is the luminance value, the axis perpendicular to the color space, 0º for black and 100º for white, it changes between these two values, the higher the L* value, the brighter the color. a* and b*: are chromatic coordinates, in CIELAB color space +a* indicates red direction, -a* indicates green, +b* indicates yellow and -b* indicates blue. Measurements were made 3 times on the charts and the color chart number 5 was taken as a reference (100% PET) [20, 21, 23]. Additionally, the whiteness indices were calculated according to Equation (1) [24, 25].

$$Whiteness\ index = 100 - \sqrt{(100-L^*)^2 + a^2 + b^2} \quad (1)$$

RESULTS AND DISCUSSION

The results of the experimental studies on the properties of recycled and virgin POY textured yarns as well as the effect of different mixing ratios are given below.

Properties of filament yarns

Table 4 shows the mechanical properties of POY yarns. The evenness, dtex number and tenacity of the yarns were similar. The elongation at break of rPET yarn was found to be slightly lower compared to the virgin PET yarns. The cross-sections of the yarns are shown in Figure 3.

Table 4. Mechanical properties of POY yarns

	Dtex/F[a]	Dtex	Elongation at break, (%)	Tenacity (cN/ dtex)	Evenness	K/C[c]
rPET	78/72	138.7	121.6±2.6	2.5	0.82	52.7
PET	78/72	138.8	124±2.8	2.4	0.83	63.4

[a]F: number of filaments, [c]K/C: shrinkage

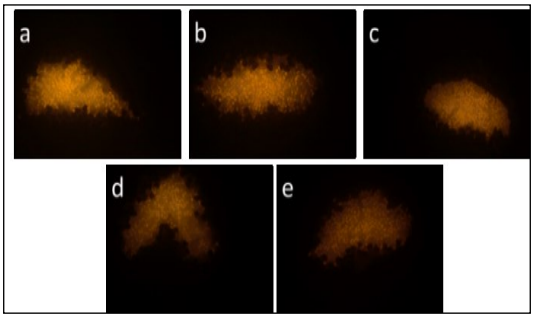

Figure 3. Images of the cross section of the yarns: a.P3 b. P4, c.P5, d. P1 e. P2

Thermal properties

The thermal properties of the yarns were determined using DSC. DSC curves of yarn samples are given in Figure 4. In DSC curves, the endothermic peaks of the fibers showed similar shapes. The melting temperatures of rPET and virgin PET were determined as 247.9 and 253.9 °C, respectively (Table 5). The melting temperatures of the blended yarns were close to that of virgin PET. The melting temperature of the blended yarns decreased with the increased rPET ratio.

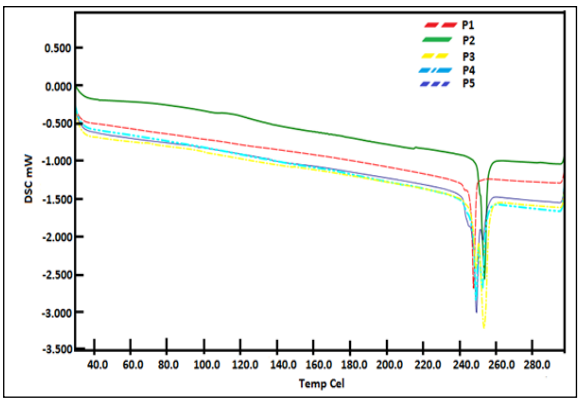

Figure 4. DSC curves with overlapping of the yarns samples. (DSC thermograms)

Table 5. Thermal properties of yarns from DSC

Sample	Blending Ratio of rPET: PET (%w/w)	Heat storage capacity (Cp) (mJ/mg)	T_m (°C)
P1	100:0	5.33	247.9
P2	0:100	3.55	253.9
P3	25:75	6.58	253.6
P4	50:50	7.42	249.1
P5	75:25	7.95	249.6

Mechanical properties of textured undyed and dyed yarns

Comparison of mechanical results of textured undyed and dyed yarns are shown in Table 6**.** Apparently, the dyed yarns have higher dtex value than the undyed ones. The elongation at break of undyed yarns were ranged between 17.13 – 23.21 %, while dyed samples were ranged between 24.35 - 29.15 %. The elongation at break of rPET yarns were lower than the virgin PET yarns. The elongation at break of both undyed and dyed yarns were reduced with the increased rPET ratio as expected.

The undyed virgin PET fiber (P2) have higher tenacity than that of undyed rPET fiber (P1). The tenacity of neat rPET (P1) and PET (P2) yarn found to be 3.57 and 3.78 cN/dtex, respectively. The undyed blended sample that have higher virgin PET ratio (P3) showed the highest tenacity (3.87 cN/tex). This increase was supposed due to the higher tenacity of PET fibers than rPET fibers [26].

Color of dyed textured yarns

The effect of blending ratio on the color characteristics of the yarns is shown in Table 7. Also, the visual appearances of the yarns are shown in Figure 5. There is not any apparent variation in dyeability between different PET yarns as a function of blending ratio. The blending ratio lead to very small changes in color coordinates. When the dyeability of the yarns is compared, it is seen that the L* values are as P3>P5>P4>P1>P2, while +a* and -b* values determined to be P1>P2= P3> P5> P4 and P2=P3>P1>P4>P5, respectively.

Table 6. Comparison of mechanical testing of textured undyed and dyed yarns

Sample code	Blending ratio (rPET: PET) % w/w	Dtex/F	Dtex	Elongation at break (%)	Maximum force (cN)	Tenacity (cN/dtex)
P1(undyed)	100:0	334/288	360.5	17.51	1285.43	3.57
P1 (dyed)			380.4	24.35	1302.96	3.43
P2 (undyed)	0:100	334/288	360.7	23.18	1360.51	3.78
P2 (dyed)			398.3	25.34	1314.81	3.30
P3 (undyed)	25:75	334/288	360.8	23.21	1394.92	3.87
P3 (dyed)			380.6	29.15	1376.95	3.62
P4 (undyed)	50:50	334/288	360.4	18.92	1223.37	3.40
P4 (dyed)			380.5	27.96	1337.99	3.52
P5 (undyed)	75:25	334/288	360.5	17.13	1269.19	3.53
P5 (dyed)			380.3	25.90	1278.23	3.36

Table 7. Color coordinates of blue dyed textured yarns

Sample	Mixing content (rpet:PET %w/w)	L*	a*	b*	ΔE	Whiteness index
P1	100:0	37.65	0.98	-41.32	3.12	25.19
P2	0:100	35.38	0.96	-41.41	-	23.24
P3	25:75	38.04	0.96	-41.41	3.46	25.46
P4	50:50	37.78	0.58	-40.95	2.95	25.51
P5	75:25	37.96	0.70	-40.86	2.98	25.71

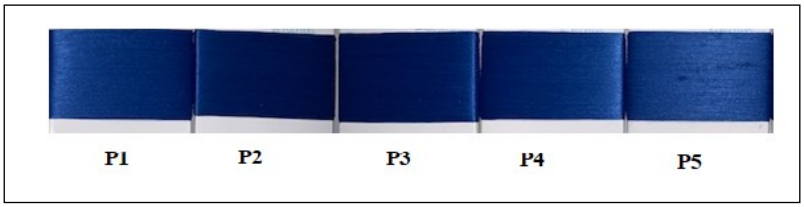

Figure 5. Color charts of dyed yarns

CONCLUSION

Recycled PET-based yarns were blended with virgin yarns to achieve circular economy goals for textile applications. The main conclusions are as follows:

- The blending ratio of rPET:PET showed no apparent effect on the dyeing properties of yarns.

- There was a reduction on elongation at break of both undyed and dyed yarns with the increased rPET ratio.
- Moreover, the melting temperature of the blended yarns slightly decreased with the increased rPET ratio.

This study brings important contributions to development possibility of blended polyester yarns from waste and virgin polyethylene terephthalate showing comparable characteristics with that of the virgin polyester yarns. The production of final yarns can provide environmental benefits due to evaluation of recycled polyethylene terephthalate.

Acknowledgement: *This research is supported by Polyteks Textile Industry Research And Education Co. The authors would like to thank Polyteks Textile Industry Research and Education Co for providing materials and analysis. Also, Sintas Bukum Boya Tekstil A.S. was acknowledged for the painting process.*

REFERENCES

1. S. Li, I.C. Vela, M. Järvien, M. Seeman, *Waste Management,* **130,** 117 (2021).
2. D.K. Barnes, F. Galgani, R.C. Thompson, M. Barlaz, *Philos. Tran.s R. Soc. B: Biological Sciences,* **364**(1526), 1985 (2009).
3. J.R. Jambeck, R. Geyer, C. Wilcox, T.R. Siegler, M. Perryman, A. Andrady, R. Narayan, K.L. *Science,* **347**(6223), 768 (2015).
4. J.P. da Costa, P.S. Santos, A.C. Duarte, T. Rocha-Santos, *Sci. Total Environ.,* **566,** 15 (2016).
5. L.C. De Sá, M. Oliveira, F. Ribeiro, T.L. Rocha, M.N. Futter, *Sci. Total Environ.,* **645,** 1029 (2018)**.**
6. *Plastics Europe*. (2016).
7. *Plastics Europe*. (2021).
8. L. Lebreton, A. Andrady, *Palgrave Communications* **5(1),** 1–11**.** (2019).
9. V. Tournier, C. Topham, A. Gilles, B. David, C. Folgoas, E. Moya-Leclair, E. Kamionka, M-L. Desrousseaux, H. Texier, S. Gavalda, *Nature* **580(7802),** 216. (2020).
10. YJ. Choi, SH. Kim, *Textile Research Journal,* **85(4),** 337. (2015).
11. D.Y. Wu, S.S. Wang, C.S. Wu, *ACS Applied Polymer Materials 2021, online publication*. (2021)
12. G. Li, Z. Jiang, W. Wang, Z. Chu, Y. Zhang, C. Wang, *Nanomaterials* **9(1),** 50. (2019).
13. J. Li, L. Chao, Q. Liao, Z. Xu, *Journal of Cleaner Production* **213,** 838. (2019).
14. S. Uyanık, *The Journal of The Textile Institute,* **110(7)***,* 1012 (2019).
15. WJ. Wu, XL. Sun, Q. Chen, Q. Qian, *Polymers,* **14(3)***,* 510 (2022).
16. Z. Guo, M. Eriksson, HDL. Motte, E. Adolfsson, *Journal of Cleaner Production*, **283,** 124579 (2021).
17. TTA. Luu, JR. Baker, *Journal of Open Innovation: Technology, Market, and Complexity,* **7(1)***,*22 (2021).
18. İ. Özkan, S. Gündoğdu, *The Journal of The Textile Institute,* **112(2)**, 264 (2021).
19. A. Telli, N. Özdil, *Tekstil ve Konfeksiyon* **23(1),** 3 (2013).
20. TS 244 EN ISO 2060. Textiles-Yarn from packages-Determination of linear density (mass per unit length) by the skein method, 1999.
21. DIN EN ISO 2062. Textiles - Yarns from packages - Determination of single-end breaking force and elongation at break using constant rate of extension (CRE) tester. 2009.
22. ISO 11357-7. Plastics - Differential scanning calorimetry (DSC) - Part 7: Determination of crystallization kinetics, 2022.
23. D. Durmus, *Color Research & Application*, **45(5),** 796 (2020).
24. M. Koosha, S. Hamedi, *Progress in Organic Coatings,* **127**, 338 (2019).
25. P. Terzioğlu, F. Güney, FN. Parın, İ. Şen, S. Tuna, *Food Packaging and Shelf Life* **30(3),** 100742 (2021).
26. E. Sarıoğlu, *Periodicals of Engineering and Natural Sciences* **5(2),** 176 (2017).

Bulgarian Chemical Communications, Volume 57, Issue 3 (pp.166-169) 2025 DOI: 10.34049/bcc.57.3.TS-EO

Determination of fatty acids in plant oils by gas chromatography, production and analysis of solid soap from these oils

T. Sabudak*, E. Ozcan

Department of Chemistry, Tekirdag Namik Kemal University, 59030, Tekirdag, Turkey

Accepted: August 17, 2025

Historically, humans have utilized various natural ingredients for medicinal and cosmetic purposes, favoring herbal cosmetics over synthetic alternatives. Given the potential for synthetic products to induce significant skin damage, natural herbs are increasingly incorporated into skincare formulations. This study focused on producing and analyzing soap *via* a cold process employing natural plant oils, and characterizing these oils using gas chromatography (GC). GC analysis revealed oleic acid (18:1), linoleic acid (18:2), and palmitic acid (16:0) as the predominant fatty acids in all oil samples. Notably, the produced natural solid soaps exhibited zero total alkali content. Based on total fatty matter values, the soaps were classified as Grade 1 and Grade 2, aligning with international standards.

Keywords: Plant oil, gas chromatography, fatty acid, natural solid soap, soap analysis.

INTRODUCTION

For centuries, plant-based preparations, including aromatic and fixed oils, have been used by various civilizations in religious rituals, for skin care, cleansing, and decoration, to enhance beauty and promote good health. There is a growing interest in cosmetic products derived from natural sources due to their beneficial effects compared to synthetic ingredients enriched with chemicals [1]. Also, the addition of herbal extracts into skincare formulations has numerous benefits, including anti-inflammatory, antioxidant, antiseptic, and antimicrobial activities [2]. Soap is one of the oldest treatment and cleaning agents in the world. The most useful soap for human health is made from natural vegetable oils without any chemicals [3]. The fact that natural soap prepared using natural products is more environmentally friendly and rich in antioxidants has become a promising alternative to soaps produced using synthetic chemicals [4].

The aim of this study is the production of soap using natural plant oils and characterization of the used oils by gas chromatography (GC). For this purpose, a cold saponification reaction was carried out without heating, using olive oil as the main raw material. In addition, some plant oils (coconut oil, castor oil, cocoa butter, shea butter, daphne oil, argan oil, meningic oil) were added to the reaction medium to increase the beneficial use of the soap on the skin. This study falls under the "Valuable Chemicals from Plant Sources" section within the framework of TUBITAK 2022-2023 Priority R&D and Innovation Topics and contributes to the development of more environmentally sensitive products and the production of valuable chemicals from plant sources [5].

EXPERIMENTAL

General experimental procedures

Chemicals used in this study and their suppliers: Daphne oil (MSA cosmetics), argan oil (MSA cosmetics), menengic oil (MSA cosmetics), castor oil (MSA cosmetics), olive oil (Simya), coconut oil (MSA cosmetics), cacao oil (MSA cosmetics), shea butter (MSA cosmetics), NaOH (Aromel Chemistry), NaCl (Aromel Chemistry), methyl orange (Zag Chemistry), Hydrochloric acid (Aromel Chemistry), dietylether (Tekkim-TK.05013001000), sodium sulfate (Sigma-Aldrich), ethanol (Isolab-920.052.5000), barium chloride (Kimyalab-V01719.901), phenolphthalein (Merck). Devices used in this study and their suppliers: Rotary evaporator (Büchi; B-491), distilled water device (Elga, DV25), ultrasonic bath (Wisd, WUC-D06H), gas chromatograph (Agilent 6890), blender (Fakir).

Determination of fatty acids in plant oils by gas chromatography

Gas chromatography method was used to determine the fatty acids in olive oil, daphne oil,

* To whom all correspondence should be sent:
E-mail: *tsabudak@nku.edu.tr*

argan oil and menengic oil used in soap making. First, the conversion of fats to methyl ester derivatives was performed. Fatty acid methyl esters were prepared as in [6]. The instrument Agilent 6890 series gas chromatograph was used for chromatographic analysis. HP-88 ((88% cyanopropyl) aryl polysiloxane, 100 m × 0.25 mm × 250 µm) capillary column was used. Operation conditions were as follows: the injector and detector temperatures were set at 250 and 280 °C, respectively. Manual injections were performed with a split ratio of 50:1. The temperature gradient was programmed as follows: an initial 11-min hold at 120°C, followed by a ramp to 175°C at 10°C/min, maintained for 10 min. Subsequent ramps included an increase to 210°C at 5°C/min (5-min hold) and a final ramp to 230°C at 5°C/min (5-min hold). Helium served as the carrier gas, delivered at 30 ml/min, with a 1 µl injection volume and a column head pressure of 54.6 kPa. The total run time was 50 min. Supelco 37 component FAME mix (10.000 mg/mL) was used as an internal standard. The fatty acids were identified by comparing their retention times to those of pure fatty acid methyl ester standards, and their amounts were determined as a percentage of the total fatty acid area, which includes all minor components.

Saponification reaction and soap formulations

In this study, natural solid soaps were synthesized, and formulations were developed to align properties like bubbling, cleansing, and lathering with public needs. For this purpose, a dedicated software (soapcalc.net) was utilized to formulate the final product. The software operates through a trial-and-error method. Oil types and mass percentages are input (Figure 1), and it calculates the corresponding soap's properties (bubbling, hardness, cleansing, conditioning, lathering, etc.) (Figure 1). Furthermore, the software program calculates the required alkali amount for the soap-making process by considering the SAP (saponification) values of oils, fats, and waxes. Figure 1 shows the software, which was used during this study. In solid soap production, the saponification reaction was carried out without heating in order not to impair the activity of the oils used in this method. Oils (olive oil, coconut oil, castor oil, cocoa butter, shea butter oil / argan oil / daphne oil / bıttım (menengic) oil) were melted by bain-marie method and treated with sodium hydroxide solution. After stirring, the mixture was poured into silicone molds and removed from the molds after 1 day. The resulting soap was kept on the shelf for about 4 weeks. In this part of the study, olive oil soap, daphne soap, argan soap and bıttım (menengic) soap were made (Figure 2).

SoapCalc © Recipe Name: E-A-KS-D:153 New INCI Names Print Recipe

Total oil weight	500 g	Sat : Unsat Ratio	42 : 58
Water as percent of oil weight	35.00 %	Iodine	56
Super Fat/Discount	6 %	INS	152
Lye Concentration	28.456 %	Fragrance Ratio	0
Water : Lye Ratio	2.5142:1	Fragrance Weight	0.00 g

	Pounds	Ounces	Grams
Water	0.386	6.17	175.00
Lye - NaOH	0.153	2.46	69.60
Oils	1.102	17.64	500.00
Fragrance	0.000	0.00	0.00
Soap weight before CP cure or HP cook	1.642	26.27	744.60

#	√	Oil/Fat	%	Pounds	Ounces	Grams
1	☐	Castor Oil	5.00	0.055	0.88	25.00
2	☐	Cocoa Butter	9.00	0.099	1.59	45.00
3	☐	Coconut Oil, 92 deg	28.00	0.309	4.94	140.00
4	☐	Olive Oil	42.00	0.463	7.41	210.00
5	☐	Shea Butter	9.00	0.099	1.59	45.00
6	☐	Argan Oil	7.00	0.077	1.23	35.00
		Totals	100.00	1.102	17.64	500.00

Soap Bar Quality	Range	Your Recipe		
Hardness	29 - 54	40	Lauric	13
Cleansing	12 - 22	19	Myristic	5
Conditioning	44 - 69	56	Palmitic	12
Bubbly	14 - 46	23	Stearic	9
Creamy	16 - 48	26	Ricinoleic	5
Iodine	41 - 70	56	Oleic	42
INS	136 - 165	152	Linoleic	9
			Linolenic	0

Fig. 1. Software used in soap formulations

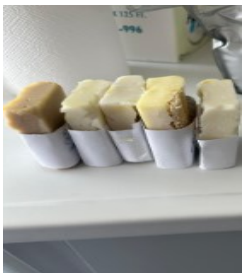

Fig. 2. Produced natural solid soaps

Analysis of produced natural solid soaps

- *Total free alkali:* 10 g soap was dissolved in 100 mL of ethanol and boiled in a water bath for 15 min. The flask was removed from the water bath and 10 % $BaCl_2$ solution was added slowly until no more precipitate was formed. Then 0.5 mL of 1 % phenolphthalein indicator was added to this solution and titrated with 0.1 N HCl acid solution. The total alkali content was calculated using the following formula [7].

$$\% \text{ Total free alkali} = [(V \times N) / m] \times (40/1000) \times 100$$

where V = volume of HCl, N = concentration of HCl, m = weight of soap.

- *Total fatty matter:* Approximately 10 g of powdered soap was diluted in 50 mL of distilled water and heated. Then, the soap solution was allowed to cool until it became clear. Two drops of methylorange (0.1 %) were added to the solution and titrated with 20 % HCl solution until the color turned red. The mixture was taken into an extraction flask and diethyl ether was added. The ether phase was washed with 10 % NaCl solution and dried over anhydrous Na_2SO_4. After removing Na_2SO_4 by

filtration, the ether phase was evaporated in a rotary evaporator and the fatty acids were dried in an oven at 70°C and weighed. Total fatty matter was calculated using the following formula [7].

$$\% \text{ Total fatty matter (TFM)} = (a \times b) \times 100 / m$$

where a=weight of the balloon with TFM, b= weight of the balloon, m= weight of soap.

RESULTS AND DISCUSSION

Determination of fatty acids in plant oils by gas chroatography

Gas chromatography was used to determine the fatty acids in olive, daphne, argan and menengic oils used in soap making. The obtained results are shown in Table 1. A total of 10 fatty acids were determined as a result of GC analysis of olive oil (Table 1).

Table 1. GC analysis results of olive oil, daphne oil, argan oil and menengic oil

No	Fatty acids	Peak area (%)			
		Olive oil	Daphne oil	Argan oil	Menengic oil
1	Lauric acid (12:0)	-	0.32	-	-
2	Myristic acid (14:0)	0.30	0.35	0.15	0.16
3	Palmitic acid (16:0)	14.78	18.50	13.46	11.58
4	Palmitoleic acid (16:1)	0.27	0.18	0.08	0.79
5	Stearic acid (18:0)	2.93	3.48	5.86	2.42
6	Oleic acid (18:1)	23.82	43.86	46.73	56.06
7	Linoleic acid (18:2)	54.44	29.64	32.66	27.91
8	Arachidic acid (20:0)	0.48	0.69	0.38	0.23
9	Linolenic acid (18:3)	2.29	0.29	0.06	0.22
10	Eicosenoic acid (20:1)	0.32	0.51	0.43	0.24
11	Behenic acid (22:0)	0.16	1.11	0.12	0.17
12	Lignoseric acid (24:0)	-	0.52	-	0.16
	Total saturated fatty acids (SFA)	18.65	25.47	19.97	14.78
	Total unsaturated fatty acids (UFA)	81.14	74.48	79.96	85.22

According to Table 1, the most abundant fatty acids are linoleic acid (54.44 %), oleic acid (23.83 %) and palmitic acid (14.78 %). A total of 12 fatty acids were determined by GC analysis of daphne oil (Table 1), the most abundant being oleic acid (43.86 %), linoleic acid (29.65%) and palmitic acid (18.50%). A total of 10 fatty acids were determined by GC analysis of argan oil (Table 1), the most abundant being oleic acid (46.74 %), linoleic acid (32.67 %), palmitic acid (13.46 %) and stearic acid (5.86 %). As a result of GC analysis of menengic oil, a total of 11 fatty acids were determined (Table 1), the most abundant being oleic acid (56.06 %), linoleic acid (27.91 %) and palmitic acid (11.59 %). According to these data, the highest unsaturated fatty acid content was determined in menengic oil (85.22 %) and the lowest was determined in daphne oil (74.48 %). The highest saturated fatty acid content was determined in daphne oil (25.47 %) and the lowest content in menengic oil (14.72 %). Oleic acid (18:1), linoleic acid (18:2) and palmitic acid (16:0) were found to be the main fatty acids with high levels in all oil varieties.

Analysis of total free alkali

Free alkali content is a critical parameter influencing soap abrasiveness. International Standards Organization (ISO) specifications mandate that soaps should contain less than 2% alkali [8, 9]. Free alkali in natural solid soaps was found 0.00 % in this study. This result proved that the sodium hydroxide used during the saponification reaction was used in the correct proportion and all of it reacted. Consumption of all of the sodium hydroxide used in the saponification reaction was considered to be a very good result.

Analysis of total fatty matter

Soap quality is significantly determined by its total fatty matter (TFM), a key metric consistently used in commercial transactions. While higher TFM often correlates with increased hardness, it generally indicates a lower quality product.

Notably, European and certain national standards classify soap based on TFM content, with Grade 1 requiring a minimum of 75% and Grade 2 a minimum of 65%. Soaps exhibiting higher total fatty matter (TFM) are known to produce richer lather, offer extended longevity, and, critically, provide superior and gentler skin cleansing [10, 8]. This study measured the TFM of soap samples and benchmarked these values against established standards (Table 2). The results indicate that the produced solid soaps align with Grade 1 and Grade 2 classifications [10, 8].

Table 2. Results of total fatty matter analysis in solid soap

Solid soaps	Total fatty matter (%)
Olive oil soap	72.53
Daphne soap	65.66
Argan soap	63.34
Menengic soap	81.00

CONCLUSION

In this study, natural solid soaps with high cleaning and foaming properties, free of chemicals and additives, were produced using natural plant oils (daphne oil, argan oil, menengic oil, olive oil, castor oil, coconut oil, cocoa butter, shea butter). Fatty acids of plant oils used in natural solid soap making were determined by gas chromatography (GC). According to the GC results, oleic acid, linoleic acid and palmitic acid were found to be the 3 fatty acids with the highest content in all plant oils. The solid soaps analyzed showed no detectable free alkali, and their total fat content was measured to be between 63% and 81%. These parameters are key indicators of soap quality and its suitability for cleansing purposes. From this, it can be concluded that the soaps produced have lower alkali content and higher TFM value. As a result, the soaps produced are of good quality (Grade 1 /2) soaps suitable for use for health and environment.

Acknowledgement: *The present study was supported by the Scientific Research Project Coordination Center (Project No: NKUBAP.01.YL.24.570).*

REFERENCES

1. K. B. Patkar, *Indian J. Plast Surg.,* **41**, 134 (2008).
2. F. Jahan, A. A. Happy, M. M. H. Chowdhury, M. A. Hossain, *J. Plant Sci.*, **7**, 86 (2019).
3. O. Goktas, B. Gıdık, *Bayburt Un. Fen Bi.l Dergisi,* **2**,136 (2019).
4. K. Rambabu, A. Achazhiyath Edathil, G. S. Nirmala, W. H. Shadi, A. F. Yousef, P. L. Show, F. Banat, *Environ. Tech. Innov.*, **20**, 101153 (2020).
5. Türkiye Bilimsel ve Teknolojik Araştırma Kurumu (TÜBİTAK) (2023). https://tubitak.gov.tr/sites/default/files/18842/arge_ve_yenilik_konu_basliklari_4.08.22.pdf
6. IUPAC Standard Methods for Analysis of Oils, Fats and Derivatives. Seventh ed. Blackwell Scientific Publications, IUPAC method 2, 3001, Report of IUPAC Working Group WG 2/87, 1987.
7. F. Sert, Osmaniye Korkut Ata Ün. Fen Bil. Enst., Osmaniye, 2021.
8. Bureau of Indian standards, DOC: CHD 20 (1861) C, May 2011.
9. The International standard specification for soaps, ISO 685: 1975.
10. K. J. Agents, B. M. Jilu, R. Fathima, J. T. Varkey, *Asian J. Sci. App. Tech.*, **2**, 8 (2013).

Bulgarian Chemical Communications, Volume 57, Issue 3 (pp. 170-174) 2025 DOI: 10.34049/bcc.57.GS-MB

In silico insight on hyaluronic acid and boron hyaluronate

G. Serdaroğlu[1*], M. Bolat[2], D. Ali Köse[3], Z. Öztemür[4], N. Karakuş[5]

[1]*Sivas Cumhuriyet University, Faculty of Education, Math. and Sci. Edu., 58140, Sivas, Turkey*
[2]*Hitit University, Vocational School of Technical Sciences, Department of Property Protection and Security, 19900, Çorum, Turkey*
[3]*Hitit University, Faculty of Arts and Sciences, Department of Chemistry, 19040, Çorum, Turkey*
[4]*Sivas Cumhuriyet University, Faculty of Medicine, Department of Orthopedic and Traumatology, 58140, Sivas, Turkey*
[5]*Sivas Cumhuriyet University, Faculty of Science, Department of Chemistry, 58140, Sivas, Turkey*

Accepted: Accepted: August 17, 2025

Hyaluronic acid (HA) and galacturonic acid (GA) core structures and their boron derivatives were investigated using *in silico* tools to predict/elucidate physicochemical and electronic profiles. First, geometry optimization and structural confirmation of the core structures and designed derivatives were performed at B3LYP/6-311G** level. Then, the thermochemistry, lipophilicity, and water solubility properties of the data set were determined to provide the main physicochemical profiles, which would have an essential role in early-stage drug-design research. Further, NBO analyses were performed to evaluate the important intramolecular interactions contributing to lowering of the stabilization energy.

Keywords: Hyaluronic acid, boron hyaluronate, DFT, solubility

INTRODUCTION

Hyaluronic acid, a natural unbranched polymer, is a member of heteropolysaccharides, and pioneering research on HA goes back to the 1880s [1]. HA and related molecular systems are getting increasing attention due to the inclusion of hydroxyl, carboxyl, acetamido, and anomeric carbons, which provide structural advantages [2-4]. The viscoelasticity and hydrophilic nature of these compounds with biocompatible and degradable properties make them very useful in biomedical applications such as regenerative medicine and target-specific therapies [5, 6]. Nowadays, *in silico* investigations provide great advantages in early-stage drug design via saving time and resource consumption in the related processes. In this regard, Azam and co-workers have investigated the adsorption mechanism of methotrexate on hyaluronic acid using DFT and molecular dynamic simulations [7]. Also, the HA-curcumin hybrid compound has been analyzed with NBO and FMO analyses at B3LYP/6-311G(d,p) level to elucidate the electronic structure and possible reactivity features [8]. In a recent work on HA in salt media has been investigated using QM and molecular dynamic simulations to enlighten the hydration and assembly of HA [9]. Wang and co-workers have performed the DFT-D simulations to evaluate the adsorption characteristics of HA onto graphene sheets to explore the possible usage in biomedical applications of graphene-hyaluronic acid (HA) composites [10].

Herein, the quantum mechanical computations were performed to evaluate the physicochemical and electronic properties of HA and the structurally similar GA (galacturonic acid) compounds, their boron-doped derivatives, and Na-salts.

Computational details

The quantum mechanical simulations of the neutral molecules and their Na-salts were performed by the G16W [11] package at B3LYP/6-311G** [12,13] level. The GaussView 6.0.16 [14] package was used to illustrate optimized structures, FMO densities, and MEP plots. The thermochemical data obtained from the simulations were evaluated using the basis of quantum statistical principles [15,16]. Also, the NBO analyses were performed to predict the intramolecular interactions, which contributed to the lowering stabilization energy [17,18].

The HOMO and LUMO energies were used to predict *I* (ionization energy) and *A* (electron affinity) [19]; then, the global reactivity indices were determined using the following equations.

$I = -E_{HOMO}$ and $A = -E_{LUMO}$ $\quad \chi = -(\frac{I+A}{2})$

$\eta = \frac{I-A}{2}$ $\quad \omega = \frac{\mu^2}{2\eta}$ $\quad \Delta N_{max} = (I+A)/2(I-A)$

$\omega^+ \approx (I+3A)^2/(16(I-A))$

$\omega^- \approx (3I+A)^2/(16(I-A))$

$\Delta\varepsilon_{back-donation} = -(\eta/4)$

* To whom all correspondence should be sent:
E-mail: *goncagul.serdaroglu@gmail.com*

wherein the terms are defined as $\chi \rightarrow$ electronic chemical potential $\eta \rightarrow$ global hardness, $\omega \rightarrow$ electrophilicity, $\Delta N_{max} \rightarrow$ maximum charge transfer capability index [20, 21], $\omega^- \rightarrow$ electrodonating power, $\omega^+ \rightarrow$ electroaccepting power [22], and $\Delta E_{back\text{-}donat.} \rightarrow$ back-donation energy [23].

The lipophilicity [24-28] and water-solubility [29,30] properties of the HA and GA derivatives were estimated using SwissADME [31] tools.

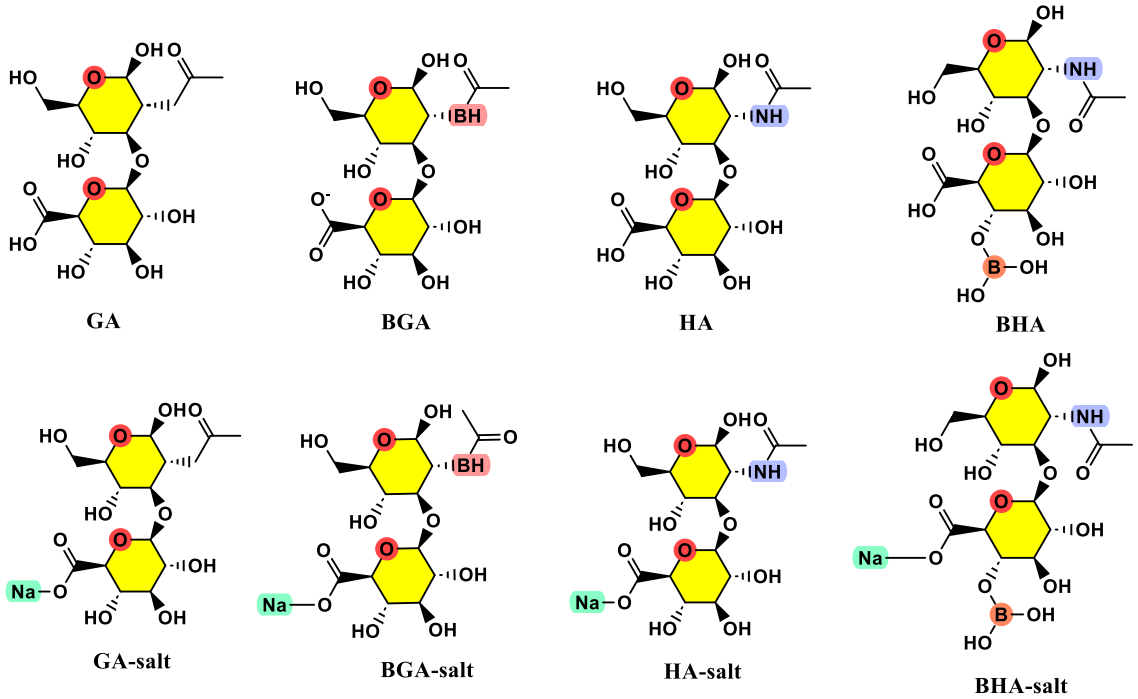

Fig. 1. Optimized chemical structures of the data set

RESULTS AND DISCUSSION

Physicochemistry

The thermochemical and physical parameters of the data set are summarized in Table 1. Accordingly, the ΔE, ΔH, and ΔG quantities of the BHA molecule were determined as -1680.871413, -1680.840013, and -1680.934043 au, respectively, whereas these values of BGA were computed as -1474.851916, -1474.822816, and -1474.911318 au. On the other hand, the BHA (6 D) molecule would have a bigger dipole moment than the others for their neutral forms, while the BGA-salt (11.45 D) would have the biggest dipole moment among the Na-salts. Moreover, the biggest polarizability value was calculated for the BHA and BHA-Na salt at 218.53 and 223.82 au, respectively. Furthermore, Cv and S values of the BHA neutral molecule were determined as 114.690 and 197.903 cal.mol/K, respectively, whereas these values for BHA-Na salt were predicted as 118.828 and 202.230 cal.mol/K. Accordingly, the BHA and BHA-Na systems would have the biggest heat capacity and entropy values for the neutral and salt forms, respectively. From Table 2, the consensus LogPo/w /w order of the neutral structures was calculated as BHA (-4.82)< HA (-3.75)< BGA (-3.48)< GA (-3.39); the boron-doped HA molecule could exhibit less electrophilic character among the compounds, and vice versa for GA molecule. Except for the iLOGP method, the approaches gave the same order as the neutral structures. Herein, the order of the lipophilicity. Also, the BHA and its Na-salt would have the highest solubility in water in comparison to the other molecules, depending on all approaches.

NBO study

Table 3 summarizes the resonance ($n \rightarrow \pi^*$) and anomeric ($n \rightarrow \sigma^*$) interactions of the HA and BHA compounds. Accordingly, the LP (1) N13 (EDi= 1.70010e)→ π* O12-C26 (EDj= 0.29999e) resonance for HA was calculated with the $E^{(2)}$ of 61.99 kcal/mol, which was the highest contribution to the lowering energy. On the other hand, the LP (2) O9 (EDi= 1.80218e)→ π* O10-C24 (EDj= 0.20798e) resonance for the BHA compound would have the biggest contribution to the lowering stabilization energy with $E^{(2)}$ of 48.32 kcal/mol. Also, the LP (1) N2 (EDi= 1.74008e)→ π* O11-C25 (EDj= 0.22282e) and LP (2) O28 (EDi= 1.84202e)→ LP (1) B (EDj= 0.42071e) interactions for BHA compound would have critical role in lowering of the stabilization energy with $E^{(2)}$ of 26.32 and 54.83 kcal/mol, respectively.

Table 1. Thermochemical and physical values of the data set

Comp.	ΔE (au)	ΔH (au)	ΔG (au)	$E_{therm.}$ (kcal/mol)	Cv (cal.mol/K)	S (cal.mol/K)	μ (D)	α (au)
GA	-1488.699821	-1488.670393	-1488.760502	275.808	105.856	189.651	2.97	203.68
BGA	-1474.851916	-1474.822816	-1474.911318	265.955	105.255	186.267	4,85	208.82
HA	-1504.788029	-1504.759238	-1504.847002	269.246	104.287	184.716	3.09	200.53
BHA	-1680.871413	-1680.840013	-1680.934043	287.409	114.690	197.903	6,00	218.53
GA-Na	-1650.493388	-1650.463057	-1650.555644	269.739	108.452	194.865	11.95	214,07
BGA-Na	-1636.620680	-1636.589568	-1636.684508	259.455	109.788	199.818	11.45	216.96
HA-Na	-1666.560761	-1666.530837	-1666.620838	263.169	107.764	189.423	4.58	209.25
BHA-Na	-1842.655690	-1842.623257	-1842.719343	280.396	118.828	202.230	8,24	223.82

Table 2. Lipophilicity and water solubility

	GA	BGA	HA	BHA	GA-salt	BGA-salt	HA-salt	BHA-salt
Lipophilicity								
iLOGP	-3.20	0.00	-0.53	0.00	0.00	0.00	0.00	0.00
XLOGP3	-1.90	-2.26	-3.05	-4.92	-3.09	-2.26	-3.63	-4.61
WLOGP	-4.18	-5.05	-5.31	-6.17	-4.15	-4.99	-5.24	-6.24
MLOGP	-3.45	-4.12	-4.46	-5.85	-3.77	-4.12	-4.37	-5.85
SILICOS-IT	-4.23	-5.99	-5.37	-7.15	-4.63	-7.30	-5.76	-8.23
Avg. LogPo/w	-3.39	-3.48	-3.75	-4.82	-3.13	-3.73	-3.80	-4.99
Water Solubility								
Log S (ESOL)	-0.84	-0.53	-0.05	1.05	-0.02	-0.67	0.31	0.79
Solubility (mg/mL)x10^2	0.578	1.16	3.53	49.8	3.95	0.898	8.54	28.4
Class	VS	VS	VS	HS	VS	VS	HS	HS
Log S (Ali)	-1.85	-1.48	-0.91	0.41	-0.39	-1.41	-0.08	0.32
Solubility (mg/mL)x10^2	0.0558	0.131	0.488	11.4	1.72	0.161	3.50	9.68
Class	VS	VS	VS	HS	VS	VS	VS	HS
Log S (SILICOS-IT)	2.80	3.16	3.16	4.62	3.06	3.11	3.41	4.25
Solubility (mg/mL)x10^5	2.51	5.75	5.69	183	4.80	5.32	10.9	82.4
Class	S	S	S	S	S	S	S	S

Table 3. NBO analysis results of the possible interactions

	Donor(i)	ED_i/e	Acceptor(j)	ED_j/e	$E^{(2)}$ kcal/mol	E(j)-E(i)/a.u	F(i.j)/a.u
HA	LP (2) O1	1.88758	σ* O3-C18	0.07364	15.92	0.58	0.086
	LP (2) O5	1.93345	σ* O2-C19	0.05344	11.01	0.62	0.074
	LP (2) O10	1.81638	π* O11-C25	0.19386	45.33	0.35	0.113
	LP (2) O11	1.84432	σ* C23-C25	0.07228	19.97	0.62	0.102
	LP (2) O12	1.87173	σ* N13-C26	0.07297	23.65	0.73	0.119
			σ* C26-C27	0.05406	18.46	0.63	0.098
	LP (1) N13	1.70010	π* O12-C26	0.29999	61.99	0.29	0.120
BHA	LP (2) O1	1.89101	σ* O3-C17	0.06881	14.05	0.58	0.082
	LP (2) O5	1.93075	σ* O2-C18	0.05813	12.71	0.61	0.079
	LP (2) O7	1.85047	LP(1) B	0.42071	39.55	0.33	0.109
	LP (2) O9	1.80218	π* O10-C24	0.20798	48.32	0.35	0.116
	LP (2) O10	1.85191	σ* C22-C24	0.07128	18.24	0.63	0.098
	LP (2) O11	1.86932	σ* N12-C25	0.06877	20.75	0.72	0.111
			σ* C25-C26	0.05191	18.83	0.65	0.101
	LP (1) N2	1.74008	π* O11-C25	0.22282	26.32	0.38	0.090
	LP (2) O28	1.84202	LP(1) B	0.42071	54.83	0.31	0.124

FMO and MEP analyses

The reactivity values obtained from FMOs' energies have been used to predict the possible reactivity directions and regions of the molecular systems, wherein the determined reactivity values of the compounds change in the following orders of

ΔE (L-H): HA (6.733)> BHA (5.94)> GA (5.88)> BGA (5.144)> BHA-salt (5.25)> HA-salt (4.945) > GA-salt (4.185)> BGA-salt (4.034)

μ: BGA (–4.316)< BHA-salt (–4.276)< BHA (–4.251)< GA-salt (–4.106)< BGA-salt (–4.025)< HA (–3.803)< HA-salt (–3.786)< GA (–3.672)

η: HA (3.366)> BHA (2.97)> GA (2.94)> BHA-salt (2.625)> BGA (2.572)> HA-salt (2.473)> GA-salt (2.092)> BGA-salt (2.017)

ω: BGA-salt = GA-Salt (0.148)> BGA (0.133)> BHA-salt (0.128)> BHA (0.112)> HA-salt (0.107)> GA (0.084)> HA (0.079)

ω^+: BGA-salt (0.083)> GA-salt (0.082)> BGA (0.066)> BHA-salt (0.061)> HA-salt (0.048)> BHA (0.047)> GA (0.030)> HA (0.025)

ω^-: GA-salt (0.233)> BGA-salt (0.231)> BGA (0.224)> BHA-salt (0.219)> BHA (0.204)> HA-salt (0.187)> GA (0.165)> HA (0.164)

ΔN_{max}: BGA-salt (1.996)> GA-salt (1.962)> BGA (1.678)>BHA-salt (1.629)> HA-salt (1.531)> BHA (1.431)> GA (1.249)> HA (1.130)

$\Delta E_{back.}$: HA (–0.842)< BHA (–0.742)< GA (–0.735)< BHA-salt (–0.656)< BGA (–0.643)< HA-salt (–0.618)< GA-salt (–0.523)< BGA-salt (–0.504)

Table 4. Chemical reactivity parameters

	H (-I)/ eV	L (-A)/ eV	ΔE (L-H)/ eV	μ/ eV	η/ eV	ω/ au	ω^+/ au	ω^-/ au	ΔN_{max}/ eV	$\Delta E_{back.}$/ eV
GA	-6,612	-0,732	5,880	-3,672	2,94	0,084	0,03	0,165	1,249	-0,735
BGA	-6,888	-1,744	5,144	-4,316	2,572	0,133	0,066	0,224	1,678	-0,643
HA	-7,17	-0,437	6,733	-3,803	3,366	0,079	0,025	0,164	1,13	-0,842
BHA	-7,221	-1,281	5,940	-4,251	2,97	0,112	0,047	0,204	1,431	-0,742
GA-Salt	-6,198	-2,014	4,185	-4,106	2,092	0,148	0,082	0,233	1,962	-0,523
BGA-salt	-6,042	-2,008	4,034	-4,025	2,017	0,148	0,083	0,231	1,996	-0,504
HA-salt	-6,259	-1,313	4,945	-3,786	2,473	0,107	0,048	0,187	1,531	-0,618
BHA-Salt	-6,901	-1,651	5,250	-4,276	2,625	0,128	0,061	0,219	1,629	-0,656

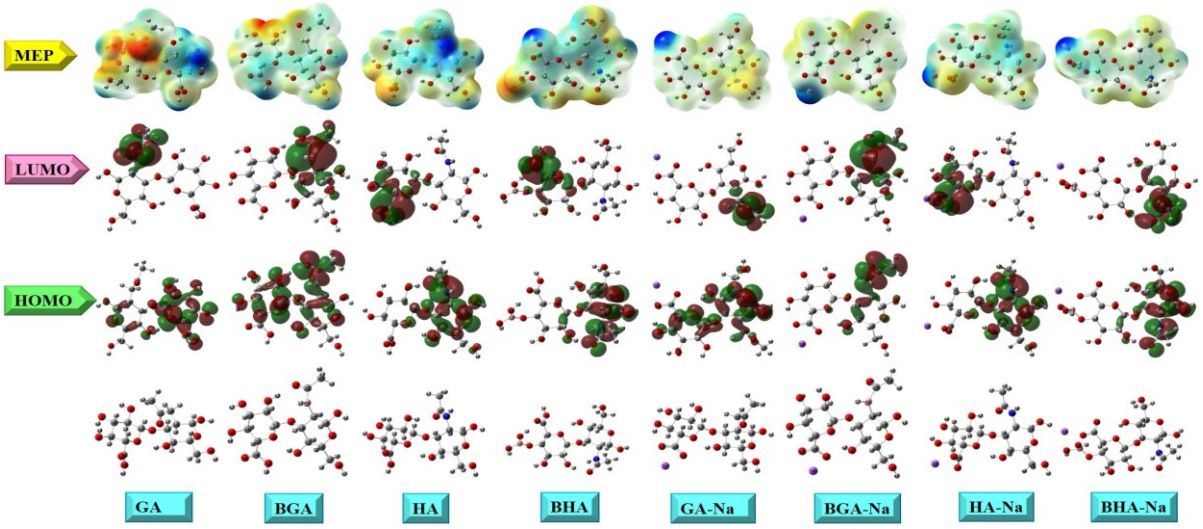

Fig. 2. Optimized structures. HOMO. LUMO. and MEP diagrams of the data set

From Table 4, the HA molecule, in comparison to the other molecules, would prefer to interact with the outer system rather than the intramolecular charge transition between the FMOs due to having the highest energy gap value (ΔE_{L-H}=6.733 eV), and vice versa for BGA-salt. The results revealed that the HA molecule would exhibit the hardest character (η=3.366 eV), less charge transfer capability (ΔN_{max}=1.130 eV), and could gain more stabilization via back donation ($\Delta E_{back.}$=–0.842 eV) than the others could. On the other hand, the BGA-salt structure would be softer (η=2.017 eV) than the others, as well as having the highest charge transfer capability (ΔN_{max}=1.996 eV) and less stabilization via back donation ($\Delta E_{back.}$=–0.504 eV). Figure 2 displays the FMOs' densities and MEP plots of the

dataset. As expected, the H atom(s) belonging to the -OH group were covered by blue color (V>0) as an indicator of the electron-poor region for the nucleophiles as a function of the electrostatic potential, whereas the O atom of the carboxyl group was covered by red (V<0) as a marker of the electron-rich region for the electrophiles. The HOMO for the GA was expanded on carboxylic acid substituted ring (right) mostly and slightly other ring, whereas the LUMO was densified on the -butan-2-one substitution. On the other hand, the HOMO for HA and BHA molecules was separated on the acetamide-substituted ring mostly, whereas the LUMO appeared on the other ring (left) substituted by carboxylic acid substituted.

CONCLUSION

Herein the HA and the structurally similar GA main compounds and their boron derivatives were investigated using computational tools. The B3LYP/6-311G** level computations were performed to predict/evaluate the optimized structures, thermochemistry, NBO and FMO analyses. SwissADME online tools were used to determine the solubility features in octanol and water, which would help to provide insight into early-stage drug-design works.

Acknowledgement: *All calculations have been carried out at TUBITAK ULAKBIM, High Performance and Grid Computing Center (TR-Grid e-Infrastructure). The author thanks the Scientific Research Projects Department of Cumhuriyet University (Project No: EĞT-2024-099).*

REFERENCES

1. G. Abatangelo, V. Vindigni, G. Avruscio, L. Pandis, P. Brun, *Cells,* **9**(7), 1743 (2020).
2. A. Fallacara. E. Baldini. S. Manfredini, S. Vertuani, *Polymers*, **10**(7), 701 (2018).
3. J. Necas, L. Bartosikova, P. Brauner, J. Kolar, *Veterinarni Medicina,* **53**(8), 397 (2008).
4. N.M. Salwowska, K.A. Bebenek, D.A. Żądło, D.L. Wcisło-Dziadecka, *J. Cosmet. Dermatol*., **15**, 520 (2016).
5. H. Pereira, D.A. Sousa, A. Cunha, R. Andrade, J. Espregueira-Mendes, J.M. Oliveira, R.L. Reis, in: J. Oliveira, S. Pina, R. Reis, J. San Roman (eds.). Osteochondral Tissue Engineering. Adv. Exp. Med. Biol., vol. 1059. Springer. Cham., 2018, p. 139.
6. R.D. Price, M.G. Berry, H.A. Navsaria, *J. Plast. Reconstr. Aesthet. Surg.,* **60**(10), 1110 (2007).
7. F. Azam, H.R. Abd El-Mageed, M.J. Anwar, D. Mahmood, *Chem. Phys. Impact*., **8**, 100573 (2024).
8. S.A.K. Kirmani, P. Ali, F. Azam, A.E. Kuznetsov, P.A. Alvi, *Comput. Theor. Chem*., **1214**, 113761 (2022).
9. S. Vasudevan, S. Chattaraj, A. Enrico, F.S. Pasqualini, *Langmuir,* **41**(6), 3852 (2025).
10. Q. Wang, W. She, X. Lu, P. Li, Y. Sun, X. Liu, W. Pan, K. Duan, *Comput. Theor. Chem.*, **1165**,112559 (2019).
11. A. D. Becke, *J. Chem. Phys*., **98**, 1372 (1993).
12. C. Lee, W. Yang, R.G. Parr, *Phys. Rev*., **B37**, 785 (1988).
13. M. J. Frisch et al. Gaussian 09W. Revision D.01. Gaussian. Inc. Wallingford CT. 2013.
14. GaussView 6.0.16. Gaussian. Inc. Wallingford CT. (2016).
15. D. A. McQuarrie, Statistical Thermodynamics. Harper & Row Publishers. New York, 1973.
16. G. Serdaroglu, S. Durmaz, *Indian J. Chem*., **49**, 861 (2010).
17. J.P. Foster, F. Weinhold, *J. Am. Chem. Soc*., **102**, 7211 (1980).
18. A.E. Reed, L.A. Curtiss, F. Weinhold, *Chem. Rev*., **88**, 899 (1988).
19. T. Koopmans, *Physica*, **1**, 104 (1934).
20. R. G. Pearson, *Proc. Natl. Acad. Sci. USA*., **83**, 8440 (1986).
21. R. G. Parr, L.V. Szentpaly, S. Liu, *J. Am. Chem. Soc*., **121**, 1922 (1999).
22. J. L. Gazquez, A. Cedillo, A. Vela, *J. Phys. Chem. A*., **111**(10), 1966 (2007).
23. B. Gomez, N. V. Likhanova, M. A. Domínguez-Aguilar, R. Martínez-Palou, A. Vela, J. L. Gazquez, *J. Phys. Chem. B.,* **110**(18), 8928 (2006).
24. A. Daina, O. Michielin, V. Zoete, *J. Chem. Inf. Model*. **54**(12), 3284 (2014).
25. T. Cheng, Y. Zhao, X. Li, F. Lin, Y. Xu, X. Zhang, Y. Li, R. Wang, *J. Chem. Inf. Model*., **47**(6), 2140 (2007).
26. S. A. Wildman, G. M. Crippen, *J. Chem. Inf. Comput. Sci.,* **39**, 868 (1999).
27. C. A. Lipinski, F. Lombardo, B. W. Dominy, P. J. Feeney, *Adv. Drug Deliver. Rev*., **46**, 3 (2001).
28. Silicos-IT. [Online]. Available: https://www.silicos-it.be.
29. J. S. Delaney, *J. Chem. Inf. Comput. Sci*.. **44**, 1000 (2004).
30. J. Ali, P. Camilleri, M. B. Brown, A. J. Hutt, S. B. Kirton, *J. Chem. Inf. Model*., **52**, 2950 (2012).
31. A. Daina, O. Michielin, V. Zoete, *Sci Rep*., **7**, 42717 (2017).

Bulgarian Chemical Communications, Volume 57, Issue 3 (pp. 175-180) 2025 DOI: 10.34049/bcc.57.3.GS

Computational evaluation of cymenes: substituent group effect, pharmacokinetics, and drug-likeness

G. Serdaroğlu

[1]*Sivas Cumhuriyet University, Faculty of Education, Math. and Sci. Edu., 58140, Sivas, Turkey*

Accepted: August 17, 2025

In this work, the *p*-cymene (CYM) and its less common isomers, ortho- and meta-cymene (OCYM and MCYM), were investigated using *in silico* tools to predict and elucidate the physicochemical, electronic, and pharmacokinetic properties, which would be helpful in early-stage drug-design. First, the $–CH_3$, $-NH_2$, and -C≡N functionalized cymenes were optimized and verified using frequency computations, at B3LYP/6-311 G** level. Then, lipophilicity, water solubility, pharmacokinetics, and drug-likeness scores of the compounds were evaluated in light of the *in silico* computations. FMO and MEP analyses of the dataset were performed to depict the possible reactivity directions and sites.

Keywords: cymene, substituent effect, DFT, pharmacokinetics, drug likeness

INTRODUCTION

Cymene is known as the type of monoterpene with the chemical formula of CH3C6H4CH(CH3)2 and is found in essential oils of various plants including Thymus, Protium heptaphyllum, Eucalyptus, Protium, etc [1,2]. Until now, they have been under the spotlight due to their neurodegenerative potential in CNS diseases such as anxiety, Alzheimer's disease, oxidative stress, etc [3,4]. Moreover, they have been considered natural protective agents with capabilities of antioxidant, antimicrobial, anticancer, etc due to the lipophilic character allowing them to interact with cell membranes. In addition to the bio-medicinal superiorities, *p*-cymene is used as a precursor in the organic synthesis of bio-based solvents, green chemicals, and agrochemicals [5-7]. As well known, the optimized physicochemical properties like water solubility and hydrophobicity should be in balance with each other in designing the smart agents for biomedicinal applications, which are crucial in early-level drug-design [8,9]. Herein, the functionalized *ortho*-, *para*-, and *meta*-cymene isomers have been investigated using computational tools to evaluate the relationship between the structure and pharmacokinetic characteristics. In this regard, the quantum mechanics simulations are employed to determine the optimized and confirmed structures, and then elucidate the thermochemical and physical properties.

Computational details

The DFT simulations of the cymene isomers were performed by the G16W [10] package at B3LYP/6-311G** [11,12] level, and optimized geometries, FMO amplitudes and MEP plots were visualized by the GaussView 6.0.16 [13] package. The thermochemical data obtained from the frequency computations were evaluated using the basis of statistical mechanics principles [14, 15]. The HOMO and LUMO energies were used to predict the *I* ionization energy and *A* electron affinity [16] that were used to calculated the global reactivity indices, which were $\chi \rightarrow$ electronic chemical potential $\eta \rightarrow$ global hardness, $\omega \rightarrow$ electrophilicity, $\Delta N_{max} \rightarrow$ maximum charge transfer capability index [17, 18], $\omega^- \rightarrow$ electrodonating power, $\omega^+ \rightarrow$ electroaccepting power [19], and $\Delta E_{back\text{-}donat.} \rightarrow$ back-donation energy [20]. The SwissADME [21] tools were used to predict the [22-26], water-solubility [27, 28], pharmacokinetics, and drug-likeness profiles of the dataset.

RESULTS AND DISCUSSION

Physicochemistry, pharmacokinetics, and drug likeness

Table 1 depicts the thermodynamic and physical parameters obtained from DFT computations. Accordingly, the ΔE, ΔH, and ΔG quantities of CYM structure were calculated at -389.399730, -389.388182, and -389.436934 au, whereas these values for MCYM and OCYM were predicted at -389.399727, -389.388194, and -389.436823 au and -389.392086, -389.380915, and -389.427065 au, respectively: the para-positioned CH3 group on the main structure lowered these quantities. Also, the $E_{therm.}$ values of CYM, C-1, C-2, and C-3 were calculated as 139.184, 157.462, 150.560, and 139.558 kcal/mol, respectively: the $–CH_3$ substitu-

* To whom all correspondence should be sent:
E-mail: *goncagul.serdaroglu@gmail.com*

tion increased the thermal energy higher than the other substituent groups (-NH_2 and -C≡N). A similar trend in E_{therm} was calculated for the less common isomers MCYM and OCYM. On the other hand, the -C≡N group for *p*-CYM derivatives increased the heat capacity and entropy more than the other substituent groups, while the –CH3 group for the MCYM and OCYM could cause an increase in the heat capacity and entropy. From Table 1, the -C≡N substituted isomers would have the highest dipole moment and polarizability index. Namely, the μ (D) and α (au) orders of CYM structures were calculated as CYM (0.087) < C-1 (0.423) < C-2 (1.666) < C-3 (4.538) and CYM (110.811) < C-2 (120.859) < C-1 (123.636) < C-3 (126.757), respectively. On the other hand, the μ (D) and α (au) orders for MCYM were determined as M-1< MCYM< M-2< M-3 and MCYM< M-2< M-1< M-3, respectively.

Table 2 shows the lipophilicity and solubility in water properties of the dataset. As expected, the double –CH_3 substituted derivatives would be most lipophilic among the other derivatives for all cymene isomers, as well as for all methods. Namely, the XLOGP3 and MLOGP methods for CYM and its derivatives revealed the order of lipophilicity as C-1 (4.39) > CYM (4.10) > C-3 (3.56)> C-2 (2.59) and C-1 (4.77) > CYM (4.47) > C-2 (2.76)> C-3 (2.69), respectively. Moreover, the iLOGP and WLOGP methods for MYCM derivatives were calculated as the following orders of M-1 (2.77)> MCYM (2.52)≥ M-3 (2.52) > M-2 (2.15) and M-1 (3.43)> MCYM (3.12) > M-3 (2.99) > M-2 (2.71), respectively. From the mean lipophilicity results, the –NH_2 substituted derivatives C-2, M-2, and O-2 would exhibit less lipophilicity with the logPo/w values of 2.55, 2.58, and 2.54, respectively. As expected, the –CH_3 substitution decreased the water solubility, whereas the –NH_2 functionalization increased the water solubility. Namely, the solubility values of the CYM derivatives were calculated as C-2> C-3> C-1> C-2, depending on ESOL and Ali methods, whereas the water-solubility for OCYM derivatives based on ESOL and Ali methods was determined as O-2> O-3> OCYM> O-1 and O-2> O-3> O-1> OCYM, respectively.

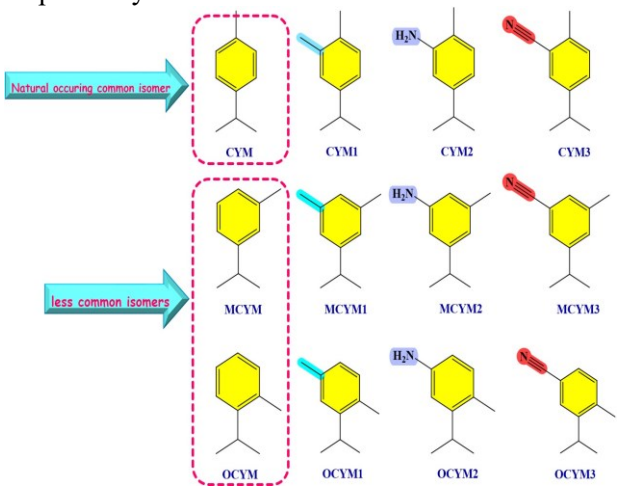

Fig. 1. Optimized chemical structures of the dataset

Table 1. Thermochemical and physical values of the data set

Comp.	ΔE (au)	ΔH (au)	ΔG (au)	$E_{therm.}$ (kcal/mol)	Cv (cal.mol/K)	S (cal.mol/K)	μ (D)	α (au)
CYM	-389.399730	-389.388182	-389.436934	139.184	39.618	102.607	0.087	110.811
C-1	-428.698818	-428.685861	-428.736544	157.462	45.501	106.671	0.423	123.636
C-2	-444.755728	-444.743036	-444.792871	150.560	45.409	104.886	1.666	120.859
C-3	-481.667217	-481.653999	-481.706033	139.558	45.581	109.515	4.538	126.757
MCYM	-389.399727	-389.388194	-389.436823	139.187	39.631	102.349	0.248	109.946
M-1	-428.700113	-428.686603	-428.741403	157.410	45.761	115.337	0.123	123.540
M-2	-444.756239	-444.743220	-444.794609	150.463	45.724	108.158	1.495	120.701
M-3	-481.666852	-481.653494	-481.706760	139.532	45.672	112.108	5.136	126.957
OCYM	-389.392086	-389.380915	-389.427065	139.421	39.469	97.132	0.454	108.847
O-1	-428.692419	-428.679299	-428.730773	157.637	45.595	108.337	0.236	122.804
O-2	-444.747960	-444.735255	-444.784605	150.689	45.543	103.866	1.478	120.029
O-3	-481.659594	-481.646603	-481.697295	139.764	45.492	106.690	5.370	126.714

Table 2. Lipophilicity and water solubility

	CYM	C-1	C-2	C-3	M-CYM	M-1	M-2	M-3	O-CYM	O-1	O-2	O-3
Lipophilicity												
iLOGP	2.51	2.70	2.17	2.49	2.52	2.77	2.15	2.52	2.43	2.70	2.08	2.44
XLOGP3	4.10	4.39	2.59	3.56	4.50	3.78	2.73	3.13	4.38	4.39	2.60	3.13
WLOGP	3.12	3.43	2.71	2.99	3.12	3.43	2.71	2.99	3.12	3.43	2.71	2.99
MLOGP	4.47	4.77	2.76	2.69	4.47	4.77	2.76	2.69	4.47	4.77	2.76	2.69
SILICOS-IT	3.29	3.77	2.55	3.27	3.29	3.77	2.55	3.27	3.29	3.77	2.55	3.27
Avg. LogPo/w	3.50	3.81	2.55	3.00	3.58	3.70	2.58	2.92	3.54	3.81	2.54	2.90
Water solubility												
Log S (ESOL)	-3.63	-3.86	-2.73	-3.37	-3.89	-3.48	-2.82	-3.10	-3.81	-3.86	-2.74	-3.10
Sol.(mg/mL)×10^{-2}	3.12	2.03	27.5	6.73	1.75	4.93	22.4	12.6	2.08	2.03	27.1	12.6
Class	S	S	S	S	S	S	S	S	S	S	S	S
Log S (Ali)	-3.81	-4.11	-2.79	-3.75	-4.22	-3.47	-2.93	-3.30	-4.10	-4.11	-2.80	-3.30
Sol.(mg/mL)×10^{-2}	2.10	1.16	24.5	2.86	0.807	4.98	17.5	8.00	1.08	1.16	23.9	8.00
Class	S	MS	S	S	MS	S	S	S	MS	MS	S	S
SILICOS-IT)	-3.57	-3.97	-3.23	-3.68	-3.57	-3.97	-3.23	-3.68	-3.57	-3.97	-3.23	-3.68
Sol. (mg/mL)×10^{-2}	3.58	1.57	8.81	3.32	3.58	1.57	8.81	3.32	3.58	1.57	8.81	3.32
Class	S	S	S	S	S	S	S	S	S	S	S	S

Table 3. Pharmacokinetics

	GI Abs.	BBB	P-gp susbt.	CYP1A2 inh.	CYP2C19 inh.	CYP2C9 inh.	CYP2D6 inh.	CYP3A4 inh.	Log Kp (skin per.) cm/s
CYM	Low	Yes	No	No	No	No	Yes	No	-4.21
C-1	Low	Yes	No	No	No	No	Yes	No	-4.09
C-2	High	Yes	No	Yes	No	No	No	No	-5.37
C-3	High	Yes	No	Yes	No	No	No	No	-4.74
MCYM	Low	Yes	No	No	No	No	Yes	No	-3.92
M-1	Low	Yes	No	No	No	No	Yes	No	-4.52
M-2	High	Yes	No	Yes	No	No	No	No	-5.27
M-3	High	Yes	No	Yes	No	No	No	No	-5.05
OCYM	Low	Yes	No	No	No	No	Yes	No	-4.01
O-1	Low	Yes	No	No	No	No	Yes	No	-4.09
O-2	High	Yes	No	Yes	No	No	No	No	-5.36
O-3	High	Yes	No	Yes	No	No	No	No	-5.05

According to Table 3, the -NH_2 and -C≡N substituted structures would exhibit high GI-absorption potency, while the –CH_3 substituted structures would have less potency in terms of it. Also, all compounds would have suitable structural and physicochemical properties for passive permeation through the BBB, which could be seen from Figure 2 as well. On the other hand, the studied derivatives would not be effluated from the CNS by the glycoprotein and thus exhibit P-gp substrate. Also, the -NH_2 and -C≡N substituted structures would have potency in terms of CYP1A2 inhibition, while the –CH3 substituted structures would not have. Moreover, none of the compounds would have a potency in terms of CYP2C19, CYP2C9, and CYP3A4 inhibition. As is well known, Kp (skin permeability) is defined as the penetration rate of a chemical substance relevant across the stratum corneum, and lipophilicity has a critical role in the skin absorption of a specific molecular system [29-31]. Herein, the log P values of CYM, MCYM, and OCYM derivatives were calculated in the ranges of (-4.09)-(-5.37), (-3.92)-(-5.27), and (-4.01)-(-5.36) cm/s, respectively: the most lipophilic structures would have higher skin permeation where as the most water-soluble structures would have the less potency in terms of skin permeation. From Table 4, the Veber and Egan rules revealed that all compounds could have structural and physicochemical necessities for drug-like potency.

Also, the Lipinski rules implied that all compounds would have proper properties for drug likeness, even though the MLOGP indexes of the $–CH_3$ substituted structures could be higher than 4.15. On the other hand, the MW of the compounds would be lower than 160 g/mol, which would be a violation of drug likeness potency depending on the Ghose approach. Moreover, Muegge's approach gave two violations: MW<200 g/mol and the number of heteroatoms<2.

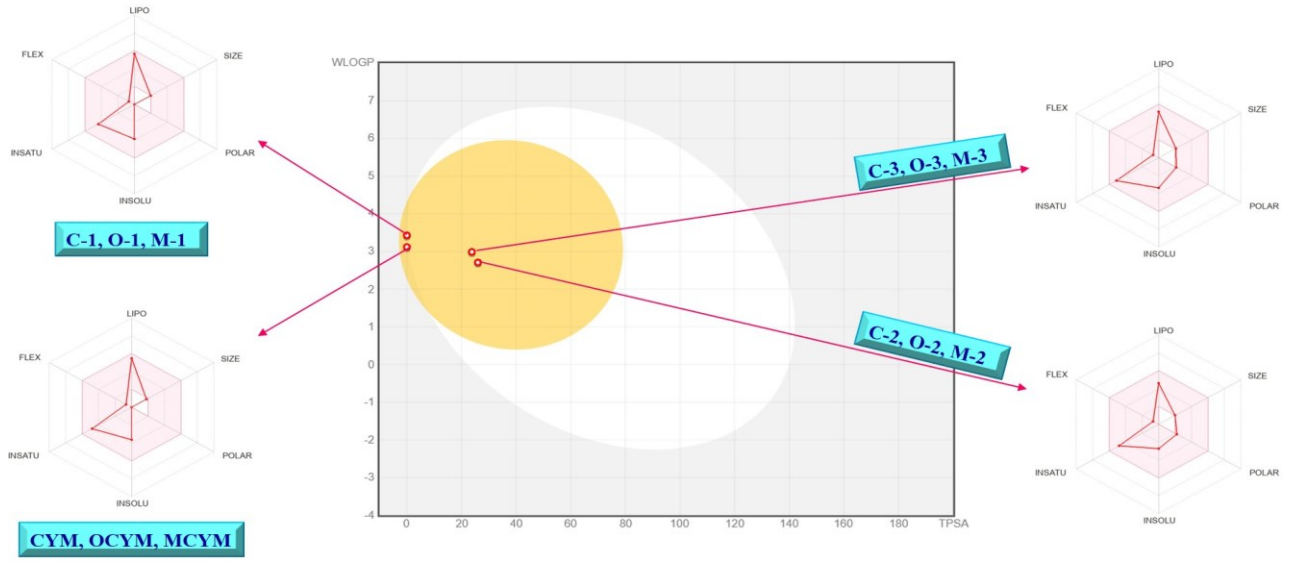

Fig. 2. Boiled-egg model and radar graphs

Table 4. Drug likeness and bioavailability scores

	Lipinski	Ghose	Veber	Egan	Muegge	Bioavail. score
CYM	Yes; MLOGP>4.15	No; MW<160	YES	YES	No; MW<200, Heteroatoms<2	0.55
C-1	Yes; MLOGP>4.15	No; MW<160	YES	YES	No; MW<200, Heteroatoms<2	0.55
C-2	YES	No; MW<160	YES	YES	No; MW<200, Heteroatoms<2	0.55
C-3	YES	No; MW<160	YES	YES	No; MW<200, Heteroatoms<2	0.55
M-CYM	Yes; MLOGP>4.15	No; MW<160	YES	YES	No; MW<200, Heteroatoms<2	0.55
M-1	Yes; MLOGP>4.15	No; MW<160	YES	YES	No; MW<200, Heteroatoms<2	0.55
M-2	YES	No; MW<160	YES	YES	No; MW<200, Heteroatoms<2	0.55
M-3	YES	No; MW<160	YES	YES	No; MW<200, Heteroatoms<2	0.55
O-CYM	Yes; MLOGP>4.15	No; MW<160	YES	YES	No; MW<200, Heteroatoms<2	0.55
O-1	Yes; MLOGP>4.15	No; MW<160	YES	YES	No; MW<200, Heteroatoms<2	0.55
O-2	YES	No; MW<160	YES	YES	No; MW<200, Heteroatoms<2	0.55
O-3	YES	No; MW<160	YES	YES	No; MW<200, Heteroatoms<2	0.55

Table 5. Chemical reactivity parameters

	H (-I) / eV	L (-A) / eV	ΔE (L-H) / eV	μ/ eV	η/ eV	ω/ au	ω^+/ au	ω^-/ au	ΔN_{max} / eV	$\Delta E_{back.}$ / eV
CYM	-6.394	-0.176	6.218	-3.285	3.109	0.064	0.018	0.138	1.057	-0.777
C-1	-6.265	-0.079	6.186	-3.172	3.093	0.060	0.016	0.132	1.026	-0.773
C-2	-5.472	0.122	5.595	-2.675	2.797	0.047	0.011	0.109	0.956	-0.699
C-3	-7.015	-1.534	5.480	-4.274	2.740	0.123	0.057	0.214	1.560	-0.685
MCYM	-6.507	-0.168	6.340	-3.337	3.170	0.065	0.018	0.140	1.053	-0.792
M-1	-6.422	-0.080	6.342	-3.251	3.171	0.061	0.016	0.136	1.025	-0.793
M-2	-5.479	0.041	5.520	-2.719	2.760	0.049	0.012	0.112	0.985	-0.690
M-3	-7.199	-1.528	5.671	-4.363	2.836	0.123	0.056	0.217	1.539	-0.709
OCYM	-6.508	-0.167	6.341	-3.337	3.170	0.065	0.018	0.140	1.053	-0.793
O-1	-6.275	-0.089	6.185	-3.182	3.093	0.060	0.016	0.133	1.029	-0.773
O-2	-5.395	0.003	5.398	-2.696	2.699	0.049	0.012	0.111	0.999	-0.675
O-3	-7.062	-1.477	5.585	-4.270	2.792	0.120	0.054	0.211	1.529	-0.698

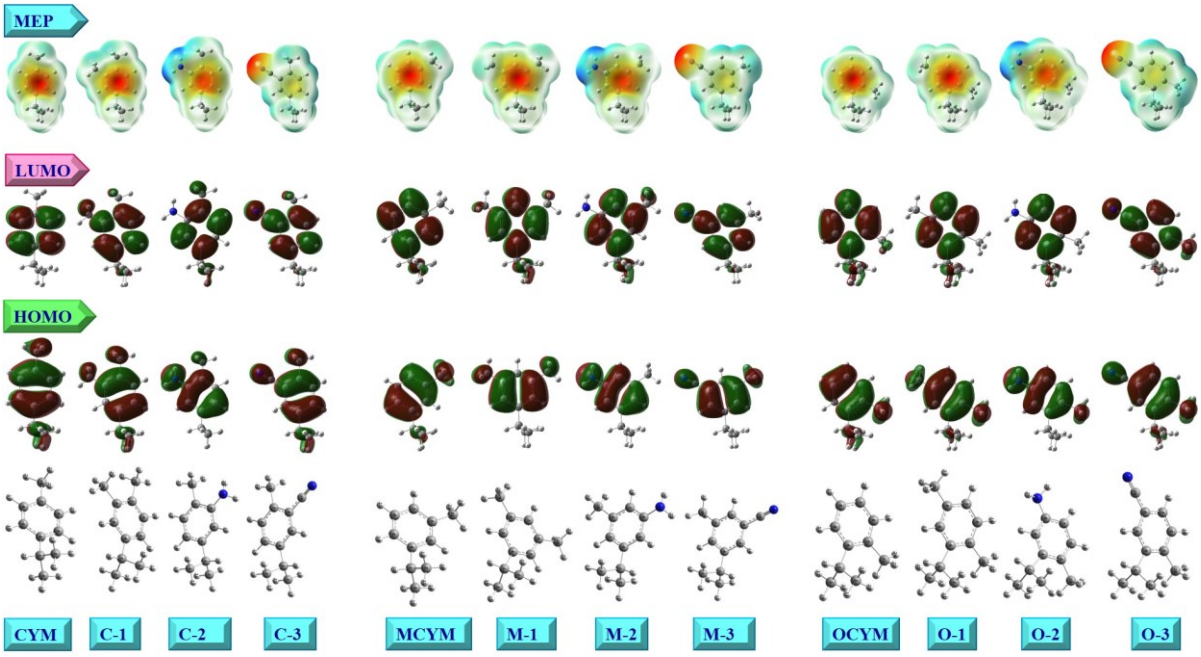

Fig. 3. Optimized structures, HOMO, LUMO, and MEP diagrams of the data set

FMO and MEP analyses

The FMO analyses provide an insight into chemical reactivity trends and sites for the molecular systems relevant. According to Table 5, the energy gap order of CYM and its derivatives was calculated as CYM (6.218) > C-1 (6.186) > C-2 (5.595) > C-3 (5.480): the core cymene structure would prefer the intermolecular actions instead of the intramolecular charge movement from HOMO to LUMO due to having biggest energy gap value. Moreover, the ΔE_{L-H} orders of MCYM and OCYM derivatives were determined as M-1 (6.342) > MCYM (6.340) > M-3 (5.671) > M-2 (5.520) and OCYM (6.341) > O-1 (6.185) > O-3 (5.585) > O-2 (5.398), respectively. Among all structures, the M-1 would have the highest energy gap, while the O-2 could have the lowest ΔE_{L-H} value. Moreover, the μ (eV) values implied that the -C≡N substituted compounds C-3 (-4.274), M-3 (-4.363), and O-3 (-4.270) could be more stable than the other substituted structures due to having the lowest values, and vice versa for –NH2 substituted counterparts. The η (eV) order of the compounds was calculated as η (eV): M-1 (3.171) > MCYM= OCYM (3.170) > CYM (3.109) > C-1= O-1 (3.093) > M-3 (2.836) > C-2 (2.797) > O-3 (2.792)> M-2 (2.760) > C-3 (2.740) > O-2 (2.699): the M-1 structure would be the hardest molecule, while the O-2 would be the softer one among the compounds. The ω (au) values of the -C≡N substituted compounds C-3 (0.123), M-3 (0.123), and O-3 (0.120) would be the highest value among their groups, due to the lone pair of the N atom. Moreover, the C-3 (1.560), M-3 (1.539), and O-3 (1.529) compounds would have the highest charge transfer capability (eV) among the compounds. Last, CYM (-0.777 eV), MCYM (-0.792 eV), and OCYM (-0.793 eV) structures would gain more stability via back donation due to having the lowest $\Delta E_{back.}$ values.

Also, the HOMO of CYM, C-1, and C-3 derivatives covered the whole surface, whereas the HOMO of C-2 was densified on the substituted aromatic ring mostly except for the isopropyl group. Also, the isopropyl group for the M-1, M-2, M-3, and O-2 structures could not be host to HOMO, while the HOMO for MCYM, OCYM, O-1, and O-3 structures was expanded on the isopropyl group, more or less, in addition to the aromatic ring. The LUMO for C-2, M-2, and O-2 molecules would not distributed on the -NH2 group, which implied that this group could not have a role in electrophilic attack reactions. Except for the -C≡N functionalized derivatives, the aromatic ring for all compounds would be covered by red color (V<0) as a sign of the electron rich region that depicted the suitable region for electrophiles. Also, the Hs of –NH2 group were covered by blue (V>0) as a marker of the electron-poor region that implied the suitable site for nucleophiles.

CONCLUSION

In this work, the DFT computations revealed that the -C≡N substitution on the cymene isomers could gain the core structure more polarizability as well as responsible for the highest dipole moment of C-3, M-3, and, O-3 structures. On the other hand, -NH_2 functionalized structures would exhibit more

solubility in water, whereas the $–CH_3$ substitution gain to the structure relevant more lipophilicity, as expected. MEP plots of the dataset implied that the aromatic ring for all compounds would be covered by red color (V<0) that depicted the suitable region for electrophiles, except for -C≡N decorated derivatives. Moreover, the Hs of $–NH_2$ group were covered by blue (V>0) that showed the suitable site for nucleophiles.

Acknowledgement: *All calculations have been carried out at TUBITAK ULAKBIM, High Performance and Grid Computing Center (TR-Grid e-Infrastructure). The author thanks the Scientific Research Projects Department of Cumhuriyet University (Project No: EĞT-2023-098).*

REFERENCES

1. A. Marchese, C.R. Arciola, R. Barbieri, A.S. Silva, S.F. Nabavi, A.J. Tsetegho Sokeng, M. Izadi, N.J. Jafari, I. Suntar, M. Daglia, S.M. Nabavi, *Materials*, **10**(8), 947 (2017).
2. A. Balahbib, N. El Omari, N. El Hachlafi, F. Lakhdar, N. El Menyiy, N. Salhi, H.N. Mrabti, S. Bakrim, G. Zengin, A. Bouyahya, *Food Chem. Toxicol.,* **153,** 112259 (2021).
3. T.M. de Oliveira, R.B.F. de Carvalho, I.H.F. da Costa, G.A.L. de Oliveira, A.A. de Souza, S.G. de Lima, R.M. de Freitas, *Pharm. Biol*., **53**(3), 423 (2015).
4. B. Seifi-Nahavandi, P. Yaghmaei, S. Ahmadian, M. Ghobeh, A. Ebrahim-Habibi, *J. Diabetes Metab. Disord*., **19**, 1381 (2020).
5. L. Caputo, G. Amato, L. De Martino, V. De Feo, F. Nazzaro, *Int. J. Mol. Sci*., **24**(7), 6073 (2023).
6. M. Kamitsou, G.D. Panagiotou, K.S. Triantafyllidis, K. Bourikas, A. Lycourghiotis, C. Kordulis, *Appl. Catal. A Gen.*, **474**, 224 (2014).
7. M.A. Martín-Luengo, M. Yates, M.J. Martínez Domingo, B. Casal, M. Iglesias, M. Esteban, E. Ruiz-Hitzky, *Appl. Catal. B. Environ*., **81**(3–4), 218 (2008).
8. B. Testa, P. Crivori, M. Reist, P.A. Carrupt, *Perspect. Drug Discov. Des.*, **19**, 179 (2000).
9. T. Chmiel, A. Mieszkowska, D. Kempińska-Kupczyk, A. Kot-Wasik, J. Namieśnik, Z. Mazerska, *Microchem J.*, **146**, 393 (2019).
10. M. J. Frisch et al. Gaussian 09W, Revision D.01, Gaussian, Inc, Wallingford CT, 2013.
11. A. D. Becke, *J. Chem. Phys*., **98**, 1372 (1993).
12. C. Lee, W. Yang, R.G. Parr, *Phys. Rev*., **B37**, 785 (1988).
13. GaussView 6.0.16, Gaussian, Inc, Wallingford CT, (2016).
14. D. A. McQuarrie, Statistical Thermodynamics, Harper & Row Publishers, New York, **1973**.
15. G. Serdaroglu, S. Durmaz, *Indian J. Chem*., **49**, 861 (2010).
16. T. Koopmans, *Physica*, **1**, 104 (1934).
17. R. G. Pearson, *Proc. Natl. Acad. Sci. USA*., **83**, 8440 (1986).
18. R. G. Parr, L.V. Szentpaly, S. Liu, *J. Am. Chem. Soc*., **121**, 1922 (1999).
19. J. L. Gazquez, A. Cedillo, A. Vela, *J. Phys. Chem. A*., **111**(10), 1966 (2007).
20. B. Gomez, N. V. Likhanova, M. A. Domínguez-Aguilar, R. Martínez-Palou, A. Vela, J. L. Gazquez, *J. Phys. Chem. B.,* **110**(18), 8928 (2006).
21. A. Daina, O. Michielin, V. Zoete, *Sci Rep*., **7**, 42717 (2017).
22. A. Daina, O. Michielin, V. Zoete, *J. Chem. Inf. Model*. **54**(12), 3284 (2014).
23. T. Cheng, Y. Zhao, X. Li, F. Lin, Y. Xu, X. Zhang, Y. Li, R. Wang, *J. Chem. Inf. Model*., **47**(6), 2140 (2007).
24. S. A. Wildman, G. M. Crippen, *J. Chem. Inf. Comput. Sci.,* **39**, 868 (1999).
25. C. A. Lipinski, F. Lombardo, B. W. Dominy, P. J. Feeney, *Adv. Drug Deliver. Rev*., **46**, 3 (2001).
26. Silicos-IT. [Online]. Available: https://www.silicos-it.be.
27. J. S. Delaney, *J. Chem. Inf. Comput. Sci*.. **44**, 1000 (2004).
28. J. Ali, P. Camilleri, M. B. Brown, A. J. Hutt, S. B. Kirton, *J. Chem. Inf. Model*., **52**, 2950 (2012).
29. Y. Chang, C. Chen, C. Chen, Procedia Eng., **45**, 875 (2011).
30. P. Chen, C. Chen, W. Huang, C. Chang, Molecules, **23**, 911 (2018).
31. S. Soriano-Meseguer, E. Fuguet, A. Port, M. Rosés, *ADMET DMPK*, **8**, 16 (2020).

Bulgarian Chemical Communications, Volume 57, Issue 3 (pp. 181-184) 2025 DOI: 10.34049/bcc.57.3.RO-DU

Improved biobutanol recovery through mixed-matrix PVDF membrane with hydrophobic MAF-6 as filler

R. Ozdemır, D. Unlu*

Bursa Technical University, Faculty of Engineering and Natural Sciences, Chemical Engineering Department, 16310, Bursa, Turkey

Accepted: August 17, 2025

In this study, enhancing the hydrophobicity of the membrane by using MAF-6 was considered an effective strategy to improve the performance of organophilic pervaporation (PV) membranes. This was achieved by incorporating superhydrophobic MAF-6 into polyvinylidene fluoride (PVDF) polymer to create mixed matrix membranes (MMMs). Various characterization techniques were employed to assess the morphologies of the MAF-6 nanocrystals and the membranes, including BET and SEM. The pervaporation experiments involving butanol/water mixtures demonstrated that the MMMs exhibited enhanced flux and separation factors compared to the PVDF pristine membrane. The optimal flux achieved was 1.35 g/m² h, with a separation factor of 16.7. This enhancement in performance was attributed to the hydrophilicity and high porosity of MAF-6, which effectively overcame the trade-off effect usually observed in such membranes.

Keywords: Biobutanol, MAF-6, membrane, PVDF, pervaporation

INTRODUCTION

The global transition toward renewable energy sources gained momentum in the late 1990s, driven by rising petroleum prices, increasing raw material costs, and depletion of fossil fuel reserves [1, 2]. Biofuels, including densified agricultural residues, ethanol, butanol, hydrogen, and biodiesel, are produced through biochemical or thermochemical conversion of various plant and organic wastes [3]. Among these, butanol—a flammable alcohol—emerges as a promising biofuel. It offers several benefits over bioethanol such as being non-hygroscopic, having a higher heating value, better compatibility with gasoline and diesel, and causing less corrosion and flammability concerns. Additionally, butanol is extensively used as an industrial solvent [2, 3]. The production of biofuels *via* acetone-butanol-ethanol (ABE) fermentation has a long history dating back to 1861 and has regained interest amid the ongoing search for alternative fuels, particularly after renewed focus on ABE fermentation for butanol production since the 1960s [4].

Conventional techniques for recovering butanol from fermentation broths include distillation, adsorption, extraction, and gas stripping, but each method faces certain limitations. Pervaporation, a membrane-based separation process, offers an alternative that can overcome some of these challenges. In pervaporation, the liquid feed contacts one side of the membrane, while the permeate is collected as vapor on the opposite side under vacuum. The membrane's selectivity depends on the relative solubility and diffusivity of the components within the membrane matrix. Therefore, developing membranes with a strong affinity for the target compound is essential for achieving efficient pervaporation performance [5].

Mixed matrix membranes (MMMs) are hybrid materials that effectively combine the flexibility and ease of processing of polymers with the selectivity and durability of inorganic fillers. This combination provides a promising approach for improving separation performance, especially in gas separation and pervaporation applications. MMMs consist of an organic polymer matrix embedded with dispersed inorganic fillers such as zeolites, metal–organic frameworks (MOFs), carbon nanotubes, silica, and graphene oxide. The aim is to leverage the mechanical flexibility and manufacturability of polymers alongside the high selectivity, thermal stability, and chemical resistance of inorganic fillers. The polymer component provides mechanical strength and ease of fabrication. Typical polymers used are polyvinylidene fluoride (PVDF), polysulfone (PSf), polyimide (PI), poly(ether-block-amide) (PEBAX), and polydimethylsiloxane (PDMS). In the present study, VDF was preferred as

* To whom all correspondence should be sent:
E-mail: *derya.unlu@btu.edu.tr*

polymer matrix material and MAF-6 as inorganic additive [6-7].

PVDF is a high-performance membrane material, which has received extensive attention due to its excellent heat resistance, chemical resistance, and mechanical properties. PVDF is a well-known hydrophobic polymer that is used in the pervaporation process [8-10].

MAF-6 is a type of metal-organic framework (MOF) known for its remarkable hydrophobicity, which arises from the uniform distribution of ethyl groups on its pores and particle surfaces, as well as its RHO topology. It features a high surface area of 1622 m^2/g and a large pore aperture of 0.76 nm, exceeding the molecular kinetic diameter of 1-butanol (0.50 nm). This structural characteristic facilitates the efficient adsorption and diffusion of butanol molecules [11].

In this study, pervaporative recovery of biobutanol was investigated with mixed-matrix PVDF membrane with hydrophobic MAF-6 as filler. MAF-6 and mixed matrix membrane were characterized by BET and SEM, respectively. The effect of MAF-6 concentration and feed butanol concentration on the separation performance was investigated.

EXPERIMENTAL

Materıals

Ethanol, 1-butanol, methanol, n-hexane, 2-ethylimidazole, cyclohexane and 25% aqueous ammonia solution were sourced from Merck. Zinc hydroxide ($Zn(OH)_2$) was supplied by Thermo Scientific Chemicals. The polyvinylidene fluoride (PVDF) polymer was obtained from Solvay.

MAF-6 synthesıs and characterızatıon

$Zn(OH)_2$ was dissolved in aqueous ammonia solution (solution A). 2-Ethylimidazole was dissolved in a solution containing ethanol and cyclohexane (solution B). Both solutions were stirred separately at room temperature until dissolved. Solution A was slowly poured over solution B to bring the two solutions together. The resulting solution was collected by centrifugation. The remaining solid portion was dried in an oven at 80 °C for 12 h [11].

MAF-6 was characterized by scanning electron microscopy (SEM) and surface area analysis (Brunauer-Emmet-Teller (BET) method).

Mixed matrix membrane synthesis and characterization

5 wt. % PVDF was stirred in DMF until homogeneous. To the homogeneous solution obtained, 0.25 wt. %, 0.5 wt. %, 0.75 wt. % and 1 wt. % of the synthesized MAF-6 particles were added and mixed. The prepared MAF-6-doped PVDF membrane was poured onto a Teflon surface and allowed to dry at 120°C for 5 h. The dried membrane was carefully removed from the surface and made ready for use. The membrane was characterized by scanning electron microscopy (SEM).

Pervaporative recovery of biobutanol

The pervaporation recovery of biobutanol was carried out using a laboratory-scale pervaporation system. This setup consists of a membrane cell containing the membrane and feed mixture, a mechanical mixer to ensure uniform mixing, a vacuum pump to maintain low pressure on the permeate side, and cooling traps for collecting the permeated vapor. The membrane is positioned inside the membrane cell, and the feed mixture is pumped into the cell, with the mechanical mixer providing thorough homogenization. Using hydrophobic membranes, biobutanol from the mixture selectively permeates through the membrane during the process, while water remains in the feed as it cannot pass through. In pervaporation, one side of the membrane is in contact with the liquid feed, while the opposite side is under vacuum. Biobutanol passes through the membrane and evaporates under reduced pressure on the permeate side. The biobutanol vapor is then condensed back into liquid form in the cooling traps using liquid nitrogen. The separation performance of the membrane was assessed by determining flux and selectivity, calculated as described in Equations 1 and 2, respectively.

$$Flux = \frac{\text{Mass of permeate}}{\text{Effective Membrane Area} * \text{time}} \quad (1)$$

$$Selecitivity = \frac{\frac{Y_B}{Y_W}}{\frac{X_B}{X_W}} \quad (2)$$

Y is the percentage by weight in the permeate side and X is the percentage by weight in the feed side. Biobutanol concentration was determined by gas chromatography.

RESULTS AND DISCUSSION

MAF-6 characterization

The surface area of the synthesized MAF-6 was obtained as 795.936 m^2/g. Figure 1 shows the SEM image of MAF-6. It can be seen that all samples have uniform particle size distributions. The morphology of the crystals represents a rhombohedral dodecahedron structure.

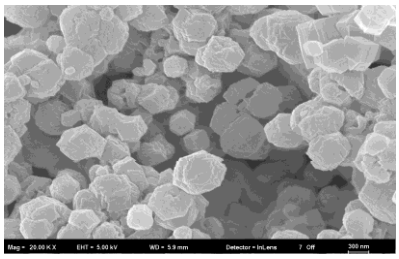

Figure 1. SEM image of MAF-6

Mixed matrix membrane characterization

Figure 2 shows the SEM image of the MAF-6 doped PVDF membrane.

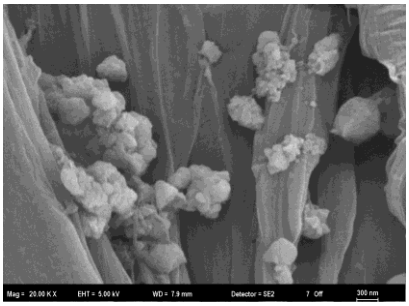

Figure 2. SEM image of MAF-6-doped PVDF membrane.

MAF-6 is observed to be dispersed in the membrane. It exhibits a structure compatible with PVDF. No gap formation is observed between the membrane and MAF-6.

PERVAPORATION RESULTS

Effect of MAF-6 concentratıon

Membranes containing three different MAF-6 loading concentrations (1%, 3% and 5%) were employed in the experimental study for the pervaporative recovery of biobutanol. The tests were performed at room temperature using butanol-water mixture with a butanol content of 10%. The influence of MAF-6 concentration on the membrane's separation performance is presented in Figure 3. It is observed that the flux value increases as the amount of MOF increases. The reason for this can be interpreted as acceleration of material transfer by increasing the surface area with the increase in the amount of metal organic framework. In addition, as the amount of MOF increases, the hydrophobic character of the membrane increases, absorbing more butanol and allowing its transport. Therefore, the flux value increases. It was also observed that the selectivity increased with increasing MOF amount. While the increase in MOF leads to an increase in hydrophobic region, it also adsorbs more butanol molecules, which leads to an increase in selectivity [12-15].

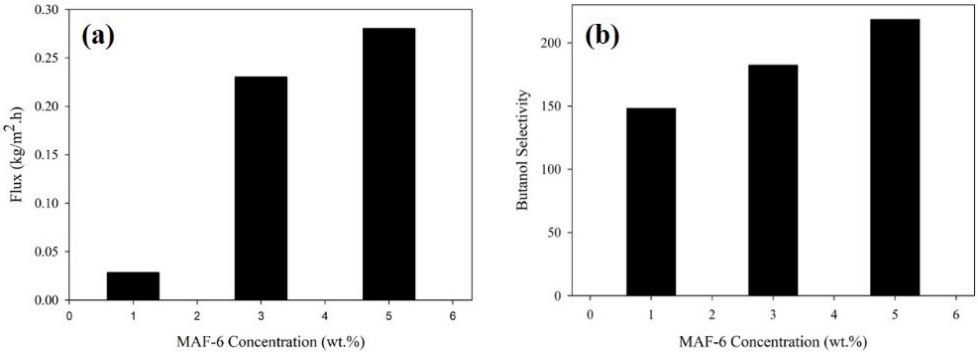

Figure 3. Effect of MAF-6 concentration on flux and selectivity

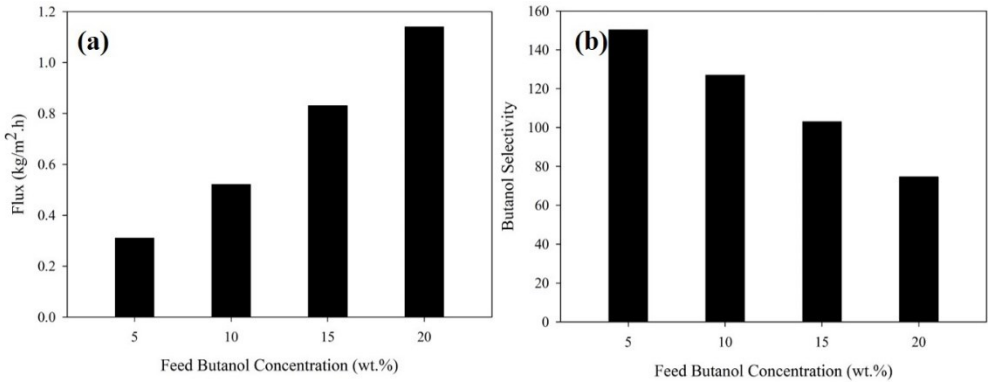

Figure 4. Effect of feed butanol concentration on flux and selectivity

Effect of feed butanol concentratıon

Figure 4 displays the results of the pervaporative recovery of biobutanol conducted at room temperature using a 5 wt.% MAF-6-doped mixed matrix membrane. The study examined the impact of varying feed butanol concentrations by testing butanol-water mixtures containing 5, 10, 15, and 20 wt% butanol.

As the concentration of butanol in the feed mixture rises, the overall permeation flux through the hydrophobic membrane increases due to a greater sorption of butanol into the membrane matrix. This sorption induces membrane swelling, which expands the free volume and enhances molecular mobility, thereby facilitating the diffusion of butanol. Because of the membrane's hydrophobic nature, butanol has much higher solubility and diffusivity than water, resulting in a significant increase in butanol flux. As a result, the membrane's selectivity for butanol over water generally improves with increasing feed butanol concentration, especially at low to moderate levels [16-18].

CONCLUSION

This study systematically examined how MOF content and feed butanol concentration affect the performance of hydrophobic mixed matrix membranes. The findings showed that increasing the MOF loading in the membrane significantly boosted the total permeation flux. This enhancement is attributed to the larger surface area provided by the MOF particles, which accelerates mass transfer, and to the increased hydrophobicity of the membrane, which facilitates greater butanol sorption and transport. Additionally, membrane selectivity for butanol improved with higher MOF content, as the more hydrophobic and porous structure favored the adsorption and diffusion of butanol molecules over water. Similarly, raising the butanol concentration in the feed positively impacted membrane performance. Increased butanol levels promoted greater sorption into the hydrophobic membrane, causing swelling of the polymer matrix, expansion of free volume, and enhanced diffusivity. As a result, both butanol flux and butanol/water selectivity increased, especially at low to moderate butanol concentrations. These results suggest that optimizing MOF loading and feed composition can significantly improve membrane-based separation efficiency for butanol recovery. Optimum operating conditions were obtained by using a 5 wt. % MAF-loaded membrane at 20 wt. % feed butanol concentration. The flux and selectivity values obtained at optimum conditions are 1.14 kg/m^2.h and 74.6, respectively.

REFERENCES

1. B. Amerit, J.M. Ntayi, M. Ngoma, H. Bashir, S. Echegu, M. Nantongo, *Renew. Energy Focus*, **44**, 223 (2023).
2. W. Kamiński, E. Tomczak, A. Górak*, Ecol. Chem. Eng. S.*, **18**(1), 31 (2011).
3. C. Ding, K.L. Yang, J. He, in: Handbook of Biofuels Production, R. Luque, C.S.K. Lin, K. Wilson, J. Clark (eds.), Woodhead Publishing, 2016, p. 303.
4. N.M. Huzir, A.A. Maniruzzaman, S.B. Ismail, B. Abdullah, N.A.N. Mahmood, N.A. Umor, S.A.F.S. Muhammad, *Renew. Sustain. Energy Rev.,* **98**, 476 (2018).
5. Q. Zhao, Q. F. An, Y. Ji, J. Qian, C. Gao, *J. Membr. Sci.*, **379**, 19 (2011).
6. B. Arundhathi, M. Pabba, S.S. Raj, N. Sahu, S. Sridhar, *Membranes*, **14**, 224 (2024).
7. R.D. Noble, *J. Membr. Sci.,* **378**, 393 (2011).
8. Q. Lu, N. Li, *J. Environ. Chem. Eng.*, **9**, 106431 (2021).
9. D.Y. Hou, J. Wang, D. Qu, Z.K. Luan, X.J. Ren, *Sep. Purif. Technol*., **69**, 78 (2009).
10. Y. Choi, C. Nam, *Polymers*, **17**, 1332 (2025).
11. P. Guan, K. Ren, H. Shan, D. Cai, P. Zhao, D. Ma, P. Qin, S. Li, Z. Si, *Colloid Polym. Sci.*, **299**, 1459 (2021).
12. R. Khan, I.U. Haq, H. Mao, A.S. Zhang, L.H. Xu, H.G. Zhen, Z.P. Zhao *Sep. Purif. Technol*., **256**, 117804 (2021).
13. Q. Li , *Sep. Purif. Technol*.,178, **105** (2017).
14. G. Wu, Q. Fan, W. Sun, Z. Yu, Z. Jia, J. Ma. *Chin. J. Chem. Eng.* **42**, 312 (2022).
15. Y. Jin, Y. Xie, H. Zhu, J. Nan, F. Xiangli, G. Liu, W. Jin, *J. Membr. Sci.,* **716**, 123520 (2025).
16. J. Niemistö, W. Kujawski, R.L. Keiski, *J. Membr. Sci.,* **434**, 55 (2013).
17. V. Garcia, E. Pongracz, E. Muurinen, R.L. Keiski, *Desalination,* **241**, 201 (2009).
18. C. Cheng, F. Liu, H.K. Yang, K. Xiao, C. Xue, S.T. Yang, *Ind. Eng. Chem. Res.*, **59**, 7777 (2020).

Bulgarian Chemical Communications, Volume 57, Issue 3 (pp. 185-188) 2025 DOI: 10.34049/bcc.57.3MB-BG-YD

DFT-based theoretical investigation of hydroxyl radical-induced degradation mechanisms of antineoplastic drugs in aqueous media

M. E. Biltekin[1], B. Gurkan[2], Y. Yalcin Gurkan[1*]

[1]*Tekirdag Namık Kemal University, Department of Chemistry, Tekirdag, Türkiye*
[2]*Gebze Technical University, Department of Physics, Kocaeli, Türkiye*

Accepted: August 17, 2025

Within the first 48 hours following chemotherapy, small quantities of cytostatic drugs are excreted *via* urine, vomit, and other bodily secretions. These residues pose potential risks to human and environmental health, highlighting the need for their effective removal from wastewater streams. In this study, the degradation pathways of epirubicin and methotrexate—two commonly used antineoplastic agents—were explored using density functional theory (DFT). Optimized molecular geometries were obtained using the B3LYP functional with the 6-31G(d) basis set *via* Gaussian 09 software. Fragmentation patterns and degradation mechanisms initiated by hydroxyl radical attacks were evaluated in both gas and aqueous phases, incorporating solvation effects using the COSMO model. The findings serve as a theoretical framework to inform and support experimental degradation studies.

Keywords: Antineoplastic drugs, hydroxyl radicals, DFT, wastewater treatment, epirubicin, methotrexate

INTRODUCTION

Pharmaceutical compounds, particularly cytostatic drugs such as epirubicin and methotrexate, are frequently detected in aquatic environments due to their widespread and repeated use in cancer therapy. These compounds are frequently excreted in unmetabolized form, subsequently entering municipal wastewater systems, posing a significant risk to both aquatic life and human health due to their high bioactivity and persistence in the environment [1, 2].

Advanced oxidation processes (AOPs), especially those involving hydroxyl radicals (•OH), have gained attention as effective methods for degrading pharmaceuticals in water. Hydroxyl radicals exhibit strong oxidative potential, reacting rapidly and non-selectively with a broad spectrum of organic molecules, including aromatic rings and aliphatic side chains commonly found in cytostatic drugs [3, 4]. These radicals can initiate degradation pathways *via* hydrogen abstraction, hydroxylation, and electron transfer mechanisms, often resulting in fragmentation into smaller, less harmful species such as CO_2, NH_4^+, or NO_3^- [5].

In recent years, density functional theory (DFT) has emerged as a powerful computational tool to model and predict molecular-level interactions during oxidation processes. Compared to traditional quantum mechanical methods, DFT offers a balance between computational efficiency and accuracy, making it particularly suitable for exploring the degradation mechanisms of complex drug molecules in aqueous media [6, 7]. The B3LYP functional combined with the 6-31G(d) basis set has been shown to reliably predict bond dissociation energies, reaction pathways, and transition states in systems involving free radicals [8].

In this study, DFT was used to investigate the structural properties and fragmentation patterns of epirubicin and methotrexate under attack by hydroxyl radicals. The reaction energetics were evaluated in both gas phase and aqueous environments using the COSMO solvation model. This theoretical approach provides valuable insights into the degradation mechanisms of these pharmaceuticals and supports the development of more effective treatment strategies for contaminated wastewater.

Recent studies further support the relevance of computational chemistry in pharmaceutical degradation. Hadidi *et al*. [9] demonstrated the application of DFT in modeling the degradation of anticancer drug carmustine. Zhou *et al.* [10] and Gogate & Pandit [11] provided comprehensive reviews of AOPs' effectiveness in degrading pharmaceuticals, confirming the central role of hydroxyl radicals. Additionally, the works of Basaleh *et al. [*12] and Kumar *et al.* [13] highlight the importance of theoretical predictions in guiding experimental validation and environmental impact assessments.

* To whom all correspondence should be sent:
E-mail: *yyalcin@nku.edu.tr*

METHODOLOGY

The degradation pathways of epirubicin and methotrexate under the influence of photo-generated hydroxyl radicals (•OH) were modeled using quantum chemical calculations. Initial molecular geometries were constructed using GaussView 5.0 and subsequently optimized using the B3LYP hybrid functional and 6-31G(d) basis set within the Gaussian 09W software suite. Both gas-phase and aqueous-phase environments were considered, with solvation effects modeled using the COSMO continuum solvation approach.

Each molecule's geometry was analyzed with respect to average bond lengths, bond angles in aromatic rings, and hybridization patterns. Particular attention was given to the transition from sp^2 to sp^3 hybridization that occurs upon hydroxyl radical attack. The addition of •OH to unsaturated carbon centers, abstraction of hydrogen atoms, and electron transfer mechanisms were all considered plausible reaction pathways.

Frequency calculations were performed to confirm that all optimized structures corresponded to true minima on the potential energy surface. Theoretical reaction enthalpies and Gibbs free energies (ΔH and ΔG) were computed to evaluate the energetic favorability of possible degradation routes. This computational protocol allowed for the identification of the most reactive molecular sites and fragmentation products resulting from hydroxyl radical interaction [14-17].

RESULTS AND DISCUSSION

The optimized geometries of epirubicin and methotrexate were obtained and analyzed to identify the molecular regions most susceptible to •OH radical attack. As shown in Figure 1, the electron-rich aromatic systems and side chains were prominent reactive sites. The reaction pathways were simulated to predict the most probable fragmentation patterns initiated by hydroxyl radicals.

Figs. 2 and 3 illustrate potential degradation pathways for epirubicin and methotrexate, respectively. The degradation was modeled by examining the bond dissociation energies and Gibbs free energy changes (ΔG) for specific fragmentation reactions. Lower ΔG values indicated energetically favorable reactions. These computational results were in agreement with degradation pathways proposed in literature for structurally similar compounds.

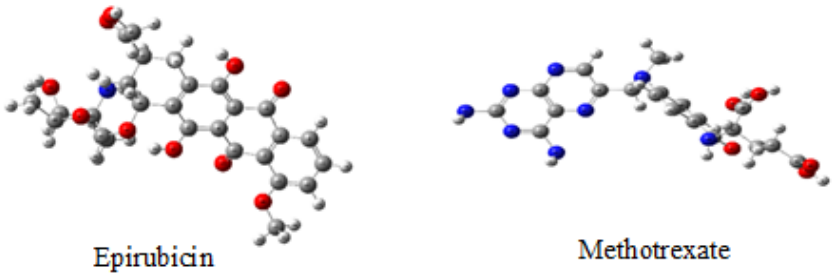

Fig. 1. Optimized geometric structure of epirubicin and methotrexate molecules *via* DFT method. (grey, C; white, H; red, O; blue, N)

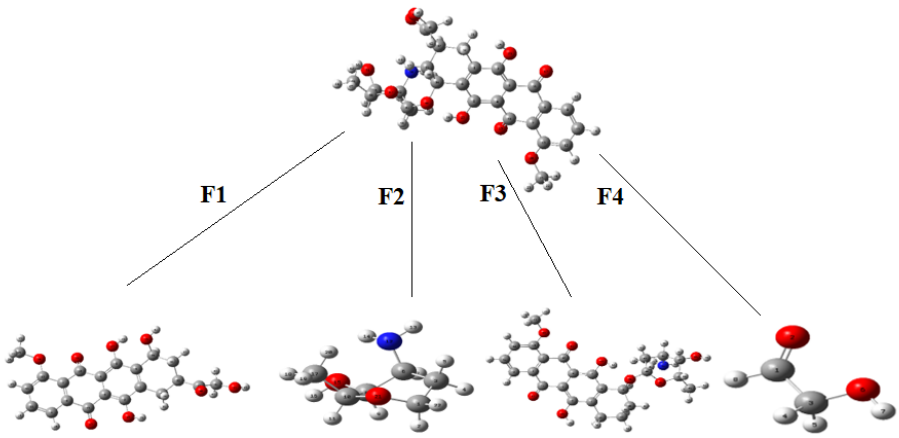

Fig. 2. Possible pathways for the photocatalytic degradation of epirubicin (grey, C; white, H; red, O; blue, N)

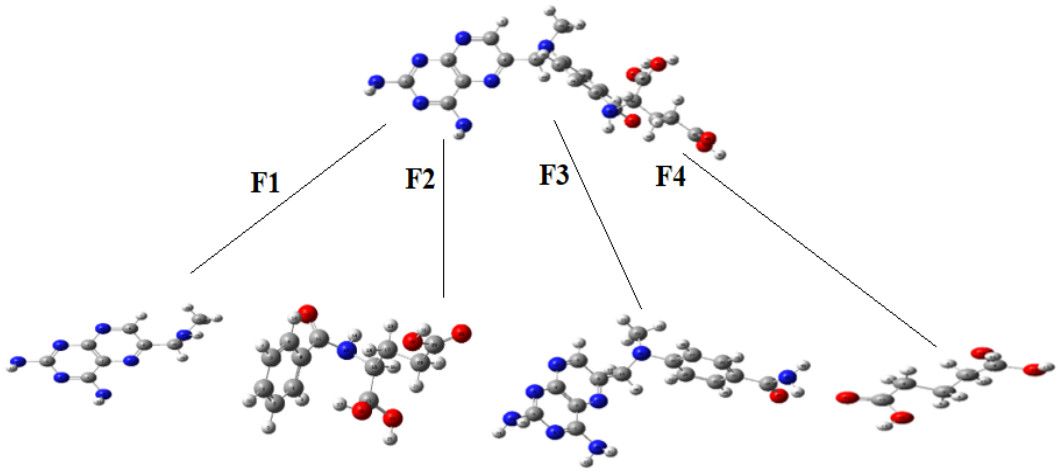

Fig. 3. Possible pathways for the photocatalytic degradation of methotrexate (grey, C; white, H; red, O; blue, N)

Table 1. Constant energy, enthalpy and Gibbs free energy values according to the DFT method.

Molecules	Phase	ΔE Energy (kcal mol^{-1})	ΔH Enthalpy (kcal mol^{-1})	ΔG Gibbs free energy (kcal mol^{-1})
Epirubicin	Gas	-1852.666498	-1852.665554	-1852.770413
	COSMO	*-1852.706760*	*-1852.705816*	*-1852.809057*
F1	Gas	-1412.423582	-1412.422638	-1412.505501
	COSMO	*-1412.458387*	*-1412.457443*	*-1412.539994*
F2	Gas	-441.420941	-441.419997	-441.464388
	COSMO	*-441.431062*	*-441.430118*	*-441.474112*
F3	Gas	-1624.879322	-1624.878378	-1624.971809
	COSMO	*-1624.911163*	*-1624.910218*	*-1625.002645*
F4	Gas	-228.961057	-228.960113	-228.992735
	COSMO	*-228.972708*	*-228.971764*	*-229.004268*

Table 2. Constant energy, enthalpy and Gibbs free energy values according to the DFT method.

Molecules	Phase	ΔE Energy (kcal mol^{-1})	ΔH Enthalpy (kcal mol^{-1})	ΔG Gibbs free energy (kcal mol^{-1})
Methotrexate	Gas	-1589.617330	-1589.616386	-1589.718600
	COSMO	*-1589.654479*	*-1589.653535*	*-1589.758458*
F1	Gas	- 694.534243	- 694.533299	-694.588342
	COSMO	*- 694.551097*	*- 694.550152*	*-694.606003*
F2	Gas	-896.256056	-896.255111	-896.322768
	COSMO	*-896.273932*	*-896.272988*	*-896.343253*
F3	Gas	-1094.172616	-1094.171672	-1094.246764
	COSMO	*-1094.200041*	*-1094.199097*	*-1094.274502*
F4	Gas	-496.637390	-496.636445	-496.683615
	COSMO	*-496.647881*	*-496.646937*	*-496.697138*

Tables 1 and 2 summarize the total electronic energy, enthalpy, and Gibbs free energy of the parent compounds and their major fragmentation products in both gas and COSMO aqueous phases. The data show that degradation is more thermodynamically favorable in the aqueous phase, supporting the hypothesis that water and its reactive species facilitate drug decomposition.

The modeled degradation products included small molecules such as CO_2, NO_3^-, and NH_4^+, indicating mineralization processes. The fragmentation patterns identified can help inform experimental setups aimed at validating these degradation routes and quantifying end-products in real wastewater samples.

CONCLUSIONS

This study presents a theoretical investigation into the degradation mechanisms of epirubicin and methotrexate, two widely used antineoplastic agents, in the presence of hydroxyl radicals. Using density functional theory (DFT), the reactivity of different molecular regions was explored, and potential degradation pathways were proposed based on energetic parameters. The results reveal that hydroxyl radical attack initiates fragmentation reactions that are more favorable in aqueous environments. These findings not only contribute to the understanding of drug breakdown in natural and engineered water systems but also offer a valuable foundation for the design of effective advanced oxidation processes (AOPs). Further experimental studies are encouraged to validate these theoretical predictions and assess the formation of degradation by-products under real-world conditions.

Acknowledgement: *The authors greatly appreciate Tekirdag Namik Kemal University Research Foundation for financial support. Project number: NKUBAP.01.GA.22.437.*

REFERENCES

1. W. Xu, G. Zhang, S. Zou, X. Li, Y. Liu, *Environ. Pollut.,* **145**, 672 (2007).
2. M. Klavarioti, D. Mantzavinos, D. Kassinos, *Environ. Intern.,* **35** ,402 (2009).
3. I. Alemzadeh, G. Borghei, L. Vafi, R. Roostaazad, *Chem. Chem. Eng.,* **17** (1), 106 (2010).
4. L. Povyakel, O. Bobyliova, S. Snoz, Y. Bardik, *Toxicology Letters*, **180**, 197 (2008).
5. V.G. Buxton, L.C. Greenstock, P.W. Helman, B.A. Ross, *Journal of Physical and Chemical Reference Data*, **17**, 513 (1988).
6. M. Anbar, P. Neta, *Int. J. Radiat Isot*, **18**, 495, (1965).
7. B. Halliwell, M. Grootveld, J.M.C. Gutteridge. *Methods of Bıochemical Analysıs*, **33**, 59 (1988).
8. N. San, M. Kilic, Z. Cinar, *J. Adv. Oxid. Technol*. **10**(1), 51 (2007).
9. S. Hadidi, F. Shiri, M. Norouzibazaz, *Structural Chemistry*, **30**, 1315 (2019).
10. X. Zhou, et al. *Catalysts*, **14**(3), 189 (2024).
11. P. R. Gogate, A.B. Pandit, *Science of the Total Environment*, **765**, 144150 (2021).
12. S. Basaleh, et al. *Molecules*, **27**(9), 2796 (2022).
13. A. Kumar, et al. *Chemosphere*, ***345***, 131234 (2024).
14. Gaussian 09, Revision B.04, in: Gaussian, Inc., 2009.
15. J.P. Stewart, *J. Comput. Chem*. **10**, 221 (1989).
16. J.P Lowe, Quantum Chemistry, 2nd edn., Academic Press, USA, 1993.
17. I. N. Lveine ,Quantum Chemistry, Boston : Alloy and Bacon Inc., 1983.

Bulgarian Chemical Communications, Volume 57, Issue 3 (pp. 189-192) 2025 DOI: 10.34049/bcc.57.3.SK-HG-DS

Treatment of lab-scale factory wastewater including disperse orange 30 dye with low cost H_2SO_4-activated rubber particle adsorbent obtained from waste tyre

S. Karagöz[1], H. K. Gürakin[2], D. Şakar[1*]

[1]Yildiz Technical University, Chemistry Department, 34220, Esenler, Istanbul, Türkiye*
[2]SETAŞ Kimya Sanayi A.Ş., Organized Industrial Zone, Karaagac Mah. 9th Street No:3 59510 Kapakli, Tekirdağ, Türkiye

Accepted: August 17, 2025

In this study, disperse orange 30 dye (DO-30) was removed from a liquid solution using cheap adsorbents made from rubber particles obtained from scrap waste tyre (WTRP) and H_2SO_4-activated rubber particles obtained from waste scrap tyre (AF-WTRP) *via* adsorption process. Adsorption isotherms and adsorption kinetics of DO-30 dye removal from synthetic wastewater by adsorption technique were investigated by changing the adsorbent dosage, contact time, dye concentration and temperature. The DO-30 dye removal from labscale factory waste water was investigated according to optimization results of synthetic waste water.

Keywords: H_2SO_4-activated rubber particles obtained from scrap waste tyre; disperse orange 30 dye; dye removal; adsorption kinetics and adsorption isotherms

INTRODUCTION

For many years, water pollution caused by textile industry dyeing processes has been one of the environmental problems. The textile industry's effluent is generally dense in mordants, surfactants, and inorganic dyes. Some textile dyes that are released into water have a severe impact on aquatic life because they are poisonous and carcinogenic. Disperse orange 30 is an azo dye that is highly soluble in organic solvents. DO-30 is used for dyeing synthetic textiles like polyester, nylon, and acrylic. Its azo structure can degrade into hazardous compounds throughout the dyeing and wastewater treatment processes [1]. These contaminants can be removed from water using physical, chemical, and biological treatments. Each approach has limits; thus, treatment processes can be combined based on the content and density of pollutant chemicals. [2] Treatment by physical methods maintains its place as a frequently preferred method from past to present with the advantage of minimum need for chemical substances in the removal process. Its simplicity, flexibility, high efficiency and the ability to recycle pollutants are among the advantages that increase its uptake [3]. Adsorption which is a surface-based process in which charged ions or molecules are attracted to the adsorbent's solid surface and adsorbed there, has recently emerged as one of the most common physical dye removal procedures [4].

In this research, DO-30 dye was removed from synthetic and labscale factory waste water solutions *via* adsorption on acid-functionalized and non acid-functionalized waste scrap tyre rubber particles. And also, to understand the adsorption process of DO-30 dye removal from waste water *via* WTRP and AF-WTRP adsorbents, the adsorption kinetics for the rate of solute adsorption and the duration of adsorbate residence at the solid-liquid interface and isotherms for figuring out how the adsorbent and adsorbate interact, as well as the adsorbent's ideal adsorption capacity, were investigated.

EXPERIMENTAL

The dispersed orange 30 dye which is (4-((2,6-dichloro-4-nitrophenyl)azo)-N-(cyanoethyl)-N-(acetoxyethyl)) (Fig. 1), has a chemical formula of $C_{19}H_{17}Cl_2N_5O_4$, with molecular weight of 450.27 g/mol is provided as solid form by the SETAŞ Company, H_2SO_4 is supplied by Sigma-Aldrich. The used devices in the experiments were Sigma brand 3-18K model ultracentrifuge device, UV-2600 Shimadzu UV/Vis spectrophotometer and Daihan Scientific multi-heat mixer.

Submicron particle size rubber particles (<300 μ) obtained from scrap waste tyres were used successfully for methyl violet dye removal from synthetic waste water [5]. 12 g of rubber powder was mixed with 60 ml of H_2SO at 1000 rpm. The acid-functionalized rubber powder was separated using a pressurized filtration technique. It was left to dry in

* To whom all correspondence should be sent:
E-mail: *dsakar@yildiz.edu.tr*

a 70 °C oven for 24 h. During the experiment, both rubber powder and rubber powder functionalized with sulfuric acid (H_2SO_4) were used as adsorbents to remove dispersed orange dye 30 from synthetic and labscale factory waste water solutions.

The calibration curve was drawn between 10 mg/L and 100 mg/L DO-30 solution concentration absorbances. The obtained calibration equation is given in Figure 1 with chemical formula of DO-30 dye and UV absorbances of solutions at 450 nm.

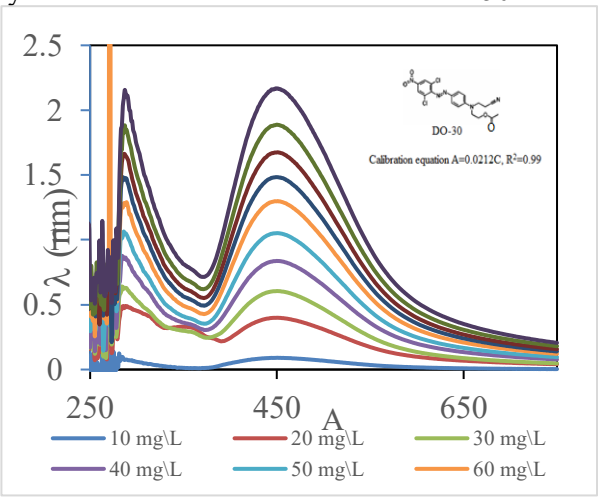

Figure 1. UV spectra of DO-30 dye solutions at different concentrations

RESULTS AND DISCUSSION

The DO-30 dye adsorption activation time on WTRP and AF-WTRP adsorbents was determined 0.4 g adsorbent 100 mg/L DO-30 solution in 10, 30, 60, 90, 120 and 150 min at room temperature. The adsorption spectra of the solutions were obtained with a UV-VIS spectrophotometer after adsorption activation time passed, the solutions were centrifuged for 10 min, the solution concentrations at equilibrium, Ce were calculated from the calibration curve according to their absorbance at 450 nm, and dye removal yield percentages (RY%) of WTRP and AF-WTRP adsorbents were given at Table 1.

Table 1 Adsorption activation time effect on DO-30 removal yield with WTRP and AF-WTRP adsorbents

WTRP				AF-WTRP		
t (min)	A	C_e (mg/L)	RY (%)	A	C_e (mg/L)	RY (%)
10	0.48	22.60	77.40	0.39	18.62	81.38
30	0.50	23.59	76.41	0.39	18.26	81.74
60	0.61	28.64	71.36	0.39	18.56	81.44
90	0.51	24.09	75.91	0.36	16.98	83.02
120	0.56	26.40	73.60	0.35	16.67	83.33
150	0.54	25.60	74.40	0.51	23.92	76.08

The best DO-30 dye removal yield was obtained with AF-WTRP due to the acidic functions of the adsorbent. The activation time increase did not affect the dye removal yield of DO-30 with WTRP and AF-WTRP according to Table 1.

The temperature effect on dye removal percent of WTRP and AF-WTRP adsorbents was studied in the temperature range of 25-30-40-50-60 °C in a 100 mg/L DO-30 solution for 90 min.

Table 2. Temperature effect on the adsorption of DO-30 on WTRP and AA-WTRP adsorbent

WTRP				AF-WTRP		
T (°C)	A	C_e (mg/L)	RY (%)	A	C_e (mg/L)	RY (%)
25	0.66	31.10	68.90	0.59	27.77	72.23
30	0.67	31.76	68.24	0.69	32.61	67.39
40	0.58	27.52	72.48	0.61	28.56	71.44
50	0.69	32.50	67.50	0.62	29.33	70.67
60	0.38	17.92	82.08	0.33	15.68	84.32

The temperature affected the adsorption of DO-30 dye on WTRP and AF-WTRP adsorbents. It is seen from Table 2 that the dye removal yield increased from 60 % to 80 % with increasing temperature.

Adsorption isotherms such as Freundlich [6] and Temkin [7] were applied for the adsorption of DO-30 dye on WTRP and AF-WTRP adsorbents with 0.4 g adsorbents at room temperature for 10 min and intial DO-30 dye concentrations as 50-100-150-200-250-300 mg/L. The results are given in Table 3.

Table 3. Concentration effect on the adsorption of DO-30 on WTRP and AF-WTRP

WTRP				AF-WTRP		
C_{DO} (mg/L)	A	C_e (mg/L)	RY (%)	A	C_e (mg/L)	RY (%)
50	0.58	27.33	45.34	0.64	30.32	39.35
100	0.94	44.41	55.59	1.08	51.03	48.97
150	1.27	59.75	60.17	1.46	69.03	53.98
200	1.63	77.05	61.47	1.81	85.19	57.40
250	1.93	90.90	63.64	2.12	100.21	59.92
300	2.28	107.44	64.19	2.58	121.86	59.38

The Freundlich adsorption isotherm of $logQ_e$ and $logC_e$ was plotted and Temkin adsorption isotherm was plotted linear q_e *versus* lnC_e adsorption of DO-30 with WTRP and AF-WTRP adsorbents. The adsorption isotherms were given in Figs. 2 and 3 for DO-30 dye adsorption during 10 min at room temperature with WTRP and AF-WTRP, respectively.

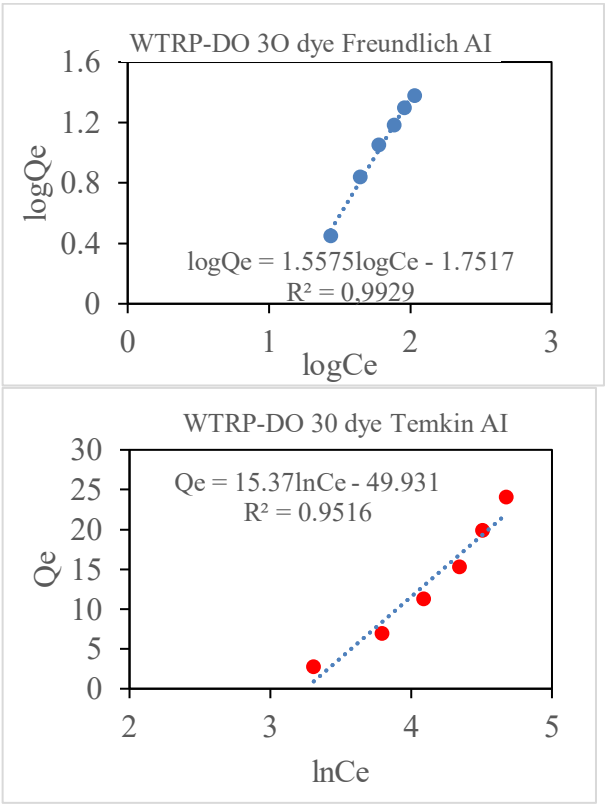

Figure 2. Freundlich and Temkin adsorption ısotherms of DO 30 dye on WTRP

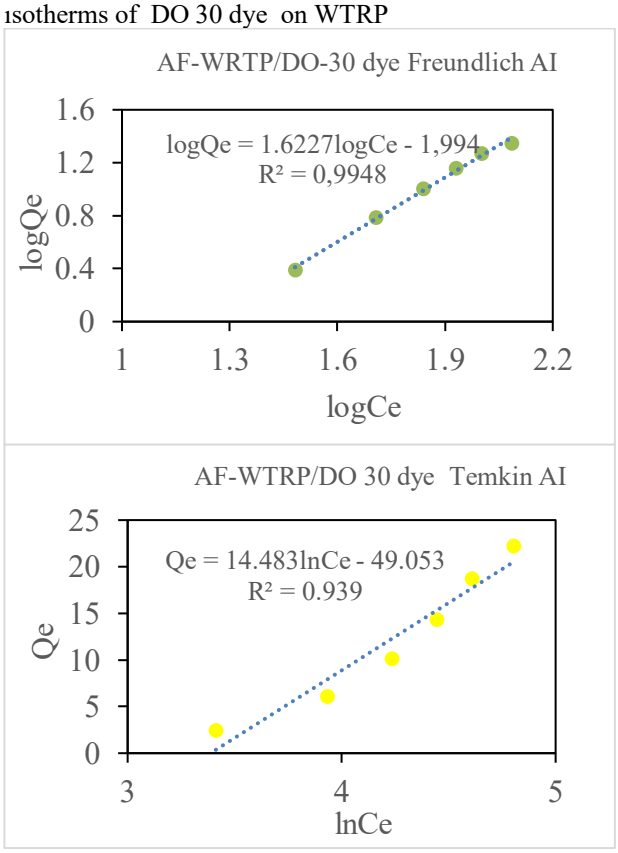

Figure 3. Freundlich and Temkin adsoprtion ısotherms of DO-30 dye adsorption on AF-WTRP

The regression coefficients of Freundlich and Temkin adsorption isotherms of DO-30 dye adsorption on WTRP and AF-WTRP adsorbents were determined about 0.99 and 0.94, respectively. The experimental adsorption data fit well the Freundlich isotherm model for adsorbents because of the higher correlation value than Temkin isotherms.

Adsorption kinetics is the study of the amount of adsorbate adsorbed with time, which provides information regarding adsorption speed, mechanism, and adsorbent quality. The pseudo-first [8], pseudo-second order [9], and Webber-Morris intraparticle diffusion models (W-M ID) [10] were applied and detailed results are given in the thesis [11].

The highest correlation coefficients were obtained for pseudo second order for DO-30 dye adsorption with WTRP and AF-WTRP and the second order kinetic model graphics for DO-30 dye adsorption on WTRP and AF-WTRP adsorbents are given in Figure 4.

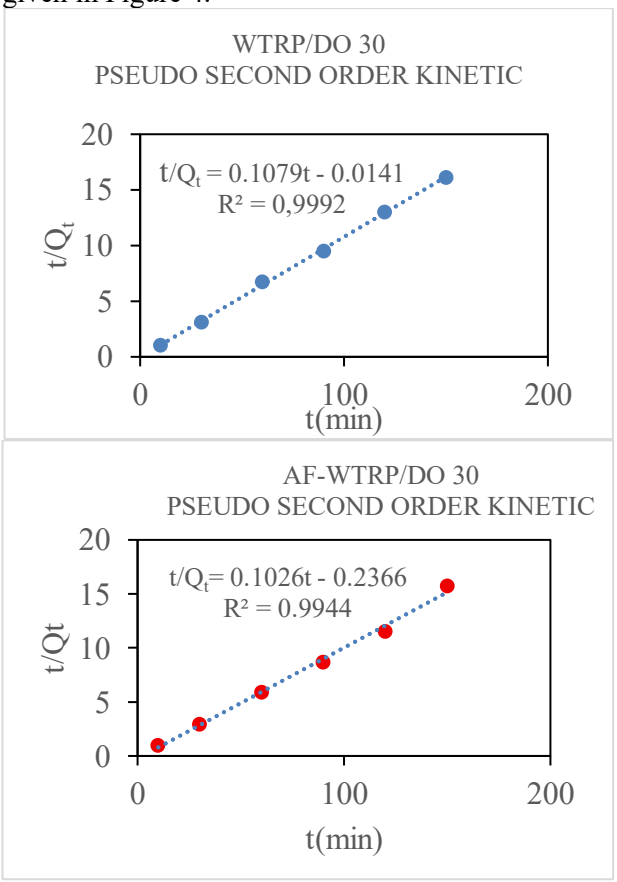

Figure 4. Pseudo second order adsorption kinetic model for DO-30 dye adsorption on WTRP and AF-WTRP adsorbents

Labscale factory waste water was supplied by SETAŞ company. The fabric was dyed in dye bath including DO-30 dye, 0.5 g/L Setalan BKF (egalizator), and Setacid PBS to adjust pH 4 and obtained labscale factory waste water solution was diluted as 10 mg/L (Fig. 5).

Figure 5 The DO-30 dyed fabric and waste water including DO-30 dye and other dye bath stuffs

The dye removal from 10 mg/L labscale waste water was carried out on 1 g WTRP and AF-WTRP adsorbents. The dye removal yields were obtained as 2.08% with WTRP and 11.31% with AF-WTRP. It was seen that the acid functionalization had positive effect to remove the DO-30 dye with WTRP.

CONCLUSION

In this study, acid-functionalized and non-acid functionalized waste scrap tyre rubber powder adsorbents were used to remove dye from synthetic and labscale waste water solutions. According to the obtained optimization results, dye removal yield of adsorbents was not significantly affected by increasing time due to the active pores adsorbing quickly DO-30 dye and the maximum dye removal yield was obtained at 10 min as 77 % for WTRP and at 90 min as 83 for AF-WTRP. The increasing temperature did significantly affect the removal of DO-30 dye from waste water with WTRP and AF-WTRP from 60 % at 25 ºC to 80 % at 60 ºC. The adsorption process of DO-30 dye with WTRP and AF-WTRP adsorbents was determined as the Freundlich adsorption isotherm and pseudo-second-order kinetic model due to the highest regression coefficients.

It was concluded that even 1 g WTRP and AF-WTRP adsorbent was effective to remove DO-30 dye from factory waste water. Hence, WTRP and AF-WTRP adsorbents can be used as cost effective alternative adsorbents for textile companies to remove dye stuffs from waste waters.

REFERENCES

1. S. P. Markandeya Shukla, A. L. Srivastav, *Water Science and Technology*, **84**(2), 445 (2021).
2. U. U. Ashar, M. Anis, G. Hussain, A.Tauseef, *International Journal of Environmental Science and Technology*, 1 (2024).
3. R. Foroutan, R. Mohammadi, S. Farjadfard, H. Esmaeili, M. Saberi, S. Sahebi, B. Ramavandi, *Environmental Science and Pollution Research*, **26,** 6336 (2019).
4. M. Tripathi, S. Singh, S. Pathak, J. Kasaudhan, A. Mishra, S. Bala, ... N. Pathak, *Toxics*, **11** (11), 940 (2023).
5. Z. Kadioglu, D. Sakar, *Bulg. Chem. Commun.,* **56** (3), 309 (2024).
6. N.D. Hutson, R.T. Yang, *J. Colloid Interf. Sci.,* 189 (2000).
7. M. Temkin, V. Pyzhev, *Acta Physicochimica U.R.S.S.,* **12**, 327 (1940).
8. S. Lagergren, *Kungliga Svenska Vetenskapsakademiens Handlingar*, **24** (4), 1 (1898)
9. Y.S. Ho, G. McKay, *Process Safety and Environmental Protection,* **76** (2), 183 (1998).
10. W.J. Weber, J.C. Morris, *Journal of the Sanitary Engineering Division,* **89** (2), 31 (1963).
11. S. Karagoz, Chemistry Graduation Thesis, Yildiz Technical University, 2025.

Bulgarian Chemical Communications, Volume 57, Issue 3 (pp. 193-197) 2025 DOI: 10.34049/bcc.57.3.KT-HG-DS

Disperse orange 30 dye removal with H_2SO_4-functionalized activated carbon: adsorption isotherms and kinetics

K. Topaç[1], H. K. Gürakin[2], D. Şakar[1]*

[1*]*Yildiz Technical University, Chemistry Department, 34220, Esenler, Istanbul, Türkiye*
[2]*SETAŞ Kimya Sanayi A.Ş., Organized Industrial Zone, Karaagac Mah. 9th Street, No 3 59510 Kapakli, Tekirdağ, Türkiye*

Accepted: August 17, 2025

Disperse orange 30 dye (DO-30) is a mono azo dye used for coloring of polyesters, nylon, natural fibres, and acetate in the textile sector. In the physicochemical treatment process known as adsorption, dissolved molecules in contaminated water form a chemical and physical bond with the surface of the adsorbent. Various synthetic and natural materials worked well as adsorbents to remove color from soiled textile effluents.

In the present study, H_2SO_4-functionalized activated carbon was synthesized and used for the adsorption of DO-30 dye from synthetic waste water. The effects of different reaction parameters such as adsorbent dosage, initial DO concentration, contact time and temperature on the adsorption of DO-30 onto activated carbon and H_2SO_4-functionalized activated carbon were investigated. To determine the best adsorption equilibrium and adsorption kinetic data of DO-30 adsorption on activated carbon and H_2SO_4-functionalized activated carbon different models for equilibrium and kinetics were applied.

Keywords: Disperse orange 30 dye; acid-activated carbon; dye removal; adsorption isotherms; kinetic and thermodynamic parameters

INTRODUCTION

As industrialization has increased, environmental contamination has emerged as a global issue. The ecosystem and the public health are seriously threatened by water resource pollution. Because of the different compounds it contains, wastewater produced by residential and commercial operations can have permanent impacts when released into the environment. Due to the high concentration of chemicals and dyestuffs in industrial waste, the textile industry currently contributes significantly to environmental contamination [1]. In terms of their molecular makeup, dyes employed in the textile industry are typically water soluble and resistant to biodegradation. Because of this, it is challenging to eliminate these chemicals using traditional therapy techniques, so additional approaches must be used. Because of their hydrophobic nature, dyes with azo groups, such disperse orange 30 (DO-30), can linger in aqueous conditions for extended periods of time and harm living things [2].

Adsorption techniques are used for eliminating these contaminants because of their ease of use, affordability, and high removal effectiveness.

Activated carbon is a popular adsorbent in adsorption processes because of its large surface area and porous structure, which allow it to bind contaminants to its surface and remove them from water [3]. Activated carbon can be functionalized using chemical techniques to improve its qualities [4]. Functionalization with sulfuric acid (H_2SO_4) by adding acidic functional groups to its surface boosts the adsorption ability of activated carbon. Activated carbon's surface becomes more polar as a result of this process, allowing for stronger interactions with dye molecules through hydrogen bonds and electrostatic forces [1]. When compared to pure activated carbon, studies reveal that H_2SO_4-functionalized activated carbon exhibits superior adsorption capabilities for hydrophobic dyes like disperse orange 30 [4].

This study aimed to compare the efficacy of activated carbon chemically functionalized with H_2SO_4 in the removal of disperse orange 30 dyestuff from aqueous solutions and assess the adsorption performance of activated carbon in this procedure. This was accomplished by conducting adsorption studies with both pure and H_2SO_4-modified activated carbon under various conditions, including

* To whom all correspondence should be sent:
E-mail: *dsakar@yildiz.edu.tr*

temperature, initial dye concentration, contact time, and adsorbent dosage (0.1 g and 0.4 g). The study examined how both adsorbents affected the removal of dyestuffs and how the modification method affected the adsorption capacity. Furthermore, the system's applicability for isotherm and kinetic models was assessed in accordance with the experimental data acquired, and conclusions on the adsorption mechanism were drawn.

EXPERIMENTAL

The disperse orange 30 dyestuff (Fig. 1) was supplied by SETAŞ, activated carbon was taken from Fluka. H_2SO_4 was purchased from Sigma-Aldrich. 30 ml of concentrated H_2SO_4 was added to 6 g of powdered pure activated carbon (PAC). The mixture was kept at 600 rpm for 6 h at approximately 80 °C. At the end of the process, the mixture was diluted and washed with distilled water. The mixture was filtered using a Nuche flask under vacuum. The H_2SO_4-functionalized activated carbon (AAC) remaining on the filter paper was kept in an oven at 70 ºC for 1 night to dry completely. Sigma brand 3-18K model ultracentrifuge device, Shimadzu UV/VIS 2600 and Daihan scientific multi-heat mixer were used.

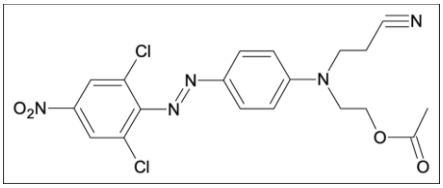

Figure 1. Chemical structure of disperse orange 30 dyestuff

Disperse orange 30 dyestuff solutions were prepared successively at concentrations of 10, 20, 30, 40, 50, 60, 70, 80, 90, and 100 mg/L with the aim to create calibration curves. To prepare the solutions, distilled water was utilized. The absorbance of the solutions at a wavelength of 450 nm was measured using a Shimadzu UV-Vis instrument. The DO-30 calibration curve is shown in Figure 2.

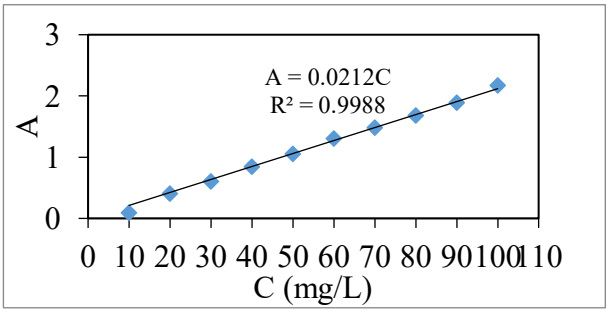

Figure 2. Calibration curve of disperse orange 30 in pure water at different concentrations obtained from absorbance changes at 450 nm wavelength

The equation A=0.0212C was used for the calibration curve. This linear equation's formulation is essential for computing modifications in the experiment's later stages.

RESULTS AND DISCUSSION

The pure activated carbon (PAC) and H_2SO_4-functionalized activated carbon (AAC) were used to remove disperse orange 30 dyestuff from synthetic waste water solutions *via* adsorption process. The parameters such as contact time (10–30-60-90-120-150 min), temperature (25-30-40-50-60 °C), initial dye concentration (50-100-150-200-250-300 mg/L), and adsorbent dosage (0.1 and 0.4 g) were examined.

The percent dye removal (DR, %) of DO was calculated using Eq. 1:

$$\%DR = \frac{(Co-Ce).100}{Co} \quad (1)$$

where $Co(mg/L)$ and $Ce(mg/L)$ are DO-30 dye solution concentrations at the initial and equilibrium stage, respectively.

To determine the optimal adsorption time and adsorbent dosage, 100 mg/L DO solutions at 700 rpm on PAC and AAC adsorbents were measured for 10-30-60-90-120-150 min, 0.1 and 0.4 g adsorbents, respectively. Centrifugation was carried out after sample collection, and absorbance measurements were taken to ascertain the removal effectiveness. Ce values were calculated from the calibration curve according to their absorbance at 450 nm, and dye removal percent (DR, %) of PAC and AAC adsorbents was calculated according to Eq. 1 and the results are given in Table 1.

Table 1. Contact time and adsorbent dosage of DO-30 dye removal with PAC and AAC adsorbents as 0.1 and 0.4 g.

	PAC			AAC		
t (min)	A	Ce (mg/L)	DR (%)	A	Ce (mg/L)	DR (%)
10	0.94	44.37	55.63	0.74	34.80	65.19
10*	0.36	16.85	83.15	0.41	19.24	80.76
30	0.96	45.21	54.79	0.75	35.46	64.54
30*	0.35	16.55	83.44	0.39	18.70	81.29
60	0.99	46.73	53.26	0.86	40.35	59.65
60*	0.44	20.85	81.58	0.38	18.07	81.93
90	1.12	53.03	46.97	0.89	42.32	57.68
90*	0.44	20.85	79.15	0.39	18.83	81.17
120	1.00	47.18	52.82	0.92	43.43	56.57
120*	0.49	23.33	76.67	0.39	18.46	81.54
150	0.98	46.59	53.41	0.98	46.29	53.71
150*	0.52	24.47	75.53	0.38	18.06	81.94

*0.4 g adsorbent results

As the adsorbent amount and the contact time increased, the removal of DO-30 dye increased as well.

The temperature effect on DO-30 dye removal from synthetic waste water was examined on 0.1 and 0.4 g of PAC and AAC adsorbents with 10, 60 and 90 min at 25, 30, 40, 50 and 60 ºC. The highest DO-30 dye removal results were obtained with 0.4 g adsorbent at 90 min and are given in Table 2.

Table 2. Temperature effect on DO-30 dye (100 mg/L) removal with 0.4 g of PAC and AAC adsorbents for 60 and 90 min

	PAC			AAC		
T (ºC)	A	C_e (mg/L)	DR (%)	A	C_e (mg/L)	DR (%)
25	0.56	26.34	73.66	0.72	34.18	65.82
25*	0.58	27.39	72.61	0.54	25.34	74.66
30	0.46	21.77	78.23	0.89	41.84	58.16
30*	0.50	23.71	76.29	0.55	25.79	74.21
40	0.53	24.90	75.09	0.75	35.55	64.45
40*	0.54	25.61	74.39	0.47	22.02	77.98
50	0.31	14.82	85.18	0.63	29.49	70.51
50*	0.37	17.38	82.62	0.42	19.62	80.38
60	0.14	6.47	93.53	0.39	18.43	81.57
60*	0.10	4.72	95.28	0.12	5.45	94.55

*These results refer to 90 min.

The highest DO-30 dye removal was 95% obtained with 0.4 g adsorbent at 90 min with increasing temperature at 60 ºC.

Adsorption isotherms are crucial for maximizing the utilization of any adsorbent because they explain how the adsorbate and adsorbent interact. The stability of the contacts between the adsorbent and the adsorbate, as well as the adsorption affinity of molecules, are revealed by the shape of the isotherm. Adsorption isotherms can be expressed mathematically in a variety of ways; some are empirical and require the correlation of experimental data, while others are based on a simplified physical description of adsorption [5].

In this study, the Freundlich and Temkin adsorption ısotherms were applied for DO-30 adsorption on 0.4 g of PAC and AAC for 90 min at room temperature for 50, 100, 150, 200, 250 and 300 mg/L DO-30 initial concentrations. The Temkin isotherm states that because of interactions between the adsorbent and adsorbate, the heat of sorption should decrease linearly with sorption coverage on the adsorbent [6, 7].

The linear q_e *vs* lnC_e plot was created for the Temkin adsorption isotherm, and the slope and intersection point of this linear plot were used to determine the Temkin adsorption isotherm parameters, lnA and b, respectively. For Freundlich adsorption isotherm, the linear log qe *vs* log Ce plot was drawn and the kinetic parameters, n and K_F, were obtained from the slope and the intersection point of this linear plot, respectively. The results are displayed in Table 3. Figures 3 and 4 show the Temkin isotherms for PAC and AAC, respectively. The Freundlich isotherms for PAC and AAC are given in Figs. 5 and 6.

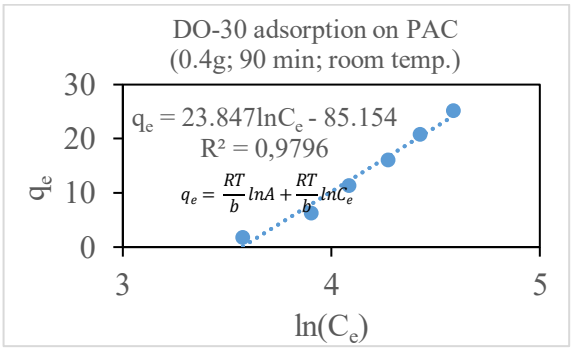

Figure 3. Temkin adsorption isotherm: DO-30 dye adsorption on PAC

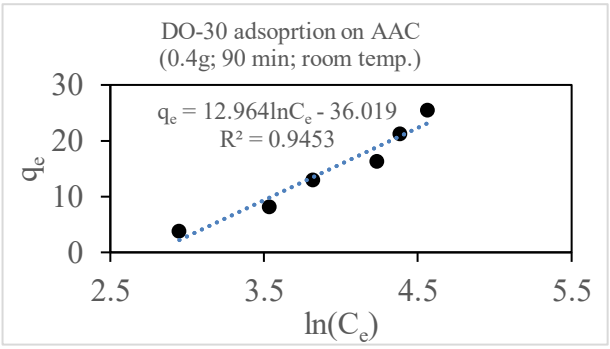

Figure 4. Temkin adsorption isotherm:DO-30 dye adsorption on AAC

It was found that the experimental adsorption data of DO-30 dye adsorption suited the Freundlich and Temkin isotherm models well based on the regression coefficients of these two isotherms (Table 3).

The rate at which a sorbate is retained or released from an aqueous solution to a solid-phase interface is referred to as adsorption kinetics. The pseudo-first, pseudo-second order and Webber-Morris intraparticle diffusion models (WM-ID) kinetic analysis was applied to determine the kinetics of DO-30 adsorption from synthetic waste water solutions by 0.4 g PAC and AAC adsorbents between 20 to 160 min time period and the results are given in Table 4.

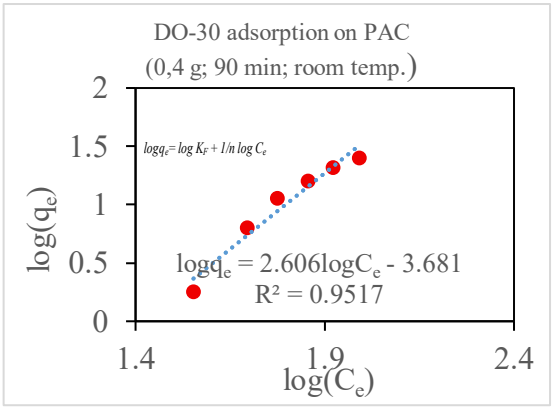

Figure 5. Freundlich adsorption isotherm: DO-30 dye adsorption on PAC

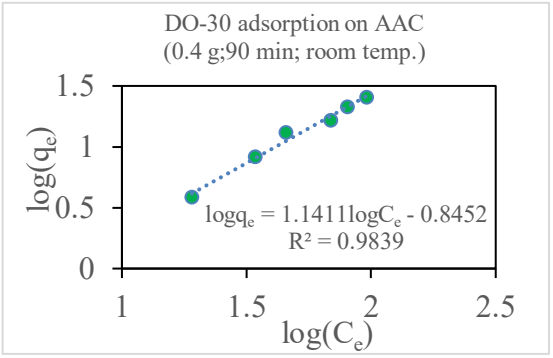

Figure 6. Freundlich adsorption isotherm:DO-30 dye adsorption on AAC

Table 3. Parameter values of the adsorption models for DO-30 adsorption on PAC and AAC adsorbents

Isotherm		PAC	AAC
Freundlich	$\log K_F$ ($L.mg^{-1}$)	-3.68	-0.84
	n	0.38	0.88
	R^2	0.95	0.98
Temkin	lnA	-3.57	-2.78
	B	103.9	191.1
	R^2	0.98	0.95

Table 4. Adsorption kinetic parameters: k_1 (min^{-1}), k_2 ($g.mg^{-1}.min^{-1}$) and k_3 ($mg.g^{-1}.min^{-1/2}$), C, R^2 for DO-30 adsorption on 0.4 g PAC and AAC adsorbents

Kinetic model	Parameters	PAC	AAC
Pseudo 1st	k_1	4.10^{-5}	3.10^{-6}
	R^2	0.9655	0.4346
Pseudo 2nd	k_2	0.035	0.44
	R^2	0.999	1
WM ID	k_3	7.75	41.86
	C	85.657	79.812
	R^2	0.898	0.4952

As shown in Table 4, the correlation coefficient of determination of the pseudo-second-order kinetic model exceeded 0.99 and 1 for PAC and AAC. These results indicated that the pseudo-second-order model was more suitable for the adsorption of DO-30 dye onto the PAC and AAC adsorbents.

DO-3 dye adsorption thermodynamic investigation on 0.4 g PAC and AAC adsorbents at 25, 30, 40, 50, 60 °C temperatures at 10, 50 and 90 tim were done and adsorption free energy, adsorption enthalpy and adsorption entropy were calculated. The results are given in Table 5.

The adsorption process's viability and spontaneous nature without the requirement for an external energy source were demonstrated by the negative ΔG factor. The study's negative ΔG values (Table 4) demonstrated that the adsorption process that eliminated DO-30 happened on its own without the assistance of an outside energy source. The endothermic nature of the process is suggested by the positive values of ΔH°, which also show that the amount adsorbed at equilibrium increases as the temperature rises. When DO-30 dye is adsorbed onto PAC and AAC adsorbents, the solid–solution interface becomes more random, as indicated by the positive values of ΔS°.

Table 5. Thermodynamic parameters in the adsorption of DO-30 on the PAC and AAC adsorbents

	PAC			AAC		
t (min)	-ΔG°* (J/mol)	ΔH° (J/mol)	ΔS° (J/molK)	-ΔG° (J/mol)	ΔH° (J/mol)	ΔS° (J/molK)
10	2468.34	3389.04	20.73	2238.73	6574.05	29.07
60	2548.15	34542.18	123.21	1624.01	21141.67	73.99
90	2415.43	22611.59	83.41	2677.71	36264.01	128.43

* ΔG° values refer to 298 K.

CONCLUSION

Acid functionalized and pure activated carbon have been used to produce low-cost adsorbents to remove DO-30 from an aqueous solution. The highest DO-30 dye removal results were obtained as 0.4 g adsorbent at 60 ºC during 90 min. The plot of the adsorption isotherms showed that the Temkin model better represents the adsorption of DO-30 on PAC, and Freundlich model - for the AAC adsorbent.The kinetic studies proved that the adsorption of DO-30 on PAC and AAC adsorbents fitted the pseudo-second-order kinetic model with good correlation and this process was spontaneous endothermic according to thermodynamic parameters.

REFERENCES

1. M. T. Yagub, T. K. Sen, S. Afroze, H. M. Ang, *Advances in Colloid and Interface Science,* **209**, 172 (2014).
2. G. Crini, P. M. Badot, *Progress in Polymer Science*, **33(4),** 399 (2008).
3. G. N. Rameshaiah, M. Sowmya, *International Journal of Science and Research*, **4(6),** 1204 (2015).
4. O. S. Bello, M. A. Ahmad, *Water Resources and Industry*, **2**, 90 (2012).
5. M. Musah, Y. Azeh, J. T. Mathew, M. T. Umar, Z. Abdulhamid, A. I. Muhammad, *Caliphate Journal of Science & Technology*, **1,** 20 (2022).
6. S. A. Obaid, *Journal of Conference Series,* **1664**, 012011 (2020).
7. P. Sampranpiboon, P. Charnkeitkong, X. Feng, *WSEAS Transaction on Environment and Development*, 35 (2014).

Bulgarian Chemical Communications, Volume 57, Issue 3 (pp. 198-201) 2025 DOI: 10.34049/bcc.57.3.ME-OS

Farma-Bant: obtaining a wound covering membrane from *Calendula Officinalis, Centella Asiatica* and *Carthamus Tinctorius* plant extract mixtures

M. D. Evcimen, Ö. Yaşa Şahin*

Private Bahcesehir College, Department of Chemistry, Istanbul, Turkey

Accepted: August 17, 2025

Studies and practical applications related to wound dressings used in wound treatment around the world hold significant importance. These wound dressings cover the wound, protect the skin from external factors, and contribute to the healing process. When examining wound healing practices, it is evident that plants have been used since ancient times. For this purpose, antimicrobial plants have been incorporated into wound dressings in an effort to accelerate healing.

In this study, it was aimed to extract the plant compounds from *Centella Asiatica* (Indian Pennywort), *Carthamus Tinctorius* (Safflower) and *Calendula Officinalis* (Marigold) each possessing different pharmacological properties and to integrate a mixture of these extracts, prepared in specific ratios, into adhesive bandages commonly used for minor cuts and injuries. To investigate the release of the plant extracts from the bandage, time dependent UV-VIS spectroscopic measurements were performed in phosphate-buffered saline (PBS) which simulates body fluid. A swelling test was conducted to evaluate the fluid absorption capacity, and microscopy was used to observe whether the plant extracts were successfully incorporated into the wound dressing material.

Keywords: Marigold, Indian Pennywort, Safflower, wound dressing, antimicrobial

INTRODUCTION

Research and applications related to wound dressings used for wound treatment worldwide hold significant importance. Various types of dressings are used globally for injuries, which covers the wound to protect the skin from external factors and aid healing. The essence of modern wound care is to evaluate the wound correctly, identify the parts and keep the wound moist. At the same time, protecting the wound from bacteria and foreign substances, removing excess leakage from the wound, not harming healthy tissues during wound healing and allowing gas consumption in the wound area are among the features expected from the ideal wound care system [1]. Among the first dressings we use for minor home accidents is the adhesive bandage, an essential component of first aid kits. Additional materials added to the wound dressings used accelerate the healing process of the wound. Recently, modern dressings have incorporated various functional plants to promote faster healing and protect against infections. Antimicrobial plants have been integrated into dressings to expedite healing.

In this study, three high pharmacological plants *Centella Asiatica* (Indian Pennywort), *Carthamus Tinctorius* (Safflower) and *Calendula Officinalis* (Marigold) were highlighted. Research shows that Indian pennywort has significant wound healing properties [2], Safflower is used as a pain reliever and fever reducer [3] and Marigold promotes skin healing [4]. This study aims to extract the essences of these plants and incorporate them into adhesive bandages for small wounds and cuts. The release of plant extracts from the bandages was analyzed using time dependent UV-VIS spectrum measurements in a phosphate buffer saline (PBS) as artificial body fluid. Swelling test was used for the investigation of liquid absorption properties. Microscopy was also used to confirm the incorporation of plant extracts into the wound dressing.

EXPERIMENTAL:

Extraction of Indian Pennywort (Centella Asiatica) plant

10 g of dried *Centella Asiatica* plant is taken and 100 ml of a methanol-water mixture (10:90, v/v) is added. This mixture is left to stay for 1 day. The resulting mixture is then filtered and the solvent in the filtrate is removed using a rotary evaporator. After the evaporation process, the plant extract is obtained [2].

Extraction of Safflower (Carthamus Tinctorius) plant

2 g of safflower is weighed using a precision balance. Then, 10 ml of methanol is added and left to stand for 1 day. The resulting mixture is filtered,

* To whom all correspondence should be sent:
E-mail: *oznuryasa@hotmail.com*

and the solvent in the filtrate is removed using a rotary evaporator. After the evaporation process, the plant extract is obtained [5].

Extraction of Marigold (Calendula Officinalis) plant

250 mg of *Calendula Officinalis* is weighed using a precision balance. Then, 25 ml of methanol is added to the weighed plant material. The solvent is replaced every 24 hours for 3 days, and all collected solvents are combined at the end of the third day. The resulting mixture is filtered, and the solvent in the filtrate is removed using a rotary evaporator. After the evaporation process, the plant extract is obtained [6].

Integration of the extracts of three different plants into the wound dressing:

Extracts from *Centella Asiatica* (Indian Pennywort), *Carthamus Tinctorius* (Safflower) and *Calendula Officinalis* (Marigold) were each separately weighed to obtain a mass ratio of 5% [7]. Methanol was added to each weighed extract and the mixtures were combined in a beaker. This combined mixture was stirred for 24 h using a magnetic stirrer without applying any heat. The rectangular gauze part in the center of the wound dressing was removed and immersed in the extract-containing solution. The gauze was left in the solution for 24 h and then removed and left to dry at room temperature (Fig. 1).

Fig. 1. Integration of the extracts of three different plants into the wound dressing.

Release of wound dressing containing Centella Asiatica, Carthamus Tinctorius, and Calendula Officinalis extracts in phosphate buffered saline (PBS)

The wound dressing containing the three plant extracts was first weighed. Then, it was placed in 30 ml of phosphate buffered saline (PBS) and kept at a constant temperature of 37°C. A sample was taken at the 96th hour and the final weight of the dressing was measured [8]. Table 1 shows the weight wound dressing before and after 96th hour of immersion in the phosphate buffer solution.

Table 1. Weight of the wound dressing containing three different plant extracts before and after 96th hour of immersion in the phosphate buffer solution.

Weight of wound dressing containing three different plant extracts before placing in phosphate buffer solution	Weight of the wound dressing containing three different plant extracts after 96th hour of placing it in the phosphate buffer solution
0.1 g	0.03 g

To evaluate the release behavior due to degradation, UV spectrophotometric measurements were taken. The plant extract containing wound dressing was kept in 30 ml of PBS at 37°C. Samples were collected at the 48th and 96th h for UV spectrophotometric analysis (Fig. 2).

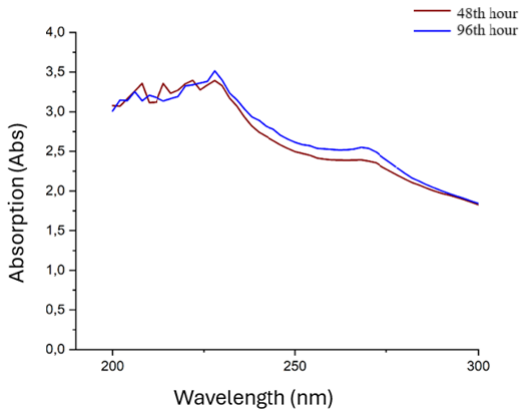

Fig. 2. UV-VIS spectra of the wound dressing coated with plant extracts taken at 48th and 96th hour.

Swelling test

A swelling test was conducted to determine the liquid absorption capacity of the wound dressing coated with three different plant extracts. A 1 cm × 1 cm piece was cut from the wound dressing and placed into phosphate buffer solution (pH=7.4) at 37 °C and kept under stirring with a magnetic stirrer [9]. At specific time intervals, the sample was removed from the phosphate buffer solution, gently blotted with a paper towel to remove excess liquid, and weighed using a precision balance. The swelling ratio of the plant extract containing wound dressing was calculated using the equation below and a time dependent graph was plotted.

$$\text{Swelling ratio} = \frac{W_s - W_d}{W_d}$$

where W_d represents the dry weight of the sample after vacuum oven drying and W_s represents the wet

weight after phosphate buffer solution immersion [9].

The weight of the wound dressing containing these additives were measured by keeping it in a shaking water bath at 37°C in phosphate buffer solution. The measured values are given in Table 2.

Table 2. Swelling weight of wound dressing containing three different plant extracts with respect to time.

Time	Wound dressing with plant extracts
0th hour	53 mg
7th hour	105 mg
24th hour	211 mg
48th hour	325 mg

Microscopic examination of wound dressing with and without plant extract mixture

The wound dressing was examined with and without plant extracts under a microscope at 100, 200 and 400× magnification. Figure 3 gives the appearance of the uncoated and coated form of the wound dressing fabric under the microscope at 100, 200 and 400× magnification.

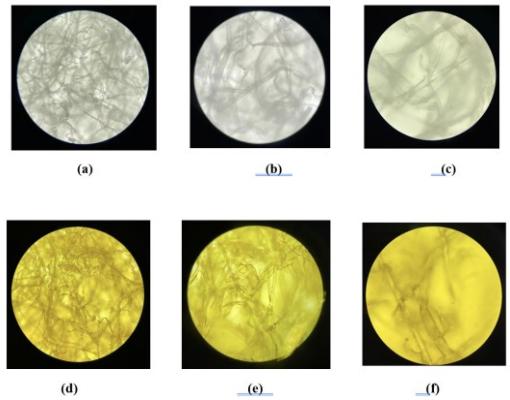

Fig. 3. Photographs of the wound dressing not coated with plant extracts (a) 100×, (b) 200×, (c) 400× magnification and photographs of the wound dressing coated with plant extracts (d)100× (e) 200× (f) 400× magnification.

Materials

In our project, *Centella Asiatica* (Indian Pennywort), *Carthamus Tinctorius* (Safflower) and *Calendula Officinalis* (Marigold) were used and methanol and distilled water were employed to obtain the plant extracts. To observe the release behavior of the plant extracts in the human body, phosphate buffered saline (PBS), a solution that closely resembles human body fluid and is considered a type of artificial body fluid, was used.

In our study, a precision balance, a rotary evaporator (for solvent removal), a Nikon Eclipse E100 microscope (for microscopic analyses), and a Shimadzu UVmini-1240 UV-Vis spectrophotometer (for investigating the release of plant extracts) were used.

RESULTS AND DISCUSSION

In this study, extracts were obtained from *Centella Asiatica* (Indian Pennywort), *Carthamus Tinctorius* (Safflower), and *Calendula Officinalis* (Marigold). The obtained extracts were incorporated into the fabric layer of a wound dressing and the release behavior of the plant extracts from the wound dressing fabric was observed in phosphate buffered saline (PBS), which closely simulates human body fluid. Samples were collected at the 48th and 96th hour from the PBS medium containing the wound dressing fabric and their release profiles were analyzed using a UV-VIS spectrophotometer. A swelling test was also performed to evaluate the fluid absorption capacity of the developed wound dressing. Additionally, microscope analyses at 100×, 200×, and 400× magnifications were conducted to compare wound dressing fabrics with and without plant extracts.

We aimed to utilize the wound-healing properties of Indian Pennywort, the analgesic effect of Safflower, and the skin repairing properties of Marigold. Initially, the plant extracts were prepared based on literature data. The extracts were then mixed in specific ratios and integrated into the wound dressing fabric. The release of these extracts was studied in phosphate buffered saline (PBS) solution, which is considered a close simulation of human body fluid. UV-VIS measurements at the 48th and 96th hour revealed significant changes in absorbance values, indicating the release of plant extracts from the wound dressing. Furthermore, weight measurements before and after immersion in PBS showed a decrease in the weight of the wound dressing fabric by the end of 96 hours, further confirming the release of the plant extracts into the buffer solution.

When the swelling test was applied to the wound dressing containing all three plant extracts, the fluid absorption percentage was found to be 513% at the 48th hour. While wound exudate nourishes the wound, excessive accumulation can interfere with proper observation and healing. Therefore, an ideal wound dressing should provide optimal fluid absorption [9]. According to the literature, an ideal wound dressing should have a fluid absorption capacity between 100% and 900% [10]. The 513% absorption value found in this study falls within this ideal range, indicating that the herbal extract-infused

wound dressing has good fluid absorption performance.

Moreover, microscopy at 100×, 200×, and 400× magnifications confirmed that the plant extracts were thoroughly integrated into the wound dressing fabric, as the coated and uncoated samples showed distinct surface differences.

CONCLUSION

In conclusion, all data obtained in this study demonstrate that the wound dressing fabric was successfully coated with *Centella Asiatica*, *Carthamus Tinctorius* and *Calendula Officinalis* extracts and that these extracts were released into the simulated human body fluid (PBS) over time.

REFERENCES

1. A. H. Kurtoğlu, A. Karataş, *Ankara Ecz. Fak. Derg,* **3**(38), 211 (2009).
2. O. Bozkaya, *Centalla Asiatica Bitki Özütü İle Kaplı Gümüş Nanopartikül İçeren Polimer Liflerin Yara İyileştirici Etkisnin In Vitro Ve In Vivo Araştırılması,* PhD Thesis*,* Hacettepe Üniversitesi, Ankara, 2021.
3. E. Kına, M. S. Özgökçe, A. Sadak, S. Kıpçak, *Yüzüncü Yıl Üniversitesi Fen Bilimleri Enstitüsü Dergisi,* **3**, 674 (2022).
4. K. A. Khalid, J. A. Teixeira da Silva, *Global Science Books,* **1**(6), 12 (2011).
5. M. S. Yolci, R. Tunçtürk, M. Tunçtürk, *International Journal of Life Sciences and Biotechnology*, **1**(5), 97 (2022).
6. Y. Balıkçı, *Türkiye'de Yetişen Aynısefa (Calendula Officinalis L.) Bitkisinin Kuersetin Ve Rutin İçeriğinin Kromatografik Ve Spektrofotometrik Yöntemler İle Tayini,* Master's Thesis, Marmara Üniversitesi, İstanbul, 2019.
7. H. K. Arıkan, İlaç Salınımı Kompozit Yara Bandı Tasarımı Ve Üretimi, Master's Thesis, Kahramanmaraş Sütçü İmam Üniversitesi, Kahramanmaraş, 2014.
8. E. Korkmaz, Ballıbaba Özütü İle Yeşil Sentezlenmiş Gümüş Nanopartikül Katkılı Plga Elektrospin Nanofiber Ve Sütür Üretimi, Karakterizasyonu Ve Antibakteriyel Aktivitesinin İncelemesi, Master's Thesis, Necmettin Erbakan Üniversitesi, Konya, 2021.
9. K. Gökyıldırım, Çay Ağacı Yağı Katkılı Polimerik Nanofiber Yara Örtüsü Üretimi Ve Karakterizasyonu, Master's Thesis, İstanbul Yeni Yüzyıl Üniversitesi, İstanbul, 2023.
10. H. Adeli, M.T. Khorasani, M. Parvazinia, *Int. J. Biol. Macromol*., **122**, 238 (2019).

Bulgarian Chemical Communications, Volume 57, Issue 3 (pp. 202-205) 2025 DOI: 10.34049/bcc.57.3.SS-EA-IK

Development of a high-performance liquid chromatography (HPLC) method for coumarin quantification in medicinal plants extracted *via* Soxhlet

S. Simsek, E. Akyol*, I. Kucuk

Yildiz Technical University, Chemical Engineering Department, Davutpasa Campus, Esenler, Istanbul 34210, Turkey

Accepted: August 17, 2025

In this study, it was aimed to develop a new high-performance liquid chromatography (HPLC) method for the efficient extraction and quantification of coumarin compound from *Helichrysum arenarium*, *Origanum onites* and *Achillea millefolium* plants by Soxhlet extraction method. Deionized water, methanol, ethanol, acetone, n-hexane and toluene were used as solvents in Soxhlet extraction and the most suitable solvent was determined by comparing the extraction efficiencies of the solvents. Experimental results revealed that there were significant differences in coumarin extraction efficiency depending on solvent type and chemical structure of the plant. Deionized water provided the highest extraction efficiency in general, while the highest coumarin concentration (0.0339 mg/mL) was obtained for *Helichrysum arenarium* when methanol was used. *Achillea millefolium* was found to have the lowest overall coumarin content. The HPLC method developed within the scope of the study provided high sensitivity, accuracy and reproducibility for coumarin quantification. The findings indicate that the choice of solvent for the analysis of coumarin-containing herbal extracts should not be based solely on polarity, but should be evaluated together with the matrix properties of the plant.

Keywords: Coumarin extraction, Soxhlet extraction, high-performance liquid chromatography (HPLC), solvent selection

INTRODUCTION

Plants produce not only primary metabolites, which are vital for their functions, but also secondary metabolites that help them adapt to their environment and defend themselves [1]. Flavonoids, a valuable group of secondary metabolites, can be found in many plant sources, especially fruits, herbs, vegetables, stems, grains, nuts, flowers and seeds. Their antioxidant capacity, ability to change enzymatic activity and impact on cellular processes have made them central to research in nutrition, pharmacology and food science [2, 3]. Both *in vitro* and *in vivo* (animal and cell model-based) studies supporting the positive effects of flavonoids on health suggest that these compounds may be promising strategic components in preventive medicine [2, 4]. Coumarin is a phenolic compound commonly found in plants [5, 6]. It is an aromatic organic compound with formula $C_9H_6O_2$. 2D structure of coumarin is given in Scheme 1. Its molecule is a benzene molecule with an unsaturated lactone ring replacing two hydrogen atoms. It belongs to the benzopyrone class and is a lactone. This class of compounds has a wide spectrum of pharmacological effects such as anti-inflammatory, analgesic, antimicrobial and lipid peroxidation-inhibitory [6, 7]. However, it has also been reported that long-term or excessive use of coumarins may have adverse effects on health [8, 9]. Therefore, accurate quantification of these compounds is of great importance for potential therapeutic applications and safety assessments.

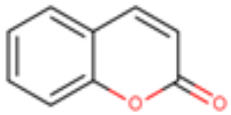

Scheme 1. 2D structure of coumarin

Helichrysum arenarium commonly known as sandy everlasting, is a coumarin-rich plant widely used in traditional medicine for treating conditions such as edema, digestive disorders, and joint pain [10]. *Origanum onites* is a highly valued herb with about 100 species distributed worldwide. Thymus species are native plants of Europe and Asia. They are also abundant in the Mediterranean region, southeastern Italy, and northwestern Africa. The genus Thymus comprises a number of highly useful medicinal plants with a range of therapeutic activities [11]. *Achillea millefolium* is a medicinal plant belonging to the Asteraceae family, widely found in the flora of Turkey and used for various purposes in traditional medicine. *Achillea millefolium* is notable for its rich content of volatile oils, phenolic compounds and flavonoids. The potential health effects of flavonoids obtained from this plant are also scientifically supported [12].

* To whom all correspondence should be sent:
E-mail: *eakyol@yildiz.edu.tr*

Efficient synthesis of these compounds from plant materials is critical to the effective use of plant resources and to increasing the bioavailability of flavonoids. In this context, although different extraction methods have been developed, Soxhlet extraction (SE) still stands out as a reference method despite its classical structure. This technique, which is based on continuous solvent recycling, effectively breaks down plant cell walls and enables flavonoids to be extracted with high yields. Recent studies have examined SE in terms of flavonoid yield of different plant materials and used the method as a basic standard to compare with innovative techniques such as ultrasonic (UAE), microwave (MAE) or supercritical fluid extraction (SFE) [13].

High-performance liquid chromatography (HPLC) is a preferred technique for analyzing complex mixtures such as natural products. Thanks to its high sensitivity, specificity and ability to separate components, it is an ideal method for determining the quantity of compounds such as coumarin. However, validation of HPLC methods is necessary to ensure that the results obtained are reliable and accurate. Method validation is the set of experimental studies that confirm that an analytical method is suitable for its intended use [14, 15]. In this context, studies on the HPLC determination and validation of coumarin from *Helichrysum arenarium*, *Origanum onites* and *Achillea millefolium* will contribute significantly to the scientific understanding of the chemical composition and potential benefits of the plant.

EXPERIMENTAL

Materials

Helichrysum arenarium, *Origanum onites*, and *Achillea millefolium* plants, which grow around Uşak province in the Aegean region of Turkey, were supplied in dried form by Amcahafızoğlu, a local herbalist in Uşak. Deionized water (CAS 7732-18-5), ethanol (CAS 64-17-5), methanol (CAS 67-56-1), acetone (CAS 67-64-1), n-hexane (CAS 110-54-3), toluene (CAS 108-88-3) were supplied by Beyanlab. Potassium dihydrogen phosphate, acetonitrile, methanol, standard coumarin (CAS 91-64-5) were supplied by Boston Chemical.

Extraction

Helichrysum arenarium, *Origanum onites* and *Achillea millefolium* leaves (5 g) were separated and weighted. They were then wrapped in filter paper, placed in a closed package inside the Soxhlet cartridge. The cartridge was placed inside the Soxhlet extractor. Solvents (deionized water, ethanol, methanol, acetone, n-hexane and toluene) were measured at 250 ml each and loaded into the solvent chamber under the Soxhlet. A reflux condenser was connected to the extractor. Cold water was passed through the condenser using a pump. After operating the heated mantle under the flask, the solvents were siphoned 15 times at an extraction temperature of 70 °C, and the solvent was allowed to reflux.

The extraction efficiency was calculated according to Eq. 1:

$$\text{Extraction efficiency (\%)} = \frac{(W-Z)}{W} \times 100 \qquad (1)$$

where: W is the initial dry plant sample (g); Z is the remaining solid after extraction (g).

Development and validation of the HPLC method for the quantification of coumarin

Shimadzu LC-2030C Plus system was used for the HPLC. The analytical column was a C18 Inertsil ODS3 5 × 4.6 × 250 mm. Acetonitrile, methanol, potassium dihydrogenphosphate and coumarin were used as chemical substances in the analysis. The method was created as a gradient phase. The mobile phase was a 60% buffer solution (0.5 g of potassium dihydrogenphosphate per 1000 ml of deionized water), a 30% acetonitrile and 10% methanol mixture, and the methanol was used as the solvent.

RESULTS AND DISCUSSION

Extraction results

After 15 siphoning cycles, the highest extraction yield for *Helichrysum arenarium* was obtained using deionized water as the solvent (22.9%). This can be explained by the high polarity and numerous hydroxyl groups present in the phenolic and flavonoid compounds found in the plant. Polar protic solvents such as deionized water, methanol, and ethanol can act as both hydrogen bond donors and acceptors due to the hydroxyl (–OH) groups in their content; this increases solubility by forming strong interactions with phenolic compounds. Deionized water has been quite effective in dissolving phenolic and flavonoid compounds in plants. Methanol and ethanol provided moderate yields of 20.72% and 17.76%, respectively. Although these solvents are soluble in phenolic substances, their yields were lower than those obtained using deionized water. Extractions using acetone (polar aprotic solvent), n-hexane, and toluene (apolar solvents) yielded very low yields (7.34%, 2.20%, and 1.70%, respectively). This indicates that *Helichrysum arenarium* contains more hydrophilic compounds than apolar compounds.

The highest extraction yield for *Origanum onites* was still obtained using deionized water (32.00%).

This result indicates that the polyphenols in *Origanum onites* are highly soluble in deionized water and that the plant matrix contains components that are easily soluble in deionized water. Methanol and ethanol provided relatively low yields of 20.60% and 14.72%, respectively. Although these solvents are effective in extracting medium-polar components, the main target components in *Origanum onites* are likely more soluble in deionized water. Extraction using solvents such as acetone (polar aprotic solvent), n-hexane, and toluene (apolar solvents) resulted in extremely low yields (3.18%, 0.94%, and 2.74%, respectively). This indicates that the target components in *Origanum onites* are not apolar.

The highest extraction yield for *Achillea millefolium* was obtained using deionized water (23.02%). This indicates that the plant contains highly polar compounds that can be extracted with deionized water. Methanol and ethanol provided relatively high yields (21.34% and 19.66%, respectively). Acetone, toluene, and n-hexane provided yields of 9.46%, 2.38%, and 4.38%, respectively. Although acetone showed a higher yield of 9.46% in this plant compared to the apolar solvents, this value is still lower than that of deionized water or alcohols. The effect of different solvents on extraction yield is shown in Fig 1.

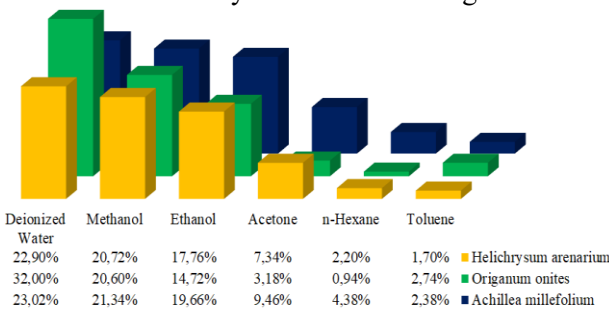

Fig. 1. Percent total phenolic compound extraction efficiency of plants by solvent type

Quantification of coumarin

A coumarin standard solution (0.2 mg/ml) was used to optimise the HPLC quantification method. Different percentages of mobile phase were trialled, then the ratio of buffer solution: acetonitrile: methanol = 60:30:10 was selected because it had good separation efficiency and met system conditions. The results of the system suitability test (SUT) and the analysis conditions are shown in Table 1.

The linearity range of the method was found to be 0.02 g/L - 0.15 g/L. The R^2 value of the method linearity data was found to be 0.992. The analytical procedure was performed according to ICH standards and the chromatogram of coumarin is given in Figure 2.

Table 1. HPLC system analysis conditions

Device	HPLC Shimadzu LC2030C PLUS
Detector	UV-Vis Detector
Column	GL Sciences Inertsil ODS-3 C18 (5 µm, 200 × 4.6 mm)
Wavelength	272 nm
Mobile phase	*Buffer solution: acetonitrile: methanol (60:30:10, h/h)
Column temperature	25 °C
Injection volume	10 µL
Analysis time	20 min
Flow rate	0.9 ml min^{-1}

*Buffer solution: 0.5 g potassium dihydrogen phosphate/1000 ml deionized water

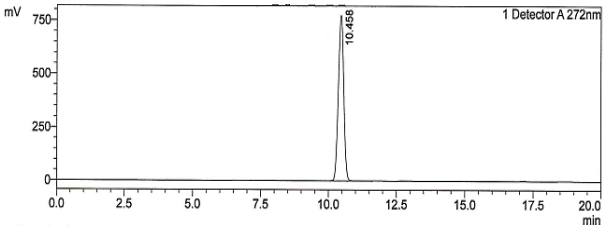

Fig. 2. Chromatogram of coumarin quantification analysis

The coumarin amounts determined using the method developed in HPLC are shown in Figure 3. When the results are examined, it is seen that the coumarin amount is low in all three plants. The highest coumarin amount, 0.033887 mg/mL, was obtained from the *Helichrysum arenarium* plant extracted with methanol solvent. Coumarin is a moderately polar compound. Moderately polar solvents, such as ethanol, dissolve these compounds more effectively than deionized water does. While the overall extraction efficiency with deionized water is high, the solubility of certain compounds, such as coumarin, may vary depending on the solvent used.

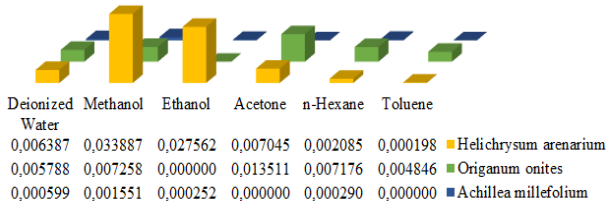

Fig. 3. HPLC results - concentration in coumarin equivalents (mg/mL)

CONCLUSION

In this study, the quantification analysis of coumarin in *Helichrysum arenarium*, *Origanum onites* and *Achillea millefolium* plants, which are used in many medicinal treatments, was carried out

by HPLC and the developed method was validated. The linearity range of the method was found to be 0.02 g/L-0.15 g/L. The R^2 value of the method linearity data was found to be 0.992. As a result, the developed method and the obtained quantitative data provide an analytical approach that will contribute to the quality control processes of similar herbal products.

Furthermore, data obtained by traditional Soxhlet extraction in the presence of different solvents clearly demonstrate the effect of solvent's polarity on extraction efficiency. Pure polar solvents, in particular, were the most effective extraction medium for all three plants studied. In this context, environmentally friendly, non-toxic, economical solvents such as deionized water are notable for their environmental sustainability and high extraction efficiency. Combining traditional yet effective methods, such as Soxhlet extraction, with these solvents is an approach that aligns with green chemistry principles.

Acknowledgement: *The present study was supported by Yildiz Technical University Scientific Research Projects Coordination Unit (Project No: FDK-2023-5966).*

REFERENCES

1. G. Tiring, S. Satar, O. Özkaya, *Bursa Uludag Üniv. Ziraat Fak. Derg.*, **35**, 203 (2021).
2. A. Ekalu, J.D. Habila, *Beni-Suef University Journal of Basic and Applied Sciences*, **9**, 45 (2020).
3. M. Li, M. Qian, Q.Jiang, B.Tan, Y. Yin, X. Han, *Antioxidants (Basel)*, **12**, 527 (2023).
4. G. Karadağ, A.D. Karaman, S. Öğüt, *JFNG*, **1**, 77 (2022).
5. N. Şen, G. Kalaycı, *Selcuk University Journal of Science Faculty*, **42**, 226 (2016).
6. M. Molnar, I. Jerković, D. Suknović, R. Bilić, B. Aladić, K. Šubarić, D. Jokić, *Molecules*, **22**, 348 (2017).
7. O.M. Tsivileva, O.V. Koftin, N.V. Evseeva, *Antibiotics (Basel)*, **11**, 1156 (2022).
8. C. Dong-Wei, Z. Yuan, D. Xiao-Yi, Z. Yu, L. Guo-Hui, F. Xue-Song, *Crit. Rev. Ana.l Chem.*, **51**, 503 (2021).
9. S.C. Heghes, O. Vostinaru, C. Mogosan, D. Miere, C.A. Iuga, L. Filip, *Front Pharmacol,*, **13**, 803338 (2022).
10. A. İnci, Ş. Saleh, K.K. Kırbağ, S. Güven, *TJST*, **18**, 345 (2023).
11. H. Majeed, T. Iftikhar, S.S. Zahra, M. Waheed, M. Niaz, S. Bashir, F. Altaf, A.A. AL-Huqail, *Essentials of Medicinal and Aromatic Crops*, 311 (2023).
12. B. Farasati Far, G. Behzad, H. Khalili, *Heliyon*, **9**, e22841 (2023).
13. X. Lin, L. Wu, X. Wang, L. Yao, L. Wang, *Journal of Applied Research on Medicinal and Aromatic Plants*, **20**, 100284 (2021).
14. N.B. Vetskov, I.S. Hinkov, K.V. Petkova-Parlapanska, E.D. Georgieva, G.D. Nikolova, Y.D. Karamalakova, *Bulg. Chem. Commun.*, **56**, 19 (2024).
15. M.J. Scotter, D.P.T. Roberts, G.O. Rees, *Anal. Methods*, **3**, 414 (2011).

Bulgarian Chemical Communications, Volume 57, Issue 3 (pp. 206-212) 2025 DOI: 10.34049/bcc.57.3.PJ-RS

Unraveling the mechanism of ruthenium (III)-catalyzed aspirin oxidation by hexacyanoferrate(III): kinetic and spectrophotometric approach

B. Gupta[1], Nikita[2], A. Rolaniya[2], A. Yadav[2], P. Jain[3], R. Sailani[2]*

[1]*Public health Lab Analyst, Technical Manager for NABL Accreditation, Food Safety and Standards Laboratory, Alwar, Rajasthan, India*

[2]*Chemical Kinetics Laboratory, Department of Chemistry, University of Rajasthan, Jaipur, Rajasthan, Indıa-302004*
[3]*Department of Chemistry, IIS-Deemed to be University, Jaipur, Rajasthan, India-302004*

Accepted: August 17, 2025

The redox reaction between aspirin and hexacyanoferrate (III), catalyzed by ruthenium (III) in alkaline medium, was thoroughly investigated. The reaction kinetics exhibit a complex dependence on both hydroxide ion and aspirin concentrations, while the reaction order with respect to the oxidant and catalyst is found to be unity. Based on the kinetic results, a plausible reaction mechanism was proposed, and the derived rate law successfully accounts for all experimental observations. Kinetic parameters were evaluated under varying conditions, and activation as well as thermodynamic parameters were accurately determined using the Arrhenius and Eyring equations.

Keywords: Aspirin; hexacyanoferrate (III); ruthenium (III); oxidation kinetics, reaction mechanism.

INTRODUCTION

Aspirin is acetyl salicylic acid and is an important drug with wide applications. It is a nonsteroidal analgesic,antiinflammatory and antipyretic agent which is used in large number of diseases such as headache, arthralgia cases where mild analgesic treatment is required. A number of methods of its determination are suggested in the literature. It is a well-known non-selective COX (cyclooxygenase) inhibitor [1], but its medical use may be associated with a variety of side effects [2–7]. Formerly, the oxidation of aspirin with a number of oxidants like potassium bromate [8], N-bromoacetamide [9], N-bromosuccinimide [10] was studied in several works.

Hexacyanoferrate (III) (HCF (III)) serves as a one-electron oxidant with a redox potential of 0.36 V, functioning as a proton or electron abstracting reagent in oxidation reactions [11, 12]. A plethora of redox reactions, involving compounds such as paracetamol, sulfanilic acid, crotyl alcohol, formazans, and ascorbic acid, have been conducted in alkaline media, both with and without catalysts. HCF (III) finds application in the oxidimetric determination of organic and inorganic compounds in both acidic and alkaline environments. Although its utilization in acidic media is limited due to complexation between the oxidized and reduced products of HCF (III), reactions in alkaline media exhibit reduced susceptibility to this complication. However, they generally suffer from slower kinetics attributed to the reduced oxidation potential of the $[Fe(CN)_6]^{3-}$/ $[Fe(CN)_6]^{4-}$ redox couple [13].

It has a number of applications in organic chemistry for synthesis [14-17] of newer organic compounds. The reagent attacks the substrate in one equivalent step producing a free radical [18, 19]. Such a free radical has several options such as attack by the oxidant, dimerization or polymerization, etc. The product hexacyanoferrate(II) is transparent to photo light, therefore, hexacyanoferrate(III) can be estimated spectrophotometrically [20] in the reaction system to monitor the kinetics of any reaction provided the reactants and products are colorless or do not exhibit any absorbance in the visible region. Additionally, in the presence of light, Fe $(CN)_6^{3-}$ ions hydrolyze gradually in acidic aqueous solutions, forming hydroxy- or aquo-penta cyanoferrate (III) complexes. This hydrolysis may lead to a shift in solution pH, particularly in neutral, unbuffered media.

To mitigate this challenge, various transition metal ions have been employed as catalysts in alkaline media, including osmium (VIII) [21-23], ruthenium (III) [24-26], (IV) [27], (VI) [28], and (VIII) [29], rhodium (III) [30], iridium (III) [31, 32], palladium (II) [33, 34], and molybdenum (IV) [35, 36].

Ru (III) acts as a catalyst in the oxidation of many organic and inorganic substrates [37, 38]. The production of many intermediary complexes and distinct oxidation states of ruthenium (III) might make the catalyzed mechanism extremely complex.

* To whom all correspondence should be sent:
E-mail: *l.p_riya@yahoo.co.in*

Although catalysis by transition metal ions depends on the nature of the substrate, oxidant, and experimental conditions, it has been reported that metal ions act as catalysts [39, 40] by one of several different paths, such as formation of complexes with reactants, oxidation of the substrate itself or through the formation of free radicals. Ruthenium (III) chloride has been used in several redox reactions particularly in acidic medium [41-43] as it is known to be an efficient, non-toxic and homogeneous catalyst.

Investigating the complexation events and reactivity patterns between aspirin and oxidants under varied reaction settings, as well as connecting kinetic concepts with thermodynamic viewpoints, are the main goals of this work. When comparing the characteristics of a variety of frequently observed reactions and deciphering reaction mechanisms, these metrics are essential.

EXPERIMENTAL

Materials and methods

Aspirin was used exactly as prescribed, with no additional care. Double-distilled water was used to make an aspirin stock solution kept at room temperature. In this investigation, AnalaR grade reaction components were used. The necessary amount of hexacyanoferrate (III) and ruthenium (III) chloride was dissolved in double-distilled water to create the solutions. The oxidant and catalyst solution was maintained in a black painted bottle and kept in a refrigerator at ~5 ˚C.

Kinetic procedure

Until otherwise noted, the reactions were carried out in glass stoppered Erlenmeyer flasks that were suspended in a water bath thermostated at ±0.1 °C and had a black coating on the outside. The time of initiation was recorded when half of the pipette's contents were discharged into the reaction mixture. The reactions were started by adding temperature-equilibrated solutions of hexacyanoferrate (III). An aliquot (5 cm^3) of the reaction mixture was periodically removed to observe the kinetics spectrophotometrically [42] at λ_{max} 420 nm (ε=1020 dm^3 mol^{-1} cm^{-1}) after the reaction mixture had been well agitated. In triplicate, the results were shown to be reproducible within ± 5 %.

Stoichiometry

The excess of HCF(III) over aspirin was used to study the reaction's stoichiometry. After completion, the reaction shows that four moles of HCF(III) are needed for every mole of aspirin. The quinone form is also confirmed by the color signal, therefore the reaction's stoichiometry matches the one shown in the following scheme:

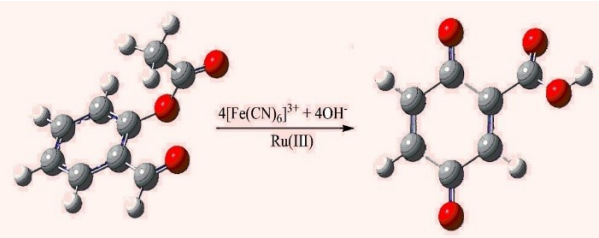

RESULTS AND DISCUSSION

Hexacyanoferrate(III) concentration dependence

While maintaining constant concentrations of the other reaction ingredients, namely aspirin [ASP] = 1.0×10^{-2} mol dm^{-3} and [Ru(III)] = 1.0×10^{-4} mol dm^{-3} at 45 °C under pseudo first order conditions, the concentration of hexacyanoferrate(III) [HCF(III)] was varied from 3.0×10^{-4} to 10.0×10^{-4} mol dm^{-3} at two fixed concentrations of [OH^-] = 0.05 and 0.075 mol dm^{-3}, respectively. Log [HCF(III)]t *vs* time was plotted in pseudo first order, and pseudo first order rate constants k (s^{-1}) were computed. The conforming order with regard to the oxidant was determined to be one, and the first order rate constants were found to be independent of the gross starting concentrations of HCF(III) (Fig.1).

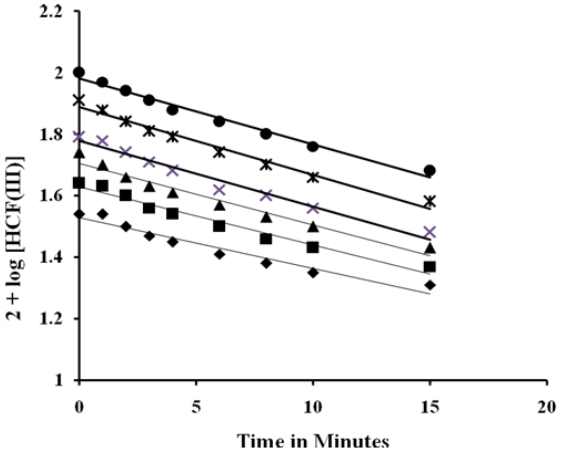

Fig. 1. Pseudo first order plots of HCF(III). [HCF(III)] = (1) ♦ 3.0×10^{-4}; (2) ■ 4.0×10^{-4}; (3) ▲ 5.0×10^{-4}; (4) × 6.0×10^{-4}; (5) ✳ 8.0×10^{-4}; (6) ● 10.0×10^{-4}; [ASP] = 1.0×10^{-2} mol dm^{-3}; [OH^-] = 0.05 mol dm^{-3} ; [Ru(III) = 1.0×10^{-4} mol dm^{-3}; 45 °C

Aspirin dependence

At four different temperatures (35, 40, 45, and 50 °C, respectively) and with constant concentrations of the remaining reaction ingredients ([HCF(III)] = 5.0×10^{-4} mol dm^{-3}; [OH^-] = 0.075 mol dm^{-3}; and [Ru (III)] = 1.0×10^{-4} mol dm^{-3}), the aspirin concentration was adjusted from 1.0×10^{-3} to 1.0×10^{-2} mol dm^{-3} (Fig. 2). Plots of pseudo first order were created. Plotting the

pseudo first order rate constant *vs* [ASP] shows that at lower aspirin concentrations, the order is one; at higher aspirin concentrations, however, the rate tends to a limiting value. Such a pattern of aspirin concentration change suggests that the aspirin order is complicated. Additional tests were carried out at two additional hydroxide ion concentrations, 0.05 and 0.1 mol dm^{-3}, to confirm this.

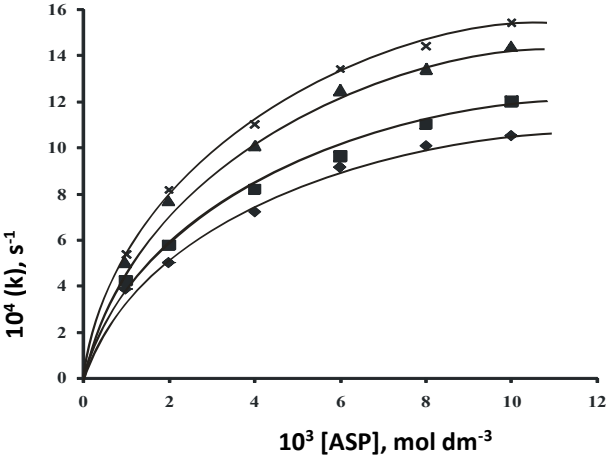

Fig. 2. Variation of aspirin at different temperatures. [HCF(III)] = 5.0×10^{-4} mol dm^{-3}; [OH^-] = 0.075 mol dm^{-3}; [Ru(III)] = 1.0×10^{-4} mol dm^{-3} Temperature ♦ 35, ■40, ▲45 and × 50 °C

Ru (III) dependence

At a given concentration of other reaction components, such as [HCF(III)] = 5.0×10^{-4} mol dm^{-3}, [ASP] = 1.0×10^{-2} mol dm^{-3}, and [OH^-] = 0.05 mol dm^{-3} at 45 °C, the concentration of [Ru (III)] was changed from 1.0×10^{-5} to 8.0×10^{-5} mol dm^{-3}. The rate rises as the concentration of [Ru (III)] increases. A straight line through the origin of a plot of the pseudo first order rate constant *v/s* [Ru (III)] showed first order dependency on the catalyst. Further confirmation of this dependence was obtained at [OH^-] = 0.075 mol dm^{-3}.

Hydroxıde ıon dependence

With the concentrations of the other reaction ingredients, namely [ASP] = 1.0×10^{-2} mol dm^{-3}, [Ru (III)] = 1.0×10^{-4} mol dm^{-3}, [I] = 0.1 mol dm^{-3}, and [HCF(III)] = 5.0×10^{-4} mol dm^{-3}, held constant, the concentration of the hydroxide ion was adjusted from 4.0×10^{-2} mol dm^{-3} to 10.0×10^{-2} mol dm^{-3} at 45 °C (ionic strength was maintained by employing sodium nitrate). The rate first rises as the hydroxide ion concentration increases, but at higher hydroxide ion concentrations, it reaches a limiting value. By conducting the reaction at two additional temperatures, such as 40 and 50 °C, respectively, this was further verified. This demonstrates how the rate changes intricately with the concentration of hydroxide ions.

Effect of ıonıc strength (ı)

By altering the concentration of $NaNO_3$ while maintaining constant concentrations of the other reaction ingredients; [ASP] = 1.0×10^{-2} mol dm^{-3}, [OH^-] = 0.075 mol dm^{-3}, [Ru (III)] = 1.0×10^{-4} mol dm^{-3}, and [HCF(III)] = 5.0×10^{-4} mol dm^{-3} at 45 °C; the impact of ionic strength was investigated. As the concentration of $NaNO_3$ rises, so does the rate.

Effect of temperature

While maintaining constant concentrations of the other reaction ingredients, namely [HCF(III)] = 5.0×10^{-4} mol dm^{-3}, [Ru (III)] = 1.0×10^{-4} mol dm^{-2}, and [I] = 0.075 mol dm^{-3}, the impact of temperature on the pace of reaction was also investigated at 35, 40, 45, and 50 °C, respectively. The Eyring equation {ln k/T v/s 1/T} was utilized to assess the activation characteristics, including energy and entropy of activation. According to the calculations, the activation energy was 15.7 ± 0.06 kJ mol^{-1} and the entropy was -171.98 ± 0.22 JK^{-1} mol^{-1}.

Test of free radıcals

Free radicals were tested by adding acrylic acid monomer into the reaction mixture, no white ppt was observed for a longer time. A free radical should be formed in view of one equivalent nature of the oxidant. It appears that the radical is formed in the solvent cage and immediately reacts without diffusing out of the cage to interact with the monomer. Probably, it is this reason that the monomer is not polymerised and no visible polymer was obtained.

Effect of hexacyanoferrate (ıı)

HCF(II), one of the reaction products, is without any effect on the rate of the reaction and even after three half-lives does not indicate deviations from first order. Also, addition of hexacyanoferrate(II) does not indicate any effect, such as observation is important in light of the fact that any equilibrium involving HCF(II) preceding the rate determining step is not involved.

Mechanısm of oxıdatıon

The catalyst $RuCl_3$ (1×10^{-5} mol dm^{-3}) in the range of (1×10^{-3} - 1×10^{-4}) mol dm^{-3} exhibits [44, 45] various types of hydroxo-aquo ruthenium (III) chloride complexes governed by equilibria (1) to (3) as follows:

$$[Ru(H_2O)_6^{3+}] + OH^- \overset{K_1}{\rightleftharpoons} [Ru(H_2O)_5OH]^{2+} \quad (1)$$

$$[Ru(H_2O)_5OH]^{2+} + OH^- \underset{}{\overset{K_2}{\rightleftharpoons}} [Ru(H_2O)_4(OH)_2]^+ \quad (2)$$

$$[Ru(H_2O)_4(OH)_2]^+ + OH^- \underset{}{\overset{K_3}{\rightleftharpoons}} [Ru(H_2O)_3(OH)_3] \quad (3)$$

Hence, no evidence for an oxo-bridged complex between catalyst and substrate was observed kinetically to account for complex dependence of the substrate and hydroxide ion respectively.

The hydroxide ion concentration range employed in the reaction (< 10^{-2} mol dm^{-3}) ascribes the reactive form of [Ru $(H_2O)_6^{3+}$] to be [Ru $(H_2O)_5OH]^{2+}$. Thus, considering Fe $(CN)_6^{3-}$, ASP (ASP has been written heretofore for aspirin and [Ru $(H_2O)_5OH]^{2+}$ to be the reactive forms of hexacyanoferrate (III), aspirin and ruthenium (III) chloride respectively, the following reaction mechanism can be proposed.

$$Ru^{III}(H_2O)_6]^{3+} + OH^- \underset{}{\overset{K_1}{\rightleftharpoons}} [Ru^{III}(H_2O)_5OH]^{2+} + H_2O \quad (4)$$

$$Ru^{III}(H_2O)_5OH]^{2+} + ASP \underset{}{\overset{K_2'}{\rightleftharpoons}} [Ru^{III}(H_2O)_5OH.ASP]^{2+} \quad (5)$$

$$[Ru^{III}(H_2O)_5OH.ASP]^{2+} + Fe(CN)_6^{3-} \xrightarrow[k]{Slow} [Ru^{IV}(H_2O)_5OH.ASP]^{3+} + Fe(CN)_6^{4-} \quad (6)$$

$$Ru^{IV}(H_2O)_5OH.ASP]^{3+} + Fe(CN)_6^{3-} \xrightarrow{Fast} [Ru^{V}(H_2O)_5OH.ASP]^{4+} + Fe(CN)_6^{4-} \quad (7)$$

$$Ru^{V}(H_2O)_5OH.ASP]^{4+} \xrightarrow{Fast} Int. + [Ru^{III}(H_2O)OH]^{2+}$$

$$Int. + 2Fe(CN)_6^{3-} \longrightarrow Products + 2Fe(CN)_6^{4-} \quad (8)$$

Such a mechanism leads to the rate law (9):

$$\frac{-d[Fe(CN)_6^{3-}]}{dt} = \frac{kK_1K_2'[Fe(CN)_6^{3-}][Ru(H_2O)_6^{3+}][ASP][OH^-]}{1+K_1[OH^-]+K_1K_2'[OH^-][ASP]} \quad (9)$$

where [$Fe(CN)_6^{3-}$] and [$Ru^{(III)}$] are the gross analytical concentrations of hexacyanoferrate(III) and ruthenium(III) respectively. [ASP] is the free equilibrium concentration of aspirin.

The rate law (9) is re-written as (10):

$$k' = \frac{kK_1K_2'[ASP][OH^-]}{1+K_1[OH^-]+K_1K_2'[ASP][OH^-]} \quad (10)$$

where k′ is an observed second order rate constant. The double reciprocal of eqn (10) yields eqn (11)

$$1/k' = \frac{(1+K_1[OH^-])}{kK_1K_2'[ASP][OH^-]} + \frac{K_1K_2'[ASP][OH^-]}{kK_1K_2'[ASP][OH^-]}$$

$$= \frac{(1+K_1[OH^-])}{kK_1K_2'[ASP][OH^-]} + \frac{1}{k} \quad (11)$$

A plot of 1/k′ *versus* 1/[ASP] was made from eqn (11) that yielded a straight line with non-zero intercept (Fig. 3). The slope of the line is given by eqn (12):

$$Slope = \frac{1+K_1[OH^-]}{kK_1K_2'[OH^-]} = \frac{1}{kK_1K_2'[OH^-]} + \frac{K_1[OH^-]}{kK_1K_2'[OH^-]}$$

$$= \frac{1}{kK_1K_2'[OH]} + \frac{1}{kK_2'} \quad (12)$$

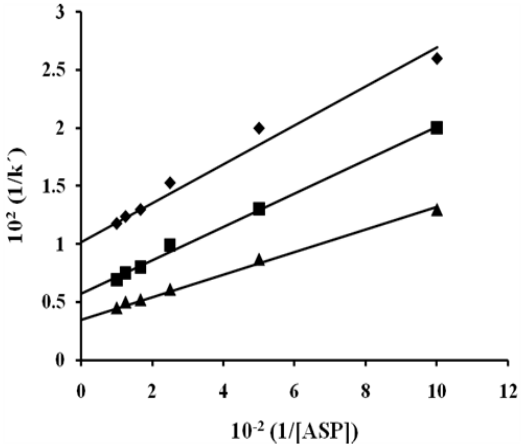

Fig. 3. Plot of 1/k′ versus 1/[ASP].
[HCF(III)] = 5.0 × 10^{-4} mol dm^{-3}; [Ru(III)] = 1.0 × 10^{-4} mol dm^{-3}; [OH^-] = ♦ 0.05, ■ 0.075, ▲ 0.1 mol dm^{-3} and 45 °C

A further plot of slope *versus* $[OH^-]^{-1}$ was made from eqn (12) that also yielded a straight line with non-zero intercept (Fig. 4).

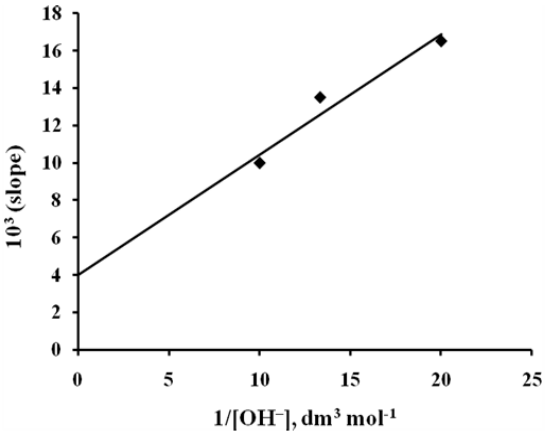

Fig. 4. Plot of slope *versus* 1/[OH^-].
[HCF(III)] = 5.0 × 10^{-4} mol dm^{-3}; [ASP] = 1.0×10^{-3} - 1.0×10^{-2} dm^{-3}; [Ru(III)] = 1.0 × 10^{-4} mol dm^{-3} and 45 °C

At 45 °C, 'K_1' was determined to be 6.15 based on the intercept-to-slope ratio. Using 'k' determined from Fig. 3, K_2' was computed from the intercept to be 25.51, 14.25, and 8.75 dm^3 mol^{-1} s^{-1} at I=0.05, 0.075, and 0.1 mol dm^{-3}, respectively. A plot of $(k')^-$

^{1} *vs* $(ASP)^{-1}$ at various temperatures, such as 14.28, 16.13, 17.86, and 20.0 s^{-1} at 35, 40, 45, and 50 °C, respectively, was used to compute 'k' from Fig. 5. I = 0.075 mol dm^{-3} was also used.

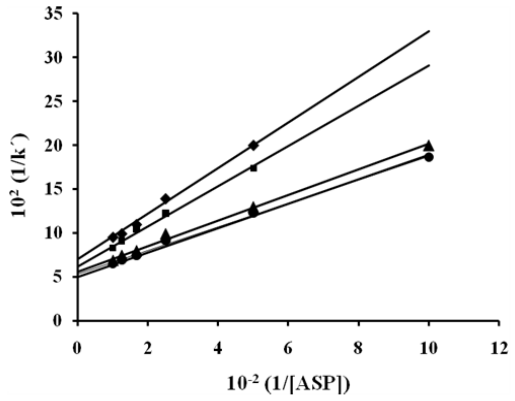

Fig. 5. Plot of 1/k′ *versus* 1/[ASP].
[HCF(III)] = 5.0 × 10^{-4} mol dm^{-3}; [Ru(III)] = 1.0 × 10^{-4} mol dm^{-3}; $[OH^{-}]$ = 0.075 mol dm^{-3} Temperatures = ♦ 35, ■ 40, ▲ 45 and ● 50 °C

The energy and entropy of activation employing rate constant (k_1) for the rate determining step to be 15.7±0.06 kJ mol^{-1} and -171.98±0.22JK^{-1} mol^{-1} respectively employing Eyring equation.

Thus, in the light of the mechanism proposed for the title reaction that accounts for all experimental observations, the reaction scheme-I can be suggested for the transfer of electrons from the substrate to the oxidant.

Not much is known about alkaline chemistry of aspirin. The likely species of this reagent is in anionic form in alkaline medium. The rate depends upon hydroxide ion concentration in a complex manner. This shows that hydroxide ion is also involved in activated complex along with aspirin and hexacyanoferrate (III). The reaction is catalyzed by ruthenium (III) chloride. So far, there is no report of any reaction between Fe $(CN)_6^{3-}$ and hydroxide ion, the involvement of the latter in the activated complex appears through the reactive form of the catalyst. The kinetic order with respect to the oxidant is one whereas a complex order is indicated by the substrate.

K^{+} and [Fe $(CN)_6^{3-}$] ion pairing is reported [46] earlier but no such ion pairing is known in case of Na^{+} and Fe $(CN)_6^{3-}$. Probably it is due to the fact that ion association decreases with increasing size of the cation [47]. Since a large concentration of sodium ions is present in the reaction system, the probability of ion-pairing between Na^{+} and [Fe $(CN)_6^{3-}$] cannot be completely ruled out. The rate of the reaction increases with increasing ionic strength, such an increase in rate cannot be assigned to interaction of unlike charged species in the rate controlling step of the reaction mechanism despite ion association of [Fe $(CN)_6^{3-}$] and Na^{+}. However, an increase in rate owing to ionic strength for six-fold variation increases rate by almost two-fold.

The variation in ionic strength does not hold good for Davies equation [48], an increase in rate with increasing ionic strength cannot be inferred even qualitatively as the reaction is between differently charged species. If it is assumed that the ion-pair such as Na^{+} $[Fe(CN)_6]^{3-}$ is more reactive than simple ionic species such as [Fe $(CN)_6^{3-}$], such a small increase in rate due to large ionic strength can be accounted for decrease in electrostatic repulsion. Specific ionic effects [49] are simply found in the presence of large concentrations of the cations, it appears that such a tendency in the title reaction is either marked by the rate dependence on hydroxide ion concentration or is absent at all.

CONCLUSION

According to the kinetic data, the order with regard to the oxidant and the catalyst, respectively, is one, whereas the reaction kinetics show a complicated dependence of the hydroxide ion and aspirin. The reaction's stoichiometry is 1:4, meaning that four moles of HCF (III) are needed for every mole of substrate. In conclusion, we believe that the likelihood of an intermediate complex forming between the oxidant and the substrate is minimal, at least when considering substitutionally inert HCF (III) under milder circumstances used in our studies. Additionally, the complexation between the catalyst and the substrate makes sense because it implies that product HCF (II) has no influence. This is significant because there is no equilibrium involving HCF(II) prior to the rate-determining step.

Acknowledgement: *R. Sailani expresses gratitude to the Department of Chemistry at the University of Rajasthan in Jaipur, Rajasthan, India, as well as her co-authors. The University Grant Commission in New Delhi, India, provided financial assistance for this work in part through the JRF. This paper is dedicated by the author, R. Sailani, to Prof. (Late) P. D. Sharma of the Chemistry Department of the University of Rajasthan in Jaipur, India*

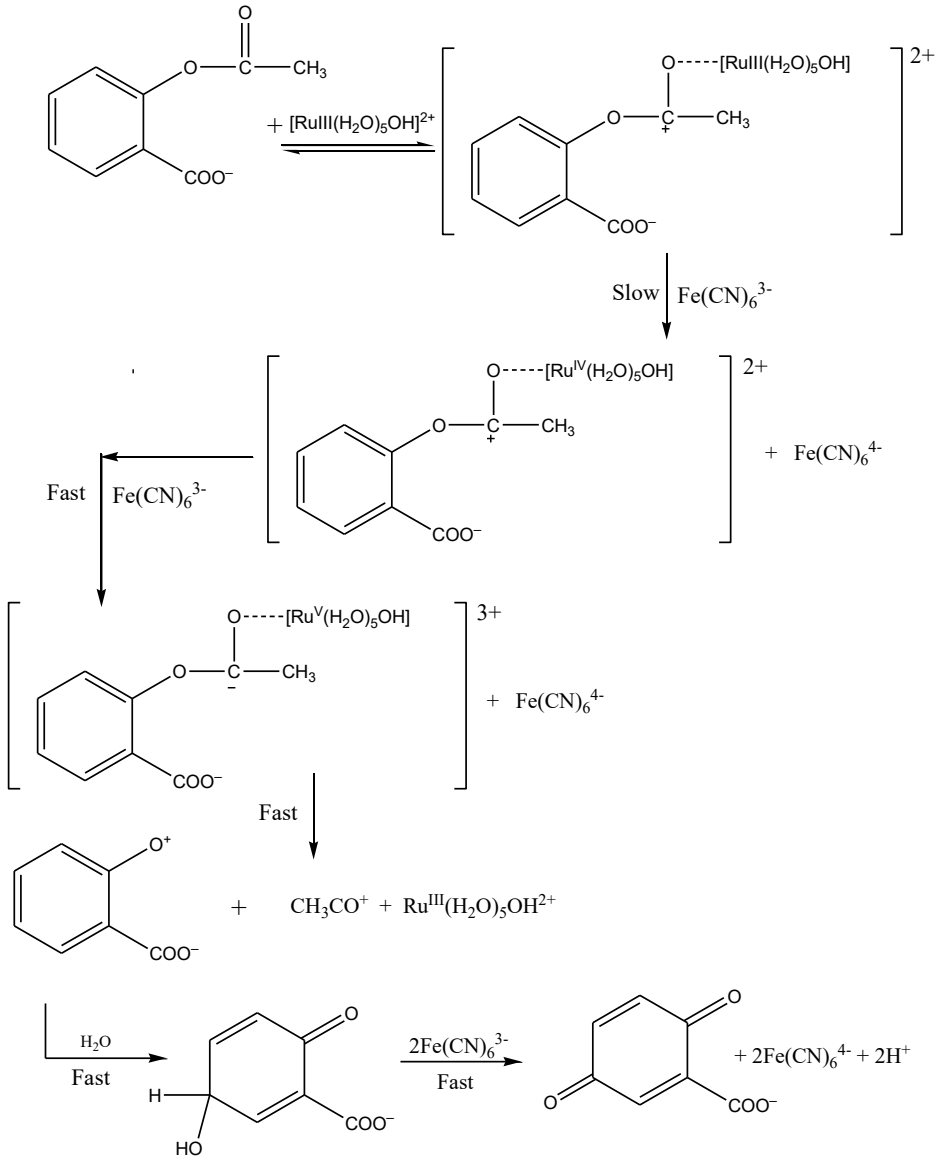

$$CH_3CO^+ + H_2O \xrightarrow{\text{Fast}} CH_3COOH + H^+$$
$$CH_3COOH + OH^- \xrightarrow{\text{Fast}} CH_3COO^- + H_2O$$
$$2H^+ + 2OH^- \xrightarrow{\text{Fast}} 2H_2O$$

Scheme I

REFERENCES

1. T. O. Cheng, *Texas Heart Inst. J.,* **34**, 392 (2007).
2. S. H. Ferreira, S. Moncada and J. R. Vane, *Braz. J. Pharmacol.*, **49**, 86 (1973).
3. H. D. Lewis, J. W. Davis, D. G. Archibald, W. E. Steinke, T. C. Smitherman, J. E. Doherty, H. W. Schnaper, M. M.LeWinter, E. Linares, J. M. Pouget, S. C. Sabharwal, E. Chesler, H. DeMots, *New Eng. J. Med.,* **309,** 396 (1983).
4. C. N. Floyd and A. Ferro, *Pharmacol. Ther.,* **141**, 69 (2014).
5. C. F. Gerhardt, *Justus Liebigs Annalen Chemie,* **87**, 149 (1853).
6. Chemical Heritage Foundation. http://www.chemheritage.org/discover/online-resources/chemistry-history/themes/pharmaceuticals/relievingsymptoms/hoffmann.aspx. Accessed 2014.
7. K. Trnavsky, M. Zachar, *Agents and Actions,* **5**, 549 (1975).
8. S. Srivastava, S. Singh, *Oxidn. Commun.*, **27**, 463 (2004).
9. A. K. Singh, A. Singh, R. Gupta, M. Saxena, B. Singh, *Trans. Met. Chem.*, **17**, 413 (1992).
10. S. Mavalang, K. Nirmal, N. Halligudi, S. T. Nandibewoor, *React. Kinet. Catal. Lett.,* **27**, 391 (2001).

11. A. I. Vovk, I. V. Muraveva, V. P. Kukhar, V. F. Baklan, *Russ. J. Gen. Chem.,* **70** 1108 (2000).
12. P.T. Speakman, W. A. Waters, *J. Chem. Soc.,* 40 (1955).
13. M. Sharma, G. Sharma, B. Agarwal, C.L. Khandelwal, P.D. Sharma, *Trans. Mat. Chem.*, **30,** 546 (2005).
14. S.K. Rajput, A. Sharma, K.N. Bapat, *Acta Ciencia Indica*, **34,** 115 (2008).
15. J.M. Leal, P.L. Domingo, B. Garcia, S. Ibeas, *J. Chem. Soc.*, *Faraday Trans.*, **89**, 3571 (1993).
16. V.N. Singh, M.C. Gangwar, B.B. Saxena, M.P. Singh, *Can. J. Chem*, **47,** 1051 (1969).
17. V.N. Sigh, M.P. Singh, B.B. Saxena, *Ind. J. Chem.*, **8**, 529 (1970).
18. M. Martinez, M. Pitarque, R.V. Eldik, *J. Chem. Soc. Dalton Trans.*, 2665 (1996).
19. E.P. Kelson, P.P. Phengsy, *Int. J. Chem. Kinet.*, **32**, 760 (2000).
20. K. Wilson, J. Walker, *J. Practical Biochemistry*, 5th ed. Cambridge University Press, (2005).
21. S. A. Farokhi, S. T. Nandibewoor, *Catal. Lett.,* **129**, 207 (2009).
22. S. Dubey, N. Sharma, C. L. Khandelwal, *Trans. Met. Chem.,* **28**, 176 (2003).
23. P. Sharma, R. Sailani, A. Meena, C. L. Khandelwal, *J. Chem. Res.* **44**, 295 (2020).
24. R.M. Naik, A. Srivastava, A. K. Verma, *Turk. J. Chem.,* **32**, 495 (2008).
25. R. M. Mulla, G. C. Hiremath, S. T. Nandibewoor, *Monatsh. Fur. Chem.*, **135**, 1489 (2004).
26. A. Rolaniya, A. Yadav, P. Jain, R. Sailani, *ChemistrySelect,* **9**, e202303734 (2024).
27. E. P. Kelson, P. P. Phengy*, Int. J. Chem. Kinet.,* **32**, 760 (2000).
28. A. Mucients, F. J. Poblete, D. Rodriguez, *Int. J. Chem. Kinet.,* **31**, 1 (1999).
29. K.P. Tandon, A. K. Singh, R. Baboo, *Oxidn. Commun.,* **28**, 611 (2005).
30. B. Prasad, R. P. Singh, *Aryabhata. Res. J. Phy. Sci.,* **6**, 127 (2003).
31. S. K. Rajput, A. Sharma, K. N. Bapat, *Acta. Cien. Ind. Chem.,* **34**, 115 (2008).
32. A. Goel, R. Sharma, *J. Chem. Eng. Mat. Sci*., **31,** 1 (2012).
33. D. S. Rana and P. C. Mathur, *J. Ind. Coun. Chem.,* **10**, 33 (1994).
34. A. Fawzy, *J. Chem. Sci*., **128**, 247 (2016).
35. Ahmad, C. M. Ashraf, *Ind. J. Chem*., **17A**, 302 (1979).
36. J. C. Swarts, C. R. Dennis, S. B. Stephen, *Reac. Kinet. Mech. Catal.,* **137**, 1 (2023).
37. R. M. Naik, A. Srivastava, A. K. Verma, *Turk. J. Chem*., **32**, 495 (2008).
38. Mulla, R. M.; Hiremath, G. C. Nandibewoor, S. T. *Monatsh. Fur. Chem*., **135**, 1489 (2004).
39. S. A. Chimatadar, A. K. Kini S. T. Nandibewoor, *Bioinorg. React. Mech.,* **5(3)**, 231 (2005).
40. A. K. Singh, S. Rahmani, B. Singh, R. K. Singh M. Singh, *J. Phys. Org. Chem*., **17(3)**, 249 (2004).
41. P.A. Prashanth, S. Ananda, K. S. Rangappa M. N.Kumara, *J. Mol. Cat. A: Chem.*, **383**, 203 (2014).
42. A. A. P. Khan, A. Khan, A. M. Asiri A. K. Singh, *Int. J. Electrochem. Sci.*, **10(1)**, 759 (2015).
43. R. V. Nadh, B. S. Sundar P. S. Radhakrishnamurti, *Rus. J. Phys. Chem. A*, **90**, 1760 (2016).
44. A.E. Mucientes, F.J. Poblete, R.E. Gabaldon, A.M. Rodriguez F. Santiago, *J. Chem. Res.(s)*, **286**, 1324 (1998).
45. W. Bottcher, G.M. Brown and N. Sutin, *Inorg. Chem.*, **18**, 1447 (1979).
46. S. J. Paton C.H. Brubaker, *J. Inorg. Chem.*, **12**, 402 (1973).
47. D. Mohan, V.K. Chhabra Y.K. Gupta, *J. Chem. Soc., Dalton. Trans.*, 1737 (1975).
48. C.W. Davies, Ion Association, Butter Norths, London, 1962.
49. Y.A. Mazid K.E. Howlett., *J. Chem. Soc.(A),* 679 (1968)

Bulgarian Chemical Communications, Volume 57, Issue 3 (pp. 213-217) 2025 DOI: 10.34049/bcc.57.3.ZO-AK

Freeze-drying of squid: a study to investigate the effect of different pre-treatments

Z. O. Ozyalcin, A. S. Kipcak*

Department of Chemical Engineering, Faculty of Chemical and Metallurgical Engineering, Yildiz Technical University, Istanbul, Türkiye

Accepted: August 17, 2025

Among food preservation methods, freeze-drying is the method that preserves nutritional and sensory qualities the most. This study investigated the freeze-drying kinetics of differently pretreated squid samples and their compatibility with mathematical models. Fresh squid samples were sliced into strips, subjected to eight pretreatments including blanching, blanching with salt, and osmotic dehydration at different salt concentrations, and then freeze-dried. Drying times were between 420 - 600 min and pretreatments were found to be effective in decreasing drying time and final moisture content. Effective moisture diffusivity values were calculated between 4.74×10^{-10} - 2.41×10^{-10}. In the compatibility tests of the drying data with the mathematical models, the control samples had an R^2 value of 0.999997 with Two-term, while all pretreated samples fit the Alibas model with R^2 values higher than 0.99999.

Keywords: Blanching; Freeze-drying; Mathematical modeling; Osmotic dehydration; Squid

INTRODUCTION

Freeze-drying, or lyophilization, is widely acknowledged as a superior method for preserving heat-sensitive food items. It operates at low temperatures, which helps in retaining the nutritional quality of moisture-rich foods like seafood. This method prevents the thermal degradation of sensitive nutrients, ensuring that seafood maintains its original nutritional profile. Freeze-drying causes less lipid oxidation compared to traditional drying methods like hot-air drying. This is crucial for seafood, which is rich in unsaturated fatty acids that are prone to oxidation. Lower lipid oxidation helps in maintaining the quality and extending the shelf life of seafood products [1, 2]. It also helps in preserving the sensory properties of color, texture, and flavor. This is particularly important for consumer acceptance and marketability [1-3].

Despite its benefits, the industrial application of freeze-drying in seafood processing is not widespread. This is due to the high costs and the need for specialized equipment. Various pretreatment methods have been explored to enhance the efficiency and quality of freeze-dried products. Blanching and osmotic dehydration (OD) are effective pretreatment methods that can significantly enhance the freeze-drying process [4, 5]. Blanching can reduce the drying time and energy consumption during freeze-drying. Also, it helps in retaining the physical and sensory qualities of the dried product, such as color, texture, and rehydration properties [6]. OD reduces the initial water content of the food, which shortens the subsequent freeze-drying time and improves energy efficiency. OD helps in maintaining the nutritional and sensory quality of the freeze-dried product [7, 8].

In the literature, there are freeze-drying studies of seafood such as shrimp, scallops, mussels, squid, shrimp, salmon [9-12]. However, very few of these studies examine the effect of pretreatment procedures before freeze-drying on the drying process. Squid is rich in essential nutrients, including high-quality protein, long-chain omega-3 fatty acids (DHA and EPA), vitamins (E, B12), and minerals (Na, K, Mg, P, Cu, Zn). Despite its low fat content, squid offers a favorable omega-3/omega-6 ratio, which is beneficial for heart health [13, 14]. This study aims to evaluate the drying characteristics of squid subjected to blanching, blanching in saltwater, and osmotic dehydration pretreatments and to determine the most suitable mathematical models for characterizing the freeze-drying behavior of both untreated and treated samples.

MATERIALS AND METHODS

Sample preparation

Squid was brought from a local fish market in Istanbul/Türkiye and stored at +4 ± 2 °C in a refrigerator (model 1050T; Arçelik, Eskişehir, Türkiye). For each experimental step, squid samples were sliced into 5.0 ± 0.15 g strips. Weights were

* To whom all correspondence should be sent:
E-mail: *skipcak@yildiz.edu.tr*

recorded using a digital balance (AS 220.R2, Radwag, Radom, Poland). Initial moisture content was determined in accordance with AOAC (2005) guidelines [15] by drying the samples for 4 h at 105 °C in a KH-45 hot air oven (Kenton, Guangzhou, China).

Drying experiments

Nine groups of squid samples (each 5.0 ± 0.15 g) were prepared under different pretreatment conditions. For blanching, samples were immersed in 100 mL of deionized water at 90 °C for 1 min (B – 1 min) or 5 min (B – 5 min). In the saltwater blanching treatment, squid were blanched in 10% (w/v) salt solutions at 90 °C for 1 min (B 10% – 1 min) and 5 min (B 10% – 5 min). Osmotic dehydration (OD) treatments involved immersing the samples in 10% and 20% (w/v) salt solutions at room temperature for 5 and 10 min each (OD 10% – 5 min, OD 10% – 10 min, OD 20% – 5 min, OD 20% – 10 min).

After pretreatments, excess surface moisture was removed, and samples were immediately transferred to a freeze dryer (Labart LFD-10N, ART Laborteknik, Istanbul, Türkiye). During the drying cycle, the vacuum was released every 60 min to allow samples to be weighed and photographed within 2 min, after which drying resumed. The process continued until the moisture content dropped below 5% of the dry matter, after which the samples were vacuum-sealed.

Mathematical modeling

Moisture transport during drying was evaluated using Fick's Second Law, which provides a theoretical basis for modeling diffusion-driven moisture migration. During the constant rate period, moisture removal primarily occurs from the surface; in the falling rate period, internal diffusion dominates [16, 17]. The moisture content (M, kg water/kg dry matter) and the dimensionless moisture ratio (MR) were calculated as in Eq. 1 [16].

$$M = \frac{m_w}{m_d} \quad (1)$$

where m_w denotes the water content (kg), and m_d denotes the dry matter content (kg). M_t is the moisture content at any moment, M_e is the equilibrium moisture content, M_0 is the initial moisture content (kg water/kg dry matter), and MR is the moisture ratio (dimensionless) [18]:

$$MR = \frac{M_t - M_e}{M_0 - M_e} \quad (2)$$

Drying data were analyzed using Statistica 8.0 (StatSoft, Tulsa, USA). The suitability of each model was initially assessed based on regression analysis. The coefficient of determination (R^2) was used to evaluate the model's accuracy, with values close to 1 indicating high correlation [18] (Eq. 3). Additional indicators such as chi-square (χ^2) and root mean square error (RMSE) were also used to evaluate model performance, with values closer to zero indicating better fit [19] (Eqs. 4, 5):

$$R^2 \equiv 1 - \frac{\sum_{i=1}^{N}\left(MR_{exp,i} - MR_{pre,i}\right)^2}{\sum_{i=1}^{N}\left(MR_{exp,i} - \left(\frac{1}{n}\right)\sum_{i=1}^{N} MR_{exp,i}\right)} \quad (3)$$

$$\chi^2 = \frac{\sum_{i=1}^{N}\left(MR_{exp,i} - MR_{pre,i}\right)^2}{N - z} \quad (4)$$

$$RMSE = \left(\frac{1}{N}\sum_{i=1}^{N}\left(MR_{exp,i} - MR_{pre,i}\right)^2\right)^{\frac{1}{2}} \quad (5)$$

where MR_{exp} and MR_{pre}, define experimental and predicted moisture ratio values. The variable N detones the total number of experiments conducted, while the variable z indicates the constant values utilized within the models.

Effective moisture diffusivity

Moisture transport during drying may occur at constant or falling rate periods, governed by complex mass transfer mechanisms. Fick's Second Law is commonly applied to estimate effective moisture diffusivity (D_{eff}) [20] (Eq. 6).

$$\frac{\partial M}{\partial t} = \nabla\left[D_{eff}(\nabla M)\right] \quad (6)$$

$$\ln(MR) = \ln\left(\frac{8}{\pi^2}\right) - \left(\pi^2 \frac{D_{eff} \times t}{4L^2}\right) \quad (7)$$

Eq. 7 represents Fick's diffusion model for unsteady-state conditions in a thin layer, assuming that moisture is removed by diffusion, shrinkage during drying is ignored, diffusion coefficients, temperature, and equivalent diameter are all constant [20]. L is the half thickness of the sample (m), and n was assumed to be 1 to simplify the calculation. D_{eff} was calculated from the slope of the linear portion of the ln(MR) *vs.* time graph.

Ten commonly used drying models were tested for their compatibility with experimental data, as summarized in Table 1.

Table 1. Mathematical model equations [21, 22]

Name of the model	Model equation
Aghbaslo *et al.*	$MR = exp\ (-k_1 t/(1 + k_2 t))$
Alibas	$MR = a.exp\ ((-kt^n) + bt) + g$
Jena and Das	$MR = a.exp\ (-kt + b\sqrt{t}) + c$
Lewis	$MR = exp\ (-kt)$
Logarithmic	$MR = a.exp\ (-kt) + c$
Midilli & Kucuk	$MR = a.exp\ (-kt^n) + bt$
Page	$MR = exp\ (-kt^n)$
Parabolic	$MR = a + bt + ct^2$
Wang and Singh	$MR = 1 + at + b\ t^2$
Two-term exponential	$MR = a.\ exp\ (-kt) + (1-a).\ exp\ (-kat)$

a, b, c, g - empirical constants; k, k_1, k_2 - drying rate constants; n - drying exponent; t - time (min).

RESULTS AND DISCUSSION

Table 2 presents the initial and final moisture contents, drying times, and wet basis moisture percentages for squid samples subjected to various pretreatment methods prior to freeze-drying. The results clearly demonstrate that both the type and duration of pretreatment significantly influence the moisture dynamics and drying efficiency of the squid.

Table 2. Drying data of squid

Sample	Initial moisture (kg W / kg DM)	Initial moisture (%)	Drying time (min)	Final moisture (kg W / kg DM)
Control	7.2337	87.85	600	0.6775
B – 1 min	6.4511	86.58	600	0.5490
B – 5 min	5.9741	85.66	540	0.2117
B 10% – 1 min	6.2253	86.16	600	0.3325
B 10% – 5 min	5.7723	85.23	420	0.2208
OD 10% – 5 min	5.7817	85.25	600	0.5080
OD 10% – 10 min	5.1766	83.81	600	0.3218
OD 20% – 5 min	4.6546	82.32	540	0.1874
OD 20% – 10 min	4.1296	80.51	480	0.1359

The control group which did not undergo any pretreatment, exhibited the highest initial moisture content (7.2337 kg W/kg dry matter) and also required the maximum drying time of 600 min to reach a final moisture content of 0.6775 kg water/kg dry matter. This highlights the necessity of pretreatment in accelerating drying and improving efficiency.

Blanching (B – 1 min and B – 5 min) resulted in reduced initial moisture contents compared to the control and substantially improved drying outcomes. Notably, B – 5 min achieved a final moisture content of 0.2117 kg water/kg dry matter in only 540 min, suggesting enhanced moisture removal and internal structure modification that facilitates drying.

Blanching in 10% salt solution (B 10%) demonstrated even more effective results. The B 10% – 5 min sample had one of the lowest initial moisture levels (5.7723 kg water/kg dry matter) and dried in only 420 min, with a final moisture content of just 0.2208 kg water/kg dry matter. This emphasizes the synergistic effect of heat and salt on cellular permeability and water loss.

Osmotic dehydration (OD) treatments showed a more gradual improvement. Samples treated with OD 10% maintained relatively high final moisture levels (0.5080 and 0.3218 kg water/kg dry matter) even after 600 min of drying. However, the OD 20% – 10 min sample showed the best performance among the OD groups, reducing the final moisture content to 0.1359 kg water/kg dry matter in only 480 min, suggesting that higher salt concentrations and longer durations promote better dehydration efficiency.

Figure 1 presents the drying curves of squid samples subjected to various pretreatment methods before freeze-drying. Across all treatments, a continuous decrease in moisture content over time was observed, reflecting the typical drying behavior of biological materials.

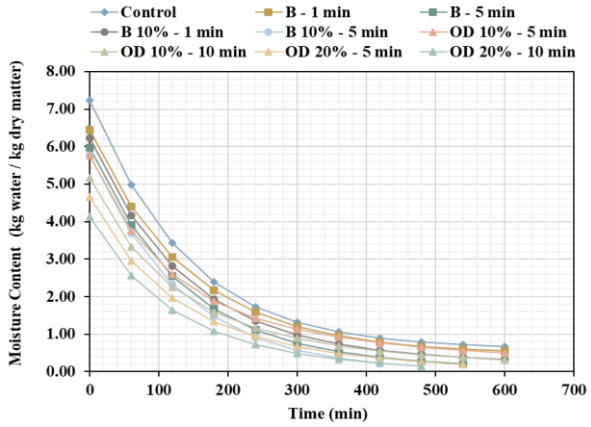

Figure 1. Moisture content *vs* drying rate graph of freeze-drying squid

Figure 2 illustrates the relationship between drying rate and moisture content, providing insight into the drying kinetics and mechanism. All curves show a distinct falling rate period, which is characteristic of freeze-drying.

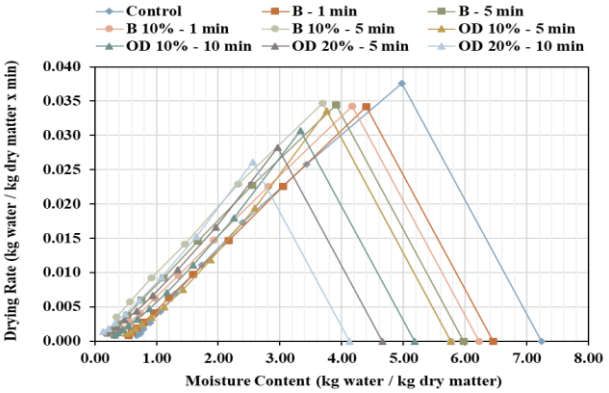

Figure 2. Drying rate *vs*. moisture content graph of freeze-drying squid

This indicates that moisture diffusion from the interior becomes the limiting step after surface moisture is removed. Table 3 demonstrates the best-fitted mathematical models with R^2 values over 0.9998.

Table 3. Mathematical model constants and statistical parameters of freeze-dried squid

S.	Model	R^2	χ^2	RMSE
Contr.	Two-term	0.9999970	0.0000010	0.0005430
	Midilli & Kucuk	0.9999276	0.0000120	0.0025802
	Aghbashlo *et al.*	0.9998512	0.0000176	0.0036992
B - 1 min	Alibas	0.9999992	0.0000001	0.0002499
	Log.	0.9999941	0.0012803	0.0305148
	Midilli & Kucuk	0.9999418	0.0000072	0.0021364
B - 5 min	Alibas	0.9999994	0.0000001	0.0002289
	Two-term	0.9999870	0.0000020	0.0010950
	Midilli & Kucuk	0.9999822	0.0000027	0.0012701
B % 10 - 1 min	Alibas	0.9999997	0.0000001	0.0001680
	Log.	0.9999937	0.0000007	0.0007288
	Midilli & Kucuk	0.9999662	0.0000045	0.0016838
B % 10 - 5 min	Alibas	0.9999957	0.0000011	0.0006543
	Two-term	0.9999850	0.0000030	0.0012310
	Jena & Das	0.9999951	0.0000010	0.0006950
OD % 10 - 5 min	Alibas	0.999997	0.0000001	0.000455
	Two-term	0.999985	0.000002	0.001061
	Aghbashlo *et al.*	0.999939	0.000006	0.002132
OD % 10 - 10 min	Aghbashlo *et al.*	0.999988	0.000001	0.000957
	Two-term	0.999987	0.000001	0.000984
	Midilli & Kucuk	0.999832	0.000019	0.003595
OD % 20 - 5 min	Alibas	0.999999	0.0000001	0.000208
	Two-term	0.999984	0.000002	0.001158
	Midilli & Kucuk	0.999910	0.000012	0.002758
OD % 20 - 10 min	Alibas	0.999998	0.0000001	0.000409
	Midilli & Kucuk	0.999938	0.000009	0.002378
	Log.	0.999905	0.000014	0.002933

Among the evaluated models, the Alibas model demonstrated consistently superior performance across almost all treatment conditions, with exceptionally high coefficients of determination (R^2) and the lowest χ^2 and RMSE values. Particularly in pretreated samples such as B - 5 min, B %10 - 1 min, and OD %20 - 5 min, the Alibas model achieved near-perfect fits (e.g., $R^2 > 0.999999$), indicating its remarkable capability in accurately describing the drying kinetics of squid during freeze-drying.

The Midilli & Kucuk model also performed well, especially in untreated (Control) and short-duration blanched samples (e.g., B - 1 min), though it generally presented slightly higher error metrics compared to Alibas. Nonetheless, it remained one of the more robust models, particularly in treatments involving mild osmotic dehydration and shorter blanching.

Interestingly, the Two-term model showed strong fitting accuracy in certain conditions like Control, B - 5 min, and OD %10 - 10 min, reflecting its adaptability to varying moisture migration patterns. However, in more intensive treatments (e.g., OD %20 - 10 min), its performance was surpassed by Alibas.

CONCLUSION

This study investigated the freeze-drying of squid with pretreatments of blanching, blanching in salt water, and osmotic dehydration. The drying experiments were conducted in 420 - 600 min. The pretreatments with longer durations and/or higher salt concentrations effectively reduced both the initial moisture load and the total drying time required to reach acceptable final moisture levels. Among all, B 10% – 5 min and OD 20% – 10 min stood out as the most efficient strategies in terms of drying performance. Among the mathematical models tested, the Alibas and Midilli & Kucuk models best described the drying kinetics. These findings reinforce the utility of pretreatments and suggest their broader application in seafood preservation technologies.

REFERENCES

1. D. Y. Li, D. Y. Zhou, F. W. Yin, X. P. Dong, H. K. Xie, Z. Y. Liu, F. Shahidi, *J. Sci. Food Agric.*, **100**, 2544 (2020).
2. D. Dziki, *Processes*, **8**, 1661 (2020).
3. V. Rajashree, S. K. S. Vijay, I. Muthuvel, S. G. G. Kavitha, A. Bharathi, M. Senthil Kumar, P. Rajiv, *Plant Sci. Today*, **11**, 5515 (2024).
4. K. Rybak, A. Wiktor, D. Witrowa-Rajchert, O. Parniakov, M. Nowacka, *Foods*, **10**, 226 (2021).
5. L. Li, M. Zhang, X. Song, W. Wang, B. Bhandari, *J. Sci. Food Agric.,* **99**, 6572 (2019).

6. T. Antal, L. Sikolya, B. Kerekes, *Prog. Agric. Eng. Sci*., **10**, 17 (2014).
7. R. M. Putri, M. A. F. Falah, *IOP Conf. Ser.: Earth Environ. Sci.*, **1200**, 012030 (2023).
8. S. Malakar, T. Manonmani, S. Deb, K. K. Dash, in Food Processing, CRC Press, 2021, p. 67.
9. Z. O. Ozyalcin, E. Güles, D. Uygunoz, F. Bozkurt, O. Sagdic, I. Doymaz, A. S. Kipcak, *TrJFAS*, **25**, 2 (2024).
10. S. Sevim, Z. O. Ozyalcin, A. S. Kipcak, *TrJFAS*, **23**, 12 (2023).
11. E. Midik, Z. O. Ozyalcin, A. S. Kipcak, *J. Chem. Technol.*, **33**, 136 (2025).
12. J. Liu, Y. Zhao, Q. Shi, X. Wu, Z. Fang, *J. Food Compos. Anal.,* **115**, 104966 (2023).
13. A. Torrinha, F. Gomes, M. Oliveira, R. Cruz, E. Mendes, C. Delerue-Matos, S. Morais, *Food Chem. Toxicol.,* **67**, 44 (2014).
14. Y. Deng, Y. Luo, Y. Wang, Y. Zhao, *Food Chem.,* **171**, 168 (2015).
15. Z. O. Ozyalcin, A. S. Kipcak, *Bulg. Chem. Commun.*, **55**, 234 (2023).
16. Z. O. Ozyalcin, A. S. Kipcak, *TrJFAS*, **21**, 135 (2021).
17. A. Ersan, A. S. Kipcak, N. Tugrul, *J. Food Sci. Technol.*, **61**, 1 (2024).
18. S. Kipcak, O. Ismail, *J. Food Sci. Technol.*, **58**, 281 (2021).
19. Z. O. Ozyalcin, A. S. Kipcak, N. Tugrul, *J. Aquat. Food Prod.*, **32**, 384 (2023).
20. A. S. Kipcak, I. Doymaz, *Int. J. Fruit Sci.*, **20**, S1222 (2020).
21. Z. O. Ozyalcin, A. S. Kipcak, *J. Aquat. Food Prod.*, **31**, 187 (2022).

Bulgarian Chemical Communications, Volume 57, Issue 3 (pp. 218-223) 2025 DOI: 10.34049/bcc.57.3.OI-FN

Evaluation of smart packaging functions of black carrot extract with polysaccharide-based films

Ö. Ipsalalı[1]*, F. Uğur Nigiz[2]

[1]*Faculty of Graduate Studies, Department of Chemical Engineering, Çanakkale Onsekiz Mart University, Turkey*
[2]*Faculty of Engineering, Department of Chemical Engineering, Çanakkale Onsekiz Mart University, Turkey*

Accepted: August 17, 2025

This work aims to assess the manufacture of polysaccharide-based films derived from carrot waste incorporating pectin (P) and a developed alginate (A) matrix with black carrot extract (BC). P was extracted from carrot waste with a hot acid extraction methodology. The extraction yield was determined to be 17.71%. Biopolymer films designated A/P and A/P/BC were produced *via* the casting technique. In the films, carrot P and A solution were utilized at varying concentrations (0–1% by weight) to attain a total biopolymer content of 2% by weight. Furthermore, BC was integrated into the film at concentrations of 0.2%, 0.4%, and 0.6% (v/v). Analyses of opacity, swelling, moisture, dynamic mechanical strength, and scanning electron microscopy (SEM) were conducted to characterize the films. Furthermore, pH values of 4, 8, and 12 were chosen to evaluate the films' sensitivity to pH. The findings indicated that P concentration significantly influenced the opacity, swelling, and moisture content of the film samples, while concurrently reducing their mechanical strength. Additionally, as the amount of BC incorporated into the films grew, both opacity and mechanical strength enhanced, while moisture content diminished. The results revealed that carrot P and BC could be utilized in the production of smart packaging films. The production of these composite films represents an innovative strategy to address food waste that would otherwise be discarded, hence mitigating environmental effect. This concept has the ability to generate sustainable biobased packaging while simultaneously minimizing waste production.

Keywords: Smart packaging, polysaccharide-based, carrot pectin

INTRODUCTION

The European Union (EU) has introduced a new bioeconomic strategy designed to safeguard the environment and enhance the standard of living of its citizens. This approach will guarantee that all packaging in the EU market is recyclable and will decrease plastic consumption by 2030 [1]. Food packaging constitutes one of the greatest global sectors. The worldwide experiencing heightened interest in sustainable, functional packaging solutions that prolong food shelf life and reduce environmental impact, propelled by growing environmental consciousness. Researchers have examined migration, heat processing, dehydration, acidification, and the integration of antimicrobial/antioxidant compounds into plastic materials to inhibit food spoiling [2-4].

Recent advancements in science and technology have led in the creation of active and intelligent food packaging. Active packaging incorporates agents that engage with food to extend its shelf life, whereas smart packaging use colorimetric agents to assess and provide information regarding food quality without direct touch [4, 5]. pH-sensitive smart packaging often comprises a biodegradable natural or synthetic polymer matrix along with a pH-sensitive indicator [6]. Colorimetric compounds (anthocyanin, betacyanin, methyl red, alizarin) utilized as pH indicators provide customers with information regarding the state of the food [7].

Alginate is an economical, biocompatible, non-toxic, biodegradable polysaccharide having film-forming capabilities. Alginate's capacity to create compatible blends with various polymers and enhance the characteristics of composite materials positions it as a promising candidate for food packaging [5,8,9]. Pectin is a natural polymer located in the middle lamella of plant cell wall. Pectin has attracted interest from researchers as a food packaging material, extending beyond conventional food applications. Pectin's film-forming capability, excellent barrier qualities, non-toxic, compatibility with other polymers, carrier material for ph-responsive pigments and adaptability render it an advantageous choice for the creation of environmentally sustainable packaging [4]. It can be acquired from multiple sources. The majority of

* To whom all correspondence should be sent:
E-Mail: *ozdeipsalali@gmail.com*

these sources consist of fruit (oranges, lemons, apple pomace) and vegetable (sugar beet, carrot, potatoes) biomass that is deemed waste after processing [10]. Pectin is extracted using dilute mineral acids such as hydrochloric acid and nitric acid in a conventional extraction method. Nonetheless, mineral acids include downsides including toxicity and damage to the environment. To deal with these issues, organic acids, specifically citric acid, may be favored for extraction [11, 12].

Carrot pulp is regarded as waste in the fruit juice industry; nevertheless, it can be utilized as animal feed or fertilizer. Pectin can be derived from biomass to provide green products with significant added value. In carrot pulp it is categorized as 'low methoxyl pectin' [13]. In the food industry, anthocyanins can be serve as a colorimetric indicator, providing a natural alternative to synthetic dyes for evaluating food quality especially in smart food packaging [14]. BC is abundant in bioactive components and contains a significant amount of anthocyanin. The anthocyanin included in black carrots demonstrates superior stability. Besides preserving its stability against light and heat, it can also preserve its characteristics at elevated pH levels [15, 16]. Tavasolli *et al.* [17] created pH-sensitive smart packaging films by incorporating anthocyanin derived from sumac into pectin-chitosan nanofibers by a solvent casting method.

This work developed films utilizing a polysaccharide-based matrix, utilizing the film-forming, non-toxic and biocompatible characteristics of alginate and pectin. Pectin was extracted from carrot pulp, and pH-sensitive films were created by including black carrot extract into the polysaccharide-based film matrix. The films were subjected to characterization tests, including mechanical strength, swelling, moisture, and opacity, to assess their suitability for smart food packaging. The extraction of pectin from carrot pulp, an agro-industrial byproduct, and the creation of pH-sensitive packaging from BC, alongside the exploration of its applicability, would substantially enrich the existing literature.

EXPERIMENTAL

Pectin extraction

Pectin was extracted from carrot pulp utilizing a typical thermal extraction method at 90°C for 80 minutes and a pH of 1.3 [13]. Subsequent to extraction, the mixture was subjected to filtration through a filter cloth and allowed to cool to ambient temperature. Ethanol was incorporated into the cooled solution at a 1:2 (v/v) ratio and allowed to precipitate in +4 °C temperature for 20 h. The precipitate was obtained by centrifugation at 1000 g for 15 min, washed with distilled water and subsequently dried in an air oven at 40 °C for 16 h to yield pectin. The pectin yield was determined by the mass difference between the dried pectin and the initial dry raw material.

BC extraction

A mixture of black carrot powder and citric acid solution was added to the flask at a ratio of 1 g to 10 mL and allowed to blend at ambient temperature. The solution underwent centrifugation at 3000 rpm for 5 min, after which the supernatant fractions were combined and adjusted with citric acid extraction solution to match the flask capacity [18].

Production of films

Film-forming solutions were prepared with a total polymer concentration of 2% (w/v) by adjusting the weight ratio of sodium alginate (A) to pectin (P) as detailed below: Formulations of 100:0, 90:10, 80:20, 70:30, 60:40, and 50:50 (A:P, w/w) were prepared, incorporating black carrot extract (BC), abundant in anthocyanins, at concentrations of 0.2%, 0.4%, and 0.6% (v/v) into the film formulation where A and P were utilized in equal ratios. The film solution was stirred at 50 °C for 1 h and cross-linked with 1% $CaCl_2$ [19]. The films were produced using the cast film method. Glycerol is preferred as a plasticiser to impart flexibility and films drying oven at 40 °C. In the last stage, physical cross-linking was executed using 2% $CaCl_2$ for an average of 30 min. The films produced were assigned as A, A9-P1, A8-P2, A7-P3, A6-P4, A5-P5, AP-BC2, AP-BC4, and AP-BC6, accordingly.

Film characterization

JEOLJSM-7100-F scanning electron microscope (SEM) was used used to study the A-P and A-P-BC films structure.

The film thickness was quantified using the Dasqua 4310 digital micrometer electronic gauge. The thickness of each film was measured at three locations: one at the center and two in the areas next to it. Tensile strength values of the films were determined by a Universal Testing Machine (Ankarin) with ASTM D882 standard.

The opacity, or light transmittance, of the films was evaluated using a UV-Vis spectrophotometer (UV1280, Shimadzu, Japan). The absorbance at 600 nm was determined using Equation 1.

$$Opacity = \frac{Abs_{600}}{x} \quad (1)$$

Abs_{600}: absorbance of the film at 600 nm, x: thickness of the film (mm).

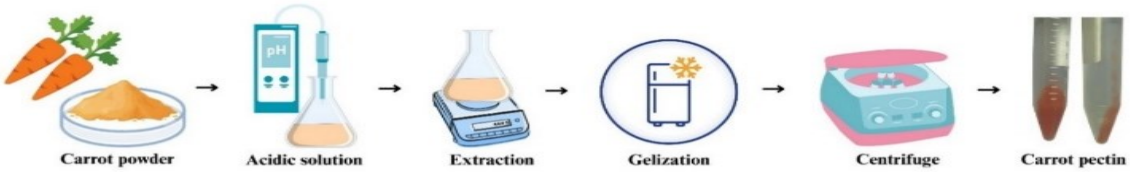

Figure 1. Schematic representation of the carrot pectin extraction

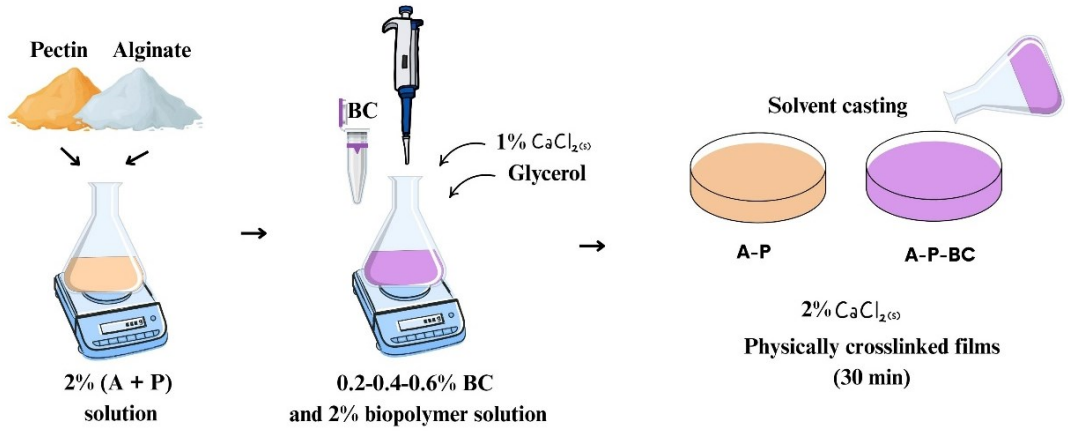

Figure 2. Schematic representation of the carrot P, A and BC composite films production

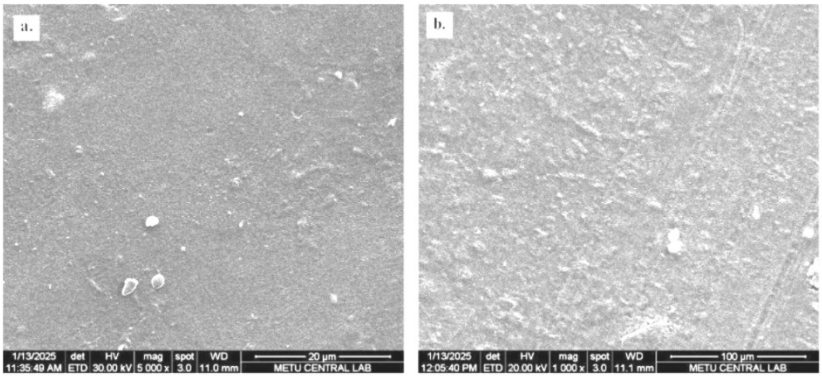

Figure 3. SEM images of (a) A5P5, (b) A-P-BC6 films

For the swelling ratio, samples of the films were weighed (Wd) and put in 30 mL of distilled water at room temperature for 24 h, after which they were taken out, wiped with filter paper and weighed again (Ws).

The swelling degree was determined using Equation 2.

$$Swelling\ ratio\ (\%) = \frac{W_s - W_d}{W_d} x100 \qquad (2)$$

The moisture content was determined by drying the films in an oven at 105 °C for 24 h until a constant weight was achieved. The moisture content was determined by dividing the difference between the starting weight (Wi) and the weight lost during drying (Ws) by the starting weight (Wi) (Equation 3).

$$Moisture\ content\ (\%) = \frac{W_i - W_s}{W_s} x100 \qquad (3)$$

For colorimetric measurement, AP-BC6 films were cut into 3 cm×3 cm squares, submerged in buffer solutions with pH values of 4, 8, and 12 at room temperature, and the films' sensitivity to varying pH conditions was evaluated [20]. The alteration in color of the films was assessed utilizing a colorimeter (Linshang, LS173, Shenzhen, China). The mean Hunter color indices (L*, a*, and b*) of the films were recorded three times. The overall color difference was determined based on the data at various pH levels utilizing Equation 4.

$$\Delta E = \sqrt{(L^* - L_0^*)^2 + (a^* - a_0^*)^2 + (b^* - b_0^*)^2} \qquad (4)$$

MATERIALS

Alginate was from Sigma Aldrich; citric acid, ethanol were of analytical grade, purchased from Merck Chemicals, Türkiye. Fresh carrots (*Daucus carota L.*) and black carrot powder (*Daucus carota ssp. sativus var. atrorubens Alef.*) were purchased from a local market in Çanakkale. Black carrot

powder was utilized in its commercially available form.

RESULTS AND DISCUSSION

The elements utilized in film development have significance for surface morphology. The physical parameters of a film influence its mechanical and optical charaeristics [21]. A and P exhibit a uniform surface structure owing to their capacity to create smooth films. Conversely, tiny particle forms were seen at certain locations in the A5-P5 film (Figure 3a). A smooth surface is seen in the AP-BC6 film, likely resulting from the compatible interaction between the biopolymer matrix and BC (Figure 3b). This may result from the gelation produced during the incorporation of the cross-linking agent, which remained undissolved despite the inclusion of a plasticizer. Nonetheless, all fabricated biocomposite films often exhibit a smooth and uniform surface, notwithstanding the presence of minor particles in the SEM pictures (Figures 4b, 4c).

The swelling percentages of the A-P film series range from 28.571% to 120.588%. A swelling percentage of 120.588% was specifically noted in the A5-P5 control films. This condition may have resulted from the hydrophilic nature of the matrix structure and the ratios of biopolymers it comprises. The swelling percentage rose concomitantly with the increase of pectin concentration in the matrix (Figure 4). This rise results from pectin's hydrophilic nature, which facilitates its interaction with water via hydroxyl groups (-OH). Films with different ratios of BC extract added also had a constant A and P ratio. Consequently, the films disintegrated in an aqueous medium within 24 h. Consequently, the swelling percentage was incalculable. Moreover, the elevated anthocyanin concentration in BC has been shown to enhance the polarity of the films, resulting in their solubility in polar solvents like water [22].

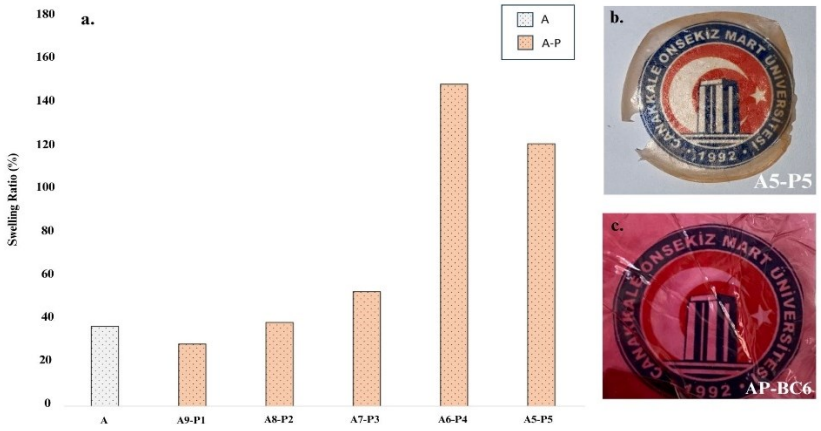

Figure 4. (a) Swelling ratio of A and A-P films, (b) A5-P5, (c) AP-BC6 biocomposite films

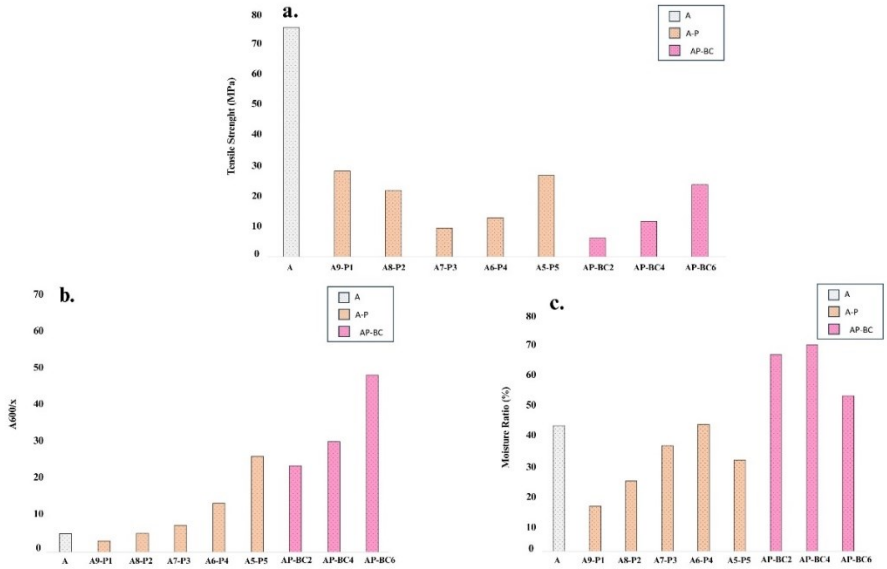

Figure 5. (a) Tensile strength, (b) Opacity, and (c) Moisture content of the biopolymer-based films.

The ability and performance of films are essential for maintaining the integrity of packaged food goods [23]. The A-P series films displayed thicknesses between 0.0287 mm and 0.053 mm, while the AP-BC series films revealed thicknesses from 0.010 mm to 0.014 mm (Figure 5a). The incorporation of BC influences film thickness, with an increase in BC correlating to greater thickness. The increase in thickness may result from the electrostatic repulsion provided by the anthocyanins in BC interacting with the biopolymers (A-P) and alterations in film density [24]. The tensile strength (TS) of pure A was 74.90 MPa, whereas the TS of A-P films varied between 9.477 and 28.019 MPa, and the TS of AP-BC films ranged from 6.167 to 23.571 MPa (Figure 2b). The incorporation of carrot pectin into the matrix resulted in a substantial reduction in mechanical strength. The maximum strength was recorded in films exhibiting an equal A-P ratio. A comparable scenario was noted in a study about renewable films composed of alginate and low-methoxyl pectin [25]. Nonetheless, as the incorporation of BC into the films increased, the mechanical strength correspondingly improved. The endurance of biocomposite films is influenced by polymer composition, intra- and intermolecular forces, and the structure of the film network.

A-P film solutions are typically apparent due to their uniform composition, with opacity increasing upon the incorporation of pectin into the films (Figure 5b). The opacity of the films markedly enhanced with higher BC concentration. The decrease in inter-chain spaces caused by double cross-linking of the films led to enhanced opacity [26]. Elevated opacity is believed to augment the films' capacity to shield light-sensitive meals from the detrimental impact of visible light [27].

The moisture percentages in A-P films were determined to be 16.071% and 45.098%, representing the lowest and highest values, respectively. The incorporation of carrot pectin into the film matrix resulted in a decrease of moisture content relative to the pure alginate film. Another study found that the moisture content of films containing alginate and pectin was 18.57% [26]. In the AP-BC film series, the moisture content varied from 55.294% to 73.333% (Figure 5c). Following the incorporation of BC into the alginate-carrot pectin films, the moisture content initially rose and subsequently declined. The hydrophilic -OH groups of polysaccharides will establish hydrogen bonds with the -OH groups in BC. This interaction may restrict the cross-linking of water molecules and polysaccharides, leading to variations in moisture content. A comparable outcome could occur contingent upon the sort of additives employed [20].

The increased content of anthocyanin components in black carrots correlates with pH-dependent variations. Table 1 presents the color spectra and color change data of the films. Certain literature research examined the pH sensitivity of the generated films without presenting a control film group [20, 28]. AP-BC6 films exhibit sensitivity to both acidic and basic buffers. At pH levels of 4, 8, and 12, the film's coloration transitioned from pale pink to brown. The color alteration transpired about 1 to 2 min. ΔE values beyond 5 signify discernible color alterations in the videos. As the pH value rises, the brightness (L*) of the films decreases, while the a* and b* values suggest a transition towards red-yellow shades, concluding in a brown tone. Films containing added BC are regarded as effective natural pH sensors.

Table 1. Colorimetric change of AP-BC6 films at pH levels 4, 8, and 12

pH	L*	a*	b*	ΔE	Color
4	75.47	18.15	9.05	32.64	
8	73.17	22.60	12.75	28.37	
12	57.24	12.00	8.11	34.55	

CONCLUSION

The development of pH-sensitive films by incorporating black carrot extract into alginate films, resulting in a suitable biocomposite with pectin derived from carrot waste, demonstrates potential for innovative smart packaging solutions. The findings indicated that the incorporation of BC into A-P films influenced their physicochemical characteristics. As the quantity of BC augmented, the film thickness, strength, and opacity escalated, whereas the moisture content diminished. The resulting films often exhibit a smooth surface and a slender structure. Films containing added BC are believed to function as natural pH indicators. The films demonstrate unpredictable actions when maintained at room temperature, rendering them more appropriate for assessing the quality of frozen food. Our research may yield novel concepts for the advancement of smart packaging, specifically with

the potential of biocomposite films derived from waste to tell consumers about freshness.

Acknowledgement: *The present study was supported by the Çanakkale Onsekiz Mart University Scientific Research Projects Coordination (Project No: FBA-2024-4847).*

REFERENCES

1. M.G. Kontominas, *Foods*, **9**, 1440 (2020).
2. D. Khedkar, R. Khedkar, Emerging technologies in food science: Focus on the developing world, 2020, p. 165.
3. E.C. Pack, K.Y. Lee, J.S. Jung, D.Y. Jang, H.S. Kim, Y.J. Koo, H.G. Lee, Y.S. Kim, K.M. Lim, S.H. Lee, D.W. Choi, *Food Pack. Shelf Life*, **30**, 100736 (2021).
4. N.S. Said, W.Y. Lee, *Molecules*, **30**, 1144 (2025).
5. O.M. Atta, S. Manan, A. Shahzad, M. Ul-Islam, M.W. Ullah, G. Yang, *Food Hydrocolloids*, **125**, 107419 (2022).
6. L. Wang, C. Yang, X. Deng, J. Peng, J. Zhou, G. Xia, C. Zhou, Y. Shen, H. Yang, *Int. J. Biol. Macromol.,* **245**, 125485 (2023).
7. R. Yekta, R. Abedi-Firoozjah, S. Azimi Salim, A. Khezerlou, K. Abdolmaleki, *Cellulose*, **30**, 9925-9953 (2023).
8. J. Chen, A. Wu, M. Yang, Y. Ge, P. Pristijono, J. Li, *Food Control*, **126**, 108063 (2021).
9. J. Kurczewska, M. Ratajczak, M. Gajecka, *Appl. Clay Sci.*, **214**, 106270 (2021).
10. M. Tsirigotis-Maniecka, E. Górska, A. Mazurek-Hołys, I. Pawlaczyk-Graja, *Polymers*, **16**, 2670 (2024).
11. Belkheiri, A. Forouhar, A.V. Ursu, P. Dubessay, G. Pierre, C. Delattre, G. Djelveh, S. Abdelkafi, N. Hamdami, P. Michaud, *Appl. Sci.*, **11**, 6596 (2021).
12. C.F. de Oliveira, D. Giordani, P.D. Gurak, F. Cladera-Olivera, L.D.F. Marczak, *Innov. Food Sci. Emerg. Technol.*, **29**, 201 (2015).
13. F. Jafari, F. Khodaiyan, H. Kiani, S.S. Hosseini, *Carbohydr. Polym.,* **157**, 1315 (2017).
14. S.S. Rosales-Murillo, J. Sánchez-Bodón, S.L. Hernández Olmos, M.F. Ibarra-Vázquez, L.G. Guerrero-Ramírez, L. Pérez-Álvarez, J.L. Vilas-Vilela, *Polymers*, **16**, 163 (2024).
15. M. Tavlasoglu, G. Ozkan, E. Capanoglu, *ACS Omega*, **7**, 32481 (2022).
16. S.E. Bilek, F.M. Yılmaz, G. Özkan, *Food Bioprod. Process.,* **102**, 72 (2017).
17. M. Tavassoli, A. Khezerlou, T.N. Moghaddam, S. Firoozy, M. Bakhshizadeh, M.A. Sani, M. Hashemi, A. Ehsani, J.M. Lorenzo, *Int. J. Biol. Macromol.*, **242**, 125044 (2023).
18. E. Ağçam, A. Akyıldız, Gıda, 40, 149-156 (2015).
19. N.C. Homem, C.A.F.D.S. Miranda, J.I.D.C. Antunes, M.T.S.P. de Amorim, H.P. Felgueiras, *Proceedings*, **69**, 4 (2020).
20. Y. Li, Z. Hu, R. Huo, Z. Cui, *Heliyon*, **9**, e14421 (2023).
21. S. Bhatia, A. Al-Harrasi, M. Jawad, Y.A. Shah, M.S. Al-Azri, S. Ullah, L.Y. Aydemir, *Int. J. Food Sci. Technol.,* **58**, 4652 (2023).
22. M. Xu, D. Fang, B.M. Kimatu, L. Lyu, W. Wu, F. Cao, W. Li, *Food Control*, 110431 (2024).
23. J. He, S. Yang, G. Goksen, X. Cong, M.R. Khan, W. Zhang, *Food Biosci.,* **58**, 103635 (2024).
24. T. Chhoden, P. Aggarwal, A. Singh, S. Kaur, *J. Food Meas. Charact.,* **18**, 5489 (2024).
25. S. Galus, A. Lenart, *J. Food Eng.,* **115**, 459 (2013).
26. C.K. Bierhalz, M.A. da Silva, T.G. Kieckbusch, *J. Food Eng.*, **110**, 18 (2012).
27. S. Roy, R. Ramakrishnan, G. Goksen, S. Singh, Ł. Łopusiewicz, *Innov. Food Sci. Emerg. Technol.*, **91**, 103550 (2024).
28. L. Prietto, T.C. Mirapalhete, V.Z. Pinto, J.F. Hoffmann, N.L. Vanier, L.T. Lim, A.R.G. Dias, E. da Rosa Zavareze, *Lwt*, **80**, 492 (2017).

Bulgarian Chemical Communications, Volume 57, Issue 3 (pp. 224-228) 2025 DOI: 10.34049/bcc.57.3.OI-FN-1

Green tea-boron nitride incorporated pumpkin pectin-alginate food packaging film preparation and characterization

Ö. Ipsalalı[1]*, F. Uğur Nigiz[2]

[1]*Faculty of Graduate Studies, Department of Chemical Engineering, Çanakkale Onsekiz Mart University, Turkey*
[2]*Faculty of Engineering, Department of Chemical Engineering, Çanakkale Onsekiz Mart University, Turkey*

Accepted: August 17, 2025

Petroleum-based packaging poses a major environmental threat to life on Earth. This type of packaging does not degrade in nature for many years and causes environmental pollution as it is difficult/costly to recycle. Packaging is used in food storage to preserve food quality, ensure food safety and extend shelf life. With the increasing need for food in the world, the demand for packaging materials is also increasing. It is therefore difficult to strike a balance between the use and recycling of packaging. Efforts should be made to design food packaging according to the type of food, to produce it in an environmentally friendly way and to be applicable in food packaging systems. Within the scope of this study, food packaging films were produced to utilize agricultural residues left by farmers after harvest and integrate them into the economy. In this study, pectin was obtained from pumpkins and mixed with alginate to make packaging films. Green tea extract (GTE) was incorporated as an enhance water permeability and strength, while boron nitride nanoparticles (nB) were selected to improve the physical attributes of the films. The use of green tea decreased the moisture content and swelling of the films while enhancing their mechanical strength. The incorporation of nB into the films enhanced their opacity and mechanical strength, while simultaneously decreasing their moisture content, swelling percentage, and water vapor permeability rate (WVPR). Future research suggests that these films may serve as food packaging materials.

Keywords: Pumpkin pectin films; boron nitride; green tea extract; food package

INTRODUCTION

Packaging is very important for the food industry. The fact that it protects the quality of the food, complies with the safety standard and extends the shelf life of the food makes it indispensable. As the demand for food increases, so does the dependence on packaging. In order to protect nature, some innovative approaches and changes (smart-active packaging) should be taken in the packaging sector [1].

Due to their biodegradability and abundant availability in various natural resources, biopolymers have attracted significant interest in the packaging industries, making them effective alternatives. Biopolymers derived from natural sources are useful for food packaging applications due to the environmentally friendly and biodegradable properties of natural materials with antimicrobial activity such as polysaccharides, proteins and lipids [2]. However, most materials alone have low thermal, chemical and mechanical resistance. Therefore, packaging properties need to be improved by blending different materials. Especially in recent years, with the developments in the field of zero waste and sustainable environment, the production of biopolymers from wastes, which replace polymeric materials, has come to the forefront both economically and environmentally [3].

Pumpkin belongs to the family *Cucurbitaceaceae* which consists of 800 species and 130 genera. It is widely cultivated in Asia and the Americas: China, India, Russia, Ukraine and the USA. In the world, it is recorded as one of the most produced agricultural products with 27.4 million tons of production. This constitutes approximately 61% of total world production [4, 5]. Recently, there has been an increase in the production of pumpkin in our country. When used on an industrial scale, it can be frozen or canned. When pumpkin is processed in the industry, the edible part of the fruit usually needs to be separated from the skin (2.6-16%), seeds (3.1-4.4%) and by-products (25%) [6-8]. During the pumpkin processing, the peels rich in pectin content are discarded. Hydrochloric acid, sulfuric acid or nitric acid are generally preferred when extracting pectin from waste [9-11].

Boron nitride is a stable material with physicochemical properties similar to those of graphene in hexagonal shape. It is a well-known nanomaterial with antibacterial properties due to its strong mechanical strength and high surface area. It was reported that the use of boron nitride led to

* To whom all correspondence should be sent:
E-Mail: *ozdeipsalali@gmail.com*

an increase in the antibacterial activity of the film and that it was not harmful to human cells due to its low cytotoxicity [12]. Behera *et al.* [13], prepared chitosan films with boron nitride nanobiocomposite and it was observed that the nB additive decreased the water solubility and moisture absorption of the film. Green tea is a significant material for packaging owing to its antioxidant capabilities, optical characteristics, antibacterial effects, and pH sensitivity. GTE augments the interaction between macromolecular polymers and increases the physical and chemical properties of the matrix [15]. The research indicates that it can enhance barrier performance in active packaging films and significantly decrease the water vapor transmission rate [16].

EXPERIMENTAL

Pumpkin pectin extraction

This method used by Güzel and Akpınar [17] in their study in 2019 was modified. Pumpkin peels were cut and dried in an oven at 40 ºC for two days. They were ground with an electronic grinder and sieved. 100 mL of citric acid solution with a pH of about 1 was prepared to extract pectin. 10 g of pumpkin powder was weighed and added to the citric acid solution. It was stirred at 80 ºC for 60 minutes and filtered. 100 mL of 96% ethanol was added to the remaining filtrate and left in the refrigerator for 12 h. The pectin was centrifuged at 3000 rpm for 15 min; the supernatant was discarded and the pectin remaining at the bottom was washed for neutralization. The washing was performed twice with 70% acidic ethanol (0.5% HCl) and 96% ethanol. Then it was centrifuged again, and the precipitated pectin was dried in an oven at 50 ºC. The pectin obtained was stored in a refrigerator.

Film preparation

Alginate (A), pumpkin pectin (PP), green tea extract (GTE) and nano boron nitride (nB) added films were produced by solution casting method. Packaging solutions containing 20% of alginate and 20% of pectin by mass, not exceeding 2% solid biopolymer content in total, were prepared. Some modifications were applied on the methods with reference to the studies of da Silva *et al.* [18] and Bierhlaz *et al.* [19]. A-PP solution was stirred at 50 ºC for 1 h to dissolve; nB was added at different ratios 1%, 0.5%, 0.1% by mass and GTE at 1 mL, 2 mL, 3 mL by volume was also added to the prepared film (Table 1). 1% $CaCl_2$ was added as a crosslinking agent into the solution. In the last step, glycerol was used as plasticizing agent. The films were dried in an oven set at 40 ºC for 1 day. 30 min. The removed films were allowed to dry at room temperature. The films produced were assigned as A, A-PP, APP-G1, APP-G2, APP-G3, APP-B1, APP-B2, APP-B3, accordingly (Table 1).

Table 1. Film composition

Code	A (wt.%)	PP (wt.%)	GTE (vol%)	nB (wt.%)
APP	1.6	0.4		
APPB1	1.6	0.4		0.1
APPB2	1.6	0.4		0.5
APPB3	1.6	0.4		1
APPG1	1.6	0.4	1	
APPG2	1.6	0.4	2	
APPG3	1.6	0.4	3	

Film characterization

The thickness of the films was measured with a digital micrometer (Dasqua 4310). The thickness was measured randomly from at least three points and the values were averaged. The film sample was cut in a rectangular shape (10 mm × 40 mm). It was placed in a UV-vis spectrophotometer (Shimadzu UV-1280) cell. At a wavelength of 600 nm the light transmittance, i.e. opacity, of the films was measured. Opacity values were calculated according to Abs600 absorbance per unit thickness (Abs600/Thickness). The moisture content of the films trapped in the standard medium was found as a percentage. It is a gravimetric method. The films were left at 105 ºC for 24 h to reach constant weight. Based on the difference between initial and final weight, the moisture content was found as a percentage. A swelling test was performed to determine the water resistance of the films and how much water they trap. To get rid of excess moisture, the samples were dried in an oven at 65 ºC for 12 h. Film specimens were cut into 10 × 40 mm pieces. The tensile strength of the films was determined according to ASTM Standard D882 using a Universal Mechanical Testing Machine (ANKARIN). The room temperature and relative humidity was 55% during the analysis. At least three replicates of each film sample were tested.

Materıals

Alginate was from Sigma Aldrich; citric acid, ethanol of analytical grade were purchased from Merck Chemicals, Türkiye. Boron nitride nanopowder (purity 99.7%, 790 nm) was from Nanografi, Türkiye. Fresh pumpkins were purchased from a local market in Çanakkale.

RESULTS AND DISCUSSION

There are tests necessary for determining the use of food packaging films. Morphology, mechanical strength and color properties also have effects on their use as packaging. Fig. 1 shows the SEM micrographs and mechanical strength of the prepared films. SEM analysis of the green tea-filled film is seen in Fig. 1a. Fig. 1b shows the analysis of the nB-doped film. As can be seen from the SEM analysis, the particle distribution on the film surface is homogeneous. However, there is clustering in some regions at nB loading. The film surface is non-porous and smooth. This is important for the barrier properties of the packaging.

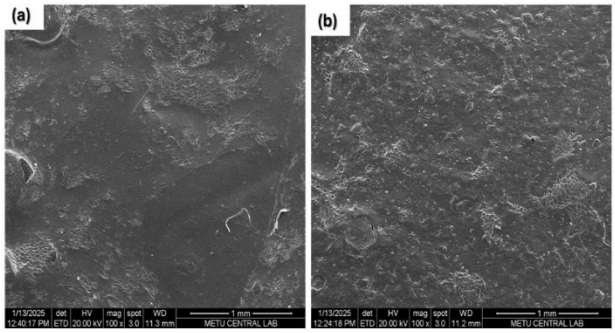

Fig. 1. SEM analysis of APP-G1 (a), APP-B1 (b) films

As seen in Fig. 2a, the opacity of APP-B films was between 37.579-76.536 Abs600/mm while APP-G was between 6.774-14.250 Abs600/mm. It was noticed that as the ratio of nB and GTE added to the films increased, the films became opaquer, and the light transmittance decreased (Fig. 2b). Visually, the appearance of the films generally reflects good properties. Therefore, consumers typically preferred transparent packaging. Films with high opacity protect food from light, air, and heat, thereby extending shelf life [20].

Table 2 shows the color properties of the films. For the APP-G films, compared to the control film, the color of the films changed towards green as the green tea extract content increased. In one study, the color analysis of starch-pectin based films with 0.25% and 0.5% green tea extract (w/v) (L*=87.82 and ΔE=12.11; L*=86.91 and ΔE= 16.16), respectively, showed similar L* and ΔE values [21]. For the APP-B film, compared to the control films, the color of the films became whiter when the B ratio added to the films increased. L* values between 87.87-92.68 indicate that the films are light colored. If ΔE > 3, the color differences of the films are easily distinguishable with the naked eye. In Table 2, all of the ΔE values of the APP-B films are above 10 and the color changes are clear. a* values are generally > 0, indicating a slight shift to red tones. b* values are also positive, indicating a shift to yellow tones (Table 2).

Table 2. Color analysis of films

Code	L*	a*	b*	ΔE
APP (Control/ Blank)	92,21	0,23	-2,22	0,43
APPB1	87,87	0,35	7,01	11,72
APPB2	89,19	-0,03	7,91	12,41
APPB3	88,31	0,76	14,23	18,78
APPG1	91,60	-0,25	2,39	13,76
APPG2	92,68	0,16	-1,92	17,95
APPG3	90,43	0,19	-2,18	17,19

The film thicknesses measured were 0.094 mm for A-PP, 0.0243-0.0350 mm for APP-B, and 0.061-0.125 mm for APP-G. The incorporation of nB significantly lowered the films' thickness, whereas the inclusion of GTE significantly enhanced the films' thickness. The tensile strength of the A-PP control film was determined to be 17.247 MPa. The tensile strength of APP-B films ranged from 16.008 to 45.152 MPa, while that of APP-G films ranged from 4.488 to 33.262 MPa (Fig. 2). Addition of nB and GTE to the films increased the strength of the films. The addition of GTE did not greatly affect the durability of the films, similar situations were observed in some studies [22]. APP-B films alone increased the mechanical strength by approximately 300% compared to A-PP films. The combination of pectin and alginate was able to improve the mechanical profiles of the films due to the compatibility between the components [23]. Moreover, it is thought that double cross-linking of the films may have enhanced mechanical strength.

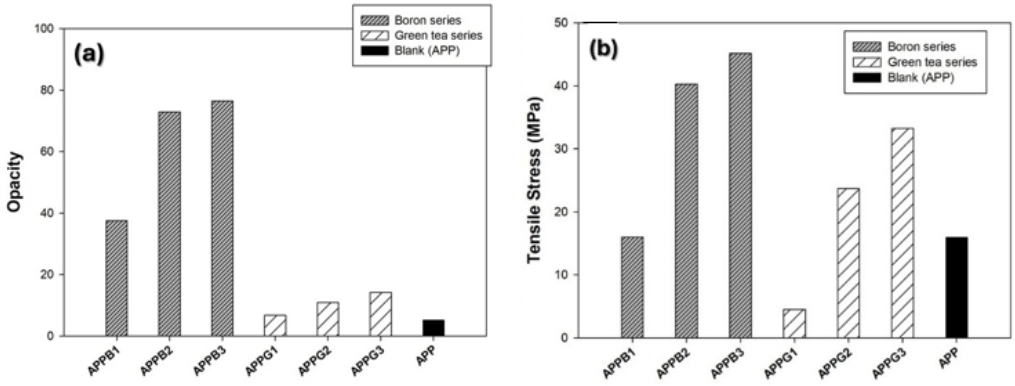

Fig. 2. Opacity (a) and appearances, (b) tensile stress APP, APP-B and APP-G films

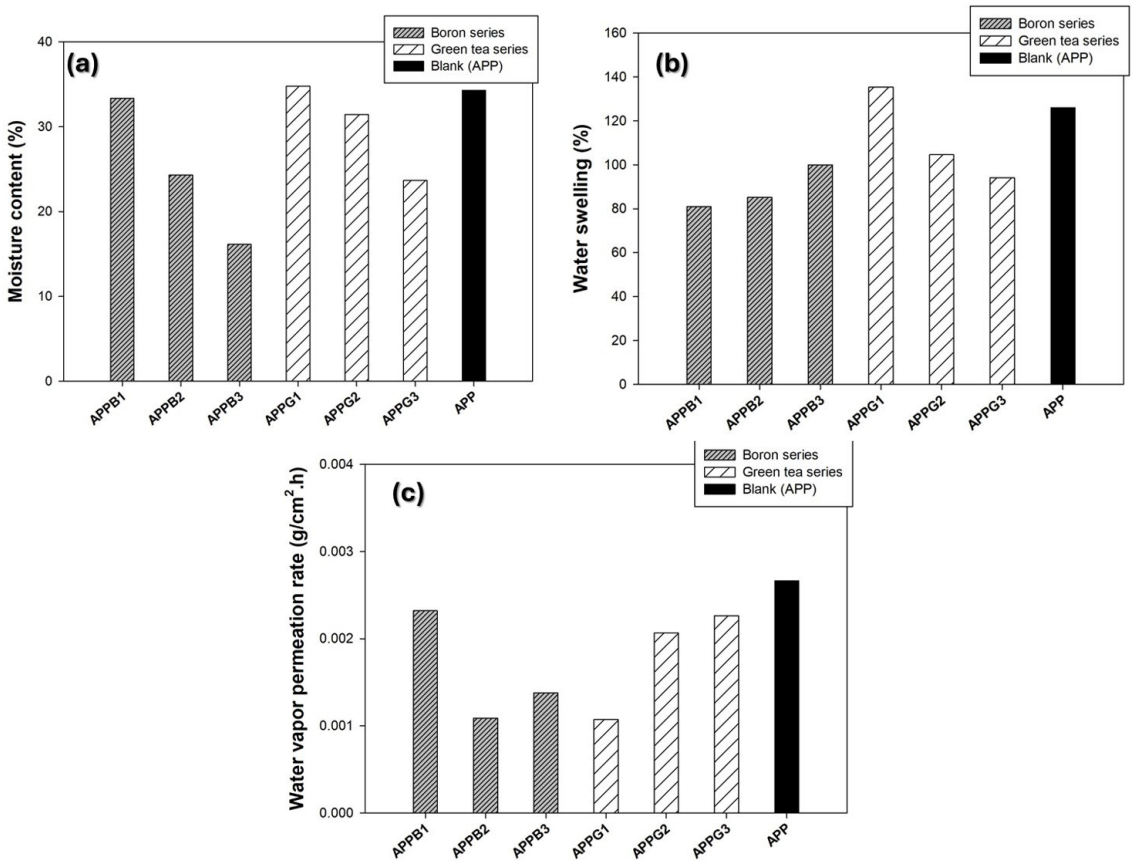

Fig. 3. Moisture content (a), water swelling (b) and water vapor permeation rate (c) of films

The barrier properties of the films are given in Fig. 3. The moisture content of APP-B films was between 16.129-33.333%, while that of APP-G films was between 23.684-34.783%. As the amount of nB increased, the moisture content significantly decreased. A similar situation was observed with the addition of green tea extract (Fig. 3a). In a previous study, Wen *et al*. [24] developed composite films by adding 2, 5 and 10% GTE to polyvinyl alcohol-based films. The moisture percentages of the films ranged between 28.7-21.7%, and the moisture percentage decreased as the addition of GTE increased. This is due to the crosslinking of polysaccharides with polyphenols [25]. Tong *et al*. [26] found 13.47% moisture content in the film produced from orange peel pectin/sodium alginate.

Swelling has the potential to directly affect the water resistance of packaging films under humid atmosphere conditions [25]. The swelling percentages ranged from 126.087% for the control group A-PP film, 85.185% to 126.667% for APP-B films, and 94.118% to 135.294% for APP-G films. The interactions that occur according to the addition of GTE and nB to A and PP containing films determine the behavior of the matrix towards water. Compared to the control group, the addition of nB decreased the swelling percentage, while the addition of GTE increased the swelling percentage of the films (Fig. 3b). The presence of phenolic compounds may explain the affinity of GTE for water molecules and the reason for the increase in swelling [22].

Since the films are intended to be used as food packaging, the water vapor permeation rate (WVPR) varies according to the moisture content and shelf life of the product to be packaged. The packaging films developed in this study are intended to be used in meat products. Therefore, films need a moderate barrier. The WVPR results show the differences in the barrier performance of the film content. The addition of nB reduced the WVPR (Fig. 3c). However, as the concentration of nB in films increases, the WVTR values slightly increase because of the hydrogen bonding effect. The best barrier property was also found in APP-G1 with the addition of GTE. This reduction may be due to the formation of hydrogen bonds between the A, PP, B and GTE matrix and oxygen, which may reduce the diffusion of water molecules in the film [27, 28].

Green tea extract which is rich in phenolic compounds, is a component with various biological activities such as antioxidant and pH sensitivity. It is seen as a potential natural additive to enhance pH sensitivity. Tea polyphenols undergo structural transformation in response to pH changes [24]. If the pH of the solution is < 7, the color of the films is

yellowish-green. If the pH of the solution was > 7, as the pH values increased, the films turned dark brown. The pH-sensitive color changes of APP-G3 film observed at pH 4, 8 and 12 are presented in Table 3.

Table 3. Color analysis at different pH ranges

pH	L*	a*	b*	ΔE	Color
4	77.55	-3.62	22.45	4.22	
8	82.97	-2.51	14.17	8.45	
12	55.01	6.41	16.85	2919	

In Table 3, L* values decreased as the pH values increased and accordingly, the films exhibited a darker color. The negative a* values indicate that the films are in a color transition towards green and the positive b* values indicate that the films are in a color transition towards yellow. According to the results obtained, APP-G3 films proved to be pH sensitive.

CONCLUSION

In this study, the potential of films composed of alginate and pectin for use as food packaging was determined by tests. In the scope of the study, it was observed that especially nB and GTE additives increased the opacity and mechanical strength of the film and decreased moisture content. In future studies, the changes in the packages in contact with real food will be examined and their shelf life will be determined. The fact that the materials selected within the scope of the study are biodegradable and all additives are food-safe, makes the potential of the produced biobased packaging important in terms of both environmental and sustainable economy.

Acknowledgement: *This study was supported by the Scientific and Technological Research Council of Turkey (TÜBİTAK) through the 1002-B Short Term R&D Funding Program (Project No: 224O314).*
This study was financially supported by the Çanakkale Onsekiz Mart University Scientific Research Project Coordination (Grant Number: FBA-2024-4847).

REFERENCES

1. N. S. Said, W. Y. Lee, *Molecules*, **30**, 1144 (2025).
2. J. Baranwal, B. Barse, A. Fais, G. L. Delogu, A. Kumar, *Polymers*, **14**, 983 (2022).
3. T. D. Moshood, G. Nawanir, F. Mahmud, F. Mohamad, M. H. Ahmad, A. Abdul Ghani, *Curr. Res. Green Sustainable Chem.*, **5**, 100273 (2022).
4. P. Nath, O. P. Dutt, S. Velayodhan, K. R. M. Swamy, *Indian J. Hort*., **36**, 171 (1979).
5. P. Ramachandran, A. K. Dhiman, S. Attri, *Indian J. Ecol.*, **44**, 685 (2017).
6. R. P. Cuco, L. Cardozo-Filho, C. da Silva, *J. Supercrit. Fluids*, **143**, 8 (2019).
7. X. Rico, B. Gullón, J. L. Alonso, R. Yáñez, *Food Res. Int*., **132**, 109086 (2020).
8. A. Hussain, T. Kausar, A. Din, M. A. Murtaza, M. A. Jamil, S. Noreen, et al., *J. Food Process. Preserv.*, **45**, e15542 (2021).
9. M. Gulfi, E. Arrigoni, R. Amadò, *Carbohydr. Polym*., **59**, 247 (2005).
10. M. D. J. C. Sanadarani, V. P. N. Prasadi, *J. Food Ind. Microbiol*., **4**, 125 (2018).
11. C. Lalnunthari, L. M. Devi, L. Badwaik, *J. Food Sci. Technol*., **57**, 1807 (2020).
12. A. Mukheem, S. Shahabuddin, N. Akbar, A. Miskon, N. Muhamad Sarih, K. Sudesh, et al., *Nanomaterials*, **9**, 645 (2019).
13. K. Behera, M. Kumari, Y. H. Chang, F. C. Chiu*, Int. J. Biol. Macromol*., **186**, 135 (2021).
14. M. Feng, L. Yu, P. Zhu, X. Zhou, H. Liu, Y. Yang, et al., *Carbohydr. Polym.,* **196**, 162 (2018).
15. S. Husna, A. W. Trifany*, J. Sci. Data Anal*., **132** (2024).
16. Z. Miao, Y. Zhang, P. Lu, *Int. J. Biol. Macromol*., **192**, 1123 (2021).
17. M. Güzel, Ö. Akpınar, *Food Bioprod. Process*., **115**, 126 (2019).
18. M. A. Da Silva, A. C. K. Bierhalz, T. G. Kieckbusch, *Carbohydr. Polym*., **77**, 736 (2009).
19. A. C. Bierhalz, M. A. da Silva, M. E. Braga, H. J. Sousa, T. G. Kieckbusch, *LWT-Food Sci. Technol.*, **57**, 494 (2014).
20. N. Yazıcıoğlu, K. Siyasal, *Food Health*, **10**, 115 (2024).
21. W. Homthawornchoo, J. Han, P. Kaewprachu, O. Romruen, S. Rawdkuen, *Polymers*, **14**, 2696 (2022).
22. V. Adımcılar, E. Torlak, F. B. Erim, *ACS Omega*, (2025).
23. S. Galus, A. Lenart, *J. Food Eng*., **115**, 459 (2013).
24. H. Wen, Y. I. Hsu, T. A. Asoh, H. Uyama, *Polym. Degrad. Stabil*., **178**, 109215 (2020).
25. T. Nisar, Z. C. Wang, A. Alim, M. Iqbal, X. Yang, L. Sun, Y. Guo, *J. Food*, **17**, 695 (2019).
26. W. Y. Tong, A. R. A. Rafiee, C. R. Leong, W. N. Tan, D. J. Dailin, Z. M. Almarhoon, et al., *Chemosphere*, **336**, 139212 (2023).
27. T. M. P. Ngo, T. M. Q. Dang, T. X. Tran, P. Rachtanapun, Int. J. *Polym. Sci.,* 2018, 5645797 (2018).
28. L. Marangoni Junior, C. R. Fozzatti, E. Jamróz, R. P. Vieira, R. M. V. Alves, *Materials*, **15**, 3881 (2022).

Bulgarian Chemical Communications, Volume 57, Issue 3 (pp. 229-234) 2025 DOI: 10.34049/bcc.57.3.SK-AK-FN

Fabrication and filtration of gum arabic doped electrospun PLA membrane for rejection of gray water pollutants

S. Kahraman[1], A. Katirci[1], F. Uğur Nigiz[2*]

[1]*Çanakkale Onsekiz Mart University, School of Graduate Studies Chemical Engineering Department, Çanakkale,Türkiye*

[2]*Çanakkale Onsekiz Mart University, Chemical Engineering Department, Çanakkale, Türkiye*

Accepted: August 17 2025

Water scarcity, which is increasing with global warming and climate change, is one of the environmental problems that require urgent solutions. Gray water treatment is one of the effective methods to address this problem. Gray water from washing machines can contain organic and inorganic pollutants. Electrospun nanofibers show promise in the removal of these pollutants owing to their high surface area and tunable properties. In this study, gum arabic (GA) doped polylactic acid (PLA) nanofiber membrane was produced by an electrospinning method for gray water filtration. GA is a functional and economical additive that complements the deficiencies of PLA and improves the hydrophilicity, mechanical strength, flexibility, and separation performance of the membrane. GA was added to the PLA membranes at 1-5%. The characterization tests revealed that GA doped membranes were successfully produced. In methylene blue filtration, the pure PLA membrane provided over 93% rejection, while this rate increased to 99% with GA additive. Emulsified oil removal was measured as 87% in the membrane with 2% GA additive. Approximately 50% rejection was achieved in linear alkyl benzene sulfonate (LAS) filtration and 100% in microplastic filtration. With GA additive, the surface contact angle decreased from 127° to 118° and hydrophilicity increased. In mechanical tests, the tensile strength of the PLA membrane without additives increased from 7 MPa to 11.8 MPa with 4% AG additive and the mechanical strength and flexibility increased significantly. In conclusion, GA doped PLA membranes are considered as an effective and sustainable option for gray water treatment.

Keywords: Electrospinning; filtration; gray water; multiple impurities; polylactic acid.

INTRODUCTION

The escalation of industrialization and urbanization has led to a significant increase in water consumption. Consequently, water consumption is escalating by 3% annually, rendering water scarcity a significant contemporary issue [1]. In particular, the treatment and reuse of gray water plays an important role in sustainable water management strategies. Gray water contains various organic and inorganic pollutants such as detergent residues, oils, dyes, and microplastics [2]. The effective removal of these pollutants is critical for both environmental and public health. Various wastewater treatment technologies are used to solve this problem [3].

Traditional treatment methods may be insufficient to completely remove such complex pollutants. In recent years, nanofiber membranes produced by the electrospinning method have become one of the most innovative materials in water purification. These membranes effectively retain contaminants thanks to their high surface area, adjustable pore structure, and high permeability. Additionally, the electrospinning method allows for the use of different polymers and additives together, enabling the modification of membrane properties as desired [4, 5]. Electrospinning is a versatile and simple technique used to produce ultra-fine fibers from polymer solutions or melts by applying a high-voltage electric field. In this process, the polymer solution is pumped through a small needle connected to a high-voltage power source. The electric field overcomes surface tension by creating a charge on the liquid surface, causing the solution to form a thin jet. As the jet moves toward a grounded collector, the solvent evaporates and solid nanofibers accumulate, resulting in a nonwoven membrane with a highly porous structure. The diameters of the resulting fibers typically range from ten nanometers to several micrometers, providing an exceptionally high surface area-to-volume ratio that is advantageous for filtration and separation applications [6]. Polylactic acid (PLA) is an aliphatic polyester obtained from renewable sources such as corn starch and exhibits biodegradable properties. Thanks to its high mechanical strength and processability, it is widely used in packaging, textiles, and medical applications. However, PLA's

* To whom all correspondence should be sent:
E-mail: filiz.ugur@comu.edu.tr

hydrophobic structure and low water permeability limit its performance in applications such as water purification. Therefore, modification studies using natural additives are being conducted to improve PLA's properties. For example, studies using biomass-derived fillers such as rice husks have increased PLA's water absorption capacity, making it more effective in water purification applications [7]. In the context of PLA, electrospinning is widely used to produce nanofiber membranes for environmental and biomedical applications. For example, a study by Gao *et al*. [8] demonstrated that nanofiber membranes produced by electrospinning using stereo-complex polylactic acid (SC-PLA) provide high efficiency in effectively trapping particulate pollutants and pathogens. These membranes offer advantages such as high hydrophobicity, small average pore size, and high porosity, supporting their promising potential in water purification applications.

Gum arabic (GA) is a natural, complex, and branched polysaccharide obtained from acacia species (particularly Acacia senegal and Acacia seyal). Due to its biocompatibility, renewability, emulsifying capacity, and low toxicity, it is widely used in the food, pharmaceutical, cosmetic, and biomaterial industries. The arabinose and galactose-based chains in GA's structure contain a high proportion of hydrophilic functional groups. This property makes it an ideal additive in polymeric systems, particularly for imparting hydrophilicity [9]. When used in conjunction with hydrophobic polymers, GA increases surface energy and reduces contact angle, thereby improving water permeability. It also improves filtration performance by increasing porosity [10, 11]. Owing to its ability to enhance mechanical properties, GA-containing polymer membranes become more flexible and durable [12]. Furthermore, its natural origin enables the development of biodegradable and environmentally friendly products. GA's antioxidant and antimicrobial effects also provide advantages in water purification, food, and biomedical applications. For example, in a study conducted by Serio *et al.* [11], nanofiber production was carried out by electrospinning using polyvinyl alcohol and GA. It was observed that GA additive reduced the fiber diameter, increased surface roughness and improved interaction with water by reducing the contact angle. Such composite fibers prepared by electrospinning method have been shown to increase the filtration performance in membrane technology.

In this study, GA doped PLA electrospun nanofiber membranes were produced and their performance in gray water treatment was evaluated. The effectiveness of the produced membranes against contaminants such as methylene blue (MB), oil, microplastics (MP), and linear alkylbenzene sulfonate (LAS) was investigated. Basic characterization tests were performed. Additionally, the surface properties, mechanical strength, water retention, and porosity of the membranes were analyzed.

EXPERIMENTAL

Materials

PLA 2003D was procured from Nature Works, possessing a molecular weight ranging from 120,000 to 160,000 g/mol. Dimethylformamide (DMF) and chloroform ($CHCl_3$) were acquired from Isolab, Turkey. Polyethylene glycol 400 (PEG) was acquired from Merck Chemicals, Turkey. Gum arabic (CAS-No: 9000-01-5) was acquired with a purity of 98%.

Method

A mixture of DMF/chloroform comprising 12.5% PLA (30% DMF by volume) and 20% PEG (by mass of PLA) was prepared at 60 °C until uniform. Prior to spinning, 1-5% GA was incorporated into the solution using the initialization procedure. In this procedure, the GA was initially coated with a thin, diluted polymer before being incorporated into the primary polymer solution. The prepared mixture was homogenized for 30 min using an ultrasonic homogenizer (Bandelin HD4050). The electrospinning procedure was conducted at a voltage of 16 kV, at ambient temperature, with a needle-collector distance of 18 cm and a feed rate of 0.05 mL/min. The fabricated membranes were immersed in distilled water for one day, subsequently dried at ambient temperature, and cured at 60 °C for 30 min.

Membranes produced by the electrospinning method were tested in the filter system shown in Scheme 1. To determine filtration performance, rejection tests were conducted using emulsified oil (soybean oil, 2%), cationic dye (MB, 5 ppm), LAS (100 ppm), and MP (polyester, 200 ppm). The filtration performance was evaluated based on the component rejection (%) as described in Equation (1).

$$R(\%) = \left(1 - \frac{Cf}{Ci}\right) * 100 \qquad (1)$$

where R (%) is the component rejection, C_i is the solute concentration before filtration, and C_f is the solute concentration after filtration.

.

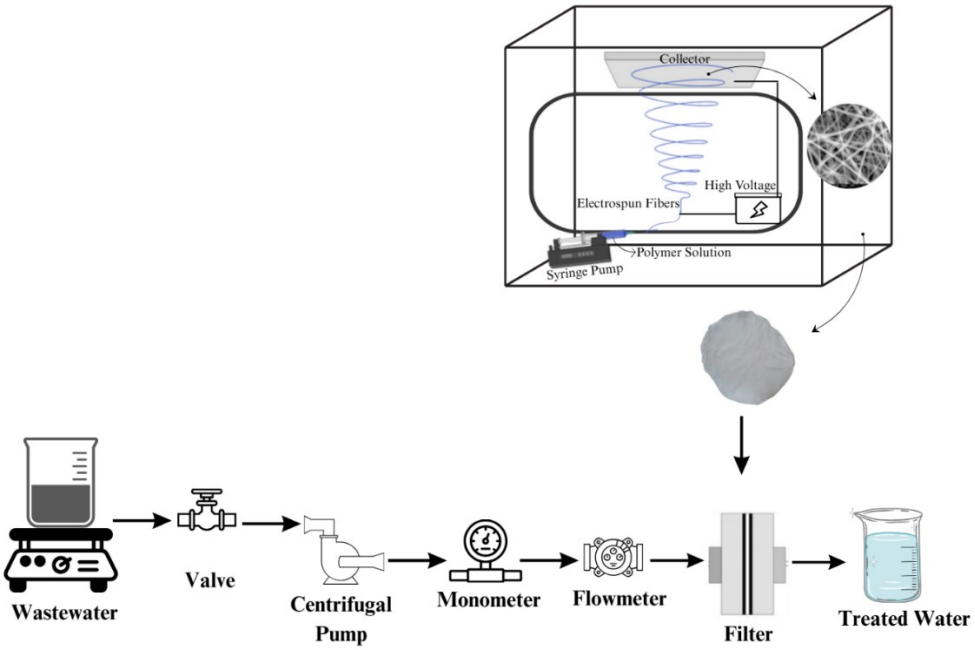

Scheme 1. Schematic diagram of membrane production and filtration test system using electrospinning.

RESULTS AND DISCUSSION

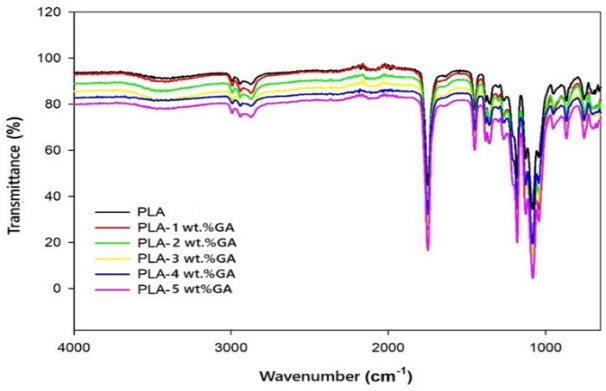

Fig. 1. FTIR spectra of PLA and GA-PLA membranes.

FTIR spectra of PLA and GA doped PLA membranes are presented in Fig. 1. In the spectrum of pure PLA, the strong band around 1750 cm^{-1} represents the characteristic ester carbonyl (C=O) stretching of PLA. The weak bands observed in the spectra in the 2995-2945 cm^{-1} range correspond to asymmetric and symmetric stretching vibrations (-CH_3) of methyl groups. In addition, the C-O-C stretching vibrations in the 1180-1080 cm^{-1} range are unique to PLA and indicate that the structural integrity of the polymer backbone is preserved [13]. The fact that GA doping doesn't produced a significant displacement effect on these bands indicates that the dopant is physically dispersed in the PLA structure without forming covalent bonds [14]. It is observed that with the increase in the doping ratio, a broad band in the range of 3300-3400 cm^1 appeared and this band was especially strong at 4% and 5% GA doping. This band can be interpreted as the contribution of hydroxyl (-OH) groups in the structure of GA to the FTIR spectrum. In the literature, it is reported that -OH groups form broad and overlapping bands in the FTIR spectra of polysaccharide-based natural additives such as GA [15].

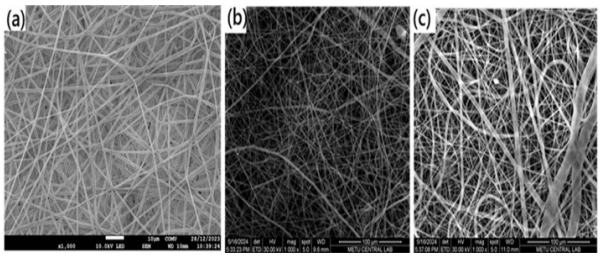

Fig. 2. SEM analysis of PLA(a), PLA-2 wt% GA(b), and PLA-4 wt% GA(c) membranes.

The scanning electron microscopy (SEM) images in Fig. 2 show the fiber morphology of pure PLA (a), 2% GA doped PLA (b) and 4% GA doped PLA (c) samples. Pure PLA fibers show a uniform, bead-free and homogeneous distribution. This structure indicates that the electrospinning conditions were optimized. At 2% GA doping, irregularity in fiber diameters and some thinning were observed. This may be due to the fact that GA increases the conductivity and viscosity of the solution [16]. 4% GA doped fibers showed thicker and more complex structures and the fibers were observed to merge in places. This indicates that the high additive rate creates negative effects such as phase separation and agglomeration.

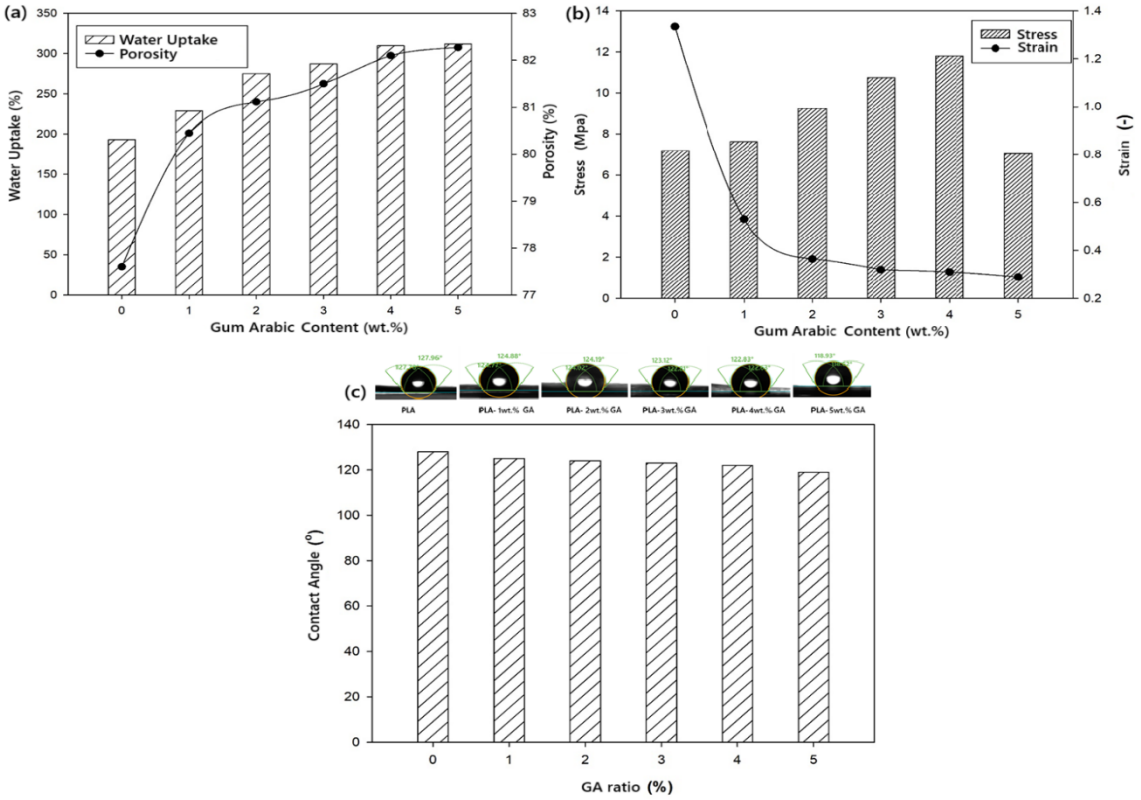

Figure 3. Water uptake and porosity results of the membranes (a), mechanical analysis of PLA and GA doped PLA membranes (b), and the contact angles of PVDF and GA doped PLA membranes (c).

As seen in Fig. 3(a), a gradual increase in both water absorption capacity and porosity was observed with the addition of 1-5% GA to the membranes. While the pure PLA membrane had a water absorption capacity of about 190%, this value reached 310% in membranes containing 5% GA. Similarly, the porosity value increased from 77% to over 82%. This increase is due to the hydrophilic nature and amorphous nature of GA. GA increases water retention by forming hydrogen bonds with water molecules thanks to its hydroxyl and carboxyl groups [17]. It is also reported in the literature that GA is used as an additive to increase porosity and improve water permeability and thus positively affects the filtration performance of membranes [18]. However, after 4%, the increase in water absorption capacity was more limited, indicating that increasing the additive amount above a certain level may indicate saturation or the structure may become too porous and the mechanical stability may decrease. This finding is important in determining the optimum admixture rate.

Figure 3(b) shows the tensile strength and strain values of PLA and GA doped PLA membranes. Significant changes were observed in the mechanical behavior of the membranes as the GA doping rate increased. Tensile strength increases at 1%-4% GA ratios. This increase can be explained by the fact that GA acts as a structural filler in the PLA matrix and increases the interaction between fibers. GA positively affected the strength by forming physical bonds with PLA thanks to its hydrophilic nature and functional groups [19]. However, there is a significant decrease in tensile strength at 5%. This can be attributed to the fact that the additive is not homogeneously distributed in the matrix, causing phase separation and creating weak points in the structure. This situation indicates that the mechanical integrity deteriorates at the point where the optimum additive ratio is exceeded. Elongation values decreased as the GA ratio increased and the structure became more brittle. This is related to the fact that GA reduces the ductility of PLA.

Figure 3(c) shows the contact angle of the membranes. While the contact angle of pure PLA is approximately 127.96°, this value decreases to 118.93° with the addition of 5% GA. This decrease is due to the hydrophilic nature of GA. GA contains many hydroxyl groups in its structure and these groups increase the wettability of the surface by forming hydrogen bonds with water molecules. This has caused the material to gain a more hydrophilic surface character with increasing GA content [17, 20].

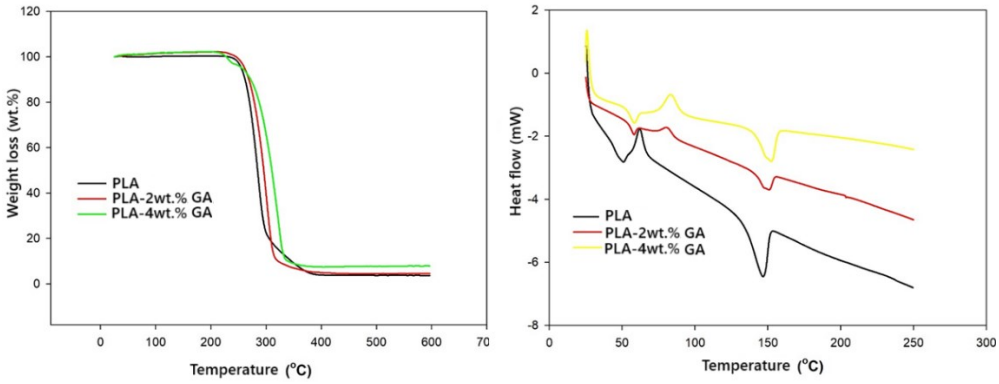

Fig 4. DSC (a) and TGA (b) analyses of PLA and GA doped PLA membranes.

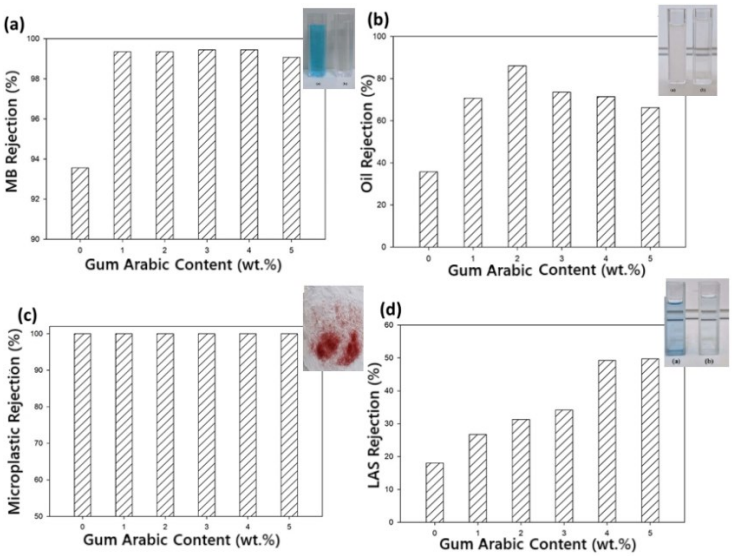

Fig. 5. Effect of GA-doped PLA membranes on rejection of pollutants: MB rejection (a), soybean oil rejection (b), microplastic rejection (c), and LAS rejection (d).

Fig. 4(a) shows TGA and Fig 4(b) DSC analysis of the membranes. The obtained TGA and DSC results reveal the positive effects of GA on PLA. The increase in thermal stability is evident by the onset of degradation at later temperatures. Moreover, changes in crystallization behavior indicate that the additive has an effect on morphology and structure ordering. The residual mass of the polymer at 2% and 4% loading increases from 3.7% to 5.5% and 8%. This shows an increase in thermal strength. GA added to PLA polymer decreased the initial enthalpy of decomposition as seen first. Because, as stated in the literature, GA does not have a degradation curve at this point and has a Tg point at 55 ºC. These findings support that the use of natural polysaccharides as additives in biodegradable polymer systems can provide not only environmental but also functional benefits [21, 22].

In Figure 5(a), while a separation value of 93% was obtained with pure PLA membrane in methylene blue filtration, dye rejection exceeded 99% in GA-containing membranes. This increase is attributed to the increase in hydrophilicity in the membrane surface properties. The hydroxyl and carboxyl groups present in the structure of GA enhance membrane-molecule interactions, facilitating the adhesion of water and dye molecules to the membrane surface [23].

The oil removal rate shown in Figure 5(b) increased with the GA content up to 2% and reached a maximum of 86%. The primary reason for this is that GA is a natural emulsifier. However, the decreasing performance beyond 3% can be attributed to excessive addition disrupting the pore structure of the membrane, negatively affecting permeability and selectivity. This highlights the need for careful optimization of the additive amount [24].

In Figure 5(c), all PLA membranes exhibit 100% microplastic rejection. Microplastic removal with electrospun nanofiber membranes is primarily governed by membrane porosity, fiber diameter, and surface charges. Reducing membrane porosity and nanofiber diameter results in greater retention of microplastic particles, as larger particles cannot pass through smaller pores. This indicates that microplastics are completely retained by mechanical

filtration due to their physical size being larger than the membrane pores [25].

Figure 5(d) shows that the LAS removal rate increases gradually with the GA ratio. The removal rate, which was 21.5% in the pure PLA membrane, reached 50% with the addition of 5% GA. Anionic surfactants such as LAS can adhere to the membrane surface due to the surface functional groups and hydrophilic structure provided by GA. Additionally, it is thought that GA enhances the adsorptive properties by increasing the surface roughness [19]. It can be said that the increase in porosity due to GA addition causes an increase in LAS removal. Porosity is suppressed after a 4% loading, and therefore LAS rejection does not increase beyond a 4% addition rate (49.6% at 5%). This indicates that GA addition structurally increases fiber hydrophilicity.

CONCLUSION

In this study, PLA membranes incorporated with GA were successfully fabricated and applied for the treatment of simulated gray water containing various pollutants. The incorporation of GA resulted in a substantial enhancement of the membrane's surface properties, including hydrophilicity, porosity, and water uptake capacity. These properties are critical for efficient pollutant separation. The characterization results demonstrated that the addition of GA not only enhanced the thermal stability and mechanical strength of the PLA membranes—as evidenced by the increase in tensile strength from 7 MPa to 11.8 MPa—but also had a positive effect on their filtration performance. The GA-modified membranes demonstrated remarkable rejection efficiencies, with 100% efficiency for microplastics, 99% for methylene blue, 87% for emulsified oil, and 50% for anionic surfactant (LAS). These results indicate that GA functions as an effective functional additive, compensating for the inherent limitations of PLA in water treatment applications.

Acknowledgement: *This current study was supported by the Çanakkale Onsekiz Mart University Scientific Research Projects Coordination Unit. (Project No: FYL-2024-4825).*

REFERENCES

1. M. O. Aijaz, S. B. Yang, M. R. Karim, I. A. Alnaser, A. D. Alahmari, F. S. Almubaddel, A. K. Assaifan, *Membranes*, **13**, 54 (2023).
2. Z. He, Y. Li, B. Qi, *Environ. Sci. Pollut. Res.*, **29**, 54025 (2022).
3. S. Z. Hu, Y. F. Deng, L. Li, N. Zhang, T. Huang, Y. Z. Lei, Y. Wang, *Langmuir*, **39**, 3770 (2023).
4. Y. Tang, Z. Cai, X. Sun, C. Chong, X. Yan, M. Li, J. Xu, *Polymers*, **14**, 2004 (2022).
5. A. A. Nayl, A. I. Abd-Elhamid, N. S. Awwad, M. A. Abdelgawad, J. Wu, X. Mo, S. Bräse, *Polymers*, **14**, 1594 (2022).
6. L. Persano, A. Camposeo, C. Tekmen, D. Pisignano, *Macromol. Mater. Eng.*, **298**, 504 (2013).
7. E. Vengadesan, S. Morakul, S. Muralidharan, P. K. Pullela, A. Alarifi, T. Arunkumar, *Discover Appl. Sci.*, **7**, 161 (2025).
8. D. Gao, R. Zhao, X. Yang, F. Chen, X. Ning, *Membranes*, **11**, 819 (2021).
9. S. Patel, A. Goyal, *Int. J. Food Prop.*, **18**, 986 (2015).
10. W. Falath, A. Sabir, K. I. Jacob, *Carbohydr. Polym.*, **155**, 28 (2017).
11. F. Serio, A. F. da Cruz, A. Chandra, C. Nobile, G. R. Rossi, E. D'Amone, C. C. de Oliveira, *Int. J. Biol. Macromol.*, **188**, 764 (2021).
12. S. S. Borkotoky, T. Ghosh, P. Bhagabati, V. Katiyar, *Int. J. Biol. Macromol.*, **125**, 159 (2019).
13. J. R. Riba, J. Cailloux, R. Cantero, T. Canals, M. L. Maspoch, *Polym. Test.*, **65**, 264 (2018).
14. D. Garlotta, *J. Polym. Environ.*, **9**, 63 (2001).
15. M. Ibrahim, M. Krejčík, K. Havlíček, S. Petrík, M. Eldessouki, *J. Eng. Fibers Fabr.*, **15**, 1558925020946451 (2020).
16. N. Rezeki, S. Surini, *Pharm. Sci. Res.*, **6** (2), 3 (2019).
17. Y. Manawi, V. Kochkodan, A. W. Mohammad, M. A. Atieh, *J. Membr. Sci.*, **529**, 95 (2017).
18. [18] Y. Manawi, V. Kochkodan, E. Mahmoudi, D. J. Johnson, A. W. Mohammad, M. A. Atieh, *Sci. Rep.*, **7** (1), 15831 (2017).
19. M. M. Aji, S. Narendren, M. K. Purkait, V. Katiyar, *J. Water Process/ Eng.*, **38**, 101569 (2020).
20. M. P. Arrieta, J. López, S. Ferrándiz, M. A. Peltzer, *Polym. Test.*, **32** (4), 760 (2013).
21. L. Suryanegara, A. N. Nakagaito, H. Yano, *Compos. Sci. Technol.*, **69** (7–8), 1187 (2009).
22. J. Jamaludin, F. Adam, R. A. Rasid, Z. Hassan, *Chemical Engineering Research Bulletin*, **19**, 80 (2017).
23. L. Kang, J. Zhang, G. Wu, M. X. Zhang, S. C. Chen, Y. Z. Wang, *ACS Sustain. Chem. Eng.*, **6** (9), 11783 (2018).
24. X. Cheng, Y. Tang, B. Wang, J. Jiang, *Waste Biomass Valorization*, **9**, 123 (2018).
25. M. A. Hanif, N. Ibrahim, F. A. Dahalan, U. F. M. Ali, M. Hasan, A. A. Jalil, *Sci. Total Environ.*, **810**, 152115 (2022).

Bulgarian Chemical Communications, Volume 57, Issue 3 (pp. 235-244) 2025 DOI: 10.34049/bcc.57.3.BS-AT-EK

Infrared drying of aronia berries: the effect of sustainable pretreatments on drying behavior

B. Salık, A. Tan, E. Kıpçak*

Department of Chemical Engineering, Faculty of Chemical and Metallurgical Engineering, Yildiz Technical University, Davutpasa Campus, Davutpasa Street No. 127, 34220, Esenler, Istanbul, Turkey

Accepted: August 17, 2025

This study investigates the infrared drying of aronia berries (*Aronia Melanocarpa*) and evaluates the effect of ultrasonic pretreatment on drying efficiency. Aronia berries are considered important functional foods due to their high antioxidant content and nutritional value. However, their short harvest season and limited shelf life hinder their commercialization. To address this, ultrasonic pretreatment was applied prior to drying to enhance process efficiency. Experiments were conducted at drying temperatures of 60°C, 70°C, and 80°C. For each temperature, aronia berries were subjected to ultrasonic pretreatment for 1, 3, 5, 10, 15, and 20 min before drying. Drying durations of pretreated samples were compared to those of untreated samples. Drying time and moisture content were measured, and the drying kinetics were analyzed. Kinetic parameters, including effective moisture diffusivity and activation energy were calculated, and the drying behavior was modeled using 14 commonly applied drying models used in the literature. The results demonstrated that ultrasonic pretreatment significantly enhanced drying performance, up to 10 min of pretreatment. The shortest drying time (120 min), highest effective moisture diffusivity ($1.20 \cdot 10^{-9}$ m^2/s) and highest activation energy (5137.6 J/mol) were obtained at 80°C infrared drying with 10 min of ultrasonic pretreatment.

Keywords: Aronia berry, drying kinetics, infrared drying, ultrasonic pretreatment

INTRODUCTION

Recently, there has been growing interest in fruits that are rich in natural antioxidants. Among them, aronia berries (*Aronia Melanocarpa*) stand out in the fields of food science and nutrition. This prominence is attributed to its exceptional concentrations of vitamins, minerals, polyphenols, flavonoids, and anthocyanins, as well as its potential to offer a wide range of health benefits. Aronia berries exhibit high antioxidant capacity and possess anti-inflammatory, anticancer, antimicrobial, antiviral, and antidiabetic properties. Furthermore, they have shown potential in inhibiting the development of some cancer types, such as colon cancer, breast cancer, leukemia, and even cancer stem cells. Their potential role in reducing the risk of cardiovascular disease has also been highlighted [1-5]. Beyond being a rich source of antioxidants, aronia berries hold great promise for applications in functional foods, nutraceuticals, and as a natural additive in the dairy, meat, and beverage industries [6-8]. Due to their high anthocyanin content, they exhibit a deep dark purple to black pigmentation, making them a valuable natural food colorant - particularly in products aimed at avoiding artificial additives [9, 10]. However, aronia berries have a very short harvest period, typically spanning from late summer to early fall. They also possess a high moisture content at the time of harvest, as they naturally thrive in wet habitats [1, 4]. As a result, they are prone to rapid deterioration, which significantly limits their shelf life. Therefore, it's crucial to implement effective preservation methods - not only to prolong shelf life, but also to maintain the functional and nutritional properties of the fruit. Drying stands out as one of the most efficient methods for food preservation.

Drying is the process of moisture removal from a substance, which helps slow down degradation and preserve quality. Under controlled conditions, moisture can be effectively removed from materials through drying, thereby preventing microbial growth and moisture-induced spoilage such as decay and mold. This is particularly important for food products with limited harvest periods, like aronia berries, as drying allows for better preservation of large quantities. Additionally, drying reduces product size, which lowers costs associated with packaging, transportation, storage, and processing, while also extending shelf life and enhancing product value [11-14]. However, the drying process is often time- and energy-intensive, as it requires the evaporation of water through the application of heat or airflow. It poses a particular challenge for berries, which are highly sensitive to heat and prone to the degradation of valuable bioactive compounds during dehydration. This challenge necessitates the exploration of new drying technologies that

* To whom all correspondence should be sent:
E-mail: *eyildir@yildiz.edu.tr*

minimize such detrimental effects [11]. Infrared drying can be considered among these promising methods.

Infrared drying enables the uniform transfer of thermal energy in the form of electromagnetic radiation. In this method, heat is applied directly to the food as radiant energy [15]. Water is known to absorb infrared radiation strongly, causing the O–H bonds to vibrate upon energy absorption. This internal heating, which takes place very rapidly, increases the water vapor pressure within the food, resulting in pore expansion and a higher rate of moisture removal [15]. Infrared drying is capable of removing moisture quickly and efficiently. Apart from reducing drying times, it also offers benefits such as lower energy consumption, simpler equipment requirements, improved product quality, and reduced overall costs [11, 16, 17].

Berries are generally coated with a waxy protective layer that hinders moisture removal during drying. This barrier can be mitigated through pretreatment techniques that alter the fruit's surface structure. Such pretreatments help to reduce the drying time, and thereby the consumption of energy, while improving the overall quality of the food product [11]. Recently, sustainable thermal and non-thermal pretreatments have been developed to avoid the adverse effects of conventional approaches, such as nutrient loss, chemical absorption, and structural damage [11]. One such sustainable non-thermal technique is ultrasonic pretreatment.

Ultrasonic (US) pretreatment involves applying mechanical waves with frequencies between 20 kHz and 1000 kHz, typically using water or osmotic solutions as the medium in an ultrasonic bath [11-13]. These waves generate a cavitation phenomenon known as the "sponge effect," where alternating compression and expansion cycles create pressure gradients within the food. These gradients lead to the formation of microchannels inside the tissues of the plants, softening the food and facilitating moisture release through ruptured cell walls. Furthermore, ultrasonic treatment helps eliminate dissolved oxygen in intracellular spaces, which enhances both heat and mass transfer during drying [11-14]. In addition to shortening drying durations, ultrasonic pretreatment is recognized as a green, environmentally friendly, non-toxic, and safe technology. Its operation at ambient temperature is another advantage, helping to preserve the nutritional value and sensory qualities of the food product [11, 12, 16, 17].

Until now, studies on aronia berries have predominantly concentrated on the extraction of bioactive compounds and their antioxidant properties, with relatively limited emphasis on drying processes. However, understanding the drying behavior of aronia berries is crucial for researchers and industry stakeholders aiming to fully exploit their potential, particularly through innovative techniques such as infrared drying and sustainable pretreatments. This study, therefore, investigates the infrared drying behavior of aronia berries, incorporating ultrasonic pretreatment. Experiments were conducted at 60°C, 70°C, and 80°C drying temperatures. For each temperature, aronia berries were subjected to ultrasonic pretreatment for 1, 3, 5, 10, 15, and 20 min before drying. The drying behavior of the pretreated berry samples was compared with that of untreated ones. Parameters including moisture content, drying time, and drying rate were evaluated, and the data were analyzed in terms of drying kinetics. Kinetic parameters of effective moisture diffusivity (D_{eff}) and activation energy (E_a) were determined, and 14 commonly used drying models were applied to characterize the drying curves.

EXPERIMENTAL

Sample preparation

The aronia berries employed in this study were bought from a local farmers market in Bulgaria. Aronia berries of similar size, with an approximate radius of 0.55 cm, were selected for the experiments. In each trial, 5 ± 0.1 g of berries were used and cut into two halves horizontally to facilitate thin-layer diffusion analysis.

Experimental methods

The initial moisture content (M_0) was calculated through AOAC method [18], by drying the aronia berry samples in a hot air oven (KH-45, Kenton, Guangzhou, China) at 105°C, for 3 h. This procedure yielded an initial moisture content of 2.9373 kg water/kg dry matter (equivalent to 74.60% on wet basis).

For infrared drying, the aronia samples were initially weighed on tared aluminum plates using the scale of a Radwag MA 50.R infrared dryer (Radwag, Radom, Poland). After weighing, the aronia samples underwent ultrasonic pretreatment. The pretreatments prior to infrared drying experiments were made by using an Alex Machine AXUY-06LAB ultrasonic bath filled with distilled water and operating at 120 W (Isolab, Escau, Germany). The pretreatment durations were 1, 3, 5, 10, 15, and 20 min. After pretreatment, all samples were halved, reweighed, and the new measurement was recorded as the initial weight for drying. The infrared drying experiments were carried out at 60°C, 70°C, and

80°C. The sample weights were recorded every 15 min to track moisture loss and drying rate. Two repetitions were conducted for each condition, and the results were averaged. Drying was terminated once the moisture content reached 7%.

Kinetic calculations

The moisture content (M), moisture ratio (MR), and drying rate (DR) of the aronia berries at each experimental condition were calculated by using Equations 1, 2 and 3 [19-21]:

$$M = \frac{m_w}{m_d} \quad (1)$$

$$MR = \frac{M_t - M_e}{M_0 - M_e} \quad (2)$$

$$DR = \frac{M_{t+dt} - M_t}{dt} \quad (3)$$

In Equation 1, m_w and m_d are the water content and the dry matter content of the aronia berries (kg), respectively. In Equations 2 and 3, t is the drying time (min), M_0 is the initial moisture content, M_e is the equilibrium moisture content, M_t is the moisture content at time t, and M_{t+dt} is the moisture content at the time t+dt (kg water/kg dry matter). Because of its relatively low value, M_e was neglected in the calculations [19, 20].

In this study, moisture diffusion for the drying process is modeled using Fick's second law of diffusion, based on several assumptions. These include negligible shrinkage, symmetrical moisture diffusion about the center, and constant diffusivity. Under these conditions, Fick's second law for moisture diffusion in a thin layer of thickness 2L is expressed as Equation 4 below [20, 22]:

$$MR = \frac{8}{\pi^2}\sum_{n=1}^{\infty}\frac{1}{(2n+1)^2}\exp\left(-\frac{(2n+1)^2\pi^2 D_{eff}\times t}{4L^2}\right) \quad (4)$$

Here, n is a positive integer that is assumed as 1 for long drying durations. D_{eff} is the effective moisture diffusivity (m^2/s), L is one half of the thickness of the sample (m), and t is the time (s). With taking n as 1, Equation 4 can be rewritten in terms of Equation 5 in the linearized form [20, 22, 23]:

$$\ln(MR) = \ln\left(\frac{8}{\pi^2}\right) - \left(\pi^2\frac{D_{eff}\times t}{4L^2}\right) \quad (5)$$

By using Equation 5, D_{eff} can be determined from the slope of the ln(MR) *versus* t graph. On the other hand, D_{eff} relation with temperature can be investigated through Arrhenius equation (Equation 6) given below [22, 24]:

$$D_{eff} = D_o\exp\left(-\frac{E_a}{R\times(T+273.15)}\right) \quad (6)$$

In Equation 6, E_a is the activation energy (kJ/mol), D_0 is the preexponential factor (m^2/s), R is the universal gas constant (kJ/mol·K) and T is the drying temperature (°C). By using this equation, E_a can be determined from the slope of $\ln(D_{eff})$ *versus* 1/T graph. Evaluating activation energy is a key aspect of drying kinetics, as it represents the energy supplied by the drying system to facilitate moisture removal. Generally, higher activation energy indicates a more rapid drying process [22].

Mathematical modeling

Fourteen mathematical models commonly cited in the literature were evaluated to describe the drying behavior of aronia berries. These models are presented in Table 1.

Table 1. The mathematical drying models applied to the experimental data [20, 22]

Model name	Model equation
Aghbaslo *et al.*	$MR = \exp(-k_1 t / (1 + k_2 t))$
Alibas	$MR = a\times\exp((-kt^n) + bt) + g$
Henderson & Pabis	$MR = a\times\exp(-kt)$
Jena *et al.*	$MR = a\times\exp(-kt + b\sqrt{t}) + c$
Lewis	$MR = \exp(-kt)$
Logarithmic	$MR = a\times\exp(-kt) + c$
Midilli & Kucuk	$MR = a\times\exp(-kt^n) + bt$
Page	$MR = \exp(-kt^n)$
Parabolic	$MR = a + bt + ct^2$
Peleg	$MR = a + t/(k_1 + k_2 t)$
Two Term Exponential	$MR = a\times\exp(-kt) + (1-a)\times\exp(-kat)$
Verma *et al.*	$MR = a\times\exp(-kt) + (1-a)\times\exp(-gt)$
Wang & Singh	$MR = 1 + at + bt^2$
Weibull	$MR = a - b\times\exp(-(kt)^n)$

In Table 1, the coefficients used in the models include constants a, b, c, and g; the drying coefficients k, k_1, and k_2; model-specific exponent n; with drying time t in min. Nonlinear regression was performed using the Levenberg-Marquardt algorithm in Statistica 8 (Statsoft Inc., Tulsa, OK). The performance of the drying models was evaluated using the coefficient of determination (R^2), reduced chi-square (χ^2), and root mean square error (RMSE), which are defined in Equations 7 to 9, respectively [22-24].

$$R^2 = 1 - \frac{\sum_{i=1}^{N}\left(MR_{exp,i} - MR_{pre,i}\right)^2}{\sum_{i=1}^{N}\left(MR_{exp,i} - \left(\frac{1}{n}\right)MR_{exp,i}\right)^2} \quad (7)$$

$$\chi^2 = \frac{\sum_{i=1}^{N}\left(MR_{exp,i} - MR_{pre,i}\right)^2}{N - z} \quad (8)$$

$$RMSE = \left(\frac{1}{N}\sum_{i=1}^{N}\left(MR_{exp,i} - MR_{pre,i}\right)^2\right)^{\frac{1}{2}} \quad (9)$$

In Equations 7-9, MR_{exp} and MR_{pre} are the experimental moisture ratios and predicted moisture

ratios, respectively. N is the total number of experiments, and z is the number of constants that were used in the model equations. The mathematical model that gave the highest R^2, while giving the lowest χ^2 and RMSE, was selected as the most convenient model to describe the drying data of the aronia berries.

RESULTS AND DISCUSSION

Moisture content and drying rate results

Fig. 1 illustrates the changes of moisture content (on the left) and drying rate (on the right) of aronia berries dried at 60°C, 70°C, and 80°C without ultrasonic pretreatment. The initial moisture content of 2.9373 kg water/kg dry matter reduced to 0.2590, 0.1940, and 0.1808 kg water/kg dry matter at temperatures of 60°C, 70°C, and 80°C, respectively. The time required to reach final moisture content of 7% (wet basis) was 450 min at 60°C, 225 min at 70°C, and 165 min at 80°C.

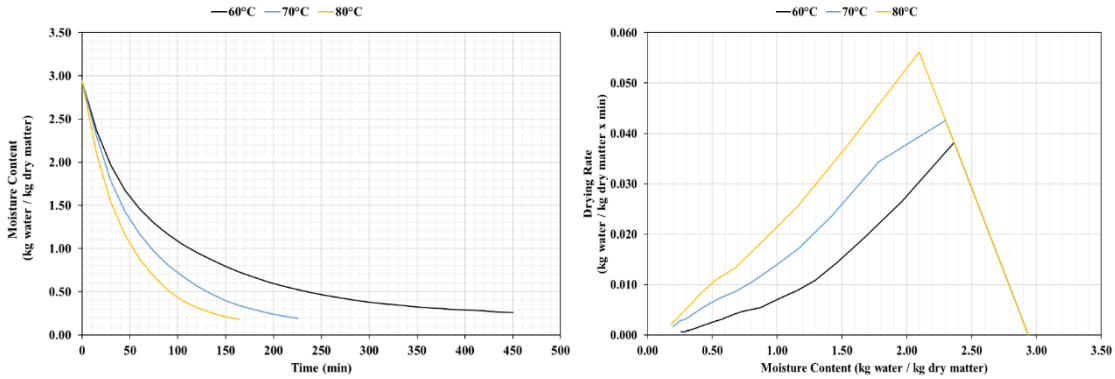

Fig. 1. Drying curves (left) and drying rate curves (right) for the infrared drying of aronia berries without pretreatment

The impact of ultrasonic pretreatment on drying performance is presented in Fig. 2, which shows the changes in moisture content and drying rate of aronia berries. In all graphs, results for 60°C are shown with black curves, whereas 70°C with blue, and 80°C with orange curves. Considering the effect of 1-min ultrasonic pretreatment (Fig. 2a), the initial moisture content of 2.9373 kg water/kg dry matter was reduced to 0.2021, 0.1927, and 0.1850 kg water/kg dry matter at 60°C, 70°C, and 80°C, respectively. The corresponding times to reach a final moisture content of 7% were 345 min at 60°C, 225 min at 70°C, and 165 min at 80°C. It was observed that 1 min of ultrasonic pretreatment significantly reduced the drying time at 60°C, while having no noticeable effect at 70°C and 80°C compared to the untreated drying times. As the ultrasonic pretreatment duration increased to 3 min (Fig. 2b), drying times further decreased at all temperatures. The drying durations were reduced to 315 min at 60°C, 210 min at 70°C, and 150 min at 80°C. A continued decrease in drying time was observed with a 5 min pretreatment (Fig. 2c), with drying times of 285 min at 60°C, 195 min at 70°C, and 120 min at 80°C. The final moisture contents were 0.1991, 0.1962, and 0.1881 kg water/kg dry matter, respectively.

Further increasing the ultrasonic pretreatment time to 10 min resulted in additional drying time reductions at 60°C (225 min) and 70°C (165 min), while the drying time at 80°C remained constant at 120 min. This ultrasonic duration yielded the shortest drying times across all pretreatment conditions. As presented in Fig. 2d, the final moisture contents of the aronia berries were 0.1992, 0.1718, and 0.1679 kg water/kg dry matter for 60, 70, and 80°C, respectively.

With a 15-min ultrasonic pretreatment, the initial moisture content of 2.9373 kg water/kg dry matter decreased to 0.2049, 0.1795, and 0.1433 kg water/kg dry matter at 60°C, 70°C, and 80°C, respectively. 240 min, 165 min, and 120 min were the drying durations at these temperatures. Compared to the 10-min ultrasonic pretreatment, a 15-min pretreatment resulted in a 15-min increase in drying time at 60°C, while no change was observed at 70°C and 80°C (Fig. 2e). Fig. 2f shows the effect of a 20-min ultrasonic pretreatment. The final moisture contents were 0.2010 kg water/kg dry matter at 60°C, 0.1939 at 70°C, and 0.1531 at 80°C. In the 60°C experiment, the drying time was observed to increase by 30 min, reaching 270 min. At 70°C, the drying duration increased to 180 min, whereas the drying time at 80°C remained unchanged at 120 min.

Overall, it can be concluded that increasing the ultrasonic pretreatment duration up to 10 min enhanced drying efficiency, particularly at lower drying temperatures. However, extending the pretreatment beyond 10 min resulted in a trend of increasing drying times at all temperatures, possibly due to changes in microstructure or moisture migration resistance.

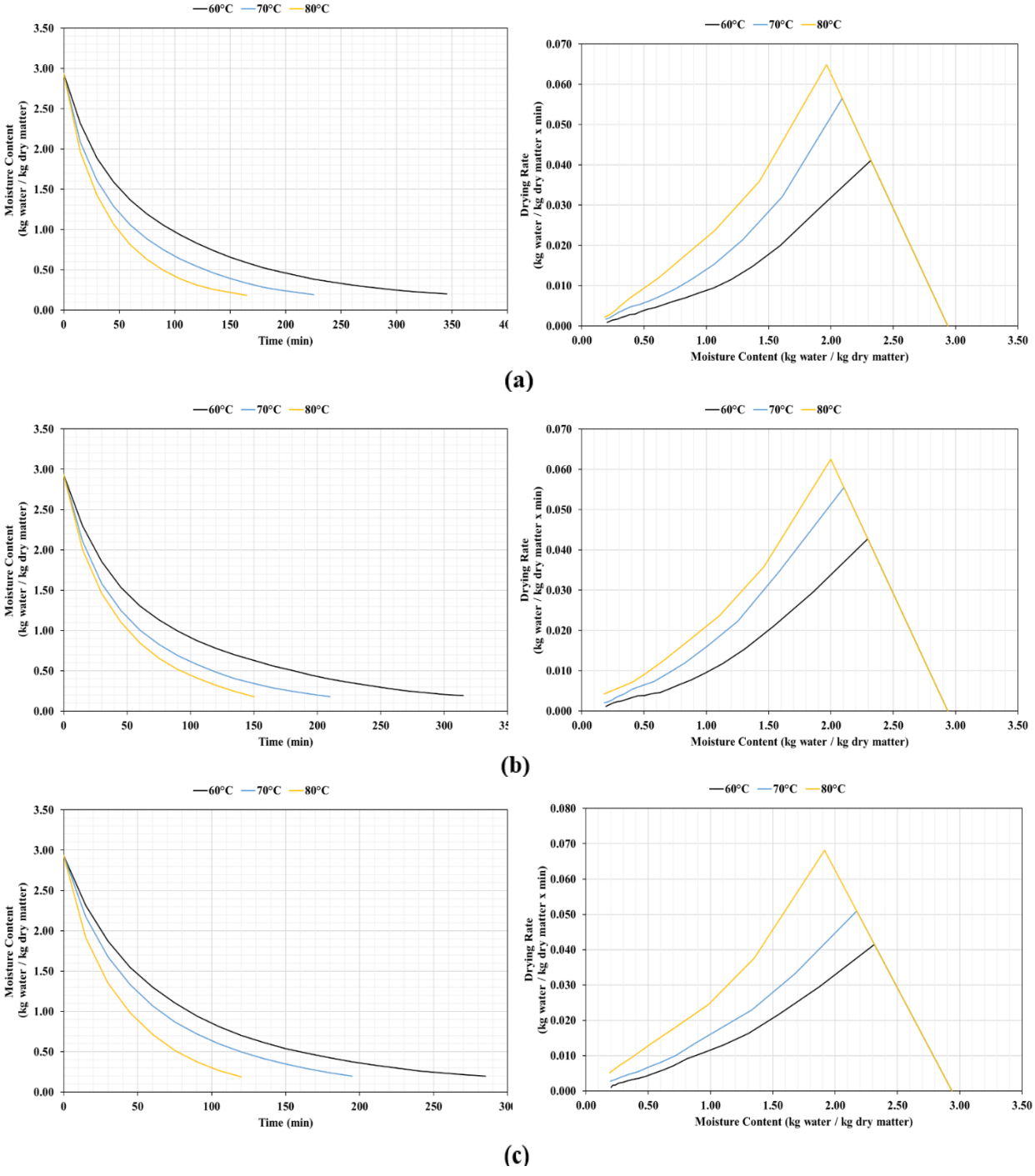

Fig. 2. The drying curves (left) and the drying rate curves (right) for the infrared drying of aronia berries with an ultrasonic pretreatment of (a) 1 min, (b) 3 min, and (c) 5 min

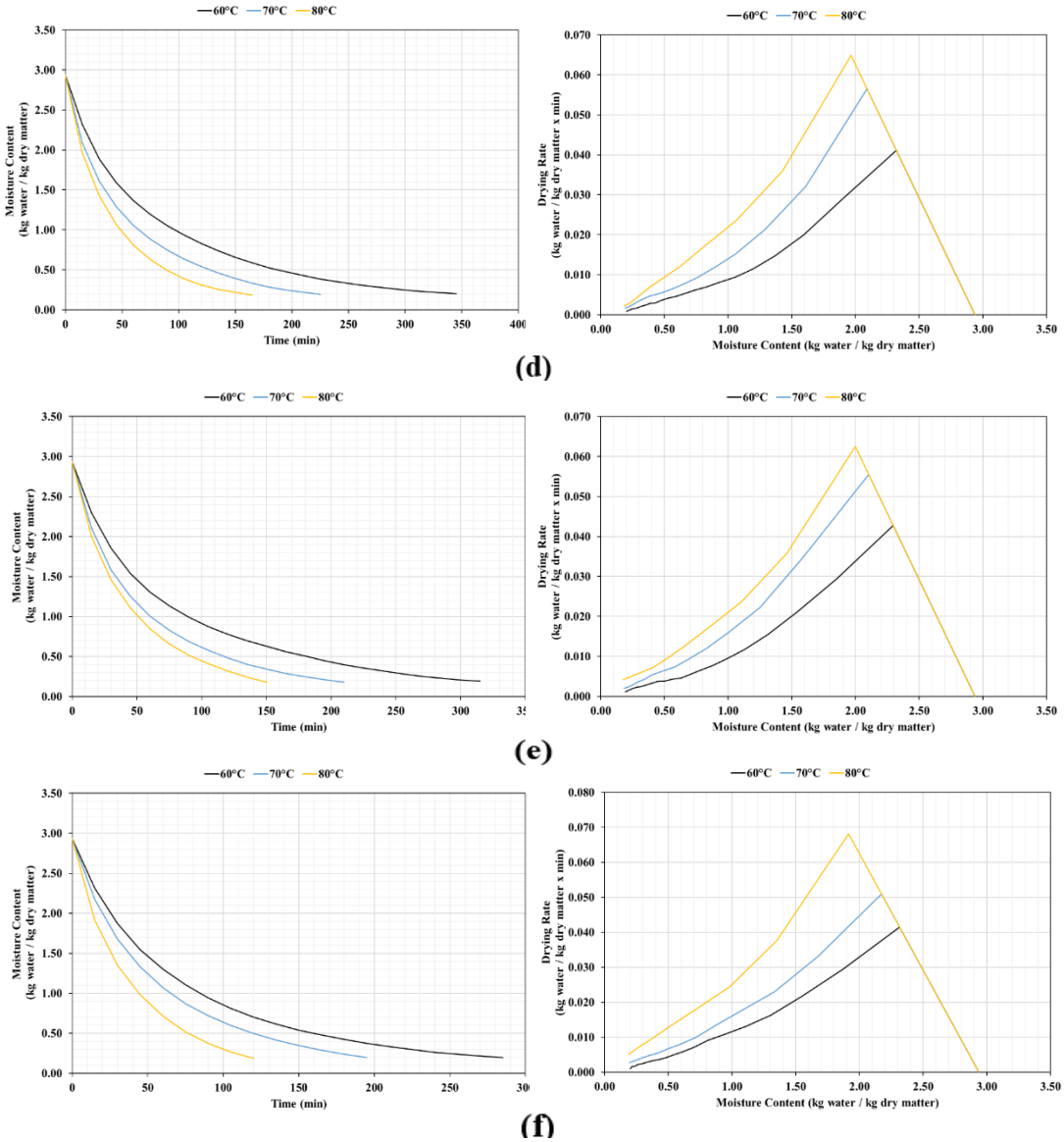

Fig. 2. (continued). The drying curves (left) and the drying rate curves (right) for the infrared drying of aronia berries with an ultrasonic pretreatment of (d) 10 min, (e) 15 min, and (f) 20 min

Several studies in the literature have investigated the impact of ultrasonic pretreatment on the drying behavior of agricultural products. Ni *et al*. [25] examined the influence of ultrasonic pretreatment, applied for durations ranging from 10 to 50 min, on the electrohydrodynamic drying of goji berries. The authors reported that ultrasonic pretreatment up to 30 min enhanced the drying rate. However, longer durations (40 and 50 min) caused a decrease in the drying rate, although all values remained lower than those of untreated samples. Yu *et al*. [26] investigated the effects of 2, 4, and 6 min of ultrasonic pretreatment on the hot air drying kinetics of *Camellia oleifera* seeds at 60 - 80°C. The experimental results showed that higher drying temperatures reduced drying time. While ultrasonic pretreatment also shortened drying time, the 2-min pretreatment duration was more effective than 4 or 6 min. The authors concluded that increasing pretreatment duration does not necessarily improve drying performance, as extended sonication may damage tissue structure and obstruct moisture migration pathways [26]. Similarly, Tan *et al.* [27] investigated ultrasonic-assisted alkali pretreatment in the hot air drying of seabuckthorn berries. Pretreatment durations of 5, 10, and 15 min resulted in drying time reductions of 5.08%, 3.06%, and 6.14%, respectively. These enhancements were said to be due to the dissolution of the waxy surface layer and the formation of micropores. However, prolonged ultrasonic pretreatment resulted in reduced drying rates, likely due to the disruption of

moisture migration pathways on the berry surface caused by extended ultrasound exposure.

Fernandes and Rodrigues [28] examined the dehydration of sapota using ultrasonic pretreatment durations of 10, 20, and 30 min prior to oven drying at 60°C. A 5.2% water loss was observed for 10 min of pretreatment, which decreased to 4.0% with a 30 min duration. In a related work on the ultrasound assisted drying of pumpkin, Karlovic *et al*. [29] tested pretreatment durations of 30, 45, and 60 min. Increasing the pretreatment duration from 30 to 45 min reduced drying time across all ultrasound power levels, attributed to structural changes caused by cavitation. However, further extension to 60 min yielded only marginal improvements. The authors concluded that excessive pretreatment durations increase energy costs without significant benefits [29]. Salehi *et al.* [30] studied the impact of ultrasonic pretreatment (5, 10, and 15 min) on drying behavior of cooked faba beans at 70°C. They found that ultrasound enhanced water extraction by disrupting the diffusion boundary layer through rapid compressions and expansions. Sonication energy was also reported for weakening the intermolecular forces of bound water, breaking chemical bonds, thereby decreasing the resistance for mass transfer. In another study, Fernandes *et al.* [31] evaluated ultrasonic pretreatment durations ranging from 10 to 90 min in the air drying of papaya. An increase in water loss was observed with longer pretreatment durations, indicating a positive correlation between ultrasound exposure time and moisture removal.

Drying kinetics results

As discussed in the Experimental part, the effective moisture diffusivity (D_{eff}) values were determined using Equation 5, based on the slope of ln(MR) *versus* drying time graphs for all experimental data. Once D_{eff} was determined, the activation energy (E_a) for each pretreatment condition was found by using the linearized form of Equation 6, from the slope of ln(D_{eff}) *versus* 1/T plots. The results for all experimental conditions investigated in this study are summarized in Table 2. As presented in Table 2, the effective moisture diffusivity values increased with both increasing drying temperature and ultrasonic pretreatment duration up to 10 min. For infrared drying of aronia berries without pretreatment, D_{eff} values ranged between $2.57 \cdot 10^{-10}$ - $8.70 \cdot 10^{-10}$ m^2/s. With a 1 min ultrasonic pretreatment, this range increased to $3.80 \cdot 10^{-10}$ - $8.74 \cdot 10^{-10}$ m^2/s. Ultrasonic pretreatment effect was particularly pronounced at 60°C drying temperature, and this positive effect was observed up to 10 min of pretreatment. At this optimum pretreatment duration, D_{eff} was calculated as $5.95 \cdot 10^{-10}$ m^2/s at 60°C, $8.52 \cdot 10^{-10}$ m^2/s at 70°C, and $1.20 \cdot 10^{-9}$ m^2/s at 80°C, while latter being the highest D_{eff} value obtained in the present study.

Table 2. Drying times, D_{eff} and E_a values for the infrared drying of aronia berries

Pretreatment type	Drying parameter	60°C	70°C	80°C
Without pretreatment	Drying time (min)	450	225	165
	D_{eff} (m^2/s)	$2.57 \cdot 10^{-10}$	$6.10 \cdot 10^{-10}$	$8.70 \cdot 10^{-10}$
	E_a (J/mol)		4032.9	
1 min US pretreatment	Drying time (min)	345	225	165
	D_{eff} (m^2/s)	$3.80 \cdot 10^{-10}$	$6.13 \cdot 10^{-10}$	$8.74 \cdot 10^{-10}$
	E_a (J/mol)		4103.1	
3 min US pretreatment	Drying time (min)	315	210	150
	D_{eff} (m^2/s)	$4.20 \cdot 10^{-10}$	$6.53 \cdot 10^{-10}$	$9.13 \cdot 10^{-10}$
	E_a (J/mol)		4176.2	
5 min US pretreatment	Drying time (min)	285	195	120
	D_{eff} (m^2/s)	$4.72 \cdot 10^{-10}$	$6.83 \cdot 10^{-10}$	$1.14 \cdot 10^{-9}$
	E_a (J/mol)		4294.2	
10 min US pretreatment	Drying time (min)	225	165	120
	D_{eff} (m^2/s)	$5.95 \cdot 10^{-10}$	$8.52 \cdot 10^{-10}$	$1.20 \cdot 10^{-9}$
	E_a (J/mol)		5137.6	
15 min US pretreatment	Drying time (min)	240	165	120
	D_{eff} (m^2/s)	$5.46 \cdot 10^{-10}$	$8.43 \cdot 10^{-10}$	$1.18 \cdot 10^{-9}$
	E_a (J/mol)		4551.5	
20 min US pretreatment	Drying time (min)	270	180	120
	D_{eff} (m^2/s)	$4.71 \cdot 10^{-10}$	$7.54 \cdot 10^{-10}$	$1.17 \cdot 10^{-9}$
	E_a (J/mol)		4340.5	

For 15 and 20 min of pretreatment, D_{eff} values were observed to show a decreasing tendency. The activation energy values followed a similar trend. Without ultrasonic pretreatment, the activation energy was found as 4032.9 J/mol. The highest E_a value, 5137.6 J/mol, was recorded when a 10-min ultrasonic pretreatment was applied. However, when the pretreatment duration was increased further to 20 min, E_a decreased to 4340.5 J/mol.

Consistent findings have been reported in the literature regarding ultrasonic pretreatment's impact on effective moisture diffusivity. In the electrohydrodynamic drying of goji berries, Ni *et al*. [25] observed the highest D_{eff} value ($4.4573 \cdot 10^{-10}$ m^2/s) at a pretreatment duration of 20 min. Longer durations of 30, 40, and 50 min resulted in decreasing D_{eff} values. Similarly, Fernandes and Rodrigues [28] investigated the oven drying of sapota at 60°C, using ultrasonic pretreatment durations of 10, 20, and 30 min. The D_{eff} increased from $4.76 \cdot 10^{-9}$ m^2/s to $5.80 \cdot 10^{-9}$ m^2/s as the sonication duration increased from 10 to 20 min. However, extending the pretreatment to 30 min led to a slight decrease in D_{eff} to $5.38 \cdot 10^{-9}$ m^2/s. In a recent study, Salehi *et al*. [30] also reported a positive correlation between ultrasonic pretreatment time and D_{eff} values during the drying of faba beans, indicating improved moisture diffusivity with increased sonication duration.

Mathematical modeling results

The mathematical modeling results for the infrared drying of aronia berries, both with and without ultrasonic pretreatment, are presented in Table 3. The table displays the performance of the best-fitting model for each experimental condition, identified based on the highest coefficient of determination (R^2), and the lowest values of the reduced chi-square (χ^2) and the root mean square error (RMSE) among the 14 models evaluated.

Table 3. Statistical parameters of the best mathematical models for infrared drying of aronia berries, with and without ultrasonic pretreatment

Infrared drying, without pretreatment		
60°C	70°C	80°C
Parabolic a = 0.997162 b = -0.002657 c = 0.000002 R^2 = 0.999891 χ^2 = 0.000181 RMSE = 0.013056	Logarithmic a = 1.904526 k = 0.002245 c = -0.905562 R^2 = 0.999979 χ^2 = 0.000003 RMSE = 0.001634	Midilli & Kucuk a = 0.999604 k = 0.003781 n = 0.956175 b = -0.001353 R^2 = 0.999965 χ^2 = 0.000003 RMSE = 0.001458
Infrared drying, 1 min ultrasonic pretreatment		
60°C	70°C	80°C
Midilli & Kucuk a = 1.001346 k = 0.044791 n = 0.762047 b = 0.000016 R^2 = 0.999927 χ^2 = 0.000000 RMSE = 0.000420	Verma et al. a = 0.645558 k = 0.010447 g = 0.052267 R^2 = 0.999980 χ^2 = 0.000001 RMSE = 0.000994	Alibas a = 1.022881 k = 0.040817 n = 0.839702 b = 0.000204 g = -0.022830 R^2 = 0.999998 χ^2 = 0.000000 RMSE = 0.000532
Infrared drying, 3 min ultrasonic pretreatment		
60°C	70°C	80°C
Verma et al. a = 0.612461 k = 0.007166 g = 0.034810 R^2 = 0.999984 χ^2 = 0.000000 RMSE = 0.000672	Verma et al. a = 0.626539 k = 0.011200 g = 0.046393 R^2 = 0.999990 χ^2 = 0.000001 RMSE = 0.000673	Alibas a = 0.849635 k = 0.041469 n = 0.880241 b = -0.000780 g = 0.150360 R^2 = 0.999998 χ^2 = 0.000000 RMSE = 0.000486

Infrared drying, 5 min ultrasonic pretreatment		
60°C	70°C	80°C
Alibas a = 0.865617 k = 0.024311 n = 0.901521 b = -0.000303 g = 0.135035 R^2 = 0.999983 χ^2 = 0.000001 RMSE = 0.001122	Verma et al. a = 0.711448 k = 0.012051 g = 0.044981 R^2 = 0.999990 χ^2 = 0.000001 RMSE = 0.000817	Alibas a = 1.098238 k = 0.041008 n = 0.830144 b = 0.000316 g = -0.098187 R^2 = 0.999995 χ^2 = 0.000001 RMSE = 0.000723
Infrared drying, 10 min ultrasonic pretreatment		
60°C	70°C	80°C
Verma et al. a = 0.205842 k = 0.045454 g = 0.010960 R^2 = 0.999997 χ^2 = 0.000000 RMSE = 0.000096	Alibas a = 0.909268 k = 0.038373 n = 0.854349 b = -0.000479 g = 0.090911 R^2 = 0.999989 χ^2 = 0.000002 RMSE = 0.001147	Alibas a = 0.974563 k = 0.039675 n = 0.904756 b = -0.000132 g = 0.025408 R^2 = 0.999999 χ^2 = 0.000000 RMSE = 0.000371
Infrared drying, 15 min ultrasonic pretreatment		
60°C	70°C	80°C
Verma et al. a = 0.514585 k = 0.029105 g = 0.008158 R^2 = 0.999974 χ^2 = 0.000000 RMSE = 0.000166	Verma et al. a = 0.208568 k = 0.072575 g = 0.015577 R^2 = 0.999997 χ^2 = 0.000000 RMSE = 0.000536	Alibas a = 0.915657 k = 0.047883 n = 0.881610 b = -0.000587 g = 0.084308 R^2 = 0.999998 χ^2 = 0.000000 RMSE = 0.000481
Infrared drying, 20 min ultrasonic pretreatment		
60°C	70°C	80°C
Verma et al. a = 0.339860 k = 0.040146 g = 0.008482 R^2 = 0.999988 χ^2 = 0.000000 RMSE = 0.000409	Alibas a = 0.864808 k = 0.029947 n = 0.968746 b = -0.000434 g = 0.135342 R^2 = 0.999993 χ^2 = 0.000001 RMSE = 0.000879	Midilli & Kucuk a = 0.999741 k = 0.034798 n = 0.934494 b = 0.000032 R^2 = 0.999990 χ^2 = 0.000002 RMSE = 0.001079

CONCLUSION

This study investigated the effect of ultrasonic pretreatment durations (1, 3, 5, 10, 15, and 20 min) on the infrared drying of aronia berries at drying temperatures of 60°C, 70°C, and 80°C. Increasing drying temperature resulted in shorter drying times. Ultrasonic pretreatment also enhanced drying efficiency, particularly up to 10 min of application. For infrared drying without pretreatment, drying times ranged between 165 and 450 min. The application of short sonication durations notably reduced drying time, especially at lower temperatures. The shortest drying times (120-225 min) were obtained with 10 min of ultrasonic pretreatment. Beyond this duration, drying times increased at 60 and 70°C, while remaining unchanged at 80°C. A similar tendency was encountered for effective moisture diffusivity and activation energy. Without pretreatment, D_{eff} values ranged from $2.57 \cdot 10^{-10}$ - $8.70 \cdot 10^{-10}$ m^2/s. With 10 min of ultrasonic pretreatment, this range increased to $5.95 \cdot 10^{-10}$ - $1.20 \cdot 10^{-9}$ m^2/s. However, longer

sonication durations resulted in a decrease in D_{eff}. Likewise, the activation energy increased from 4032.9 J/mol (no pretreatment) to 5137.6 J/mol with 10 min of pretreatment, before decreasing to 4350.5 J/mol at 20 min. Statistical analysis indicated that the models proposed by Verma *et al.,* Alibas, and Midilli & Kucuk best fit the experimental drying data.

Overall, it can be concluded that ultrasonic pretreatment of moderate durations improves the drying performance of aronia berries. As a safe, sustainable, and environmentally friendly technique, ultrasound can be effectively applied in infrared drying of aronia berries. However, excessive sonication should be avoided, as extended durations may lead to pore collapse, microchannel blockage, and hindered moisture migration, ultimately reducing drying efficiency.

REFERENCES

1. T. Jurendić, M. Ščetar, *Antioxidants*, **10** (7), 1052 (2021).
2. A. Sidor, A. Drożdżyńska, A. Gramza-Michałowska, *Trends Food Sci. Technol.*, **89**, 45 (2019).
3. A. S. Aksoy, *Turkish Journal of Agriculture - Food Science and Technology*, **11** (10): 2027 (2023).
4. D. Shi, J. Xu, L. Sheng, K. Song, *Molecules*, **29**, 1388 (2024).
5. Y. Zhang, Y. Zhaoa, X. Liu, X. Chen, C. Ding, L. Dong, J. Zhang, S. Sun, Q. Ding, S. Khatoom, Z. Cheng, W. Liu, L. Shen, F. Xiao, *J. Future Foods*, **1-2**, 168 (2021).
6. I. Buljeta, L. Jakobek, D. Kenjerić, A. Pichler, J. Šimunović, M. Kopjar, *Croat. J. Food Sci. Technol.*, **16** (1), 64 (2024).
7. M. Tolić, I. L. Jurčević, I. P. Krbavčić, K. Marković, N. Vahčić, *Food Technol. Biotechnol*. **53** (2), 171 (2015).
8. A. Wójtowicz, M. Combrzynski, B. Biernacka, R. Rózyło, M. Bakowski, K. Wojtunik-Kulesza, J. Mołdoch, I. Kowalska, *Plants*, **12**, 3276 (2023).
9. S. E. Kulling, H. M. Rawel, *Planta Med.*, 74, 1625 (2008).
10. T. Kaloudi, D. Tsimogiannis, V. Oreopoulou, *Molecules*, **27**, 4375 (2022).
11. M. Pateiro, M. Vargas-Ramella, D. Franco, A. Gomes da Cruz, G. Zengin, M. Kumar, K. Dhama, J. M. Lorenzo, *Food Chem.: X*, **16**, 100465 (2022).
12. K. J. Mothibe, M. Zhang, J. Nsor-atindana, Y. Wang, *Drying Technol.*, **29**, 1611 (2011).
13. L. Deng, A. S. Mujumdar, Q. Zhang, X. Yang, J. Wang, Z. Zheng, Z. Gao, H. Xiao, *Crit. Rev. Food Sci. Nutr.*, **59** (9), 1408 (2019).
14. R. Pandiselvam, A. Y. Aydar, N. Kutlu, R. Aslam, P. Sahni, S. Mitharwal, M. Gavahian, M. Kumar, A. Raposo, S. Yoo, H. Han, A. Kothakota, *Ultrason. Sonochem.*, **92**, 106261 (2023).
15. . Skåra, T. Løvdal, D. Skipnes, N. N. Mehlomakulu, C. R. Mapengo, R. O. Baah, M. N. Emmambux, *Food Rev. Int.*, **39** (9), 7197 (2023).
16. T. Belwal, C. Cravotto, M. A. Prieto, P. R. Venskutonis, M. Daglia, H. P. Devkota, A. Baldi, S. M. Ezzat, L. Gómez-Gómez, M. M. Salama, L. Campone, L. Rastrelli, J. Echave, S. M. Jafari, G. Cravotto, *Drying Technol.*, **40**:8, 1539 (2022).
17. Y. Sun, M. Zhang, A. Mujumdar, *Food Eng. Rev.*, **11**, 61 (2019).
18. AOAC, Association of Official Analytical Chemists, Official Methods of Analysis of AOAC International, 16th edn., AOAC International, Rockville, MD, 1995.
19. A. S. Kipcak, E. M. Derun, N. Tugrul, I. Doymaz, *Chem. Ind. Chem. Eng. Q.*, **27(3)**, 279 (2021).
20. E. Kıpçak, *Journal of the Turkish Chemical Society, Section B: Chemical Engineering*, **6** (1), 1 (2023).
21. O. Ismail, O. G. Kocabay, *Turk J. Fish. & Aquat. Sci.*, **18**, 259 (2018).
22. Z. E. Taşçı, E. Kıpçak, *Bulg. Chem. Commun.*, **55** (3), 256 (2023).
23. M. Ayriksa, A. Bahadir, A. Dağdeviren, K. Roshanaei, T. Coşkun, G. K. Ongun, M. Özkaymak, *Journal of Poyitechnic*, **25 (3)**: 1217 (2022).
24. C. Tunckal, I. Doymaz, *Renewable Energy*, **150**, 918 (2020).
25. J. Ni, C. Ding, Y. Zhang, Z. Song, W. Xu, *J. Food Process Preserv.*, **44**, 14600 (2020).
26. J. Yu, D. Huang, X. Ling, C. Xun, W. Huang, J. Zheng, L. Zhang, *Ind. Crops Prod.*, **222**, 119467 (2024).
27. S. Tan, Y. Xu, L. Zhu, Z. Geng, Q. Zhang, X. Yang, *Foods*, **11**, 3675 (2022).
28. F. A. N. Fernandes, S. Rodrigues, *Drying Technol.*, **26**, 1232 (2008).
29. S. Karlović, F. Dujmić, S. R. Brnčić, M. B. Sabolović, A. N. Grassino, M. Škegro, M. A. Šimić, M. Brnčić, *Processes*, **11**, 469 (2023).
30. F. Salehi, M. Amiri, S. Ghazvineh, *Ultrason. Sonochem.*, **110**, 107040 (2024).
31. F. A. N. Fernandes, F. I. P. Oliveira, S. Rodrigues, *Food Bioprocess Technol.*, **1**, 339 (2008).

Bulgarian Chemical Communications, Volume 57, Issue 3 (pp. 245-248) 2025 DOI: 10.34049/bcc.57.3.GO-DE-AF

Application of gas foaming technique for improving porous properties of chitosan-polyvinyl alcohol (CS/PVA) nanofiber-based biodegradable scaffolds

G. Özdemir[1]*, D. Erkoyuncu[1], A. Kantürk Figen[1]

[1]*Yildiz Technical University, Department of Chemical Engineering, Davutpasa, Istanbul, 34210, Türkiye*

Accepted: August 17, 2025

The human body consists of systems, systems are organs, organs are cells and extracellular matrix. The extracellular matrix has an important role in the human body with the task of connecting cells to each other. Due to various reasons, diseases in which the extracellular matrix is damaged have been witnessed from the past to the present. Tissue engineers are in research to improve and prevent this damage. As a result of these researches, the production of tissue scaffolds has started. Tissue scaffolds are structures designed to mimic the extracellular matrix. These scaffolds can perform functions belonging to the extracellular matrix, such as providing mechanical strength, helping to establish communication with the surrounding tissue to respond to physiological and biological changes, as well as forming suitable adhesion surfaces for cells. They may also contribute to the regeneration of the true extracellular matrix. Tissue scaffolds can be produced by many methods and one of them is the gas foaming technique. In our study, tissue scaffolds produced by this method were used and it was aimed to increase the porosity of these scaffolds.

In the experiments, tissue scaffolds were obtained by electro-spinning method and $NaBH_4$-methanol solution was used for gas foaming method. As a result, it was observed that the porosity properties of the tissue scaffolds inflated in 0.1M solution were increased. These observations were determined and documented by the analysis results.

Keywords: Polymer chemistry; biotechnology; electro-spinning; gas foaming; nanofiber; material science

INTRODUCTION

Polymeric biomaterials consist of organic polymers with varying properties and topologies. They are adaptable, easy to process, and offer customizable mechanical properties. Polymeric biomaterials can be either synthetic or naturally occurring [1].

Synthetic polymers such as polyethylene, poly(lactic-co-glycolic acid) (PLGA), and polyurethane are commonly used in biomedical applications due to their tunable properties. These polymers offer advantages such as biocompatibility, biodegradability, and controlled drug release [2].

Natural polymers derived from sources such as collagen, chitosan, and alginate often mimic the extracellular matrix components found in tissues. These biomaterials create a favorable environment promoting cell anchorage, multiplication, and new tissue formation. Natural polymers are used in wound dressings, tissue engineering scaffolds, and drug delivery systems [3]. Examples of different applications of polymeric biomaterials include:

• In drug delivery systems, polymeric matrices can be used to encapsulate and release drugs slowly, reducing side effects while enhancing therapeutic efficacy [4].

• In tissue engineering, biologically degradable polymers are used as structural scaffolds to aid in cell growth, tissue regeneration, and wound healing.

• In contact lenses, hydrogels (a type of polymeric biomaterials), are used to create soft contact lenses due to their superior oxygen permeability, biocompatibility, and comfort [5].

Various processing techniques exist to synthesize polymers and then convert them into the desired biomaterial form. After producing the desired biomaterial, surface modification techniques are used to increase the bioactivity, biocompatibility and functionality of polymeric biomaterials. Techniques related to these steps can be listed as follows.

• *Step-growth polymerization*. This reaction of difunctional monomers produces linear or branching polymers. Two typical step-growth polymerization techniques are polycondensation and polyaddition. Polyesters, polyurethanes, and polycarbonates are examples of polymers produced using step-growth polymerization [6].

• *Chain growth polymerization*. Chain-growth polymerization is the sequential addition of monomers to an active polymer chain, resulting in polymer growth. Chain growth polymerization methods include radical polymerization, anionic polymerization, and controlled/ living

* To whom all correspondence should be sent:
E-mail: *giizemmozdmr@gmail.com*

polymerization. Polymers such as polyethylene, polystyrene and polyacrylates are produced by chain growth polymerization [7].

The originality of the project is that the application of gas foaming technique to increase the porous properties of chitosan/polyvinyl alcohol (CS/PVA) nanofiber scaffolds synthesized using electrospinning technique for scaffold applications and the parametric analysis of this technique are not presented in the literature.

No studies were found on the application of gas foaming technique to improve the porous properties of CS/PVA nanofiber-based biodegradable scaffolds for drug delivery systems or as an aid in cell growth, tissue regeneration, and wound healing. Our study addressed three research questions:

1. What are the optimum conditions under which CS/PVA structured nanofibers can be synthesized by electrospinning technique?

2. Can the porous structure of the scaffold be improved by gas foaming technique? Can porosity be increased with this technique?

3. What are the effects of the change in parametric values (time, amount, etc.) of $NaBH_4$ selected as the chemical to be used and the amount of methanol used as a solvent on the porosity of the scaffold?

EXPERIMENTAL

The application of gas foaming technique in this study has four main steps.

Step I: Preparation of electrospinning solutions

Preparation of suitable solutions for the electrospinning method As detailed in Coşkuner's publication [8], polyvinyl alcohol (PVA) will be dissolved into deionized water under continuous stirring at 90 °C for 2 h to obtain a homogeneous solution with a concentration of 10% by weight. Following dissolution, the PVA solution will be allowed to cool to room temperature under continuous stirring, and mixing will continue for 24 hours. Separately, CS powder will be dissolved in a 2% by volume solution of acetic acid in water at room temperature under moderate stirring to produce a homogeneous 2.5% by weight solution. The CS and PVA solutions will then be combined in a mass ratio of 1:4 to prepare the CS/PVA mixing. The mixing solution will be stirred continuously for 24 hours at room temperature.

Step II: Synthesis of CS/PVA nanofibers

The nanofibers will be created by electrospinning at standard conditions using a plate collector wrapped in aluminum foil. Both pure and composite polymer solutions will be delivered through 10 mL syringes using a pump that precisely regulates the flow rate. The pick-up distance between the tip and the pick-up will be modified in accordance with the characteristics of the solution used. The process parameters will be empirically adjusted based on the observed Taylor cone initiation. Nanofibers will collect on flat plate collectors, subsequently allowed to dry at ambient conditions, and then preserved in a vacuum desiccator prior to characterization analyses. As the optimum condition of electrospinning, 33 kV will be applied. Collection distance is 20 cm, flow rate is 1.2 mLh^{-1}.

Step III: Characterization of CS/PVA nanofibers

Morphological characterization of fresh and used nanofibers will be performed by scanning electron microscopy (SEM). The nanofibers will be embedded in the carbon band, and an Au-Pd coating will be applied to each sample prior to analysis. Fiber diameters will be measured using the equipment's software for the extraction of numerical averages and corresponding distribution curves. Representative diameter values will be obtained by capturing images from various regions of the samples and performing random measurements across the fibers. The chemical structure of each nanofiber will be investigated in terms of chemical bonds and functional groups using Fourier transform infrared spectroscopy (FT-IR). In the attenuated total reflection (ATR) mode, measurements will be conducted with a resolution of 1 cm^{-1} using a 532 nm laser, across the spectral region spanning 650-4000 cm^{-1}.

To evaluate the potential of nanofibers for biosensing applications, it is essential to assess their stability under thermal conditions and in aqueous environments. Measurements of contact angle, *in vitro* degradation behavior, swelling capacity in phosphate-buffered saline (PBS), and morphological analysis *via* scanning electron microscopy (SEM) will all be used to determine stability. Nanofiber biodegradation will be assessed *in vitro* by quantifying sample weight loss in a PBS solution, according to a well-known approach. Initially, each sample will be dissected and weighed (W_0). Subsequently, the samples will be immersed in a PBS solution with a pH of 7.4, maintained at 37 °C for a duration of 21 days. At predetermined intervals on days 7, 14, and 21, samples will be retrieved from the solution, gently rinsed, vacuum-dried, and reweighed (W_d). *In vitro* degradation will be calculated according to the following equation [8]:

$$\textit{In vitro}\ \text{degradation}\ (D, \%) = [(W_0 - W_d) / W_0] \times 100 \quad (1)$$

The degree of swelling of the nanofibers will be analyzed by evaluating their liquid uptake capacity in PBS. The nanofiber samples will be divided into uniform square segments, their initial dry weights (W_d) will be recorded. These samples will then be immersed in a PBS solution and maintained at 37 °C. The individual sample pieces will be retrieved and weighed by wiping off excess water (W_w). The degree of swelling will be calculated using the following equation, which represents PBS absorption [8]:

$$\text{Swelling degree (SD, \%)} = [(W_w - W_d) / W_d] \times 100 \quad (2)$$

Step IV: Application of gas foaming technique to CS/PVA scaffold

Gas foaming technique will be used to increase the porosity of the obtained CS/PVA nanofiber structured biodegradable scaffold. The basis of this technique is to increase the porosity by passing through the fiber structure during the release of the H_2 gas produced by the reaction of the $NaBH_4$ compound with methanol [9].

$$NaBH_4 + 4\ CH_3OH \rightarrow NaB(OCH_3)_4 + 4\ H_2 \quad (3)$$

Different $NaBH_4$ solutions in the range of 0.1-0.3 M will be prepared with 20 mL of methanol. These solutions will be added to the CS/PVA nanofiber scaffold obtained by the electrospinning method. Hydrogen gas output will be checked at different times determined between 0-24 h. Then, the tissue scaffolds prepared under different conditions will be dried in a vacuum oven at 50 °C for 24 h. The change of porous properties of the tissue scaffolds using gas foaming technique will be measured by mercury porosimetry. The obtained data will be compared. It is aimed to increase the porosity feature by at least 50%.

RESULTS AND DISCUSSION

Due to various reasons, tissue production has been targeted for the regeneration of damaged extracellular matrix, and increasing the porosity of this tissue is essential in our study to promote cell settlement and tissue regeneration within the artificial tissue. Electrospun tissue scaffolds were used in the experiments, and their porosity was increased by applying the gas foaming technique. Nanofibers obtained by the electrospinning method were inflated using a $NaBH_4$-methanol solution through the gas foaming technique. Solutions with different concentrations were prepared, and the best increase in porosity was observed with a 0.1M $NaBH_4$-methanol solution. Additionally, the nanofiber control sample, which was only soaked in methanol, showed no change in porosity. Consequently, it was observed that the porosity of the tissue scaffolds inflated in the 0.1M solution was increased. These observations were determined through the analysis results and documented as follows:

Under an optical microscope, only polymeric bonds were observed in the control sample, whereas in the inflated sample, polymeric bonds and bubble-like structures were also observed. These bubble-like structures indicate the porosity feature in the sample. As illustrated in Figure 1, the optical microscope images of the control sample at ×1000 and ×500 magnifications are presented, while Figure 2 shows the optical microscope image of the inflated sample at ×50 magnification.

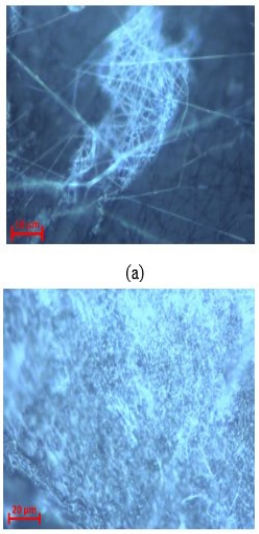

Figure 1. The image of the control sample under the optical microscope; (a) ×1000, (b) ×500

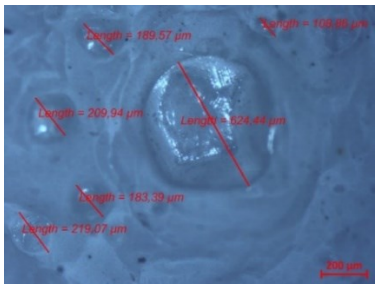

Figure 2. Measured image of the inflated sample under ×50 optical microscope

The increase in the porosity property of CS/PVA nanofibers in which gas foaming technique with $NaBH_4$-methanol was applied, was observed with an 8% increase in permeability as a result of FT-IR analysis, as shown in Figure 3.

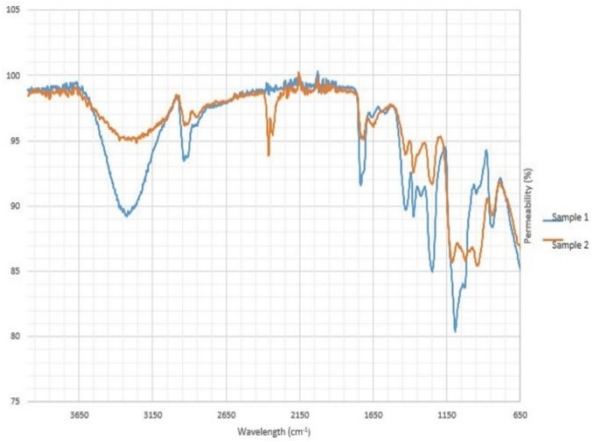

Figure 3. FT-IR spectroscopy result of CS/PVA nanofibers; (sample 1) control sample, (sample 2) swollen with $NaBH_4$–methanol solution

When the polymeric bond thicknesses of the swollen sample states (b) were observed compared to the control sample (a), it was concluded that there was an increase of 66.7% with the gas foaming technique which is depicted in Figure 4.

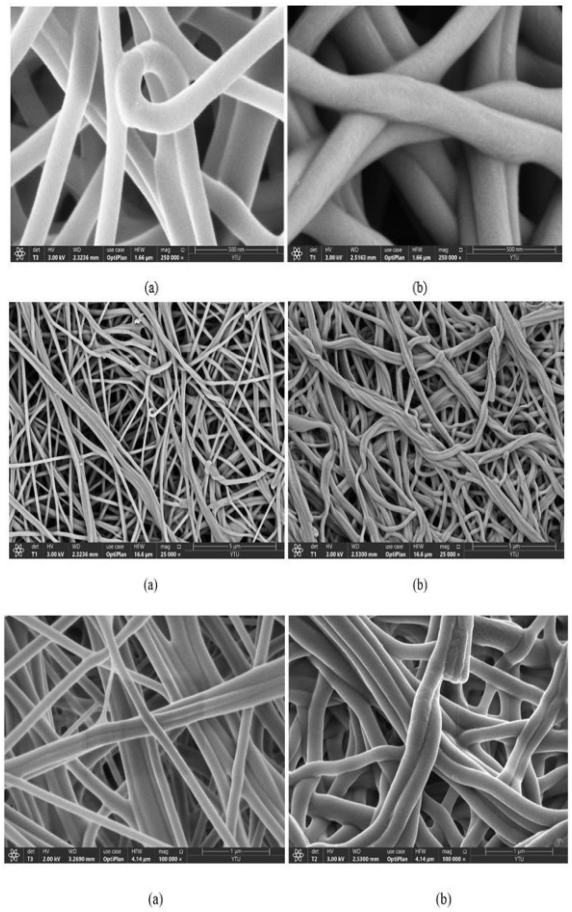

Figure 4. SEM images of the samples; (a) Control sample, (b) Sample swollen with $NaBH_4$-methanol solution

In the results of BET analysis, the surface area increased between 1.65 and 1.85 times. In addition, it was determined that the gas foaming technique increased the pore volume by 2 times compared to the control sample.

It was concluded that the nanofibers were not cross-linked as the cause of the fragmentation in the in vitro degradation and swelling degree tests.

It is suggested that nanofiber tissue that is broken down in PBS solution, which has a pH similar to body fluid, can be used in drug carrier applications. The nanofiber CS/PVA regenerated by cross-linking is predicted not to be broken down in the PBS solution, and is recommended for use in tissue regeneration or medical filters.

CONCLUSION

This study aims to produce tissue and enhance its porosity for use in the regeneration of extracellular matrix damaged due to various reasons. Porosity is crucial for cell attachment within the artificial tissue and for promoting tissue regeneration. This successfully conducted study highlights the potential of the gas foaming technique to enhance the porosity of nanofibers. In this way, nanofibers with high porosity are recommended to be used in supporting wound healing, creating artificial tissues and organs, implant materials used for bone repair, placement and growth of cartilage cells, production of biosensors used in biomedical applications and filters.

Acknowledgement: *The authors acknowledge and thank financial support from TUBITAK 2209-A-Research Project Support Programme for Undergraduate Students/2022-1.*

REFERENCES

1. R. More, A.Haubold, J. Bokros, *Biomater. Sci.,* **3**, 209 (2013).
2. H.K. Makadia, S.J. Siegel, *Polym.,* **3**, 1377 (2011).
3. E. Troy, M.A. Tilbury, A.M. Power, J.G. Wall, *Polym.,* **13**, 3321 (2021).
4. R. Langer, *Science,* **249**, 1527 (1990).
5. E.S. Place, N.D. Evans, M.M. Stevens, *Nat. Mater.,* **8**, 457 (2009).
6. M. Zhang, S.M. June, T.E. Long, *Polym. Sci.: Compr. Ref.,* **5**, 7 (2012).
7. M.C. Tanzi, S. Farè, G. Candiani, *Found. Biomater. Eng.,* **1**, 3 (2019).
8. F.B. Coşkuner, E.Y. Başaran, I.S. Bektaş, F.A. Kantürk, *Int. J. Biol. Macromol.,* **192**, 999 (2021).
9. M.K. Joshi, H.R. Pant, A.P. Tiwari, H.J. Kim, C.H. Park, C.S. Kim, *Chem. Eng. J.,* **275**, 79 (2015).

Bulgarian Chemical Communications, Volume 57, Issue 3 (pp. 249-251) 2025 DOI: 10.34049/bcc.57.3.YB-AD

The effect of modifiers on the microstructure of road bitumen and strength of asphalt concrete: a mini-review

Y. Byzova*, A. Dyuryagina, K. Ostrovnoy, T. Shirina

Manash Kozybayev North Kazakhstan University, Department of Chemistry and Chemical Technologies, Faculty of Mathematics and Natural Sciences, Pushkin Str.86, Petropavlovsk, Kazakhstan

Accepted: August 17, 2025

This review explores the effect of bitumen microstructure on the mechanical strength and cohesive properties of modified bitumen. It is shown that the morphology of structures plays a key role in ensuring high performance properties of bitumen road surfaces. Special attention is paid to the effect of polymer, surfactant, and nanomodifiers on the size, shape, and stability of microstructures in the bulk phase of the bitumen binder. The latest data on the mechanisms of bee-like structures formation, their morphology, the correlation of structure sizes with the cohesive strength of bitumen, as well as practical aspects of modifying bitumen compositions to achieve optimal strength characteristics are analyzed.

Keywords: bitumen microstructure, bee-like structures, bitumen modification, strength of asphalt concrete

INTRODUCTION

Bitumen is a highly dispersed colloidal system widely used in road construction and waterproofing materials.

The composition of petroleum bitumen can be characterized by four classes of compounds [1]:

- Saturated hydrocarbons, correlated with the softening temperature of the material and empirically measured by the penetration index;
- Aromatic and naphthenic constituents which are partially hydrogenated aromatic compounds;
- Resins, in some cases called polar aromatic components, which contain many alkyl residues and functional groups;
- Asphaltene molecules formed by a conjugated carbon core having functional groups and heterocyclic compounds and bearing alkyl side chains grafted directly to these nuclei.

Asphaltenes are associated with highly aromatic (H/C~1.0-1.3) and high molecular weight molecules [2], while resins have a higher H/C ratio (1.2-1.7), lower aromaticity and lower molecular weight compared to asphaltenes [3, 4].

Asphaltenes are the least-soluble bitumen fraction consisting of an almost continuous spectrum of several polyaromatic molecular forms and can be extracted or separated from other fractions by precipitation using a large volume of n-alkanes to crude oil [5].

MATERIALS AND METHODS

For gathering all articles, directly corresponding to the topic, databases Scopus and Google Scholar were used. A period till 2025 was set to identify the most recent research papers. Involvement criterion was the use of keywords “bitumen microstructure” or “bee-like structures” in the title. Fourteen manuscripts were comprehensively reviewed.

RESULTS AND DISCUSSION

The mechanical properties of bitumen binders are determined not only by their chemical composition, but also by their supramolecular architecture which is formed due to the self-assembly of asphaltenes and interaction with other bitumen fractions: resins, saturated and aromatic components [6].

In recent decades, atomic force microscopy (AFM) and transmission electron microscopy (TEM) have shown that characteristic morphological elements, the so-called bee-like structures, form on the bitumen surface [7]. These structures which have a characteristic periodic relief, are associated with the orderly arrangement of asphaltene aggregates and play an important role in ensuring the strength and stability of bitumen at various temperatures and loads, which is a prerequisite for the operation of bitumen as part of asphalt concrete road surfaces.

* To whom all correspondence should be sent:
E-mail: *yuliyabyzovva@gmail.com*

Modification of bitumen in order to increase its strength characteristics is one of the urgent tasks of pavement materials science. It is important to take into account how various modifiers, such as polymers (e.g., SBS), surfactants, and nanoparticles, affect the morphology of bee-like structures and, consequently, the macroscopic strength of bitumen binders.

Bee–like structures are periodic wave-like formations on the bitumen surface, observed using AFM as alternating elevations and depressions with a characteristic wavelength of 0.5-2.5 μm and an amplitude of 5-50 nm [7]. Studies by Loeber *et al.* [8] have shown that these structures are formed due to the π-π runoff of aromatic fragments of asphaltenes, leading to the formation of dense ordered aggregates at the bitumen/air or bitumen/substrate interface.

The concentration of asphaltenes plays an important role in the formation of bee-like structures: the higher their content, the higher the probability of formation of large aggregates. The ratio of resins and aromatic oils also significantly affects the microstructure of bitumen: resins stabilize dispersed asphaltene aggregates, preventing their coalescence [6].

According to Pauli *et al.* [9], bitumen with a higher degree of polarity (high content of asphaltenes and resins) exhibits more pronounced and larger bee-like structures. In contrast, bitumen with a high content of aromatic oils has less pronounced or does not exhibit these structures at all.

The size and morphology of bee-like structures have a direct effect on the cohesive strength of bitumen, i.e. on the energy required to destroy its internal structure. Loeber *et al.* [8] found that small and evenly distributed structures contribute to the formation of a stronger network of intermolecular interactions, increasing cohesive energy. On the contrary, large, sparse bee-like structures can contribute to brittle fracture due to the presence of "weak zones" in the bulk phase of bitumen. Works by Zhang *et al*. [10] on modified bitumen with SBS showed that the optimal size of bee-like structures ensures maximum resistance of asphalt concrete to fatigue failure; minimal tendency to coating cracking at low temperatures; high level of cohesive strength of the binder under prolonged loads.

Lu & Isacsson [11] found that the introduction of SBS promotes the formation of finely dispersed bee-like structures by stabilizing asphaltene aggregates. In this case, a two-phase structure is formed: a polymer grid and a bitumen matrix, where asphaltene aggregates are "embedded" in the polymer phase. This morphology of the bitumen binder leads to increased elasticity and improved cohesive strength [12].

The introduction of surfactants also has a pronounced effect on bitumen morphology by stabilizing asphaltene dispersion and preventing aggregation and formation of excessively large bee-like structures [6]. The use of cationic surfactants increases the stability of bitumen in the aquatic environment and promotes the formation of uniform fine bee-like structures; amphoteric surfactants effectively disperse asphaltenes and reduce the likelihood of flocculation. This leads to an increase in cohesive strength, especially in combination with polymer modification.

The addition of nanoparticles (SiO_2, TiO_2, nanoclay, graphene) makes it possible to significantly change the supramolecular architecture of bitumen. Xu *et al.* [13] showed that nanoparticles form a rigid framework around asphaltene aggregates. This prevents coalescence and growth of bee-like structures, contributing to the formation of a fine-grained, uniform morphology. As a result, there is a significant increase in the cohesive strength and resistance of bitumen to aging.

Modern research shows that the combined use of polymers and surfactants to modify bitumen binders makes it possible to achieve optimal morphology of bee structures: small bee-like structures; high uniformity of microstructure distribution in the bulk phase of bitumen; stability of the structure under seasonal temperature fluctuations. The synergistic effect of polymer and surface-active modifiers in bitumen provides maximum strength characteristics of the modified binder and durability of the asphalt concrete coatings being formed. So, in the work [14] it was found that the condition for achieving the minimum size of bee-like structures is the introduction of 1.0 g/dm^3 AG-4I and 1.0 g/dm^3 AS-1 into the bitumen; the average size of dispersions is 1.66 μm. In these concentration regimes, as a result of simultaneous exposure to AG-4I (polymer additive) and AS-1 (surfactant), fractions with a size of more than 4.0 μm were completely destroyed, and aggregates in the range 2.0-4.0 μm were destroyed two times; the content of fine fractions (≤2.0 μm) increased by 57.4% compared to virgin bitumen and amounted to 81.9%. A close correlation was revealed in the nature of changes in the dispersed composition of modified bitumen and the strength indicators of asphalt concrete samples. In the asphalt mixture sample made on the basis of the ternary composition “bitumen-AG-4IAS-1” (C_{AG-4I} =1.0 g/dm^3; C_{AS-1}=1.0 g/dm^3), the maximum increase in compressive strength was achieved with the smallest size of bee-like structures of modified bitumen. This

shows that the modifying role of additives is in the formation of dense, durable asphalt concrete, which is achieved due to the deep disaggregation of bitumen microdispersions and their uniform distribution over the entire volume of the binder.

Thus, controlling the size and homogeneity of bee-like structures is an important factor in the design of bitumen compositions.

CONCLUSION

Thus, summarizing the results of modern research, we can conclude:

- The size and morphology of the bee-like structures of bitumen are closely related to the strength of the asphalt concrete coatings being formed.
- The optimal size and uniform distribution of bee-like structures in the bitumen binder contribute to maximum strength, resistance to deformation and aging.
- Promising areas are combined approaches to modification and in-situ microstructure monitoring to optimize asphalt concrete formulations with the required performance characteristics.

REFERENCES

1. X. Yu, N.A. Burnham, M. Tao, *Adv. Colloid Interface Sci*., 218 (2015).
2. Q. Ouyang, Z. Xie, J. Liu, M. Gong, H. Yu, *Polymers,* **14**, 2851 (2022).
3. J. Hu, Q. Huang, N. Lou, S. Luo, *Materials,* **13**, 2558 (2020).
4. Y. Yuan, X. Zhu, K. Lee, Y. Deng, *Constr. Build. Mater.,* **237**, 117562 (2020).
5. W. Zhang, F. Wang, J. Shi, Z. Li, X. Liang, *Polymers*, **11**, 989 (2019).
6. D. Lesueur, *Adv. Colloid Interface Sci*., 145 (2009).
7. J.-F. Masson, V. Leblond, J. Margeson, S. Bundalo-Perc, *Fuel*, 85 (2006).
8. L. Loeber, O. Sutton, J. Morel, J.-M. Valleton, G. Muller, *Fuel*, **77**(8) (1998).
9. A.T. Pauli, J.F. Branthaver, W.D. Grimes, R.E. Robertson, *Transp. Res. Rec.*, 2208 (2011).
10. F. Zhang, J. Yu, J. Han, *Constr. Build.Mater.*, 203 (2019).
11. X. Lu, U. Isacsson, *Fuel*, **76**(9) (1997).
12. F. Zhang, J. Yu, J. Han, *Constr. Build. Mater.*, 203 (2019).
13. S. Xu, H. Zhu, X. Zhang, H. Yang, *Constr.Build. Mater.*, **238**, 117751 (2020).
14. A. Dyuryagina, Y. Byzova, K. Ostrovnoy, A. Demyanenko, V. Tyukanko, A. Lutsenko, *Polymers*, **16**, 1370 (2024).

Bulgarian Chemical Communications, Volume 57, Issue 3 (pp. 252-257) 2025 DOI: 10.34049/bcc.57.3.ZO-AK

Blanching and osmotic dehydration effects on lyophilized shrimp

Z. O. Ozyalcin, A. S. Kipcak*

Department of Chemical Engineering, Faculty of Chemical and Metallurgical Engineering, Yildiz Technical University, Istanbul, Türkiye

Accepted: September 10, 2025

Shrimp is the most widely consumed seafood worldwide, both as an ingredient in various dishes and as a tasty snack. Like many food products with high moisture content, shrimp are subjected to various drying processes. Among the drying systems, lyophilization is the method that preserves the nutritional values and the unique taste and texture of shrimp the most. In this study, the effects of blanching, blanching in saltwater and saltwater osmotic dehydration pretreatments on the lyophilization of shrimp were investigated. The effective moisture diffusion coefficient was calculated from the data obtained from the drying process and their compatibility with mathematical models was tested. Drying processes were completed between 240 - 360 min. It was observed that drying times could be reduced by blanching and osmotic dehydration pretreatments. In the compatibility with mathematical models, control and blanched samples fitted the Alibas model and osmotic dehydration samples fitted the Midilli & Kucuk model with R^2 values higher than 0.99999.

Keywords: Blanching; Freeze-drying; Osmotic dehydration; Saltwater; Shrimp

INTRODUCTION

Freeze-drying, also known as lyophilization, is a highly regarded method for dehydrating food, especially valuable for preserving delicate and high-quality products. This technique works by removing moisture through sublimation under low pressure, which helps maintain the food's original texture, nutrient content, and sensory characteristics—features often compromised in traditional drying processes [1, 2]. As it is a gentle process, freeze-drying is especially suitable for sensitive compounds commonly found in shrimp, such as omega-3 fatty acids, astaxanthin, and various bioactive peptides. Shrimp, like other seafood, is highly susceptible to spoilage due to its high water and protein content, as well as active endogenous enzymes. Without timely preservation, quality deteriorates rapidly. In this context, freeze-drying offers significant advantages: by drastically reducing water activity, it slows down microbial proliferation and enzymatic degradation—the main drivers of spoilage [1-5]. Research in recent years has confirmed that freeze-dried shrimp better retains its flavor, nutritional value, texture, and appearance compared to products processed through hot-air or vacuum drying [4, 6].

Despite its advantages, freeze-drying is known for being time- and energy-intensive, often requiring significant capital for equipment and operations [7]. To optimize the process and final product quality, various pre-treatment methods are employed, among which blanching and osmotic dehydration (OD) have proven effective. These techniques improve drying performance and product quality, offering benefits in terms of shelf life, nutrient retention, and sensory properties [8, 9].

Blanching, a short-term treatment involving exposure to hot water or steam, helps inactivating enzymes and altering the cell structure. This results in enhanced drying rates and better moisture diffusion during freeze-drying. Moreover, it aids in preserving color and reducing shrinkage. Products pre-treated with blanching generally show improved rehydration characteristics and reduced enzymatic browning, which contribute to superior texture and appearance [10, 11].

In contrast, osmotic dehydration involves placing food items in a concentrated solution, usually containing salt or sugar, to draw water out through osmosis. This not only pre-dehydrates the product but also helps preserve cell structure and nutritional value. OD-treated foods tend to retain better color and flavor while minimizing textural damage. For instance, studies on strawberries have shown that OD prior to freeze-drying enhances vitamin C content, antioxidant activity, and visual quality [8, 12, 13].

Mathematical modeling is another key area that supports the optimization of the freeze-drying

* To whom all correspondence should be sent:
E-mail: *skipcak@yildiz.edu.tr*

process. By applying heat and mass transfer models, researchers can predict drying kinetics and adjust parameters to minimize energy use while maximizing quality retention [14, 15]. Models typically describe the unsteady heat and mass transfer during freeze drying, involving coupled nonlinear partial differential equations to represent temperature and pressure profiles, and the position of the sublimation interface [16].

Various mathematical models are often used to study freeze-drying of seafoods. For example, squid, shrimp, mussels, and salmon have been investigated for their freeze-drying properties, effective moisture diffusivity, and quality parameters [14, 17]. The present research was conducted to fill the voids in the freeze-drying of shrimp utilizing blanching, blanching in saltwater, and osmotic dehydration pretreatments in saltwater. The effective moisture diffusion coefficient was determined using data acquired from the drying process, and its compatibility with ten established mathematical models was evaluated.

MATERIALS AND METHODS

Sample preparation

Frozen shrimp (sourced from Turkiye) were acquired from a local market and stored at a temperature of -18 ± 2 ℃ in a freezer (model 1050T; Arçelik, Eskişehir, Turkiye). Before the experiments, the shrimp were thawed at +4 ± 2 ℃ and subsequently allowed to equilibrate to room temperature in a desiccator. The shrimp samples were weighed using a AS 220.R2 digital balance (Radwag, Radom, Poland). The initial moisture content was assessed following the AOAC (2005) methodology [18], which involved drying the samples for a duration of 4 h at 105 °C in a KH-45 hot air oven (Kenton, Guangzhou, China).

Drying experiments

Shrimp samples were prepared with a weight of 5.0 ± 0.100 g across 9 sets of control and pretreatment conditions. For the blanching process, samples were submerged in beakers filled with 100 mL of deionized water at a temperature of 90°C for durations of 1 min (B–1 min) and 5 min (B–5 min). In the case of blanching using a 10% (w/v) salt solution, the samples were immersed for 1 min (B 10% – 1 min) and 5 min (B 10% – 5 min) in 100 mL of deionized water at 90 °C. For osmotic dehydration in salt solution at room temperature, the samples were placed in deionized aqueous solutions with 10% (w/v) salt and maintained for 5 min (OD 10% - 5 min), 10 min (OD 10% - 10 min) and with 20% (w/v) salt and maintained for 5 min (OD 20% - 5 min), 10 min (OD 20% - 10 min). Following the pretreatment procedures, any excess water was removed, and the samples were promptly transferred to a Labart LFD-10N freeze dryer (ART Laborteknik, Istanbul, Turkiye). Throughout the freeze-drying process, the vacuum within the drying chamber was released every 60 min, during which the samples were weighed and photographed within a time frame of less than 2 min. Subsequently, the samples were returned to the dryer, and the vacuum was reestablished. The drying process concluded, and the samples were vacuum-packed once their moisture content fell below 5% of their dry weight.

Mathematical modeling

The study of moisture diffusion during the drying process is based on Fick's second law which provides a mathematical basis for understanding how moisture travels through materials. This law is especially significant when drying processes are essential for maintaining product quality and stability. In the constant rate phase of drying, moisture is mainly extracted from the surface, while in the falling rate phase, internal diffusion takes precedence as moisture migrates from the interior to the surface [19].

The moisture content (M, kg water/kg dry matter) present in shrimp, along with its moisture ratio (MR, dimensionless), is described by Eqn. (1). In these equations, m_w denotes the quantity of water in the sample (kg), while m_d signifies the amount of dry matter (kg) [20].

$$M = \frac{m_w}{m_d} \quad (1)$$

In Equation (2), M_t indicates the moisture content at any specific time, M_0 refers to the initial moisture content, and M_e represents the moisture content at equilibrium. Given that the equilibrium moisture content is significantly lower than other moisture values, it has been disregarded in the calculations [21]:

$$MR = \frac{M_t - M_e}{M_0 - M_e} \quad (2)$$

The data collected from dried shrimp were analyzed utilizing the Statistica 8.0 software (StatSoft Tulsa, USA). Initially, the appropriateness of the model for all mathematical modeling approaches was assessed through regression parameters. One of the criteria employed to evaluate the fit of experimental data to the model equations is the coefficient of determination (R^2) value presented in Eqn. (3). An R^2 value

approaching 1 signifies a strong alignment between the data and the model [22]:

$$R^2 \equiv 1 - \frac{\sum_{i=1}^{N}\left(MR_{exp,i} - MR_{pre,i}\right)^2}{\sum_{i=1}^{N}\left(MR_{exp,i} - \left(\frac{1}{n}\right)\sum_{i=1}^{N} MR_{exp,i}\right)} \quad (3)$$

Additional evaluated criteria include the chi-square (χ^2), which represents the average of the squares of the drying data compared to the predicted data derived from the model equation, and the root mean square error (RMSE) which indicates the square root of the mean of the discrepancies between the drying data and the predicted values. The proximity of these values to 0, as defined in Eqns. (4) and (5), suggests a high degree of compatibility between the models and the drying data [23]:

$$\chi^2 = \frac{\sum_{i=1}^{N}\left(MR_{exp,i} - MR_{pre,i}\right)^2}{N - z} \quad (4)$$

$$RMSE = \left(\frac{1}{N}\sum_{i=1}^{N}\left(MR_{exp,i} - MR_{pre,i}\right)^2\right)^{\frac{1}{2}} \quad (5)$$

The terms MR_{exp} and MR_{pre}, as defined in Equations (3-5), denote the moisture ratio values derived from both experimental and model equations, respectively. The variable N signifies the total number of experiments conducted, while the variable z indicates the constant values utilized within the models.

Effective moisture diffusivity

During the drying process of food products, moisture is removed from the structure at either a constant or diminishing rate, revealing a complex mass transfer mechanism. Fick's second law of diffusion is commonly employed to ascertain the effective moisture diffusivity coefficient (D_{eff}) in food products (Eqn. 6). The value of D_{eff} is influenced by numerous factors, including the components present in the food structure, moisture content, drying temperature, and porosity of the food [24]:

$$\frac{\partial M}{\partial t} = \nabla\left[D_{eff}(\nabla M)\right] \quad (6)$$

The effective moisture diffusivity (D_{eff}) can be determined from the slope of the ln(MR) *versus* time plot (Eqn. 7):

$$\ln(MR) = \ln\left(\frac{6}{\pi^2}\right) - \left(\pi^2 \frac{D_{eff} \times t}{R^2}\right) \quad (7)$$

Ten mathematical models, the formulations of which are presented in Table 1, were employed to assess the compatibility of the models commonly studied in drying processes.

RESULTS AND DISCUSSION

Table 2 presents the initial and final moisture contents, along with the drying durations, for shrimp samples subjected to various pretreatment methods prior to freeze-drying. The initial moisture content ranged from 77.47% to 86.42%, corresponding to an initial moisture load of 3.4382 to 6.3626 kg water / kg dry matter (DM). These variations reflect the influence of different pretreatment conditions on the water-holding capacity of the samples.

Table 1. Mathematical model equations [21, 24]

Model name	Model equation
Aghbaslo *et al.*	$MR = exp\ (-k_1t/(1 + k_2t))$
Alibas	$MR = a.exp\ ((-kt^n) + bt) + g$
Jena and Das	$MR = a.exp\ (-kt + b\sqrt{t}) + c$
Lewis	$MR = exp\ (-kt)$
Logarithmic	$MR = a.exp\ (-kt) + c$
Midilli & Kucuk	$MR = a.exp\ (-kt^n) + bt$
Page	$MR = exp\ (-kt^n)$
Parabolic	$MR = a + bt + ct^2$
Wang and Singh	$MR = 1 + at + b\,t^2$
Two-term Exponential	$MR = a.\ exp\ (-kt) + (1-a).\ exp\ (-kat)$

*a, b, c, g, are coefficients; n is the drying exponent unique to each equation; k, k_1, k_2, are drying coefficients specific to each equation; t indicates time (min).

The control group, which received no pretreatment, exhibited an initial moisture content of 86.02% and required 360 min of freeze-drying to reach a final moisture content of 0.053 kg W/kg DM. Similarly, B–5 min sample showed a comparable initial moisture level (86.42%) but achieved a significantly lower final moisture (0.0047 kg W/kg DM), suggesting enhanced drying efficiency. B–5 min reduced the initial moisture content to 82.22% and required 300 min of drying, resulting in a final moisture content of 0.1167 kg W/kg DM. Samples treated with 10% salt solution (B10%–1 min and B10%–5 min) displayed progressively lower initial moisture levels (84.21% and 77.47%, respectively), with the 5-min sample requiring only 240 min to dry, indicating a substantial acceleration in moisture removal.

In contrast, osmotic dehydration (OD) treatments demonstrated a different pattern. The OD 10% – 5 min and OD 10% – 10 min samples had moderate initial moisture levels (~82–83%) but resulted in higher final moisture contents (0.515 and 0.1181 kg W/kg DM, respectively), suggesting that osmotic pretreatment may hinder complete

water removal, potentially due to solute uptake affecting water mobility. OD 20% treatments (5 and 10 min) led to higher initial moisture values (~84%) and required 300 and 240 min of drying, respectively, but still retained higher final moisture (0.29 and 0.1934 kg W/kg DM) compared to the control.

The temporal variation of moisture content and the relationship between moisture content and drying rate are presented in Figures 1 and 2. As depicted in Figure 2, it is evident that the pretreated samples transitioned into the falling rate period sooner, attributable to their elevated moisture content. Table 3 presents the compatibility results of best-fitted mathematical models with R^2 values over 0.9999.

Table 2. Drying data of shrimp

Sample	Initial moisture (%)	Initial moisture (kg W / kg DM)	Drying time (min)	Final moisture (kg W / kg DM)
Control	86.02	6.1507	360	0.0530
B – 1 min	86.42	6.3626	360	0.0047
B – 5 min	82.22	4.6255	300	0.1167
B 10% – 1 min	84.21	5.3317	360	0.0650
B 10% – 5 min	77.47	3.4382	240	0.0896
OD 10% – 5 min	83.05	4.9012	300	0.5150
OD 10% – 10 min	81.97	4.5471	300	0.1181
OD 20% – 5 min	84.86	5.6067	300	0.2900
OD 20% – 10 min	84.28	5.3613	240	0.1934

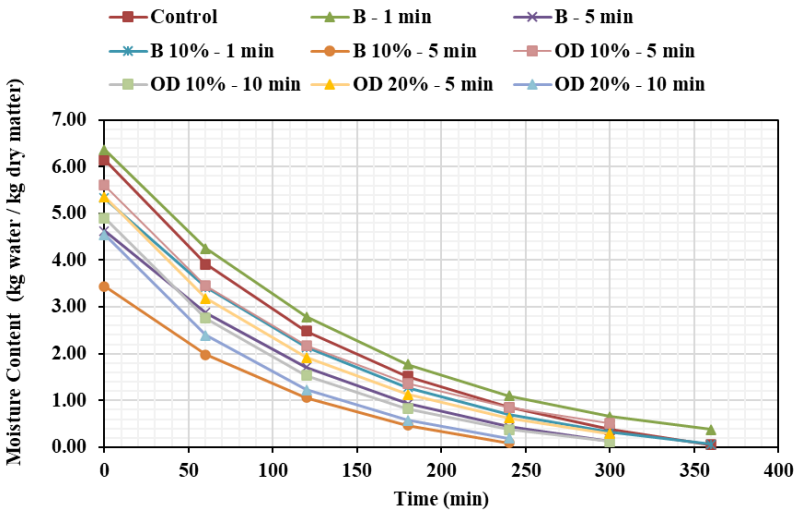

Figure 1. Moisture content *vs.* drying rate graph of freeze-drying shrimp

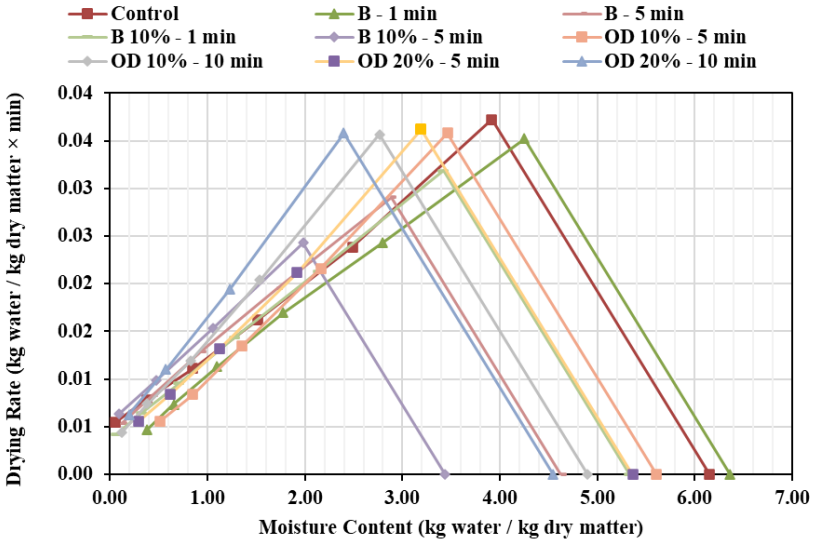

Figure 2. Drying rate *vs*. moisture content graph of freeze-drying shrimp

Table 3. Mathematical model constants and statistical parameters of freeze-dried shrimp

Sample	Model	R^2	χ^2	RMSE
Control	Alibas	0.99999998	0.0000001	0.000182
	Midilli & Kucuk	0.99999641	0.0000009	0.000626
	Verma *et al.*	0.99998960	0.0000040	0.001518
B - 1 min	Alibas	0.99999772	0.0000010	0.000479
	Aghbashlo *et al.*	0.99999234	0.0000011	0.000877
	Logarithmic	0.99993275	0.0000120	0.002599
B - 5 min	Alibas	0.99999945	0.0000002	0.000232
	Verma *et al.*	0.99999929	0.0000001	0.000263
	Midilli & Kucuk	0.99999391	0.0000014	0.000771
B %10 - 1 min	Alibas	0.99999975	0.0000001	0.000167
	Logarithmic	0.99999601	0.0000012	0.000697
	Midilli & Kucuk	0.99999359	0.0000016	0.000839
B %10 - 5 min	Alibas	0.99999991	0.0000001	0.000001
	Midilli & Kucuk	0.99999915	0.0000005	0.000321
	Logarithmic	0.99999601	0.0000012	0.000697
OD %10 - 5 min	Alibas	0.99999870	0.0000008	0.000356
	Midilli & Kucuk	0.99999663	0.0000010	0.000574
	Verma *et al.*	0.99998827	0.0000023	0.001072
OD %10 - 10 min	Alibas	0.99999629	0.0000025	0.000649
	Midilli & Kucuk	0.99999622	0.0000013	0.000655
	Verma *et al.*	0.99999162	0.0000019	0.000976
OD %20 - 5 min	Midilli & Kucuk	0.99999997	0.00000001	0.000018
	Aghbashlo *et al.*	0.99972728	0.0000433	0.005374
	Verma *et al.*	0.99927421	0.0001537	0.008767
OD %20 - 10 min	Midilli & Kucuk	0.99999951	0.0000003	0.000241
	Verma *et al.*	0.99999810	0.0000006	0.000476
	Logarithmic	0.99997934	0.0001115	0.001569

Among the tested models, the Alibas and the Midilli & Kucuk models consistently outperformed others across nearly all sample groups, achieving the highest coefficients of determination (R^2) and the lowest error metrics (χ^2 and RMSE). This consistency indicates that these models are highly effective at capturing the complex moisture dynamics during freeze-drying, regardless of whether the shrimp underwent boiling or osmotic dehydration.

Notably, the Midilli & Kucuk model showed exceptional performance in samples treated with ultrasound-assisted osmotic dehydration at higher concentrations and durations (e.g., OD %20 – 5 min), with near-perfect R^2 and minimal errors, suggesting that this model is particularly suited to capturing the enhanced moisture diffusion effects introduced by ultrasound treatment.

CONCLUSION

This study examined the freeze-drying properties of shrimp that had been blanched, blanched in salt water, osmotically dehydrated, and control samples. The drying durations were found between 240 - 360 min. Overall, blanching and blanching in salt water pretreatments enhanced moisture diffusivity and drying efficiency, while osmotic dehydration appeared less effective in reducing the final moisture content under the given conditions. When the compatibility of mathematical models with freeze-drying data was examined, the Alibas and the Midilli & Kucuk models yielded the best fit.

REFERENCES

1. D. Dziki, *Processes*, **8**, 1661 (2020).
2. S. Latif, M. Sohaib, S. Iqbal, M. H. Mushtaq, M. T. Sultan, *AIMS Agric. Food*, **10**, 247 (2025).
3. C. Aktar, G. N. Ural, A. H. M. Kaya, O. K. Topuz, *Acta Aliment.*, **53**, 464 (2024).
4. D. Y. Li, D. Y. Zhou, F. W. Yin, X. P. Dong, H. K. Xie, Z. Y. Liu, F. Shahidi, *J. Sci. Food Agric.*, **100**, 2544 (2020).
5. S. Mašić, I. Vujčić, *Nukleonika*, **66**, 4 (2021).
6. X. Xuan, L. Wen, Y. Cui, H. Shang, X. Lin, J. Ling, *Sci. Technol. Food Ind.*, **40**, 79 (2019).
7. T. Zhu, F. Jameel, P. Pibulchinda, V. Kshirsagar, A. Alexeenko, in *Principles and Practices of Lyophilization in Product Development and Manufacturing*, Springer, Cham, 2023, p. 405.
8. R. M. Putri, M. A. F. Falah, *IOP Conf. Ser.: Earth Environ. Sci.*, **1200**, 012030 (2023).
9. A. Ciurzyńska, A. Lenart, *Żywność Nauka Technol. Jakość*, **20**, (2013).
10. F. Richter Reis, in: New Perspectives on Food Blanching, 2017, p. 123.
11. S. S. Ferreira, F. Monteiro, C. P. Passos, A. M. Silva, D. F. Wessel, M. A. Coimbra, S. M. Cardoso, *Food Res. Int.*, **132**, 109055 (2020).
12. B. D. S. Pinto, A. C. C. D. Melo, E. F. D. Costa Jr., A. O. S. D. Costa, *Ciênc. Rural*, **53**, e20200935 (2022).
13. S. Malakar, T. Manonmani, S. Deb, K. K. Dash, in Food Processing, CRC Press, 2021, p. 67.
14. Z. O. Ozyalcin, E. Güles, D. Uygunoz, F. Bozkurt, O. Sagdic, I. Doymaz, A. S. Kipcak, *TrJFAS*, **25**, 2 (2024).
15. S. Sevim, Z. O. Ozyalcin, A. S. Kipcak, *TrJFAS*, **23**, 12 (2023).
16. P. Levin, M. Buchholz, V. Meunier, U. Kessler, S. Palzer, S. Heinrich, *Processes*, **10**, 548 (2022).
17. E. Midik, Z. O. Ozyalcin, A. S. Kipcak, *J. Chem. Technol.*, **33**, 136 (2025).
18. AOAC, Official Method of Analy*sis*, 18th edn., Association of Officiating Analytical Chemists, Washington DC, 2005.
19. Z. O. Ozyalcin, A. S. Kipcak, *Bulg. Chem. Commun.*, **55**, 234 (2023).
20. Z. O. Ozyalcin, A. S. Kipcak, *TrJFAS*, **21**, 135 (2021).
21. A. Ersan, A. S. Kipcak, N. Tugrul, *J. Food Sci. Technol.*, **61**, 1 (2024).
22. S. Kipcak, O. Ismail, *J. Food Sci. Technol.*, **58**, 281 (2021).
23. Z. O. Ozyalcin, A. S. Kipcak, N. Tugrul, *J. Aquat. Food Prod.*, **32**, 384 (2023).
24. A. S. Kipcak, I. Doymaz, *Int. J. Fruit Sci.*, **20**, S1222 (2020).
25. Z. O. Ozyalcin, A. S. Kipcak, *J. Aquat. Food Prod.*, **31**, 187 (2022)

Instructions about Preparation of Manuscripts

General remarks: Manuscripts are submitted in English by e-mail. The text must be prepared in A4 format sheets using Times New Roman font size 11, normal character spacing. The manuscript should not exceed 15 pages (about 3500 words), including photographs, tables, drawings, formulae, etc. Authors are requested to use margins of 2 cm on all sides.

Manuscripts should be subdivided into labelled sections, e.g. INTRODUCTION, EXPERIMENTAL, RESULTS AND DISCUSSION, etc. **The title page** comprises headline, author(s)' names and affiliations, abstract and key words. Attention is drawn to the following:

a) **The title** of the manuscript should reflect concisely the purpose and findings of the work. Abbreviations, symbols, chemical formulae, references and footnotes should be avoided. If indispensable, abbreviations and formulae should be given in parentheses immediately after the respective full form.

b) **The author(s)'** first and middle name initials and family name in full should be given, followed by the address (or addresses) of the contributing laboratory (laboratories). **The affiliation** of the author(s) should be listed in detail (no abbreviations!). The author to whom correspondence and/or inquiries should be sent should be indicated by an asterisk (*) with e-mail address.

The abstract should be self-explanatory and intelligible without any references to the text and containing up to 250 words. It should be followed by keywords (up to six).

References should be numbered sequentially in the order, in which they are cited in the text. The numbers in the text should be enclosed in brackets [2], [5, 6], [9−12], etc., set on the text line. References are to be listed in numerical order on a separate sheet. All references are to be given in Latin letters. The names of the authors are given without inversion. Titles of journals must be abbreviated according to Chemical Abstracts and given in italics, the volume is typed in bold, the initial page is given and the year in parentheses. Attention is drawn to the following conventions: a) The names of all authors of a certain publications should be given. The use of "et al." in the list of references is not acceptable; b) Only the initials of the first and middle names should be given. In the manuscripts, the reference to author(s) of cited works should be made without giving initials, e.g. "Bush and Smith [7] pioneered...". If the reference carries the names of three or more authors it should be quoted as "Bush et al. [7]", if Bush is the first author, or as "Bush and co-workers [7]", if Bush is the senior author.

Footnotes should be reduced to a minimum. Each footnote should be typed double-spaced at the bottom of the page, on which its subject is first mentioned. **Tables** are numbered with Arabic numerals on the left-hand top. Each table should be referred to in the text. Column headings should be as short as possible but they must define units unambiguously. The units are to be separated from the preceding symbols by a comma or brackets. Note: The following format should be used when figures, equations, etc. are referred to the text (followed by the respective numbers): Fig., Eqns., Table, Scheme.

Schemes and figures. Each manuscript should contain or be accompanied by the respective illustrative material, as well as by the respective figure captions in a separate file. As far as presentation of units is concerned, SI units are to be used. However, some non-SI units are also acceptable, such as °C, ml, l, etc. Avoid using more than 6 (12 for review articles) figures in the manuscript. Since most of the illustrative materials are to be presented as 8-cm wide pictures, attention should be paid that all axis titles, numerals, legend(s) and texts are legible.

The authors are required to submit the text with a list of three individuals and their e-mail addresses that can be considered by the Editors as potential reviewers. Please note that the reviewers should be outside the authors' own institution or organization. The Editorial Board of the journal is not obliged to accept these proposals.

The authors are asked to submit **the** final text (after the manuscript has been accepted for publication) in electronic form by e-mail. The main text, list of references, tables and figure captions should be saved in separate files (as *.rtf or *.doc) with clearly identifiable file names. It is essential that the name and version of the word-processing program and the format of the text files is clearly indicated. It is recommended that the pictures are presented in *.tif, *.jpg, *.cdr or *.bmp format. The equations are written using "Equation Editor" and chemical reaction schemes are written using ISIS Draw or ChemDraw programme.

EXAMPLES FOR PRESENTATION OF REFERENCES

REFERENCES

1. D. S. Newsome, Catal. Rev.–Sci. Eng., 21, 275 (1980).
2. C.-H. Lin, C.-Y. Hsu, J. Chem. Soc. Chem. Commun., 1479 (1992).
3. R. G. Parr, W. Yang, Density Functional Theory of Atoms and Molecules, Oxford Univ. Press, New York, 1989.
4. V. Ponec, G. C. Bond, Catalysis by Metals and Alloys (Stud. Surf. Sci. Catal., vol. 95), Elsevier, Amsterdam, 1995.
5. G. Kadinov, S. Todorova, A. Palazov, in: New Frontiers in Catalysis (Proc. 10th Int. Congr. Catal., Budapest (1992), L. Guczi, F. Solymosi, P. Tetenyi (eds.), Akademiai Kiado, Budapest, 1993, Part C, p. 2817.
6. G. L. C. Maire, F. Garin, in: Catalysis. Science and Technology, J. R. Anderson, M. Boudart (eds.), vol. 6, Springer Verlag, Berlin, 1984, p. 161.
7. D. Pocknell, GB Patent 2 207 355 (1949).
8. G. Angelov, PhD Thesis, UCTM, Sofia, 2001, pp. 121-126.
9. JCPDS International Center for Diffraction Data, Power Diffraction File, Swarthmore, PA, 1991.
10. CA 127, 184 762q (1998).
11. P. Hou, H. Wise, J. Catal., in press.
12. M. Sinev, private communication.
13. http://www.chemweb.com/alchem/articles/1051611477211.html.

Texts with references which do not match these requirements will not be considered for publication!!!

Papers presented at the 11th International Conference on New Trends in Chemistry, April 25-27, 2025, Bologna, Italy

CONTENTS